

---

2           **Consolidation and longevity of the CMS**  
3           **Resistive Plate Chamber system in view of the**  
4           **High-Luminosity LHC Upgrade**

---

5



Alexis Fagot

Thesis to obtain the degree of  
Doctor of Philosophy in Physics  
Academic year 2018-2019





<sup>7</sup>

<sup>8</sup> Promotors: Dr. Michael Tytgat  
Prof. Dr. Dirk Ryckbosch

<sup>9</sup>  
<sup>10</sup> Ghent University  
<sup>11</sup> Faculty of Sciences  
<sup>12</sup> Department of Physics and Astronomy  
<sup>13</sup> Proeftuinstraat 86, B-9000 Ghent, Belgium  
<sup>14</sup> Tel.: +32 9 264.65.28  
<sup>15</sup> Fax.: +32 9 264.66.97

<sup>16</sup>



Alexis Fagot

Thesis to obtain the degree of  
Doctor of Philosophy in Physics  
Academic year 2018-2019





17

## Acknowledgements

18

19

*XX/XX/2018*

*Alexis Fagot*



# Table of Contents

21	<b>Acknowledgements</b>	i
22	<b>Nederlandse samenvatting</b>	vii
23	<b>English summary</b>	ix
24	<b>1 Introduction</b>	1-1
25	<b>2 Investigating the TeV scale</b>	2-1
26	2.1 The Standard Model of Particle Physics . . . . .	2-1
27	2.1.1 A history of particle physics . . . . .	2-2
28	2.1.2 Construction and validation of the Standard Model . . . . .	2-14
29	2.1.3 Investigating the TeV scale . . . . .	2-15
30	2.2 The Large Hadron Collider & the Compact Muon Solenoid . . . . .	2-20
31	2.2.1 LHC, the most powerful particle accelerator . . . . .	2-20
32	2.2.2 Timeline of operation . . . . .	2-23
33	2.2.3 High Luminosity LHC . . . . .	2-25
34	2.2.4 The Compact Muon Solenoid experiment . . . . .	2-25
35	2.2.4.1 The silicon tracker . . . . .	2-27
36	2.2.4.2 The calorimeters . . . . .	2-27
37	2.2.4.3 The muon system . . . . .	2-28
38	<b>3 Muon Phase-2 Upgrade</b>	3-1
39	3.1 Motivations for HL-LHC and the upgrade of CMS . . . . .	3-1
40	3.2 Description of the muon system . . . . .	3-5
41	3.2.1 The Drift Tubes . . . . .	3-5
42	3.2.2 The Cathode Strip Chambers . . . . .	3-6
43	3.2.3 The Resistive Plate Chambers . . . . .	3-7
44	3.3 Necessity for improved electronics . . . . .	3-8
45	3.4 New detectors and increased acceptance . . . . .	3-10
46	3.4.1 Gas electron multipliers . . . . .	3-12
47	3.4.2 Improved forward resistive plate chambers . . . . .	3-15
48	3.5 Impact on Level-1 Trigger and physics performance . . . . .	3-17
49	3.6 Ecofriendly gas studies . . . . .	3-20
50	<b>4 Physics of Resistive plate chambers</b>	4-1
51	4.1 Principle . . . . .	4-1
52	4.2 Rate capability and time resolution of Resistive Plate Chambers . . . . .	4-3
53	4.2.1 Operation modes . . . . .	4-3
54	4.2.2 Standard gas mixture for RPCs operated in collider experiments . . . . .	4-5
55	4.2.3 Detector designs and performance . . . . .	4-9

---

56	4.2.3.1	Double-gap RPC . . . . .	4-12
57	4.2.3.2	Multigap RPC (MRPC) . . . . .	4-13
58	4.2.3.3	Charge distribution and performance limitations . . . . .	4-17
59	4.3	Signal formation . . . . .	4-19
60	4.3.1	Energy loss at intermediate energies . . . . .	4-20
61	4.3.2	Primary ionization . . . . .	4-24
62	4.3.3	Development and propagation of avalanches . . . . .	4-28
63	4.3.4	Drift and diffusion of the electron cloud . . . . .	4-32
64	4.3.5	Space charge effect & streamers . . . . .	4-34
65	4.4	Effect of atmospherical conditions on the detector's performance . . . . .	4-38
66	<b>5</b>	<b>Longevity studies and Consolidation of the present CMS RPC subsystem</b>	<b>5-1</b>
67	5.1	Testing detectors under extreme conditions . . . . .	5-2
68	5.1.1	GIF . . . . .	5-4
69	5.1.2	GIF++ . . . . .	5-5
70	5.2	Preliminary studies at GIF . . . . .	5-7
71	5.2.1	RPC test setup . . . . .	5-7
72	5.2.2	Geometrical acceptance of the setup layout to cosmic muons . . . . .	5-9
73	5.2.2.1	Description of the simulation layout . . . . .	5-10
74	5.2.2.2	Simulation procedure . . . . .	5-11
75	5.2.2.3	Results and limitations . . . . .	5-12
76	5.2.3	Photon flux at GIF . . . . .	5-14
77	5.2.4	Results and discussions . . . . .	5-17
78	5.3	Longevity tests at GIF++ . . . . .	5-20
79	5.3.1	Selection and characterization of CMS RPCs for longevity at GIF++ . . . . .	5-20
80	5.3.2	RPC test setup . . . . .	5-22
81	5.3.3	GIF++ data flow . . . . .	5-24
82	5.3.4	Measurements performed during beam periods . . . . .	5-26
83	5.3.4.1	Efficiency scans . . . . .	5-26
84	5.3.4.2	Rate scans . . . . .	5-26
85	5.3.4.3	Offline analysis and Data Quality Monitoring . . . . .	5-27
86	5.3.5	Measurements performed during irradiation periods . . . . .	5-28
87	5.3.5.1	Longevity scans . . . . .	5-29
88	5.3.5.2	Daily rate monitoring scans . . . . .	5-30
89	5.3.5.3	Weekly noise monitoring scans . . . . .	5-31
90	5.3.5.4	Weekly source scans . . . . .	5-31
91	5.3.5.5	Weekly current scans . . . . .	5-32
92	5.3.5.6	Resistivity measurements . . . . .	5-32
93	5.3.6	Results and discussions . . . . .	5-32
94	<b>6</b>	<b>Improved RPC investigation and preliminary electronics studies</b>	<b>6-1</b>
95	6.1	FEE candidate for the production of iRPCs . . . . .	6-1
96	6.1.1	CMS RPCROC: the RPC upgrade baseline . . . . .	6-2
97	6.1.2	INFN Front-End Electronics: a robust back-up solution . . . . .	6-3
98	6.2	Preliminary tests at CERN . . . . .	6-3
99	<b>7</b>	<b>Conclusions and outlooks</b>	<b>7-1</b>
100	7.1	Conclusions . . . . .	7-1
101	7.2	Outlooks . . . . .	7-1

---

<b>A</b>	<b>A data acquisition software for CAEN VME TDCs</b>	<b>A-1</b>
102	A.1 GIF++ DAQ file tree . . . . .	A-1
103	A.2 Usage of the DAQ . . . . .	A-2
104	A.3 Description of the readout setup . . . . .	A-3
105	A.4 Data read-out . . . . .	A-3
106	A.4.1 V1190A TDCs . . . . .	A-4
107	A.4.2 DataReader . . . . .	A-7
108	A.4.3 Data quality flag . . . . .	A-10
109	A.5 Communications . . . . .	A-12
110	A.5.1 V1718 USB Bridge . . . . .	A-13
111	A.5.2 Configuration file . . . . .	A-14
112	A.5.3 WebDCS/DAQ intercommunication . . . . .	A-17
113	A.5.4 Example of inter-process communication cycle . . . . .	A-17
114	A.6 Software export . . . . .	A-18
115		
116	<b>B</b>	<b>B-1</b>
117	B.1 GIF++ Offline Analysis file tree . . . . .	B-1
118	B.2 Usage of the Offline Analysis . . . . .	B-2
119	B.2.1 Output of the offline tool . . . . .	B-3
120	B.2.1.1 ROOT file . . . . .	B-3
121	B.2.1.2 CSV files . . . . .	B-5
122	B.3 Analysis inputs and information handling . . . . .	B-6
123	B.3.1 Dimensions file and IniFile parser . . . . .	B-7
124	B.3.2 TDC to RPC link file and Mapping . . . . .	B-8
125	B.4 Description of GIF++ setup within the Offline Analysis tool . . . . .	B-9
126	B.4.1 RPC objects . . . . .	B-9
127	B.4.2 Trolley objects . . . . .	B-10
128	B.4.3 Infrastructure object . . . . .	B-10
129	B.5 Handeling of data . . . . .	B-12
130	B.5.1 RPC hits . . . . .	B-13
131	B.5.2 Clusters of hits . . . . .	B-14
132	B.6 DAQ data Analysis . . . . .	B-15
133	B.6.1 Determination of the run type . . . . .	B-16
134	B.6.2 Beam time window calculation for efficiency runs . . . . .	B-17
135	B.6.3 Data loop and histogram filling . . . . .	B-18
136	B.6.4 Results calculation . . . . .	B-21
137	B.6.4.1 Rate normalisation . . . . .	B-21
138	B.6.4.2 Rate and activity . . . . .	B-23
139	B.6.4.3 Correction of muon performance parameters . . . . .	B-25
140	B.6.4.4 Strip masking tool . . . . .	B-27
141	B.6.4.5 Output CSV files filling . . . . .	B-29
142	B.7 Current information extraction . . . . .	B-31



143

## Nederlandse samenvatting –Dutch Summary–

144



## English summary



# List of Figures

146

- |     |      |   |      |
|-----|------|---|------|
| 147 | 2.1  | Solar spectrum with spectral lines as it visually appeared to Fraunhofer. . . . .   | 2-2  |
| 148 | 2.2  | Through the gold foil experiment, Rutherford could show that most of the mass of atoms was contained in a positively charged nucleus and could then propose a more accurate atomic model than that of Thomson. . . . .  | 2-3  |
| 150 |      |   |      |
| 151 | 2.3  | Figure 2.3a: The orbits in which the electron may travel according to the Bohr model of the hydrogen atom. An electron jumps between orbits and is accompanied by an emitted or absorbed amount of electromagnetic energy ( $h\nu$ ). The orbits radius increases as $n^2$ . Figure 2.3b: Elliptical orbits with the same energy and quantized angular momentum $l = 0, 1, \dots, n - 1$ in the case $n = 5$ . Figure 2.3c: Illustration of quantum mechanical orbital angular momentum. The cones and plane represent possible orientations of the angular momentum vector for $l = 2$ and $m = -2, -1, 0, 1, 2$ . | 2-5  |
| 152 |      |   |      |
| 153 |      |   |      |
| 154 |      |   |      |
| 155 |      |   |      |
| 156 |      |   |      |
| 157 |      |   |      |
| 158 | 2.4  | Figure 2.4a: The spectral lines of mercury vapor lamp anomalous Zeeman effect without magnetic field (A) and with magnetic field (B - transverse Zeeman effect & C - longitudinal Zeeman effect). Figure 2.4b: Stern-Gerlach experiment: Silver atoms traveling through an inhomogeneous magnetic field and being deflected up or down depending on their spin. . . . .   | 2-6  |
| 159 |      |   |      |
| 160 |      |   |      |
| 161 |      |   |      |
| 162 |      |   |      |
| 163 | 2.5  | Figure 2.5a: decay of a $\mu$ -meson in an emulsion. Figure 2.5b: track of a $\pi$ -meson in an emulsion signed by Lattes, Powell, and Occhialini. . . . .  | 2-8  |
| 164 |      |   |      |
| 165 | 2.6  | Figure 2.6a: Meson octet. Figure 2.6b: Baryon octet. Figure 2.6c: Baryon decuplet. .  | 2-9  |
| 166 |      |   |      |
| 167 | 2.7  | Discovery of the $J/\Psi$ by both SPEAR (SLAC [74]) in Figure 2.7a and AGS (BNL [75]) in Figure 2.7b. In Figure 2.7a, the cross section versus energy is showed for (a) multi hadron final states, (b) $e^+e^-$ final states, and (c) $\mu^+\mu^-, \pi^+\pi^-$ and $K^+K^-$ final states.   | 2-10 |
| 168 |      |   |      |
| 169 | 2.8  | Figure 2.8a: the color field of QCD only allows for "white" baryons, particles composed of quarks, to exist. Examples are given for mesons, composed of a quark and its anti-quark, and hadrons, composed of three differently colored quarks or anti-quarks. Other exotic baryons have been predicted and observed, such as tetraquarks and pentaquarks. Figure 2.8b: a crossed analysis performed thanks to the data collected by various experiments at different energies have showed that the coupling constant evolves as predicted by the mechanism of asymptotic freedom [87]. . . . .                      | 2-11 |
| 170 |      |   |      |
| 171 |      |   |      |
| 172 |      |   |      |
| 173 |      |   |      |
| 174 |      |   |      |
| 175 |      |   |      |
| 176 | 2.9  | Energy spectrum of beta particles emitted by a source of $^{210}Bi$ . . . . .   | 2-12 |
| 177 | 2.10 | As explained through Figure 2.10a, the Wu experiment consisted in measuring the preferred direction of emission of beta rays of a Cobalt source placed in a stable magnetic field aligned, in one case, and anti-aligned, in the other case, with the nuclear spin. The result of Figure 2.10b showed a violation of parity. . . . .  | 2-13 |
| 178 |      |   |      |
| 179 |      |   |      |
| 180 |      |   |      |

181	2.11	The elementary particles of the Standard Model are shown along with their properties. Their interactions with the strong, weak and electromagnetic forces have been made explicit using color squares. In the left column, the scalar Higgs boson is depicted. The center is focused on the matter particles, the fermions, and the right column on the force carriers, the gauge bosons. The role of the Higgs boson in electroweak symmetry breaking is highlighted, and the corresponding way properties of the various particles differ in the (high-energy) symmetric phase (top) and the (low-energy) broken-symmetry phase (bottom) are shown. . . . .	2-15
182			
183			
184			
185			
186			
187			
188			
189	2.12	Figure 2.12a: Total proton-proton cross-section as a function of the collisions center-of-mass energy $\sqrt{s}$ [116] with cosmic-ray data from Akeno Observatory and Fly's Eye Collaboration. Figure 2.12b: Total proton-(anti)proton and interaction channel cross-sections in the TeV scale. . . . .	2-16
190			
191			
192			
193	2.13	Rotation curve (points) of the galaxy M33 compared with best fitting model (line). The short-dashed line represents the rotation profile that would be expected from the observation of the stellar disc alone [128]. . . . .	2-17
194			
195			
196	2.14	Cosmic Microwave Background as measured by the space observatory Planck which mean temperature is $T_\gamma = (2.7255 \pm 0.0006)\text{K}$ with anisotropies of the order of a few $\mu\text{K}$ . . . . .	2-18
197			
198			
199	2.15	CERN accelerator complex. . . . .	2-20
200			
201	2.16	Pictures of the different accelerators. From top to bottom: first the LINAC 2 and the $Pb$ source of LINAC 3. Then the Booster and the LEIR. Finally, the PS, the SPS and the LHC. . . . .	2-21
202			
203	2.17	Figure 2.17a: schematics of the LHC cryodipoles. 1: Superconducting Coils, 2: Beam pipe, 3: Heat exchanger Pipe, 4: Helium-II Vessel, 5: Superconducting Bus-bar, 6: Iron Yoke, 7: Non-Magnetic Collars, 8: Vacuum Vessel, 9: Radiation Screen, 10: Thermal Shield, 11: Auxiliary Bus-bar Tube, 12: Instrumentation Feed Throughs, 13: Protection Diode, 14: Quadrupole Bus-bars, 15: Spool Piece Bus-bars. Figure 2.17b: magnetic field and resulting motion force applied on the beam particles. . . . .	2-22
204			
205			
206			
207			
208			
209			
210	2.18	The LHC quadrupoles (Figure 2.18a) showed together with the magnetic fields and resulting focussing force applied on the beam by two consecutive quadrupoles (Figure 2.18b). . . . .	2-23
211			
212			
213	2.19	Distribution of the four-lepton invariant mass for the $ZZ \rightarrow 4l$ analysis as presented by both ATLAS [112] and CMS [113] in 2012. . . . .	2-23
214			
215	2.20	Detailed timeline projection of LHC and HL-LHC operation until 2039 showing the evolution of the instantaneous and integrated luminosity as designed (Figure 2.20a) and in the ultimate case where the instantaneous luminosity is increased to $7.5 \times 10^{34}\text{cm}^{-2}\text{s}^{-1}$ thanks to a new increase of instantaneous luminosity during Run 5 (Figure 2.20b) [175–177]. . . . .	2-24
216			
217			
218			
219			
220	2.21	Picture of the CMS barrel. The red outer layer is the muon system hosted into the red iron return yokes. The calorimeters are the blue cylinder inside in magnet solenoid and the tracker is the inner yellow cylinder built around the beam pipe. . . . .	2-26
221			
222			
223	2.22	View of the CMS apparatus and of its different components. . . . .	2-26
224			
225	2.23	Slice showing CMS sub-detectors and how particles interact with them. . . . .	2-27
226			
227	2.24	The CMS tracker. . . . .	2-27
228	2.25	Figure 2.25a: The electromagnetic calorimeter. Figure 2.25b: The lead tungstate crystals composing the ECAL. . . . .	2-28
	2.26	The CMS hadron calorimeter barrel. . . . .	2-28

229	2.27	A quadrant of the muon system, showing DTs (yellow), RPCs (blue), and CSCs (green). . . . .	2-29
230			
231	3.1	The measured transit time of an HSCP in CMS is compared to the transit time of a particle traveling at near the speed of light [177]. . . . .	3-2
232			
233	3.2	Slice of the CMS detector showing examples of passage of SM particles and R-hadrons. On the one hand, lepton-like HSCPs will appear to behave like slow and heavy muons. On the other hand, R-hadrons are likely to convert into other kind of charged or neutral R-hadrons due to interactions inside the detector volume. . . . .	3-2
234			
235	3.3	Distribution of the energy-loss $dE/dx$ as described by Bethe-Bloch formula through the estimator $I_h$ with increasing particle momentum for tracks in the 13 TeV data. The estimator depends on the charge deposition of the particles per unit length in the silicon detectors of CMS which is related to their energy loss as explained in a publication by the CMS Collaboration [181]. The simulated HSCPs are singly or multiply charged particles with masses of 400 and 1000 GeV. . . . .	3-3
236			
237	3.4	Distribution of the average number of interactions per crossing (pileup) for pp-collisions in 2011 (red), 2012 (blue), 2015 (purple), 2016 (orange), 2017 (light blue), and 2018 (navy blue). The overall mean values and the minimum bias cross sections are also shown [189]. . . . .	3-4
238			
239	3.5	Absorbed dose in the CMS Cavern after an integrated luminosity of $3000 \text{ fb}^{-1}$ . Using the interaction point as reference, R is the transverse distance from the beamline and Z is the distance along the beamline [177]. . . . .	3-4
240			
241	3.6	Figure 3.6a: Barrel wheel with its detector rings and return yokes. Figure 3.6b: CSC endcap disk with the two CSC stations. The outer station is made of 10 deg detectors while the inner station is made of 20 deg detectors. Figure 3.6c: RPC endcap disk. The inner station is not equipped, leaving the inner CSC station visible. . . . .	3-5
242			
243	3.7	Figure 3.7a: Cross section of a DT module showing the two superlayers measuring the $\phi$ coordinate, perpendicular to the cross section plane, and the superlayer measuring the $\eta$ coordinate, placed in between the two others with a honeycomb plate and parallel to the cross section plane. The DT detector is sandwiched in between 2 RPCs whose readout strips are perpendicular to the cross section plane, measuring the $\phi$ coordinate. Figure 3.7b: A DT cell is shown together with its electric field. The path of a muon through a superlayer is shown. . . . .	3-6
244			
245	3.8	Figure 3.8a: Cathode strips and anode wire layout of a CSC panel. Figure 3.8b: Avalanche development and charge collection by anode wires and induction on cathode strips inside of a CSC panel. . . . .	3-7
246			
247	3.9	Muon track reconstruction through the six panels of a CMS CSC using the information of anode wire groups and cathode strip charge distribution combined with comparator bits to decide on which half strip the muon is more likely to have passed. . . . .	3-7
248			
249	3.10	Double-gap layout of CMS RPCs. Muons passing through the gas volumes will create electron-ions pairs by ionising the gas. This ionisation will immediately translate into a developing avalanche. . . . .	3-8
250			
251	3.11	Extrapolated fraction of failing channels of the present DT MiC1 electronics as a function of the integrated luminosity for different scenarios until LS4 [177]. . . . .	3-8
252			
253	3.12	The event loss fractions as a function of the instantaneous luminosity is compared for CFEBs (Phase-1) and DCFEBs (Phase-2) at different CSC locations. HL-LHC luminosity is marked with the dashed brown line [177]. . . . .	3-9
254			
255	3.13	Comparison of the simulated time residuals in between reconstructed and true muon times without (blue) and with (red) the upgraded RPC link system [177]. . . . .	3-9
256			



325	3.24	Measured average charge per avalanche as a function of the effective electric field for different gas gap thickness in double-gap RPCs using HPL electrodes [177]. . . . .	3-17
326			
327	3.25	Level-1 Trigger data flow during Phase-2 operations [177]. . . . .	3-17
328			
329	3.26	Efficiency of the L1 trigger in the endcap region after Phase-2 upgrade in the case CSC/GEM/RPC hits are requested in at least two stations out of four (3.26a) and in all four stations (3.26b) [177]. . . . .	3-18
330			
331	3.27	Comparison of L1 trigger performances for prompt muons with and without the ad- dition of GEMs in the region $2.1 <  \eta  < 2.4$ at Phase-2 conditions [177]. GEMs would allow a reduction of the trigger accept rate by an order of magnitude (Fig- ure 3.27a) while increasing the trigger efficiency (Figure 3.27b). . . . .	3-19
332			
333	3.28	The angular resolution on reconstructed muon tracks in the GEM overlap region $2.0 <  \eta  < 2.15$ is compared for Phase-2 conditions in the case CSC are alone (Figure 3.28a) and in the case the GEMs' data, including ME0, is combined to which of CSCs (Figure 3.28b) [177]. . . . .	3-19
334			
335	3.29	Resolution of the LCT ambiguous events thanks to the combination of CSC and iRPC readout data. Using CSCs only, two pairs of hits are possible [177]. . . . .	3-20
336			
337	3.30	Efficiency (Figure 3.30a [202]) and cluster size (Figure 3.30b) of a standard double- gap RPC operated with $CO_2$ mixtures for different ratios of $SF_6$ . . . . .	3-21
338			
339	3.31	Efficiency of a CMS double-gap RPC operated with 30% of $HFO$ , 4.5% of $iC_4H_{10}$ , 1% of $SF_6$ and 64.5% of $CO_2$ [202]. . . . .	3-21
340			
341	3.32	The efficiency (solid lines) and streamer probability (dashed lines) of $HFO/CO_2$ (Figure 3.32a) and $CF_3I/CO_2$ (Figure 3.32b) based gas mixtures as a function of the effective high-voltage are compared with the present CMS RPC gas mixture represented in black [177, 202]. The detector used for the study is a single-gap RPC with similar properties than CMS RPCs. The streamer probability is defined as the proportion of events with a deposited charge greater than 20 pC. . . . .	3-22
342			
343	3.33	Efficiency (open symbols) and cluster size (full symbols) of an iRPC as a function of the effective voltage for the standard CMS gas mixture and an environmental- friendly gas mixture [177]. . . . .	3-22
344			
345			
346	4.1	Different phases of the avalanche development in the RPC gas volume subjected to a constant electric field $E_0$ . a) An avalanche is initiated by the primary ionisation caused by the passage of a charged particle through the gas volume. b) Due to its growing size, the avalanche starts to locally influence the electric field. c) The electrons, lighter than the cations reach the anode first. d) The ions reach the cathode. While the charges have not recombined, the electric field in the small region around the avalanche stays affected and locally blinds the detector. . . . .	4-2
347			
348	4.2	Movement of the charge carriers in an RPC. Figure 4.2a: Voltage across an RPC whose electrodes have a relative permittivity of 5 at the moment the tension is ap- plied. Figure 4.2b: After the charge carriers moved, the electrodes are charged and there is no voltage drop over the electrodes anymore. The full potential is applied on the gas gap only. Figure 4.2c: The streamer discharge initiated by a charged particle transports electrons and cations towards the anode and cathode respectively. . . . .	4-4
349			
350	4.3	Typical oscilloscope pulses in streamer mode (Figure 4.3a) and avalanche mode(Figure 4.3b). In the case of streamer mode, the very small avalanche signal is visible. . . . .	4-4
351			
352	4.4	Rate capability comparison for the streamer and avalanche mode of operation. An order of magnitude in rate capability for a maximal efficiency drop of 10% is gained by using the avalanche mode over the streamer mode. . . . .	4-5
353			

- 372        4.5 Comparison of the charge distribution of signals induced by cosmic muons in an  
373            RPC operated with a gas mixture of argon, butane and bromotrifluoromethane ( $CF_3Br$ ).  
374            The  $Ar/C_4H_{10}$  is kept constant at 60/40 in volume while the total amount of  $CF_3Br$   
375            in the mixture is varied: 0% (Figure 4.5a), 4% (Figure 4.5b) and 8% (Figure 4.5c) [209]. . . . . 4-6
- 376        4.6 Comparison of the efficiency and streamer probability, defined as the fraction of  
377            events with an induced charge 10 times larger than that of the average avalanche,  
378            with and without irradiation by a 24 GBq  $^{137}Cs$  source of an RPC successively  
379            operated with a 90/10 mixture  $C_2H_2F_4/i-C_4H_{10}$  (Figure 4.6a) and a 70/5/10/15  
380            mixture of  $Ar/i-C_4H_{10}/CO_2/C_2H_2F_4$  (Figure 4.6b) [210]. . . . . 4-6
- 381        4.7 Comparison of the fast charge ratio with and without irradiation by a 24 GBq  $^{137}Cs$   
382            source of an RPC successively operated with a 90/10 mixture  $C_2H_2F_4/i-C_4H_{10}$   
383            (Figure 4.7a) and a 70/5/10/15 mixture of  $Ar/i-C_4H_{10}/CO_2/C_2H_2F_4$  (Figure 4.7b).  
384            The results are provided for both single-gap and double-gap operation [210]. . . . . 4-7
- 385        4.8 Efficiency (circles and stars with 30 mV and 100 mV thresholds respectively) and  
386            streamer probability (opened circles) as function of the operating voltage of a 2 mm  
387            single-gap HPL RPC flushed with a gas mixture containing (a) 5%, (b) 2%, (c) 1%  
388            and (d) no  $SF_6$  [212]. . . . . 4-8
- 389        4.9 Evolution of the efficiency, working voltage, and voltage at 50% of maximum ef-  
390            ficiency for CMS Barrel (Figure 4.9a) and Endcap (Figure 4.9b) RPCs obtained  
391            through yearly voltage scans since 2011. The working voltage of each RPC is up-  
392            dated after each voltage scan to ensure optimal operation [227]. . . . . 4-9
- 393        4.10 Comparison of the rate capability of 8 mm and 2 mm wide RPCs. The lines are  
394            linear fits on the data [229]. . . . . 4-10
- 395        4.11 Distributions of the induced charge of fast signals on 2 mm (Figure 4.11a) and 8 mm  
396            (Figure 4.11b) RPCs exposed to a radiation rate of 100 Hz/cm<sup>2</sup>. Average induced  
397            charge of fast signals as a function of the high voltage applied on 2 mm and 8 mm  
398            RPCs (Figure 4.11c). In the case of the 2 mm RPC, a saturation of the pre-amplifier  
399            was observed. The average of the distribution is underestimated, and the median is  
400            showed together with the average to account for this bias [229]. . . . . 4-11
- 401        4.12 Time distributions of the leading, trailing, and average of both leading and trailing  
402            edges for 2 mm (top row) and 8 mm (bottom row) RPCs exposed to a 100 Hz/cm<sup>2</sup>  
403            radiation rate. The data was collected with RPCs operated at the voltage correspond-  
404            ing to the knee of the efficiency distribution, defined as the point where 95% of the  
405            maximum efficiency is obtained [229]. . . . . 4-12
- 406        4.13 Possible double-gap RPC layouts: a) "standard" 1D double-gap RPC, as used in  
407            CMS experiment, where the anodes are facing each other and a 1D read-out plane  
408            is sandwiched in between them, b) double read-out double-gap RPC as used in AT-  
409            LAS experiment, where the cathodes are facing each other and 2 read-out planes  
410            are used on the outer surfaces. This last layout can offer the possibility to use a 2D  
411            reconstruction by using orthogonal read-out planes. . . . . 4-13
- 412        4.14 Comparison of performance of CMS double and single-gap RPCs using cosmic  
413            muons [225]. Figure 4.14a: Comparison of efficiency sigmoid. Figure 4.14b: Volt-  
414            age distribution at 95% of maximum efficiency. Figure 4.14c:  $\Delta_{10\%}^{90\%}$  distribution. . . . . 4-13
- 415        4.15 Representation of different RPC layouts (wide gap on Figure (a), double-gap on  
416            Figure (b) and multigap on Figure (c)), of the corresponding sensitive volume in  
417            gray, and of the associated avalanche size [215]. . . . . 4-14

418	4.16 Time distributions of the leading, trailing, and average of both leading and trailing edges for multigap RPCs consisting in two 4 mm (Figure 4.16a) and four 2 mm (Figure 4.16b) exposed to a 100 Hz/cm <sup>2</sup> radiation rate. The data was collected with RPCs operated at the voltage corresponding to the knee of the efficiency distribution, defined as the point where 95% of the maximum efficiency is obtained [215]. . . . .	4-15
419		
420		
421		
422		
423	4.17 Presentation of a study of a possible ALICE MRPC cell using 250 µm gas gaps, 620 µm outer glass electrodes, and 550 µm inner floating electrodes (Figure 4.17a), and of its time resolution performance as a function of the applied high voltage for different radiation levels referred through different filter settings of the 740 GBq <sup>137</sup> Cs source the former CERN GIF facility [230]. . . . .	4-15
424		
425		
426		
427		
428	4.18 Particle identification applied to electrons in the STAR experiment. The identification is performed combining ToF and $dE/dx$ measurements [235]. . . . .	4-16
429		
430	4.19 Comparison of the detector performance of ALICE ToF MRPC [236] at fixed applied voltage (in blue) and at fixed effective voltage (in red). The effective voltage is kept fixed by increasing the applied voltage accordingly to the current drawn by the detector.	4-17
431		
432		
433	4.20 Ratio between total induced and drifting charge have been simulated for single-gap, double-gap and multigap layouts [237]. The total induced charge for a double-gap RPC is a factor 2 higher than for a multigap. . . . .	4-18
434		
435		
436	4.21 Charge spectra have been simulated for single-gap, double-gap and multigap layouts [237]. It appears that when single-gap shows a decreasing spectrum, double and multigap layouts exhibit a spectrum whose peak is detached from the origin. The detachment gets stronger as the number of gaps increases. . . . .	4-18
437		
438		
439		
440	4.22 The maximal theoretical efficiency is simulated for single-gap, double-gap and multi-gap layouts [237] at a constant gap thickness of 2 mm and using an effective Townsend coefficient of 9 mm <sup>-1</sup> . . . . .	4-19
441		
442		
443	4.23 Mass stopping power as a function of $\beta\gamma = p/Mc$ for positive muons in copper [115]. The total stopping power is indicated with a solid line and local components with dashed lines. The vertical bands are used to indicate boundaries between different approximations used at different energy range. . . . .	4-19
444		
445		
446		
447	4.24 Mean mass stopping power for liquid hydrogen, as used in bubble chambers, gaseous helium, carbon, aluminum, iron, tin, and lead without the inclusion of radiative effect at higher $\beta\gamma$ necessary for pions and muons in denser materials [115]. . . . .	4-21
448		
449		
450	4.25 Mean excitation energies normalized to the atomic number as adopted by the ICRU [115, 241, 242]. . . . .	4-22
451		
452	4.26 Mean mass stopping power at minimum ionization as a function of the atomic number [115]. . . . .	4-22
453		
454	4.27 Example of straggling function $f(\Delta)$ of particles passing through 1.2 cm of Argon gas with a $\beta\gamma$ of 3.6 and represented with a solid line. The original Landau distribution is showed with a dashed line [243]. . . . .	4-23
455		
456		
457	4.28 Evolution of straggling functions $f(\Delta)$ of particles passing through a volume of Argon gas with a $\beta\gamma$ of 3.6 with increasing thickness $x$ [243]. . . . .	4-23
458		
459	4.29 Photoabsorption cross section as computed by HEED for nobles gases with different electric shell numbers [239]. . . . .	4-25
460		
461	4.30 Photoabsorption cross section as computed by HEED for typical RPC gas mixtures [239]. The RPC mixture with CO <sub>2</sub> corresponds to the mixture used by CALICE SD-HCAL [247] while the other one was foreseen for the experiment ATLAS [248] but has been changed since then. . . . .	4-26
462		
463		
464		

465	4.31 Distributions of number of electrons (left) and energy loss (right) for a 5 GeV/c muon passing through 1.2 mm of Helium (Figure 4.31a), Argon (Figure 4.31b) or a typical RPC gas mixture (Figure 4.31c) [239]. . . . .	4-27
466		
467		
468	4.32 Figure 4.32a: Mean cluster density for muons through different gas volumes [239]. Figure 4.32b: Distribution of the number of electrons per cluster for a 5 GeV/c muon traveling through a mixture of 96.7% $C_2H_2F_4$ , 3% i- $C_4H_{10}$ and 0.3% $SF_6$ [239, 248]. . . . .	4-28
469		
470		
471		
472	4.33 Townsend and attachment coefficient for a typical 96.7/3/0.3 mixture of $C_2H_2F_4$ /i- $C_4H_{10}$ / $SF_6$ , at a temperature $T = 296.15$ K and a pressure $P = 1013$ hPa [239, 248]. . . . .	4-29
473		
474		
475	4.34 Comparison of the distribution law of Furry and the Poisson law for $\bar{n} = 5$ [251]. . . . .	4-29
476		
477	4.35 Single-electron avalanche size distribution in a proportional counter filled with methanol at different $E/p$ values. (a) 70, (b) 76.5, (c) 105, (d) 186.5, (e) 426V/cm torr [252]. . . . .	4-30
478		
479		
480		
481	4.36 Figure 4.36a: Comparison of avalanche size distributions for different values of Townsend and attachment coefficients. The effective Townsend coefficient is the same for both distributions. Figure 4.36b: Fluctuation in avalanches size for avalanche started by a single electron with $\alpha = 13 \text{ mm}^{-1}$ and $\eta = 3.5 \text{ mm}^{-1}$ [248]. . . . .	4-32
482		
483		
484		
485		
486		
487	4.37 Figure 4.37a: Electrons mean drift velocity $v_D$ in pure $C_2H_2F_4$ and typical RPC gas mixtures. Figure 4.37b: Transverse diffusion coefficient in pure $C_2H_2F_4$ and a typical RPC gas mixture. Figure 4.37c: Longitudinal diffusion coefficient in pure $C_2H_2F_4$ and a typical RPC gas mixture. All results are given with a pressure $P = 760$ Torr and a temperature $T = 296.15$ K [239]. . . . .	4-33
488		
489		
490	4.38 Comparison of the free charge carriers in the gas after a time $t = 7.90$ ns in the case where no diffusion is taken into account to simulate the avalanche (Figure 4.38a) and in the case where the diffusion is implemented (Figure 4.38b) [239]. . . . .	4-33
491		
492	4.39 Schematic representation of an avalanche and of the electric field deformation it causes due to the local concentration of charge carriers [221]. . . . .	4-35
493		
494		
495		
496	4.40 Evolution of the charge induced by an avalanche started by a single electron in a 1.2 mm thick RPC with an applied electric field of 54 kV/cm in the case space charge is not taken into account (Figure 4.40a) and in the case it is implemented into the simulation (Figure 4.40b). The total induced charge is correlated to the size of the avalanche [239]. . . . .	4-36
497		
498		
499		
500	4.41 Distributions of charge carriers within the gas volume of a 1.2 mm thick RPC and the corresponding deformation of the electric field at different time steps with an applied electric field of 55.5 kV/cm [239]. . . . .	4-37
501		
502		
503	4.42 Representation of the weighting field in the volume of an RPC and the resulting induced current in the strip placed at 1 V and its neighbour connected to the ground. The induced current corresponds, as can be understood from Formula 4.22 [221]. . . . .	4-38
504		
505	4.43 Schematics of CMS RPC FEE logic. . . . .	4-39
506		
507	4.44 Equivalence in between the charge of the induced signal in input of the CMS FEE and the signal strength on the output of the pre-amplifier. . . . .	4-39
508		

506	4.45 Description of the principle of a CFD. A comparison of threshold triggering (left) 507 and constant fraction triggering (right) is shown in Figure 4.45a. Constant fraction 508 triggering is obtained thanks to zero-crossing technique as explained in Figure 4.45b. 509 The signal arriving at the input of the CFD is split into three components. A first 510 one is delayed and connected to the inverting input of a first comparator. A sec- 511 ond component is connected to the noninverting input of this first comparator. A 512 third component is connected to the noninverting input of another comparator along 513 with a threshold value connected to the inverting input. Finally, the output of both 514 comparators is fed through an AND gate. . . . .	4-40
515	4.46 Typical efficiency sigmoid of a CMS RPC detector. The black dots correspond to the 516 data, the blue line to the sigmoid fit and the opened cross to the knee and working 517 extracted from the fit line. . . . .	4-41
518	4.47 Effect of the temperature variation on the rate (Figure 4.47a) and the efficiency (Fig- 519 ure 4.47b) of an RPC [253]. . . . .	4-42
520	4.48 Effect of the pressure variation on the rate (Figure 4.48a) and the efficiency (Fig- 521 ure 4.48b) of an RPC [254]. . . . .	4-43
522	5.1 Mean RPC Barrel (left column) and Endcap (right column) rate (top row) and current 523 (bottom row) as a function of the instantaneous luminosity as measured in 2017 $p$ - 524 $p$ collision data. . . . .	5-2
525	5.2 Figure 5.2a: The hit rate per region (Barrel, Endcap) is linearly extrapolated to 526 HL-LHC highest instantaneous luminosity ( $5 \times 10^{34} \text{ cm}^{-2} \text{ s}^{-1}$ ) using the rate as 527 a function of instantaneous luminosity recorded by RPCs in 2017 showing a linear 528 dependence. Figure 5.2b: The integrated charge per region (Barrel, Endcap) is ex- 529 trapolated to HL-LHC integrated luminosity ( $3000 \text{ fb}^{-1}$ ) using the data accumulated 530 in 2016 in every HV channel. . . . .	5-3
531	5.3 CMS RPC mean integrated charge in the Barrel region (Figure 5.3a) and the Endcap 532 region (Figure 5.3b). The integrated charge per year is shown in blue. The red curve 533 shows the evolution of the accumulated integrated charge through time. The blank 534 period in 2013 and 2014 corresponds to LS1. The total integrated charge for the 535 entire operation period (Oct.2009 - Dec.2017) is estimated to be about $1.66 \text{ mC/cm}^2$ 536 in the Barrel and $4.58 \text{ mC/cm}^2$ in the Endcap. . . . .	5-3
537	5.4 Layout of the test beam zone called X5c GIF at CERN. Photons from the radioactive 538 source produce a sustained high rate of random hits over the whole area. The zone is 539 surrounded by 8 m high and 80 cm thick concrete walls. Access is possible through 540 three entry points. Two access doors for personnel and one large gate for material. 541 A crane allows installation of heavy equipment in the area. . . . .	5-4
542	5.5 $^{137}\text{Cs}$ decays by $\beta^-$ emission to the ground state of $^{137}\text{Ba}$ (BR = 5.64%) and via the 543 662 keV isomeric level of $^{137}\text{Ba}$ (BR = 94.36%) whose half-life is 2.55min. . . . .	5-5
544	5.6 Floor plan of the GIF++ facility. When the facility downstream of the GIF++ takes 545 electron beam, a beam pipe is installed along the beam line (z-axis). The irradiator 546 can be displaced laterally (its center moves from $x = 0.65 \text{ m}$ to $2.15 \text{ m}$ ), to increase 547 the distance to the beam pipe. . . . .	5-6
548	5.7 Simulated unattenuated current of photons in the xz plane (Figure 5.7a) and yz plane 549 (Figure 5.7b) through the source at $x = 0.65 \text{ m}$ and $y = 0 \text{ m}$ [263]. With angular 550 correction filters, the current of 662 keV photons is made uniform in xy planes. . . . .	5-6

- 551        5.8 Description of the RPC setup. Dimensions are given in mm. A tent containing RPCs  
 552        is placed at 1720 mm from the source container. The source is situated in the center  
 553        of the container. RE-4-2-BARC-161 chamber is 160 mm inside the tent. This way,  
 554        the distance between the source and the chambers plan is 2060 mm. Figure 5.8a  
 555        provides a side view of the setup in the  $xz$  plane while Figure 5.8b shows a top view  
 556        in the  $yz$  plane. . . . . 5-7
- 557        5.9 RE-4-2-BARC-161 chamber is inside the tent as described in Figure 5.8. In the  
 558        top right, the two scintillators used as trigger can be seen. This trigger system has an  
 559        inclination of  $10^\circ$  relative to horizontal and is placed above half-partition B2 of the  
 560        RPCs. PMT electronics are shielded thanks to lead blocks placed in order to protect  
 561        them without stopping photons from going through the scintillators and the chamber. 5-8
- 562        5.10 Hit distributions over all three partitions of RE-4-2-BARC-161 chamber is showed.  
 563        Top, middle and bottom figures respectively correspond to partitions A, B, and C.  
 564        The profiles show that some events still occur in other half-partitions than B2, which  
 565        corresponds to strips 49 to 64, in front of which the trigger is placed, contributing to  
 566        the inefficiency of detection of cosmic muons. In the case of partitions A and C, the  
 567        very low amount of data can be interpreted as noise. On the other hand, it is clear  
 568        that a little portion of muons reach the half-partition B1, corresponding to strips 33  
 569        to 48. . . . . 5-8
- 570        5.11 Signals from the RPC strips are shaped by the FEE described on Figure 5.11a.  
 571        Output LVDS signals are then read-out by a TDC module connected to a computer or  
 572        converted into NIM and sent to scalers. Figure 5.11b describes how these converted  
 573        signals are put in coincidence with the trigger. . . . . 5-9
- 574        5.12 Results are derived from data taken on half-partition B2 only. On the 18<sup>th</sup> of June  
 575        2014, data has been taken on chamber RE-4-2-BARC-161 at CERN building 904  
 576        (Prevessin Site) with cosmic muons providing us a reference efficiency plateau of  
 577         $(97.54 \pm 0.15)\%$  represented by a black curve. A similar measurement has been done  
 578        at GIF on the 21<sup>st</sup> of July with the same chamber giving a plateau of  $(78.52 \pm 0.94)\%$   
 579        represented by a red curve. . . . . 5-10
- 580        5.13 Representation of the layout used for the simulations of the test setup. The RPC  
 581        read-out plane is represented as a yellow trapezoid while the two scintillators as blue  
 582        cuboids looking at the sky. The green plane corresponds to the muon generation  
 583        plane within the simulation. Figure 5.8a shows a global view of the simulated setup.  
 584        Figure 5.8b shows a zoomed view that allows to see the two scintillators as well as  
 585        the full RPC plane. . . . . 5-11
- 586        5.14 Geometrical acceptance distribution as provided by the Monte Carlo simulation. . . . . 5-12
- 587        5.15 Correction of the efficiency without source. The efficiency after correction gets  
 588        much closer to the Reference measurement performed before the study in GIF by  
 589        reaching a plateau of  $(93.52 \pm 2.64)\%$ . . . . . 5-13
- 590        5.16 Hit distributions over read-out partition B of RE-4-2-BARC-161 chamber to-  
 591        gether with skew distribution fits corresponding to forward and backward coming  
 592        muons. . . . . 5-14
- 593        5.17 Figure 5.17a shows the linear approximation fit performed on data extracted from  
 594        table 5.2. Figure 5.17b shows a comparison of Formula 5.5 with the simulated flux  
 595        using  $a$  and  $b$  given in figure 5.17a in formulae 5.3 and the reference value  $D_0 =$   
 596        50 cm and the associated flux for each absorption factor  $F_0^{ABS}$  from table 5.1. . . . . 5-16

597	5.18 Efficiency (Figure 5.18a) and cluster size (Figure 5.18b) of chamber RE-4-2-BARC-161 measured at GIF with Source OFF (red) and Source ON using different absorber settings: ABS 5 (green), ABS 2 (blue) and ABS 1 (yellow). The results are compared to the Reference values obtained with cosmics. . . . .	5-17
601	5.19 Rates in chamber RE-4-2-BARC-161 measured at GIF with Source OFF (red) and Source ON using different absorber settings: ABS 5 (green), ABS 2 (blue) and ABS 1 (yellow). On Figure 5.19b, the rates of Figure 5.19a were normalized to the measured efficiency, and constant fits are performed on Source ON data showing the gamma rate in the chamber. . . . .	5-18
606	5.20 Evolution of the voltages at half maximum and at 95% of the maximum efficiency (Figure 5.20a), and of the maximum efficiency (Figure 5.20b) as a function of the rate in chamber RE-4-2-BARC-161. The data is extracted from the fits in Figures 5.18a and 5.19b. . . . .	5-18
610	5.21 Presentation of a double-gap endcap RPC with its three RPC gaps. Due to the partitioning of the read-out strips into three rolls, the TOP layer of gap is divided into two gaps: TOP NARROW (TN) and TOP WIDE (TW). The BOTTOM (B) only consists in one gap. . . . .	5-19
614	5.22 Current density and charge deposition per gamma avalanche, defined as the current density normalized to the measured rate taken from Figure 5.19a as a function of the effective high voltage in chamber RE-4-2-BARC-161 measured at GIF with Source ON using different absorber settings: ABS 5 (green), ABS 2 (blue) and ABS 1 (yellow). . . . .	5-20
618	5.23 Characterization of CMS RPC detectors foreseen to be used at GIF++ for longevity studies of the present system. Using cosmic muons, efficiency (Figure 5.23a) and cluster size (Figure 5.23b) were measured as well as noise rate (Figure 5.23c) and current density (Figure 5.23d). For each detector, the working voltage, defined as in Formula 4.25, was extracted from sigmoid fits performed in Figure 5.23a and the values of efficiency, cluster size, noise rate and current density at this voltage are reported using open crosses. . . . .	5-21
626	5.24 CMS RPC setup inside of GIF++ bunker during test beam (Figure 5.24a) and ageing periods (Figure 5.24b). The space in between the RPCs and the source is usually used by other detectors while the space in between T1 and the upstream wall is not filled. Due to the presence of the beam pipe, the trolley is moved away from the beam line during irradiation periods and placed farther away from the source for less intense irradiation. The position of the trolley can vary due to the use of the space by other setups and is then not exact. In the contrary, the position of the chambers in the trolley is fixed and given in Figure 5.24c. . . . .	5-23
634	5.25 Visualisation of the main data flows in GIF++. The yellow flow lines correspond to the DIP flow used for source, environmental and gas information. The red flow lines are for the CAEN flow through which the WebDCS communicates the voltages to be applied on the detectors using pressure and temperature information and retrieves the monitored voltages and currents. Finally, the blue flow lines correspond to the DAQ flow through which the RPC data is collected from the TDCs by the computer. . . . .	5-24
640	5.26 DIP monitoring history accessed through GIF++ WebDCS interface. . . . .	5-25
641	5.27 Example of DQM page available on CMS RPC WebDCS in GIF++. The rate measured in one of the tracking chambers, namely GT1_20_20-BKL_JUL16_4, is presented here. The DQM page allows clicking on each histogram to extend its view and to navigate through the histograms thanks to the left and right arrows. . . . .	5-27

645	5.28 Example of DQM ROOT Browser page available on CMS RPC WebDCS in GIF++. The strip activity profile, defined as the rate profile normalized to the mean rate, in one of the tracking chambers, namely GT1_20_20-BKL_JUL16_4, is presented here. Available ROOT files and histograms can be browsed thanks to the left panel showing the directory and files structures. . . . .	5-28
650	5.29 Longevity statistics of chamber RE2-2-NPD-BARC-9 in GIF++. For each month since July 2017, the integrated charge (in blue) as well as the time efficiency of irradiation (in gray) is reported. . . . .	5-28
655	5.30 Example of current monitoring (Figure 5.30a) and of corresponding integrated charge (Figure 5.30b) of chamber RE2-2-NPD-BARC-09. The decrease of current is re- lated to a decrease of the voltage due to the daily rate scan procedure or to periods during which the source was turned OFF. . . . .	5-29
660	5.31 Example of rate (Figure 5.31a) and current (Figure 5.31b) monitoring of chamber RE2-2-NPD-BARC-09 with increasing integrated charge. The variations of the rate and current are correlated and corresponds to change of source irradiation, gas flow, gas humidity, or environmental conditions. . . . .	5-30
665	5.32 Example of strip activity of chamber RE2-2-NPD-BARC-09 monitoring through time. The activity of a strip is defined as the rate of the individual channel normalized to the mean rate measured in the corresponding read-out partition. . . . .	5-31
670	5.33 Total integrated charge in the irradiated RPCs, RE2-2-NPD-BARC-9 and RE4-2-CERN-165, before starting August 2018 test beam period. The irradiation of the RE2 chamber started in June 2016 while the RE4 chamber couldn't be irradiated before November 2016. . . . .	5-33
675	6.1 PETIROC 2A block diagram. . . . .	6-2
680	6.2 The PETIROC time jitter as a function of the input signal amplitude, measured with and without internal clocks. . . . .	6-3
685	A.1 (A.1a) View of the front panel of a V1190A TDC module [264]. (A.1b) View of the front panel of a V1718 Bridge module [265]. (A.1c) View of the front panel of a 6U 6021 VME crate [277]. . . . .	A-3
690	A.2 Module V1190A <i>Trigger Matching Mode</i> timing diagram [264]. . . . .	A-4
695	A.3 Structure of the ROOT output file generated by the DAQ. The 5 branches ( <code>EventNumber</code> , <code>number_of_hits</code> , <code>Quality_flag</code> , <code>TDC_channel</code> and <code>TDC_TimeStamp</code> ) are visible on the left panel of the ROOT browser. On the right panel is visible the histogram cor- responding to the variable <code>nHits</code> . In this specific example, there were approximately 50k events recorded to measure the gamma irradiation rate on the detectors. Each event is stored as a single entry in the <code>TTree</code> . . . . .	A-10
700	A.4 The effect of the quality flag is explained by presenting the content of <code>TBranch</code> <code>number_of_hits</code> of a data file without <code>Quality_flag</code> in Figure A.4a and the con- tent of the same <code>TBranch</code> for data corresponding to a <code>Quality_flag</code> where all TDCs were labelled as <code>GOOD</code> in Figure A.4b taken with similar conditions. It can be noted that the number of entries in Figure A.4b is slightly lower than in Figure A.4a due to the excluded events. . . . .	A-12
705	A.5 Using the same data as previously showed in Figure A.4, the effect of the quality flag is explained by presenting the reconstructed hit multiplicity of a data file with- out <code>Quality_flag</code> in Figure A.5a and the reconstructed content of the same RPC partition for data corresponding to a <code>Quality_flag</code> where all TDCs were labelled as <code>GOOD</code> in Figure A.5b taken with similar conditions. The artificial high content of bin 0 is completely suppressed. . . . .	A-12

693	A.6	WebDCS DAQ scan page. On this page, shifters need to choose the type of scan (Rate, Efficiency or Noise Reference scan), the gamma source configuration at the moment of data taking, the beam configuration, and the trigger mode. These information will be stored in the DAQ ROOT output. Are also given the minimal measurement time and waiting time after ramping up of the detectors is over before starting the data acquisition. Then, the list of HV points to scan and the number of triggers for each run of the scan are given in the table underneath. . . . .	A-14
700	B.1	Example of expected hit time distributions in the cases of efficiency (Figure B.1a) and noise/gamma rate per unit area (Figure B.1b) measurements as extracted from the raw ROOT files. The unit along the x-axis corresponds to ns. The fact that "the" muon peak is not well defined in Figure B.1a is due to the contribution of all the RPCs being tested at the same time that don't necessarily have the same signal arrival time. Each individual peak can have an offset with the ones of other detectors. The inconsistancy in the first 100 ns of both time distributions is an artefact of the TDCs and are systematically rejected during the analysis. . . . .	B-16
708	B.2	The effect of the quality flag is explained by presenting the reconstructed hit multiplicity of a data file without <code>Quality_flag</code> . The artificial high content of bin 0 is the effect of corrupted data. . . . .	B-21
711	B.3	Display of the masking tool page on the webDCS. The window on the left allows the shifter to edit <code>ChannelsMapping.csv</code> . To mask a channel, it only is needed to set the 3rd field corresponding to the strip to mask to 0. It is not necessary for older mapping file formats to add a 1 for each strip that is not masked as the code is versatile and the default behaviour is to consider missing mask fields as active strips. The effect of the mask is directly visible for noisy channels as the corresponding bin turns red. The global effect of masking strips will be an update of the rate value showed on the histogram that will take into consideration the rejected channels. . . . .	B-28



# List of Tables

719

720	3.1	Details of the greenhouse fluorinated gases used in CMS and of their GWP [177]. . .	3-20
721	4.1	Properties of the most used electrode materials for RPCs. . . . .	4-3
722	5.1	Total photon flux ( $E\gamma \leq 662$ keV) with statistical error predicted considering a 723 $^{137}\text{Cs}$ activity of 740 GBq at different values of the distance $D$ to the source along 724 the x-axis of irradiation field [261]. . . . .	5-14
725	5.2	Correction factor $c$ is computed thanks to Formula 5.4 taking as reference $D_0 =$ 726 50 cm and the associated flux $F_0^{ABS}$ for each absorption factor available in table 5.1.	5-15
727	5.3	The data at $D_0$ in 1997 is taken from [261]. Using Formula 5.5, the flux at $D$ , 728 including an error of 1 cm, can be estimated in 1997. Then, taking into account the 729 attenuation of the source activity, the flux at $D$ can be estimated at the time of the 730 tests in GIF in 2014. Assuming a sensitivity of the RPC to $\gamma s = 2 \times 10^{-3}$ , an 731 estimation of the hit rate per unit area is obtained. . . . .	5-16
732	5.4	Summary of the characterization measurement performed in Ghent on CMS RPC 733 detectors foreseen to be used at GIF++ for longevity studies of the present system. 734 For each detector, the working voltage, defined as in Formula 4.25, was extracted 735 from sigmoid fits performed in Figure 5.23a and the values of efficiency, cluster size, noise rate and current density at this voltage are reported. . . . .	5-22
737	A.1	Inter-process communication cycles in between the webDCS and the DAQ through 738 file string signals. . . . .	A-18



# List of Acronyms

## List of Acronyms

741	AFL	Almost Full Level
742	ALCTs	Anode local charged track boards
743	BARC	Bhabha Atomic Research Centre
744	BCS	Bardeen–Cooper–Schrieffer
745	BLT	Block Transfer
746	BMTF	Barrel Muon Track Finder
747	BNL	Brookhaven National Laboratory
748	BSM	Physics beyond the Standard Model
749	BR	Branching Ratio
750	CAEN	Costruzioni Apparecchiature Elettroniche Nucleari S.p.A.
751	CERN	European Organization for Nuclear Research
752	CFD	Constant Fraction Discriminator
753	CFEBs	cathode front-end boards
754	CKM	Cabibbo–Kobayashi–Maskawa
755	CMB	Cosmic Microwave Background
756	CMS	Compact Muon Solenoid
757	CSC	Cathode Strip Chamber
758	CuOF	copper-to-optical-fiber translators
759	DAQ	Data Acquisition
760	DCS	Detector Control Software
761	DMBs	Data acquisition mother boards
762	DQM	Data Quality Monitoring
763	DT	Drift Tube
764	EDM	electric dipole moment
765	ECAL	electromagnetic calorimeter
766	EMTF	Endcap Muon Track Finder
767	FCC	Future Circular Collider
768	FEB	Front-End Board
769	FEE	Front-End Electronics
770	FWHM	full-width-at-half-maximum
771	GEANT	GEometry ANd Tracking - a series of software toolkit platforms developed by CERN
772		
773	GEB	GEM Electronics board
774	GEM	Gas Electron Multiplier
775	GIF	Gamma Irradiation Facility
776	GIF++	new Gamma Irradiation Facility
777	GWP	Global Warming Potential
778	HCAL	hadron calorimeter

779	HEP	High-Energy Physics
780	HL-LHC	High Luminosity LHC
781	HPL	High-pressure laminate
782	HSCPs	Heavy Stable Charged Particles
783	HV	High Voltage
784	ICRU	International Commission on Radiation Units & Measurements
785	iRPC	improved RPC
786	IRQ	Interrupt Request
787	ISR	Intersecting Storage Rings
788	LEIR	Low Energy Ion Ring
789	LEP	Large Electron-Positron
790	LHC	Large Hadron Collider
791	LS1	First Long Shutdown
792	LS2	Second Long Shutdown
793	LS3	Third Long Shutdown
794	LSP	lightest supersymmetric particle
795	LV	Low Voltage
796	LVDS	Low-Voltage Differential Signaling
797	MC	Monte Carlo
798	MCNP	Monte Carlo N-Particle
799	MiC	Minicrate electronics
800	MiC1	first version of Minicrate electronics
801	mip's	minimum ionizing particles
802	MRPC	Multigap RPC
803	MSSM	Minimal Supersymmetric Standard Model
804	mSUGRA	minimal SUper GRAvity
805	NIM	Nuclear Instrumentation Module logic signals
806	OH	Optohybrid Board
807	OMTF	Overlap Muon Track Finder
808	OTMBs	Optical TMBs
809	PAI	Photo-Absorption Ionisation
810	PAIR	Photo-Absorption Ionisation with Relaxation
811	PMT	PhotoMultiplier Tube
812	PS	Proton Synchrotron
813	PU	pile-up
814	QCD	Quantum Chromodynamics
815	QED	Quantum Electrodynamics
816	RADMON	Radiation Monitoring
817	RMS	Root Mean Square
818	ROOT	a framework for data processing born at CERN
819	RPC	Resistive Plate Chamber
820	SC	Synchrocyclotron
821	SiPM	Silicon Photomultiplier
822	SLAC	Stanford Linear Accelerator Center
823	SM	Standard Model
824	SPS	Super Proton Synchrotron
825	SUSY	supersymmetry
826	TDC	Time-to-Digital Converter
827	TDR	Technical Design Report

828	TMBs	Trigger mother boards
829	ToF	Time-of-flight
830	TPG	trigger primitives
831	webDCS	Web Detector Control System
832	WIMPs	Weakly Interacting Massive Particles
833	YETS	Year End Technical Stop



# 1

834

835

## Introduction

836 Grasping an understanding of the world in which they are leaving in has always been part of human  
837 life. Beyond the metaphysical questioning of our origins and purpose, curiosity has brought mankind  
838 to question its surroundings. Following the philosophy of the ancient Greeks and Indians came  
839 the development of the sciences as the systematic experimentation aimed at testing hypothesis and  
840 reproducing results obtained by fellow natural philosophers. With the industrial revolution and the  
841 organisation of science, it became possible to go always further in the understanding of the universe  
842 and of the matter in particular. Investigation on the constituent of matter proved to require more  
843 and more powerful machines in order to break apart the bricks of the world into ever smaller pieces,  
844 study their behaviour and extract new knowledge to help the development of humanity. So far, the  
845 largest and most powerful machine that was built to study the particles composing matter and test  
846 the models thought by physicists to explain their behaviour is the Large Hadron Collider (LHC),  
847 a circular particle accelerator used to collide protons and heavy ions. After only a few years of  
848 investigations conducted thanks to the LHC, several discoveries, predicted by the existing models,  
849 have been made. In the future, in order to boost the discovery potential on the LHC and be able to  
850 test hypotheses lying beyond the already acknowledged models, the instantaneous luminosity, i.e.  
851 the rate of particle interactions, will be slightly increased into a so-called High Luminosity phase to  
852 boost its discovery potential.

853 As the Large Hadron Collider will see its instantaneous luminosity be increased, the detectors  
854 on the different experimental sites will have to suffer an increased background irradiation due to the  
855 byproducts of the interaction of the beams with the infrastructure. This will cause for the detectors  
856 a stress which implications need to be understood throughout the High Luminosity LHC (HL-LHC)  
857 phase of operations. In the case of the Compact Muon Solenoid (CMS) experiment, it is important  
858 to understand if the detectors that will be subjected to the higher levels of radiation will be able to  
859 sustain higher detection rates while displaying the same performance they have so far been operated  
860 at and if this level of performance of the detectors will stay stable for a period longer than ten years.  
861 More specifically, the detectors placed very close to the beam line will be the most subjected to the  
862 change of luminosity. In CMS, the endcap detectors will then be particularly affected by the stronger

863 background radiation. The endcap detectors compose a part of the muon system of CMS and among  
864 them, the Resistive Plate Chamber (RPC) plays a key role in providing the experiment a reliable  
865 trigger on potentially interesting data. This PhD work takes place into this very specific context of  
866 muon detector consolidation and certification for the HL-LHC period in order to provide the CMS  
867 experiment with robust new detectors and confirm that the present system will survive through the  
868 next 20 years.

869 CMS experiment main focus revolves around testing the Standard Model (SM) of particle physics  
870 using a multipurpose detector design to detect the interaction products of the protons and ions col-  
871 liding along the LHC. Looking at the successive evolution of the theoretical models that gave birth  
872 to the SM, the need for very intense particle beams in high energy physics experiment becomes clear  
873 in that the higher the center-of-mass energy for each interaction, the greater the probe on very small  
874 cross-section processes predicted by the theory, justifying the successive increase in beam energy  
875 and intensity at LHC.

876 The implications for LHC experiments and in particular for the CMS detector explain the need for  
877 longevity and rate capability studies conducted on the Resistive Plate Chambers which are an impor-  
878 tant part of its Muon System as it is needed to certify the quality of operation of the trigger detectors  
879 throughout the lifetime of HL-LHC.

880 RPCs are gaseous detectors which physics principles are non trivial and are still being investigated.  
881 Nevertheless, key processes driving the electron multiplication in the gas volume, rate capability and  
882 ageing have been successfully identified and will define the parameters that will have to be taken into  
883 consideration while producing the detectors extending the pseudo-rapidity coverage of RPCs toward  
884 the beam line as well as the ones to be monitored during the on-going longevity and rate capability  
885 certification campaign.

886 On the one hand, the present RPC sub-system consists in two different RPC productions. Indeed,  
887 most of the RPC detectors were produced in view of the start of LHC activities in 2010. These detec-  
888 tors were build in between 2007 and 2008 to equip the barrel and the three disks of each endcaps of  
889 the CMS apparatus. But during the First Long Shutdown (LS1) of LHC in between end of 2012 and  
890 2015, a fourth disk of endcap was added in order to reinforce the redundancy of the endcap trigger.  
891 Hence, new RPC detectors using the same technology were built in between 2012 and 2013. These  
892 two sets of detector productions only differ in the properties of the High-pressure laminate (HPL)  
893 used for their electrodes that could lead to a different ageing rate. This is why spare detectors of  
894 both production periods have been tested over the past years to certify their good operation through  
895 HL-LHC.

896 On the other hand, producing detectors to equip a highly irradiated region such as the extension of  
897 CMS RPC endcaps requires to substantially improve the ageing properties of the chosen technology  
898 by reducing the charge deposition per ionizing particle. This can be achieved both by modifying the  
899 design of the detector volume or by improving the signal to noise ratio of the Front-End Electron-  
900 ics (FEE) used to process the charge collected by the read-out strips making them more sensitive to  
901 weaker signals. Two improved RPC (iRPC) designs were selected and tested in order to extend of  
902 CMS endcap coverage.

903 Thanks to the study presented in this document, preliminary conclusions will be brought on the pro-  
904 duction of iRPCs and on the longevity of the present RPC system, providing with a better understand  
905 of the future performance of the RPC sub-system within the CMS experiment.

# 2

906

907

## Investigating the TeV scale

908 Throughout history, physics experiment became more and more powerful in order to investigate finer  
909 details of nature to help understanding the building blocks of matter and the fundamental interactions  
910 that bind them in the microscopic world. Nowadays, the Standard Model of particle physics is the  
911 most accurate theory designed to explain the behaviour of particles and is able to make very precise  
912 predictions that are constantly verified. Nevertheless, some hints of new physics are visible as bricks  
913 are still missing to obtain a global description of the Universe.

914 To highlight the limits of the SM and test the different alternative theories, evermore powerful  
915 machines are needed. It is in this context that the Large Hadron Collider has been thought and built  
916 to accelerate and collide particles at energies exceeding anything that had been done before. Higher  
917 collision energies and high pile-up imply the use of enormous detectors to measure the properties of  
918 the interaction products. The Compact Muon Solenoid is a multipurpose experiment that have been  
919 designed to study the proton-proton collisions of the LHC and give answers on various high-energy  
920 physics scenarios such as different supersymmetry (SUSY) extensions to the Standard Model or  
921 Extra Dimensions models.

922 This Chapter will be the occasion to go through the history of the Standard Model of Particle  
923 Physics to understand the research conducted today in High-Energy Physics (HEP) facilities. From  
924 the discovery of the atom and of its inner structure to the development of the theories governing  
925 the fundamental interactions, all the elements leading to the construction SM will be discussed.  
926 Furthermore, highlights on the Physics beyond the Standard Model (BSM) will be given to replace  
927 the document in the context of today's research. Finally, a full description of the LHC and of the  
928 CMS detector will be provided.

### 929 **2.1 The Standard Model of Particle Physics**

930 In the early 21<sup>st</sup> century it is now widely accepted that matter is made of elementary blocks referred  
931 to as *elementary particles*. The physics theory that classifies and describes the best the behaviour and  
932 interaction of such elementary particles is the so-called Standard Model. The SM formalizes three of

933 the four fundamental interactions (electromagnetic, weak and strong interactions). Its development  
 934 happened since the 1960s thanks to a strong collaboration between theoretical and experimental  
 935 physicists.

### 936 2.1.1 A history of particle physics

937 The idea that nature is composed of elementary bricks, called *atomism*, is not contemporary as it  
 938 was already discussed by Indian or Greek philosophers during antiquity. In Greece, atomism has  
 939 been rejected by *Aristotelianism* as the existence of *atoms* would imply the existence of a void that  
 940 would violate the physical principles of Aristotle philosophy. Aristotelianism has been considered  
 941 as a reference in the european area until the 15<sup>th</sup> century. With the *Rinascimento*, antic text and  
 942 history started to be more deeply studied. The re-discovery of Platon's philosophy allowed opening  
 943 the door to alternative theories and give a new approach to natural sciences where experimentation  
 944 would become central. A new era of knowledge was starting. By the beginning of the 17<sup>th</sup> century,  
 945 atomism was re-discovered by philosophers. The very first attempt at estimating the number of  
 946 *particles* in a volume was provided by Magnenus in 1646 by calculating that the number of *particles*  
 947 in a stick of incense [1]. He found a value of the order of  $10^{18}$  simply by considering the time  
 948 necessary to smell it everywhere in a large church after the stick was lit on. It is now known that this  
 949 number only falls short only by 1 order of magnitude.

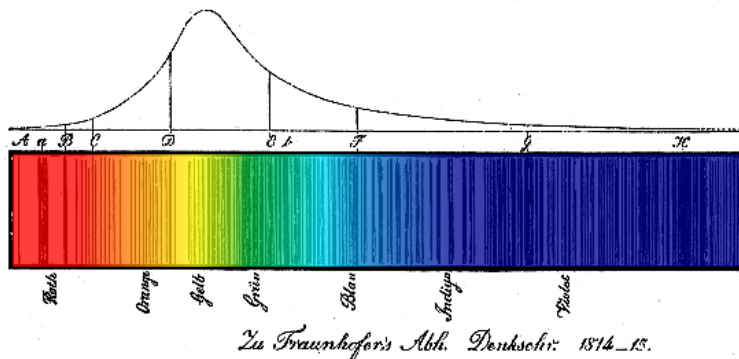
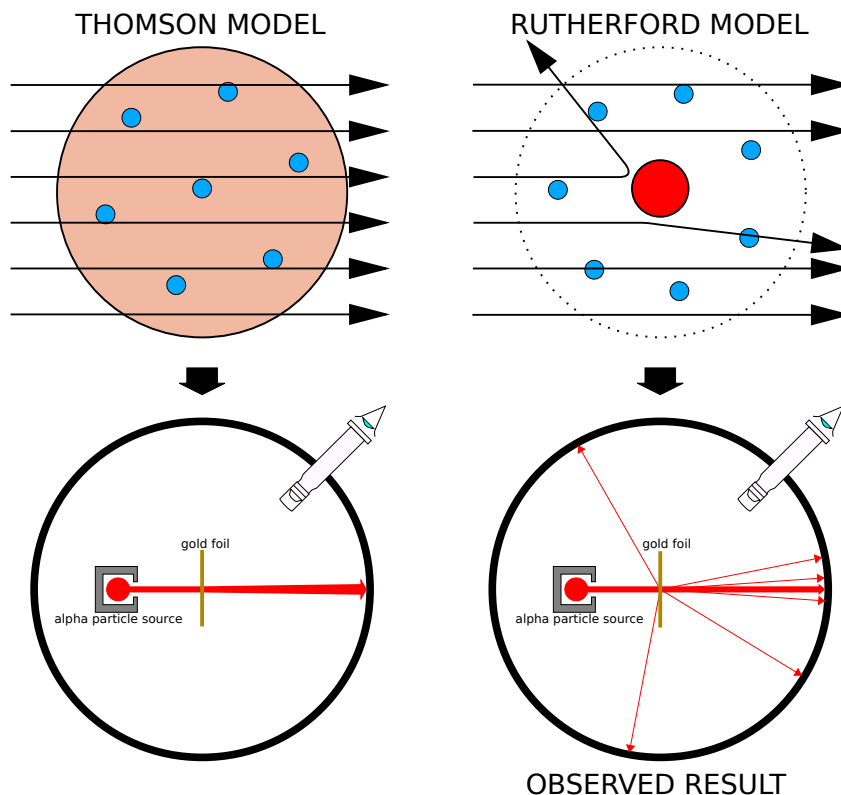


Figure 2.1: Solar spectrum with spectral lines as it visually appeared to Fraunhofer.

950 An alternative philosophy to atomism popularized by Descartes was *corpuscularianism*. Built on  
 951 ever divisible corpuscles, contrary to atoms, its principles were mainly used by alchemists like New-  
 952 ton who would later develop a corpuscular theory of light. Boyle combined together ideas of both  
 953 atomism or corpuscularianism leading to mechanical philosophy. The 18<sup>th</sup> century has seen the  
 954 development of engineering providing philosophical thought experiments with repeatable demon-  
 955 stration and a new point of view to explain the composition of matter. Lavoisier greatly contributed  
 956 to chemistry and atomism by publishing in 1789 a list of 33 chemical elements corresponding to  
 957 what are now called *atoms* [2]. In the early 19<sup>th</sup> century Dalton summarized the knowledge on  
 958 composition of matter [3]. In his atomic model, the atoms are ball-like constituents of the chemical  
 959 elements. All atoms of a given element are identical, in size, mass, and other properties while the  
 960 atoms of different elements differ. He also considered that atoms cannot be divided into smaller  
 961 particles, created nor destroyed and that they combine into chemical compounds. The essence of  
 962 chemical reaction was then the combination, separation or rearrangement of atoms. Soon after,

963 Fraunhofer invented the spectrometer and discovered the spectral lines in the sunlight spectrum, as  
 964 showed in Figure 2.1 [4]. These were later linked to the absorption by chemical elements present in  
 965 the solar atmosphere by Kirchhoff and Bunsen. The rise of atomic physics, chemistry and mathematical  
 966 formalism unraveled the different atomic elements and ultimately, the 20<sup>th</sup> century saw the  
 967 very first sub-atomic particles.

968 **Discovery of the inner structure of the atom**



*Figure 2.2: Through the gold foil experiment, Rutherford could show that most of the mass of atoms was contained in a positively charged nucleus and could then propose a more accurate atomic model than that of Thomson.*

969 The negatively charged *electron* was the first to be discovered in 1897 by Thomson after three  
 970 decades of research on cathode rays [5]. He proved that the electrification observed in an elec-  
 971 troscope, as reported by Perrin [6], was due to the rays themselves. Hence, they had to be composed  
 972 of electrically charged particles. In 1900, Becquerel showed the *beta rays* emitted by radium had the  
 973 same charge over mass ratio as was measured by Thomson for cathode rays, pointing to electrons as  
 974 a constituent of atoms [7]. This discovery leads to Thomson's plum pudding atomic model in which  
 975 electrons are embed into a uniform positively charged atom [8]. In 1907, Rutherford and Royds  
 976 showed that *alpha* particles were helium ions [9]. Indeed, once captured in a tube and subjected to  
 977 an electric spark causing an electron avalanche, they could combine with two electrons to form a  
 978  ${}^4\text{He}$ .

This discovery was directly followed by the constraint of the atom structure in between 1908 and 1913 through the Geiger–Marsden gold foil experiments in which the deflection angle of alpha particles fired at a very thin gold foil was measured [10–13]. It highlighted that atoms were mainly empty with nearly all their mass contained into a tiny positively charged *nucleus*. With these two observations, Rutherford could formulate the Rutherford planetary model of the atom in 1911 [14], shown together with the Thomson plum pudding model in Figure 2.2. The link between atomic number and number of positive and negative charges contained into the atoms would fast be understood. Hence, the different kinds of element transmutations appeared to be purely nuclear processes making clear that the electromagnetic nature of chemical transformations could not possibly change nuclei. A new branch in physics appeared to exclusively study nuclei: *nuclear physics*. By studying alpha emission and the product of their interaction with nitrogen gas, Rutherford reported in 1919 the very first nuclear reaction [15]. It leads to the discovery that the hydrogen nucleus was composed of a single positively charged particle that was later baptised *proton* [16]. This idea came from 1815 Prout’s hypothesis proposing that all atoms are composed of “*protyle*” (i.e. hydrogen atoms) [17, 18]. By using scintillation detectors, Rutherford could highlight typical hydrogen nuclei signature and understand that the impact of alpha particles with nitrogen would knock out a hydrogen nucleus and produce an oxygen 17, as showed in Formula 2.1 and would then postulate that protons are building bricks of all elements.



With this assumption and the discovery of *isotopes* together with Aston, elements with identical atomic number but different masses, Rutherford proposed that all elements’ nuclei but hydrogen are composed of both charged particles, protons, and of chargeless particles, which he called *neutrons* [16, 19]. These neutral particles helped maintaining nuclei as one, as charged protons were likely to electrostatically repulse each other. He then introduced the idea of a new force, a *nuclear* force. The first idea concerning neutrons was a bond state of protons and electrons as it was known that the beta decay, emitting electrons, was taking place in the nucleus. However, it was then shown that electrons being confined into the nucleus would hardly be possible due to Heisenberg’s uncertainty principle. Finally, in 1932, following the discovery of a new neutral radiation, Chadwick could discover the neutron as an uncharged particle with a mass similar to that of the proton which would solve the nucleus puzzle [20–24].

### 1008 Development of the Quantum Electrodynamics

Historically, the development of the quantum theory revolved around the question of emission and absorption of discrete amount of energy through light. Einstein used the initial intuition of Planck about the black-body radiation to develop in 1905 a model to explain the photoelectric effect in which light was described by discrete *quanta* now called *photons* [25, 26]. For this model, Einstein introduced the concept of wave-particle duality as classical theory was not able to describe the phenomenon. With the new understanding of atoms and of their structure, classical theories also proved unable to explain atoms’ stability. Indeed, using classical mechanics, electrons orbiting around a nucleus should radiate an energy proportional to their angular momentum and hence, loose energy through time and the spectrum of energy emission should then be continuous. However, it was known since the 19<sup>th</sup> century and the discovery of spectral lines that the emission spectrum of material was discrete [4].

In 1913, quantum physics was introduced into the atomic model by Bohr to overcome the electron's energy loss due to orbiting radiation emission [27]. Using the correspondence principle stating that for large enough numbers the quantum calculations should give the same results than the classical theory, he proposed the very first quantum model of the hydrogen atom explaining the line spectrum by introducing the *principal quantum number*  $n$  describing the electron shell. The same year, Moseley confirmed Bohr's model through the Moseley's law [28]. Debye and then Sommerfeld extended it by introducing the quantization of the angular momentum [29]. The quantization the z-component of the angular momentum led to the *second and third quantum numbers*, or *azimuthal and magnetic quantum number*,  $l$  and  $m$ . The second defines the orbital angular momentum of the electrons on their shells and hence, the shape of the orbital, while the third the available orbital on the subshell for each electron as shown in Figure 2.3.

Nevertheless, although the model was not only limited to spherical orbitals anymore, making the atom more realistic, the Zeeman effect couldn't be completely explained by just using  $n$ ,  $l$  and  $m$  [30–33] nor could the result of the Stern-Gerlach experiment [34]. Both experiments are shown in Figure 2.4. A solution was brought after Pauli in 1925 proposed together with his exclusion principle the idea of a new quantum degree of freedom in order to resolve the apparent problem [35, 36]. This degree of freedom was interpreted as an intrinsic angular momentum vector associated to the particle itself, not to the orbital [37], and associated to a new quantum number  $s$ , the *spin projection quantum number* explaining the lift of degeneracy to an even number of energy levels [38]. The new quantum number helped in theorizing the neutron as a neutral particle rather than a bond state of a proton and an electron confined in the nucleus itself.

The introduction of the *spin* happened one year after another attempt of improvement of the theory was made by De Broglie in his Ph.D. thesis [39]. The original formulation of the quantum theory only considered photons as energy quanta behaving as both waves and particles. De Broglie proposed that *all* matter are described by waves and that

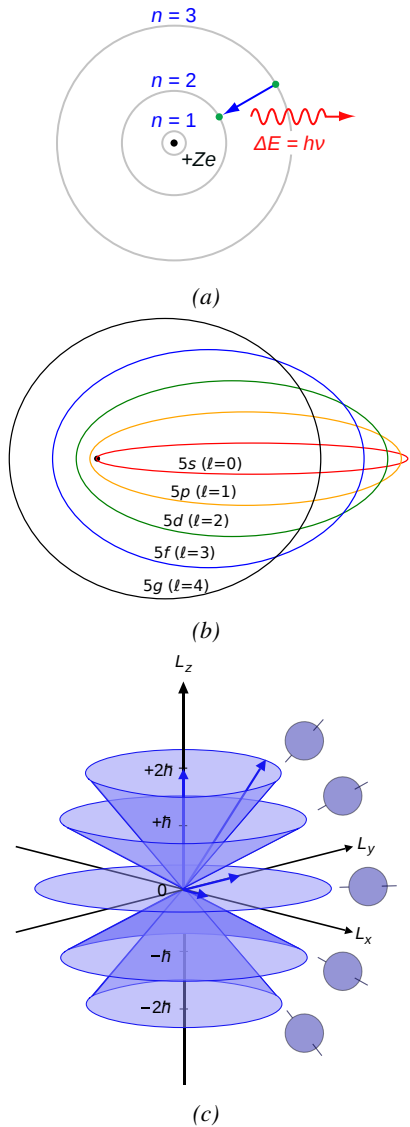


*Figure 2.3: Figure 2.3a: The orbits in which the electron may travel according to the Bohr model of the hydrogen atom. An electron jumps between orbits and is accompanied by an emitted or absorbed amount of electromagnetic energy ( $h\nu$ ). The orbits radius increases as  $n^2$ . Figure 2.3b: Elliptical orbits with the same energy and quantized angular momentum  $l = 0, 1, \dots, n - 1$  in the case  $n = 5$ . Figure 2.3c: Illustration of quantum mechanical orbital angular momentum. The cones and plane represent possible orientations of the angular momentum vector for  $l = 2$  and  $m = -2, -1, 0, 1, 2$ .*

that all matter are described by waves and that

their momentum is proportional to the oscillation of quantized electromagnetic field oscillators. This interpretation was able to reproduce the previous version of the quantum energy levels by showing that the quantum condition involves an integer multiple of  $2\pi$ , as shown by Formula 2.2.

$$(2.2) \quad p = \hbar k \Leftrightarrow \int pdx = \hbar \int kdx = 2\pi\hbar n$$

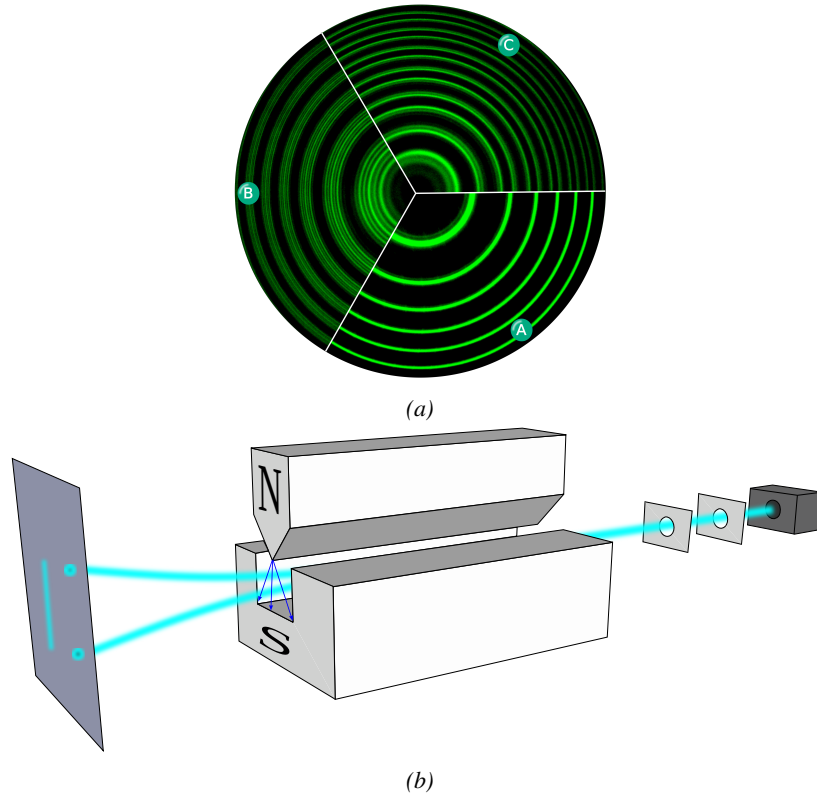


*Figure 2.4: Figure 2.4a: The spectral lines of mercury vapor lamp anomalous Zeeman effect without magnetic field (A) and with magnetic field (B - transverse Zeeman effect & C - longitudinal Zeeman effect). Figure 2.4b: Stern-Gerlach experiment: Silver atoms traveling through an inhomogeneous magnetic field and being deflected up or down depending on their spin.*

Although the intuition of De Broglie about the wave-particle duality of all matter was a step in the right direction, his interpretation was semiclassical and it is in 1926 that the first full quantum wave equation would be introduced by Schrödinger to describe electron-like particles, reproducing the previous semiclassical formulation without inconsistencies [40]. This complex equation describes the evolution of the wave function  $\Psi$  of the quantum system, defined by its position vector  $\mathbf{r}$  and time  $t$  as an energy conservation law, in which the hamiltonian of the system  $\hat{H}$  is explicit, by solving the Equation 2.3.

$$(2.3) \quad i\hbar \frac{\partial}{\partial t} |\Psi(\mathbf{r}, t)\rangle = \hat{H} |\Psi(\mathbf{r}, t)\rangle$$

1076     The spin was then included into Schrödinger equation by Pauli to take into account the interaction  
 1077     with an external magnetic field, as shown in Equation 2.4 in which the Hamiltonian operator is a  $2 \times 2$   
 1078     matrix operator due to the Pauli matrices [38].  $\mathbf{A}$  is the vector potential and  $\phi$  is the scalar electric  
 1079     potential.

$$(2.4) \quad i\hbar \frac{\partial}{\partial t} |\Psi\rangle = \left[ \frac{1}{2m} (\sigma \cdot (\mathbf{p} - q\mathbf{A})^2 + q\phi) \right] |\Psi\rangle$$

1080     Later in 1927, Dirac went further in his paper about emission and absorption of radiation by  
 1081     proposing a second quantization not only of the physical process at play but also of the electromagnetic  
 1082     field [41]. His equation provided the ingredients to the first formulation of *Quantum Electrodynamics (QED)*  
 1083     and the description of photon emission by electrons dropping into a lower energy state  
 1084     in which the final number of particles is different than the initial one. Nevertheless, in order to properly  
 1085     treat electromagnetism, the incorporation of the special relativity developed by Einstein was  
 1086     necessary. Derived in 1928, the Dirac equation, shown as Equation 2.5, similarly to Schrödinger  
 1087     equation, is a single-particle equation but it incorporates special relativity in addition to quantum  
 1088     mechanics rules [42].

$$(2.5) \quad i\hbar\gamma^\mu \partial_\mu \psi - mc\psi = 0$$

1089     It features the  $4 \times 4$  gamma matrices  $\gamma^\mu$  built using  $2 \times 2$  Pauli matrices and the unitary matrix,  
 1090     the 4-gradient  $\partial_\mu$ , the rest mass  $m$  of any half integer spin massive particle described by the wave  
 1091     function  $\psi(x, t)$ , also called a Dirac spinor and the speed of light  $c$ . In addition to perfectly reproduce  
 1092     the results obtained with quantum mechanics so far, it also provided *negative-energy solutions* that  
 1093     would later be interpreted as a new form of matter, *antimatter* [43, 44]. In the non-relativistic limit,  
 1094     the Dirac equation gives a theoretical justification to the Pauli equation that was phenomenologically  
 1095     constructed to account for the spin.

1096     The successes of the QED were soon followed with theoretical problems as computations of any  
 1097     physical process involving photons and charged particles were shown to be only reliable at the first  
 1098     order of the *perturbation theory* [45]. At higher order of the theory, divergent contributions were  
 1099     appearing giving nonsensical results. Only two effects were contributing to these infinities.

- 1100       • The self-energy of the electron (or positron), the energy that the particle has due to its own  
     1101       interaction with its environment.
- 1102       • The vacuum polarization, virtual electron–positron pairs produced by a background electro-  
     1103       magnetic field in the vacuum which is not an "empty" space. These virtual pairs affect the  
     1104       charge and current distributions generated by the original electromagnetic field.

1105     Solving this apparent problem was done by carefully defining the concepts of each observable,  
 1106     for example mass or charge, as these quantities are understood within the context of a non-interacting  
 1107     field equation. From the experimental point of view, they are abstractions as what is measured is  
 1108     "renormalized observables" shifted from their "bare" value by the interaction taking place in the  
 1109     measuring process. The infinities needed to be connected to corrections of mass and charge as those  
 1110     are fixed to finite values by experiment. This was the intuition of Bethe in 1947 who successfully  
 1111     computed the effect of such *renormalization* in the non-relativistic case [46]. Full covariant formula-  
 1112     tions of QED including renormalization were achieved by 1949 by Tomonaga, Schwinger, Feynman,

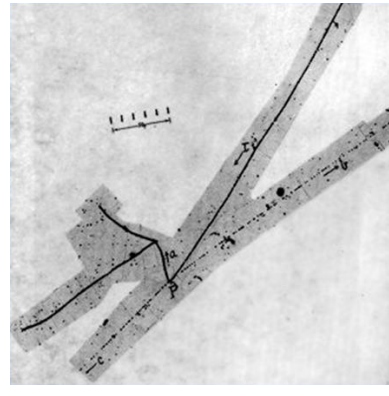
1113 and Dyson [47]. With the resolution of infinities, QED had mostly reached its final form, being still  
 1114 today the most accurate physical theory, and would serve as a model to build all other quantum field  
 1115 theories.

### 1116 Development of the quark model and Quantum Chromodynamics

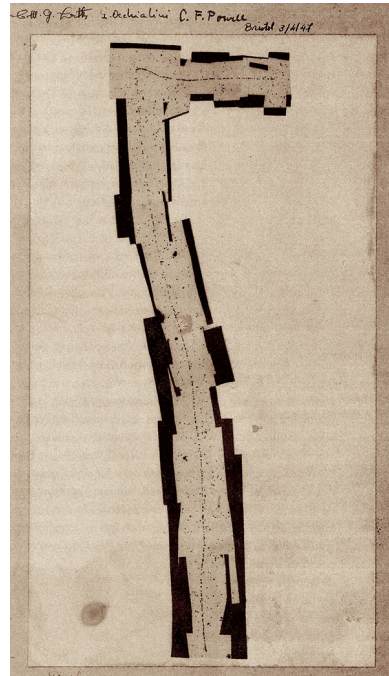
1117 To explain the nuclear force that holds *nucleons*  
 1118 (protons and neutrons) together, Yukawa proposed  
 1119 in 1934 the existence of a force carrier called *meson*  
 1120 due to its predicted mass in the range in between the  
 1121 electron and nucleon masses [48]. Discovered in  
 1122 1936 by Anderson and Neddermeyer [49, 50], and  
 1123 confirmed using bubble chambers in 1937 by Street  
 1124 and Stevenson [51], a first meson candidate was ob-  
 1125 served in the decay products of cosmic rays. As-  
 1126 suming it had the same electric charge as electrons  
 1127 and protons, this particle was observed to have a  
 1128 curvature due to magnetic field that was sharper  
 1129 than protons but smoother than electrons resulting  
 1130 in a mass in between the two. But its properties  
 1131 were not compatible with Yukawa's theory, which  
 1132 was emphasized by the discovery of a new candi-  
 1133 date in 1947, again in cosmic ray products using  
 1134 photographic emulsions [52–54]. The detections of  
 1135 the mu-meson and of the pi-meson in emulsions are  
 1136 showed in Figure 2.5.

1137 This new candidate, although it had a similar  
 1138 mass than the already believed *meson*, would rather  
 1139 decay into it. For distinction, the first candidate  
 1140 would then be renamed "*mu meson*" when the sec-  
 1141 ond would be the "*pi meson*". The *mu meson* was  
 1142 behaving like a heavy electron and didn't partici-  
 1143 pate in the strong interaction whereas the pion was  
 1144 believed to be the carrier of the nuclear interaction.  
 1145 This led to classify the *mu* in a new category of par-  
 1146 ticles that shared similar properties called *leptons*  
 1147 under the name of *muon* together with the electron.  
 1148 The *pi meson* was finally found to be a triplet of par-  
 1149 ticles: a positively charged, a negatively charged,  
 1150 and a neutral particle. The neutral *pi meson* has  
 1151 been more difficult to identify as it wouldn't leave  
 1152 tracks on emulsions nor on bubble chambers and  
 1153 needed to be studied via its decay products. It was  
 1154 ultimately identified in University of California's  
 1155 cyclotron in 1950 through the observation of its decay into 2 photons [55].

1156 Also discovered in 1947 but in cloud chamber photographs, the *K meson* has also been an impor-



(a)



(b)

Figure 2.5: Figure 2.5a: decay of a  $\mu$ -meson in an emulsion. Figure 2.5b: track of a  $\pi$ -meson in an emulsion signed by Lattes, Powell, and Occhialini.

tant step towards the establishment of the Standard Model [56]. A triplet of particles, two charged and a neutral, with a mass roughly half that of a proton, were reported. These particles were baptised *K meson* in contrast to the "light" *pi* and *mu* "L-mesons". The particularity of the *K* is their very slow decays with a typical lifetime of the order of  $10^{-10}$ s much longer than the  $10^{-23}$ s of *pi*-proton reactions. The concept of *strangeness*, a new quantum number was then introduced thanks to an idea of Pais as an attempt to explain this phenomenon as *strange* particles appeared as the pair production of a strange and anti-strange particle [57].

With the development of synchrotrons, the particle *zoo* grew to several dozens during the 1950s as higher energies were reachable through acceleration. In 1961, a first classification system, called *Eightfold Way*, was proposed by Gell-Mann [58]. It found its roots in the Gell-Mann–Nishijima formula, which relates the electric charge  $Q$ , the third component of the isospin  $I_3$ , the *baryon* number  $B$  and the strangeness  $S$ , as showed in Formula 2.6 [59–61].

$$(2.6) \quad Q = I_3 + \frac{1}{2}(B + S)$$

The isospin is a quantum number introduced in 1932 to explain symmetries of the newly discovered neutron using representation theory of SU(2) [62]. The baryon number, was introduced by Nishijima as a quantum number for baryons, i.e. particles of the same family as nucleons [59]. The mesons were classified in an octet and baryons of spin  $\pm \frac{1}{2}$  and  $\pm \frac{3}{2}$  were respectively classified into an octet and a decuplet, as shown in Figure 2.6. To complete the baryon decuplet, Gell-Mann predicted the existence of baryon  $\Omega^-$  which would later be discovered in 1964 [63].

Gell-Mann, and independently Zweig, then proposed a full theoretical model in which *hadrons* (strongly interacting particles, i.e. mesons and baryons) were not elementary particles anymore [64–66]. They were rather composed of three flavors of particles called *quarks* and their anti-particles. The three flavors were called *up*, *down* and *strange*. *Up* and *down* were used to explain the nucleons and non-strange mesons, while *strange* came into the composition of hadrons showing strangeness. *Up* and *down* flavors were discovered in 1968 thanks to the deep inelastic scattering experiments conducted at the Stanford Linear Accelerator Center (SLAC) [67, 68], and *strange* could only be indirectly validated even though it provided a robust explanation to *kaon* (*K*) and *pion* ( $\pi$ ).

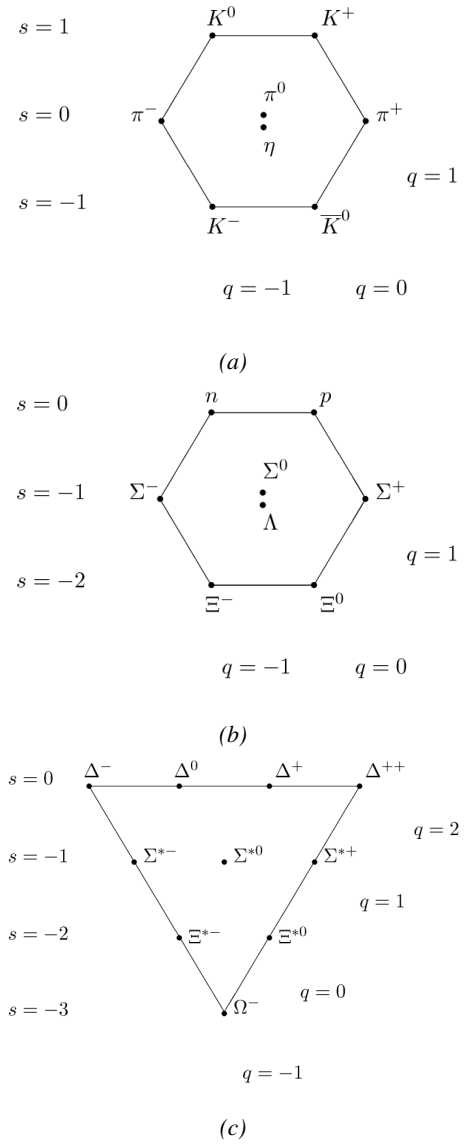
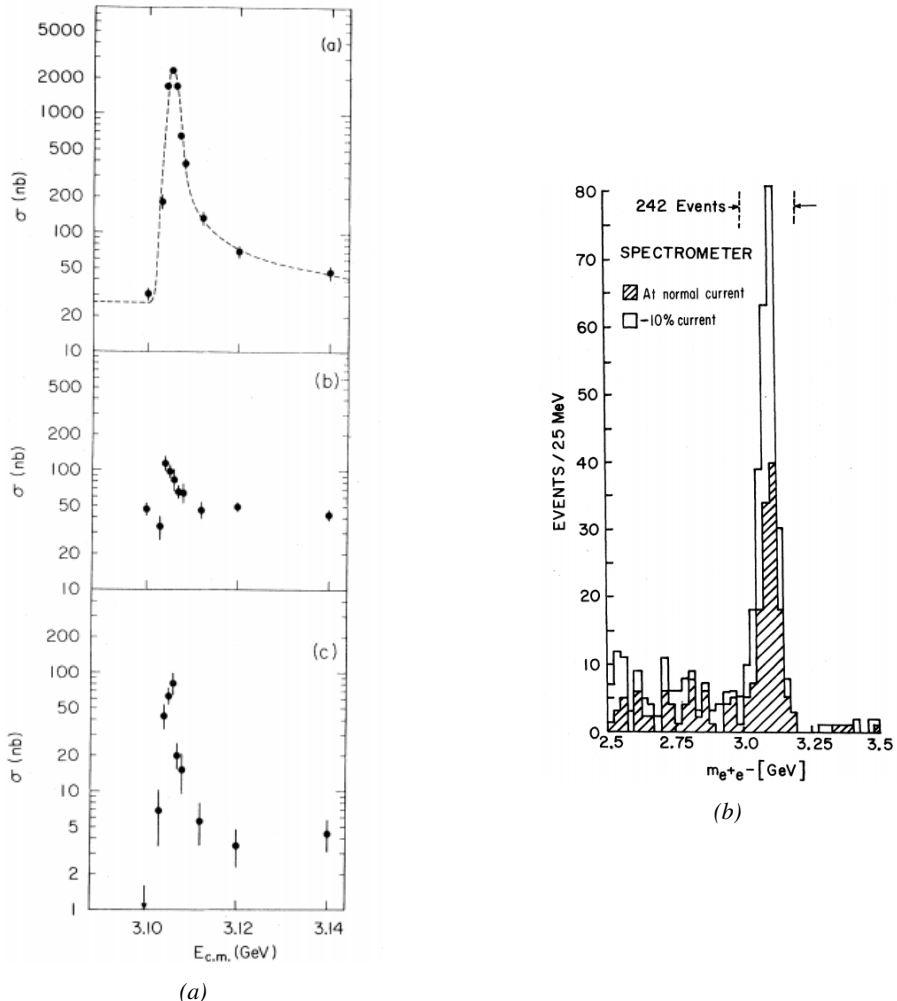


Figure 2.6: Figure 2.6a: Meson octet. Figure 2.6b: Baryon octet. Figure 2.6c: Baryon decuplet.

However, in the decade following the Gell-Mann-Zweig quark model proposition, several improvement to the model were brought. First by Glashow and Bjorken the same year that predicted the existence of a fourth quark flavor, the *charm*, that would equalize the then known number of quarks and leptons [69, 70]. Finally in 1973 by Kobayashi and Maskawa that increased the number of quarks to six to explain the experimental observation of CP violation [71, 72]. These two quarks were referred to as *top* and *bottom* for the first time in 1975 [73]. It's only after these additions to the quark model that finally the *charm* was discovered in 1974 at both SLAC and Brookhaven National Laboratory (BNL) [74, 75]. A meson in which the *charm* is bonded with an *anti-charm*, called  $J/\psi$  and presented in Figure 2.7, helped convince the physics community of the validity of the model. The *bottom* was discovered soon after in 1977 in Fermilab [76] and indicated the existence of the *top* that resisted to discovery until Fermilab's experiments CDF and D $\emptyset$  in 1995 due its very large mass and the energy needed to produce it [77, 78].



*Figure 2.7: Discovery of the  $J/\Psi$  by both SPEAR (SLAC [74]) in Figure 2.7a and AGS (BNL [75]) in Figure 2.7b. In Figure 2.7a, the cross section versus energy is showed for (a) multi hadron final states, (b)  $e^+e^-$  final states, and (c)  $\mu^+\mu^-$ ,  $\pi^+\pi^-$  and  $K^+K^-$  final states.*

As remarked by Struminsky, due to mesons such as  $\Omega^-$  or  $\Delta^{++}$ , the first SU(3) model already should have possessed an additional quantum number [79]. Indeed, these mesons are composed of three identical quarks, respectively three *strange* and *up* quarks, with parallel spins, which should be forbidden by the exclusion principle. Independently, Greenberg, and Han and Nambu proposed an additional SU(3) degree of freedom for the quarks [80, 81]. It was later referred to as *color charge gauge*, that could interact through *gluons*, the gauge boson octet corresponding to this degree of freedom. The color field is presented in Figure 2.8a. Nevertheless, as observing free quarks to prove their existence proved to be impossible, two visions of the quarks were argued. On one side, Gell-Mann proposed to see quarks as mathematical construct instead of real particles, as they are always confined, implying that quantum field theory would not describe entirely the strong interaction. He promoted the S-matrix approach to treat the strong interaction. Opposed to this vision, Feynman on the contrary argued that quarks are real particles, that he would call *partons*, that should be described as all other particles by a distribution of position and momentum [82]. The implications of quarks as point-like particles were verified at SLAC and helped abandon the S-matrix to the benefit of QFT [83]. The concept of *color* was then added to the quark model in 1973 by Fritzsch and Leutwyler together with Gell-Mann to propose a description of the strong interaction through the theory of Quantum Chromodynamics (QCD) [84]. The discovery the same year of asymptotic freedom within the QCD by Gross, Politzer, and Wilczek, allowed for very precise predictions thanks to perturbation theory [85, 86]. The evolution of the gauge constant of QCD with respect to the energy as described by asymptotic freedom is showed in Figure 2.8b.

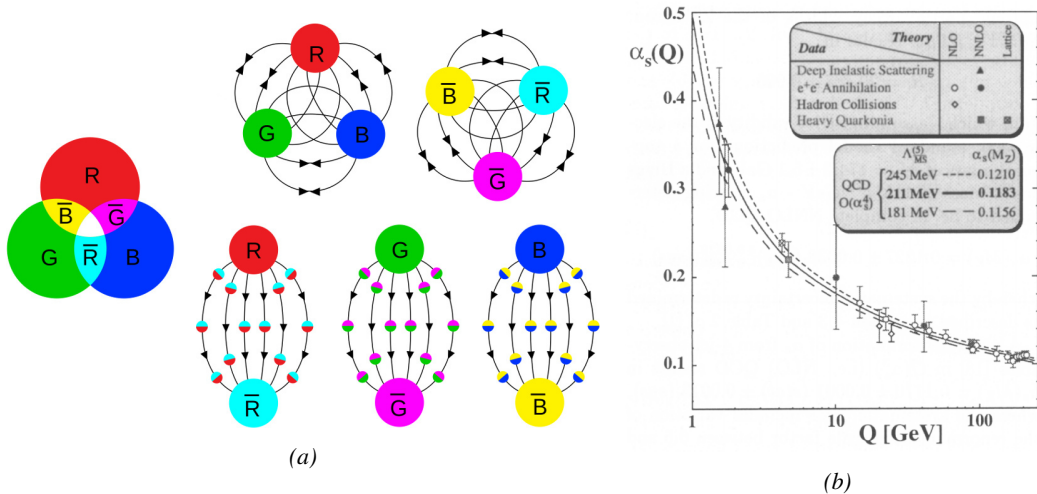
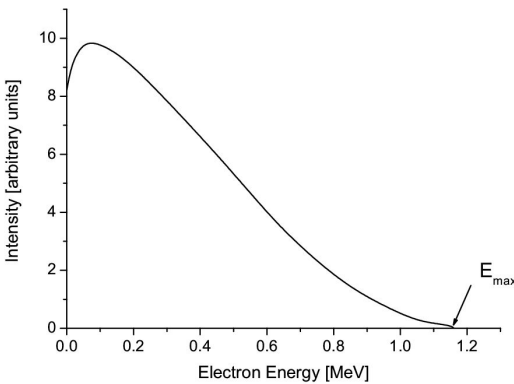


Figure 2.8: Figure 2.8a: the color field of QCD only allows for "white" baryons, particles composed of quarks, to exist. Examples are given for mesons, composed of a quark and its anti-quark, and hadrons, composed of three differently colored quarks or anti-quarks. Other exotic baryons have been predicted and observed, such as tetraquarks and pentaquarks. Figure 2.8b: a crossed analysis performed thanks to the data collected by various experiments at different energies have showed that the coupling constant evolves as predicted by the mechanism of asymptotic freedom [87].

1232 **The Weak interaction, spontaneous symmetry breaking, the Higgs mechanism and the Elec-**  
 1233 **troweak unification**

1234 The weak interaction is the process that causes radioactive decays. Thanks to the neutron discov-  
 1235 ery [23], Fermi could explain in 1934 beta radiations through the beta decay process in which the  
 1236 neutron decays into a proton by emitting an electron [88]. Though the missing energy observed dur-  
 1237 ing this process triggered a huge debate about the apparent non-conservation of energy, momentum  
 1238 and spin of the process, Fermi, as Pauli before him [89], proposed that the missing energy was due to  
 1239 a neutral not yet discovered particle that was then baptised *neutrino*. The impossibility to detect such  
 1240 a particle left some members of the scientific community sceptical, but hints of energy conservation  
 1241 and of the existence of the neutrino were provided by measuring the energy spectrum of electrons  
 1242 emitted through beta decay, as there was a strict limit on their energy, as showed in Figure 2.9.



1253 *Figure 2.9: Energy spectrum of beta particles emitted by a source*  
 1254 *of  $^{210}\text{Bi}$ .*

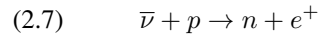
1255 constraint the beta decay theory of Fermi and extend it to the case of the muon, Konopinski and  
 1256 Mahmoud proposed in 1953 that the muon decay would eject a particle similar to the neutrino [91].  
 1257 They predicted the existence of a muon neutrino that would be different to the one involved in the  
 1258 beta decay, related to the electron. With this, the idea of *lepton number* arised. The *muon neutrino*  
 1259 was successfully detected in 1962 by Lederman, Schwartz, and Steinberger [92].

1260 The theory could not be valid though as the probability of interaction, called *cross-section*, would  
 1261 have been increasing without limitation with the square of the energy. Fermi had proposed a two  
 1262 vector current coupling but Lee and Yang noted that an axial current could appear and would violate  
 1263 parity [93]. Gamov and Teller had already tried to account for such parity violation by describ-  
 1264 ing Fermi's interaction through allowed (parity-violating) and superallowed (parity-conserving) de-  
 1265 cays [94]. The Wu experiment in 1956 confirmed the parity violation [95], as showed by Figure 2.10.  
 1266 But the success of QED as a quantum field theory sparked the development of similar theory to de-  
 1267 scribe the weak interaction.

1268 As previously discussed, the great success of QED was built on an underlying symmetry, inter-  
 1269 preted as a gauge invariance so that the effect of the force is the same in all space-time coordinates,  
 1270 and of the possibility to renormalize it in order to resolve infinities. In 1967, Weinberg found a  
 1271 way to unite both the electromagnetic and weak interaction into a gauge theory involving four gauge  
 1272 bosons, three of which are massive and carry out the weak interaction and the last is a massless bo-

1243  
 1244  
 1245  
 1246  
 1247  
 1248  
 1249  
 1250  
 1251  
 1252  
 1253  
 1254  
 1255  
 1256  
 1257  
 1258  
 1259  
 1260  
 1261  
 1262  
 1263  
 1264  
 1265  
 1266  
 1267  
 1268  
 1269  
 1270  
 1271  
 1272  
 1273

It's only 30 years later in 1953 that it was discovered by the team of Cowan and Reines using the principle of inverse beta decay described through Formula 2.7 [90].



The experiment consisted in placing water tanks sandwiched in between liquid scintillators near a nuclear reactor with an estimated neutrino flux of  $5 \times 10^{13} \text{ cm}^{-2} \text{ s}^{-1}$ . However, in order to explain the absence of some reactions in the experiment of Cowan and Reines and

son carrying the electromagnetic interaction [96]. Among the three massive bosons, two are charged and one is neutral, similarly to the previously theorized *pi meson* vector of the Yukawa model [48] and all have a mass much greater than nucleons and thus a very short life time implying a finite very short range, contrary to the contact interaction originally proposed by Fermi.

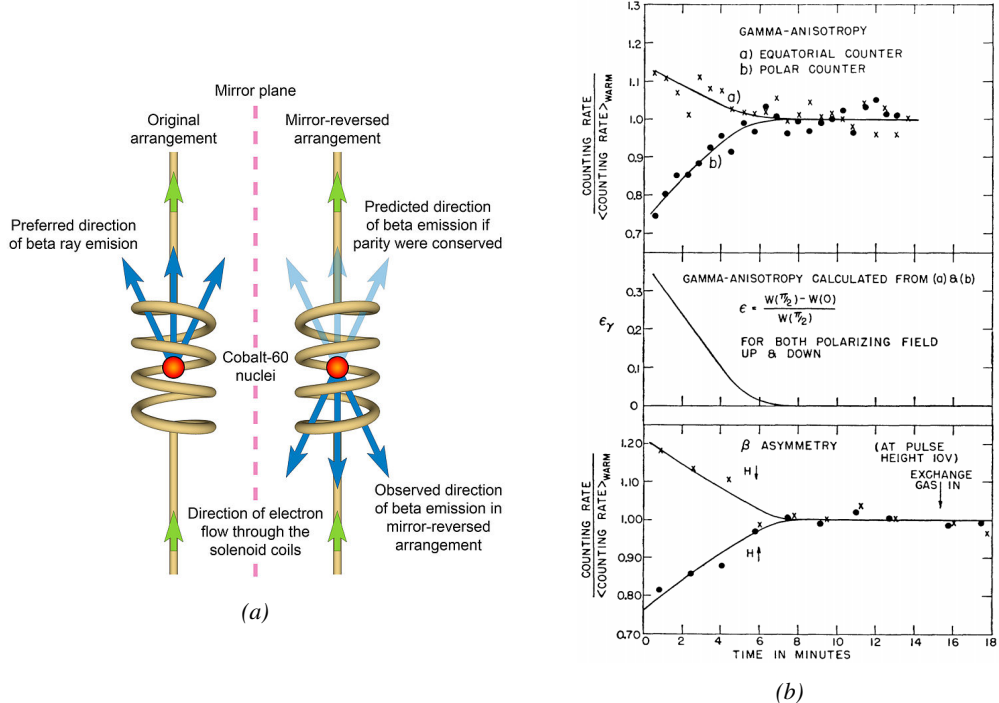


Figure 2.10: As explained through Figure 2.10a, the Wu experiment consisted in measuring the preferred direction of emission of beta rays of a Cobalt source placed in a stable magnetic field aligned, in one case, and anti-aligned, in the other case, with the nuclear spin. The result of Figure 2.10b showed a violation of parity.

Breakthroughs in other fields of physics contributed in giving theoretical support and interpretation to the unified electroweak theory. The stepping stone was the use of spontaneous symmetry breaking that was inspired to Nambu at the beginning of the 1960s [97, 98] following the development of the Bardeen–Cooper–Schrieffer (BCS) superconductivity mechanism in 1957 [99]. Cooper had shown that BCS pairs, pairs of electrons bound together at low temperature, can have lower energy than the Fermi Energy and are responsible for superconductivity. This led to the discovery of Goldstone-Nambu bosons [100, 101] as a result of the spontaneous breaking of the chiral symmetry in a theory describing nucleons and mesons developed by Nambu and Jona-Lasinio in 1961, and now understood as a low-energy approximation of QCD. Similarly to the mechanism of energy gap appearance in superconductivity, the nucleon mass is suggested to be the result of a self-energy of a fermion field and is studied through a four-fermion interaction in which, as a consequence of the symmetry, bound states of nucleon-antinucleon pairs appear and can be regarded as virtual pions. Though the symmetry is maintained in the equations, the ground state is not preserved. Goldstone showed that the bound states correspond to spinless bosons with zero mass [101].

Although the model in itself didn't revolutionize particle physics, spontaneous symmetry breaking was generalized to quantum field theories. As all fundamental interactions are described using

gauge theories based on underlying symmetries, processes such as the chiral symmetry breaking were introduced soon after the publication of Nambu and Jona-Lasinio. In 1962, Anderson, discussed the implications of spontaneous symmetry breaking in particles physics [102]. He did so by following the idea of Schwinger who suggested that zero-mass vector bosons were not necessarily required to describe the conservation of baryons, contrary to the bosons emerging from chiral symmetry breaking [103]. A model was finally independently built in 1964 by Brout and Englert [104], Higgs [105], and Guralnik, Hagen, and Kibble [106], who discovered that combining an additional field into a gauge theory in order to break the symmetry, the resulting gauge bosons acquire a nonzero mass. Moreover, Higgs stated that this implied the existence of at least one new massive, i.e. self-interacting, scalar boson corresponding to this additional field, that is now known as *Higgs boson*. The Higgs mechanism today specifically refers to the process through which the gauge bosons of the weak interaction acquire mass. In 1967, Weinberg could point to the Higgs mechanism to integrate a Higgs field into a new version of the electroweak theory in which the spontaneous symmetry breaking mechanism of the Higgs field would explicitly explain the masses of the weak interaction gauge bosons and the zero-mass of photons [96].

### 2.1.2 Construction and validation of the Standard Model

The Standard Model of particle physics was built in the middle of the 1970s after the experimental confirmation of the existence of quarks [107]. It is based on the assembly of the models previously introduced and describing the fundamental interactions and their gauge bosons, except for gravitation, as well as the way elementary "matter" particles interact with the fields associated with these force carriers. In this sense, the development of QED and the unification of the electroweak interaction, of the Yukawa interaction and of QCD, and of the Higg mechanism made it possible to explain most of the contemporary physics.

In the SM, "matter" particles, are described by twelve fermion fields of spin  $\frac{1}{2}$  obeying the Fermi-Dirac statistics, i.e. subjected to the Pauli exclusion principle. To each fermion is associated its corresponding anti-particle. The fermions are classified according to the way they interact and thus according to the charges they carry. Six of them are classified as quarks ( $u, d, c, s, t$ , and  $b$ ) and are subjected to all interactions and the six others as leptons ( $e^-, \mu^-, \tau^-, \nu_e, \nu_\mu$ , and  $\nu_\tau$ ). Leptons are not subjected to the strong interaction and among them, the three neutrinos only interact weakly as they are neutral particles, which explains why they are so difficult to detect. The gauge boson fields are the gluons  $g$  for the strong interaction, the photon  $\gamma$  for the electromagnetic interaction and the weak bosons  $W^+, W^-,$  and  $Z^0$  for the weak interaction. Finally, the Higgs field  $H^0$  is responsible, through the spontaneous symmetry breaking, of the mixing of the massless electroweak boson fields  $W_1, W_2, W_3,$  and  $B$  leading to the observable states  $\gamma, W^+, W^-,$  and  $Z^0$  that can gain mass while interacting with the Higgs field. This picture of the SM is summarized through Figure 2.11 where the antifermions are not shown.

When the model was first finalized, the existence of the weak gauge bosons, of the charm, of the third quark generation composed of top and bottom quarks to explain the observed CP violation was not proven but the predictions were measured with good precision in the years following [74–78]. The weak bosons  $W$  and  $Z$  were discovered during the next decade in 1983 [108–111]. The very last predicted elementary particle of the model that was not observed yet proved to be very difficult to observe. The Higgs boson needed the start of the LHC to finally be observed in 2012 [112, 113]. A few years more of tests were necessary to measure its properties to confirm the observation of a scalar boson compatible with the predicted Higgs boson  $H^0$  [114].

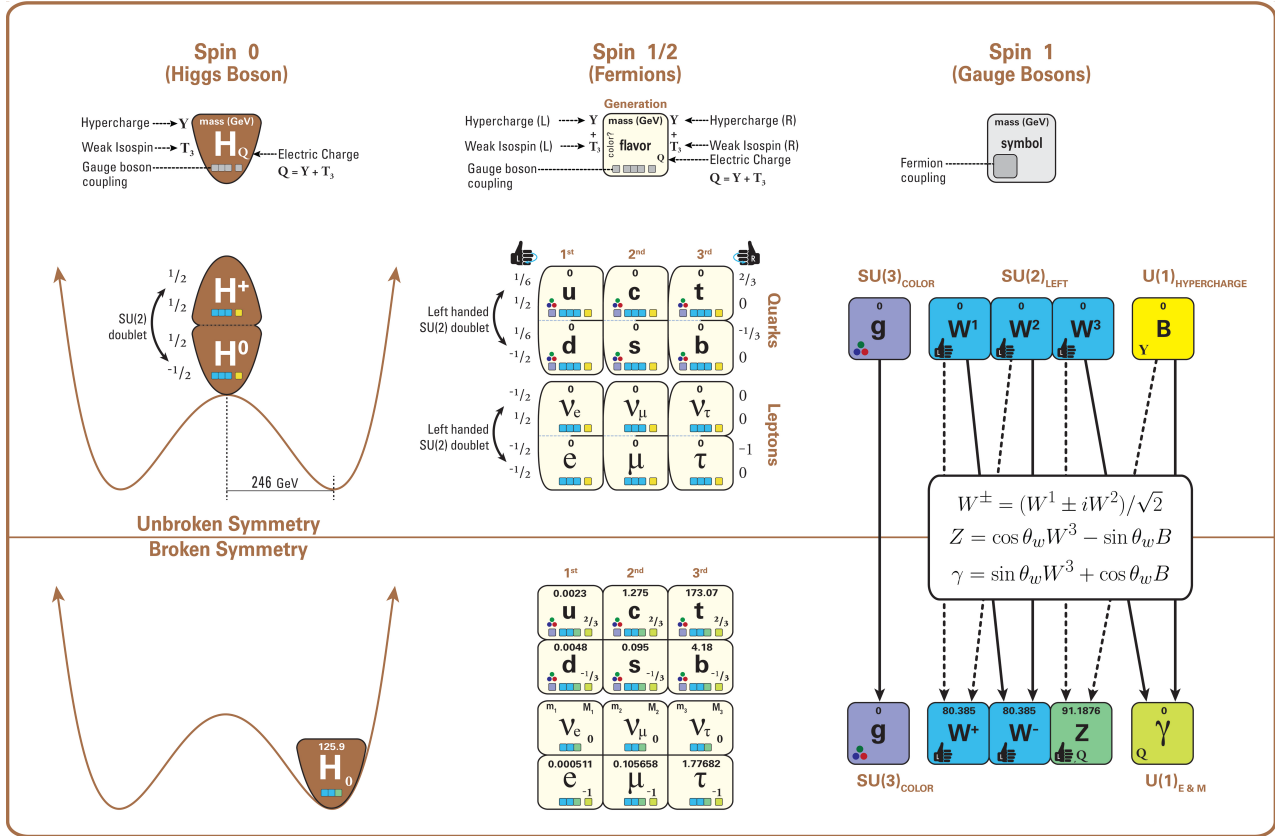


Figure 2.11: The elementary particles of the Standard Model are shown along with their properties. Their interactions with the strong, weak and electromagnetic forces have been made explicit using color squares. In the left column, the scalar Higgs boson is depicted. The center is focused on the matter particles, the fermions, and the right column on the force carriers, the gauge bosons. The role of the Higgs boson in electroweak symmetry breaking is highlighted, and the corresponding way properties of the various particles differ in the (high-energy) symmetric phase (top) and the (low-energy) broken-symmetry phase (bottom) are shown.

### 1338 2.1.3 Investigating the TeV scale

1339 In High-Energy Physics, the number of experimental events depends on the total interaction cross-  
 1340 section of the colliding particles and of the *instantaneous luminosity* [115]. The luminosity is a  
 1341 quantity providing an information on the interaction rate normalised to the interaction cross-section.  
 1342 The relationship between number of events  $N$ , cross-section and instantaneous luminosity  $\mathcal{L}$  is given  
 1343 in Formula 2.8.

$$(2.8) \quad \mathcal{L} = \frac{1}{\sigma} \frac{dN}{dt} \Leftrightarrow N = \sigma \int \mathcal{L} dt = \sigma \mathcal{L}_{int}$$

1344 The integral of the luminosity over time is referred to as the *integrated luminosity*  $\mathcal{L}_{int}$ . In fact,  
 1345 the instantaneous luminosity can be deduced from the beam parameters. New colliders now use  
 1346 bunched beams. The instantaneous luminosity then depends on the bunch crossing frequency  $f_{BX}$ ,  
 1347 on the number of particles contained in each bunch  $n$ , and on the RMS transverse beam sizes in the

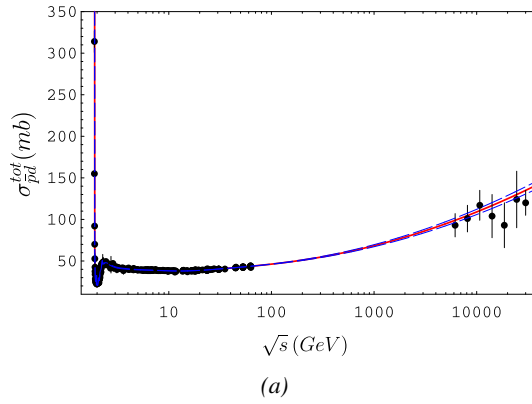
horizontal,  $\sigma_x^*$ , and vertical directions,  $\sigma_y^*$ , at the level of the interaction point. The beam sizes can be assumed to be identical, leading to the relation of Formula 2.9.

$$(2.9) \quad \mathcal{L} = f_{BX} \frac{n^2}{\sigma^*}$$

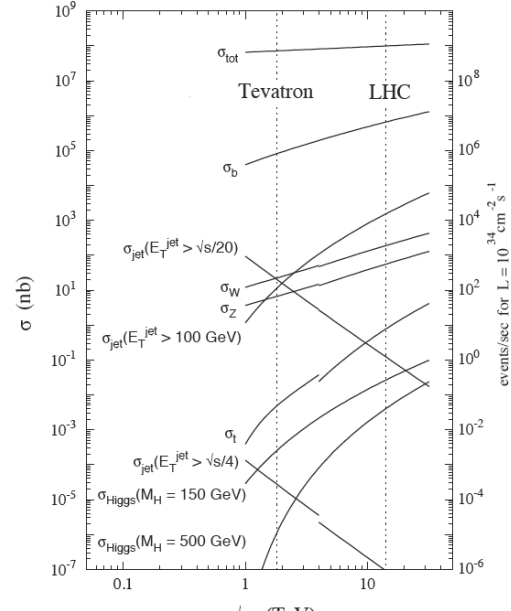
This expression doesn't depend on time anymore and leads to a simple estimation of the integrated luminosity and hence, knowing the cross-section of each available physics channel, to the expected number of events in each channel. The total interaction cross section is the sum of all the different output channels allowed by the interaction process. In the case of highly relativistic protons, the proton-proton (pp) total cross-section increases with the center-of-mass energy of interactions, as can be seen from Figure 2.12.

Enhancing rare processes that allow to finely test the Standard Model is then achieved through an increase in both energy and luminosity. At the energy range that were scanned thanks to high-energy colliders, the SM has so far been a well tested theory. Nevertheless, several hints of physics going beyond its scope have been observed.

**Dark matter and gravity:** The discrepancy of velocity dispersion of stars in galaxies with respect to the visible mass they contain is known since the end of the 19<sup>th</sup> century where Kelvin proposed that this problem could be solved if a great majority of the stars would be dark bodies, idea strongly criticized by Pointcaré [117]. Throughout the 20<sup>th</sup> century, physicists like Kapteyn [118] or Zwicky [119, 120], showed the first hints of a *dark matter* by studying star velocities and galactic clusters, followed by robust measurements of galaxy rotation curves by Babcock which suggested that the mass-to-luminosity ratio was different from what would be expected from watching the visible light [121]. Later in the 1970s, Rubin and Ford from direct light observations [122] and Rogstad and Shostak from radio measurements [123] showed that the radial velocity of visible objects in galaxies was increasing with increasing distance to the center of



(a)



(b)

Figure 2.12: Figure 2.12a: Total proton-proton cross-section as a function of the collisions center-of-mass energy  $\sqrt{s}$  [116] with cosmic-ray data from Akemo Observatory and Fly's Eye Collaboration. Figure 2.12b: Total proton-(anti)proton and interaction channel cross-sections in the TeV scale.

increasing with increasing distance to the center of

the galaxy. An example of galaxy rotation curve is provided in Figure 2.13. Finally observation of lensing effect by galaxy clusters, temperature distribution of hot gas in galaxies and clusters, and the anisotropies in the Cosmic Microwave Background (CMB), showed in Figure 2.14, kept on pointing to a *dark matter* [124]. From all the data accumulated, the visible matter would only account to no more than 5% of the total content on the visible universe [125]. Alternative theories have tried to investigate modified versions of the General Relativity as this theory is only well tested at the scale of the solar system but is not sufficiently tested on wider ranges or even theories in which gravitation is not a fundamental force but rather an emergent one [126, 127]. But so far, such theories have difficulties to reproduce all the experimental observations as easily as through dark matter.

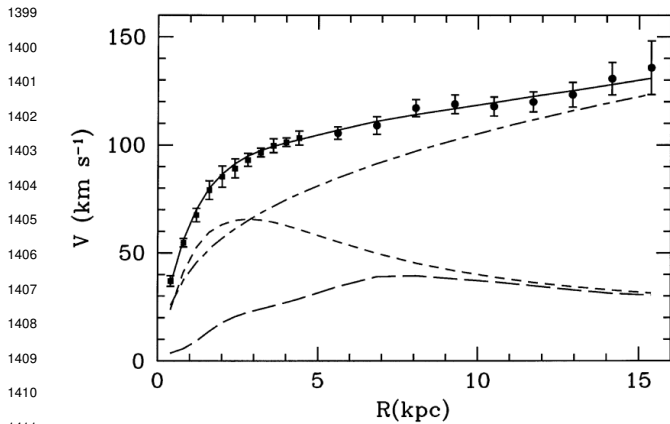


Figure 2.13: Rotation curve (points) of the galaxy M33 compared with best fitting model (line). The short-dashed line represents the rotation profile that would be expected from the observation of the stellar disc alone [128].

into a light Higgs boson compared to the *Planck Mass*. In the SM, the Higgs mass is left to be a measured parameter rather than a calculated one even though the model requires a mass in between 100 and 1000 GeV/c<sup>2</sup> to stay unitary. Nevertheless, quantum corrections to the Higgs mass coming from its interactions with virtual particles should make the scalar boson much heavier than what measured [130]. Through the MSSM, the stability of fermion masses would provide stability to the Higgs boson mass via the introduction of a fermionic super partner.

On top of providing a solution to the Hierarchy Problem, the model comes with heavy dark matter candidates in the TeV scale [131]. Indeed, in the case *R-parity* is not violated, the lightest supersymmetric particle (LSP) cannot decay and could then explain the dark matter. The LSP in the model is neutral and can only interact through the weak and gravitational interactions. Typical candidates are the *neutralino*, the *sneutrino* or the *gravitino*.

Finally, gravity is not explained through the SM, and huge difficulties are encountered when trying to include it. The strength of gravitational interaction is expected to be negligible at the scale of elementary particles, nevertheless, adding gravitation in the perspective of developing a "theory of everything" leads to divergent integrals that could not be fixed through renormalization. Extensions to the MSSM, and in particular minimal SUper GRAvity (mSUGRA), include general relativity as mediator of the symmetry breaking. mSUGRA gives access to the hidden sector in which the MSSM only interacts gravitationally and suppresses the infinities arising from attempts to include gravity into the SM thanks to possible renormalization [132].

Signatures for the MSSM would come from the super partners of quarks and gluons that can

A possible theory to offer dark matter candidates would be *supersymmetry* (SUSY) which proposes a relationship in between bosons and fermions in the frame of the Minimal Supersymmetric Standard Model (MSSM). In this model, each elementary particle, through a spontaneous space-time symmetry breaking mechanism would have a *super partner* from the other family of particles, pairing bosons and fermions together. The model was first introduced as a way to solve the *Hierarchy Problem* [129]. The discrepancy between the strength of the weak force and gravity translates

decay into an LSP that could then be identified as missing energy as it escapes the detectors undetected. But even in the case MSSM predictions are not to be seen, the other models treating dark matter also propose Weakly Interacting Massive Particles (WIMPs) that could be observed in similar ways than LSPs [133]. Moreover alternative models exist to provide solutions to the Hierarchy Problem. The most investigated models are extra dimensions such as Arkani-Hamed Dimopoulos Dvali [134, 135], Kaluza–Klein [136, 137] or Randall-Sundrum models [138, 139] that usually also include gravitation. Finally, alternative models also exist for the production of dark matter candidates. Models with a hidden valley that would unravel the existence of a new group of light particles through the extension of the SM with a new confining gauge group [140].

1445

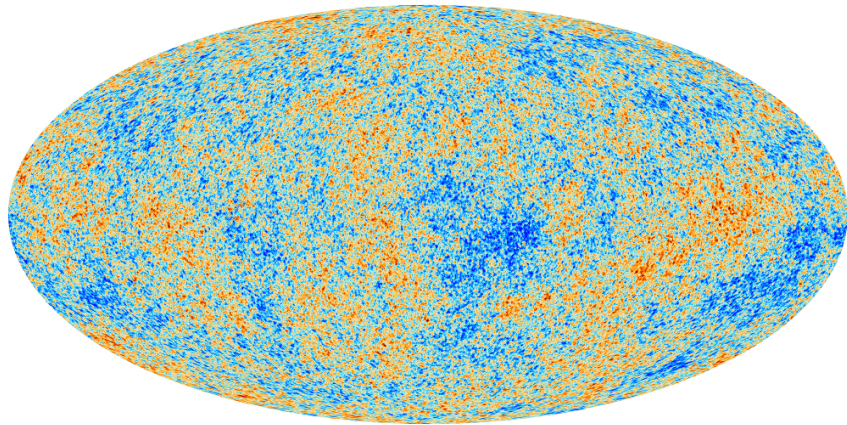


Figure 2.14: Cosmic Microwave Background as measured by the space observatory Planck which mean temperature is  $T_\gamma = (2.7255 \pm 0.0006)\text{K}$  with anisotropies of the order of a few  $\mu\text{K}$ .

1446 **Baryon asymmetry:** Another intriguing fact is that the universe is dominated by matter. However,  
 1447 the SM predicted that matter and antimatter should have been created in equal amounts. For an inter-  
 1448 action to produce matter and antimatter at different rates within the SM, three necessary conditions  
 1449 were highlighted by Sakharov[141]. First of all, there must be a violation of the baryon number  $B$ .  
 1450 Then, there must be a C-symmetry and CP-symmetry violation. The C-symmetry violation must  
 1451 happen to make sure that the processes creating more baryons than antibaryons are not compensated  
 1452 by processes creating more anti-baryons and similarly, the CP-symmetry violation makes sure that  
 1453 there are not equal numbers of left-handed baryons and right-handed anti-baryons produced. Fi-  
 1454 nally, the interactions must happen out of thermal equilibrium to make sure that CPT-symmetry does  
 1455 not balance the processes increasing the baryon number with processes doing otherwise [142]. An  
 1456 out-of-equilibrium interaction implies a new unstable heavy particle.

1457 The favoured model to explain this imbalance is the *baryogenesis* that requires electroweak sym-  
 1458 metry breaking to be first order phase transition to fall within the scope of SM [143, 144]. This  
 1459 means that the symmetry breaking process must involve the absorption or release of a fixed latent  
 1460 heat. Through the baryogenesis, the phase transition breaks P-symmetry spontaneously and allows  
 1461 for CP-symmetry violation. In turn, the CP violation makes the amplitude of interactions involving  
 1462 quarks different than the ones involving anti-quarks leading to the greater creation rate of baryons  
 1463 with respect to anti-baryons. The key to this baryon net creation would be found into the *sphaleron*.  
 1464 A sphaleron is a particle-like saddle point of the energy functional that appears at the top of the

transition barrier and that could be created if a sufficiently large amount of energy is brought as the tunneling effect through the barrier is largely suppressed for electroweak interactions. The existence of the sphaleron would allow violation of the conservation of  $B$  but also of the leptonic number  $L$  while conserving  $B - L$ . The detection at  $p - p$ -colliders of such a transition is foreseen to be made through processes with high-multiplicity final states such as  $u + u \rightarrow e^+ \mu^+ \tau^+ t\bar{t} b\bar{c} c\bar{s} d\bar{d} + X$  [145]. To be probed, the sphaleron transition requires an energy  $E_{sph} \approx 9$  TeV. Nevertheless, if such transition cannot be observed, other BSM models such as the WIMP baryogenesis could be then observed thanks to the detection of displaced vertices, featuring the decay of a WIMP leading to violation of  $B$  [146].

Another possibility to explain the apparent asymmetry would be the existence of an electric dipole moment (EDM) in any fundamental particle that would permit matter and antimatter particles to decay at different rates [147]. Indeed, the presence of an EDM violates in itself both  $P$  and  $T$  symmetries. Experiments are able to probe for the EDM of various fundamental particles such as the electron [147], the charm and strange quarks [148] or even a heavy neutrino EDM [149].

1479

**Neutrino mass and sterile neutrino scenario:** The SM considers neutrinos to be massless. But it was showed in the late 1960s by the Homestake experiment that the flux of solar neutrinos (i.e.  $\nu_e$ ) measured didn't match the predicted values [150]. The mechanism of neutrino oscillations as a solution to the discrepancy was proposed by Pontecorvo [151] and confirmed in the early 2000s by the Sudbury Neutrino Observatory [152]. This oscillation implies that neutrinos that can be observed are a superposition of massive neutrino states. The research on neutrino oscillation is already quite advanced with experiments looking at atmospheric, reactor or beam neutrinos in order to determine the elements of the mixing matrix (Pontecorvo–Maki–Nakagawa–Sakata matrix [153]) similar to the Cabibbo–Kobayashi–Maskawa (CKM) matrix describing the mixing of quarks [72]. Nevertheless, no answer to the origin of neutrino mass is yet provided.

Explaining the light non-zero mass of the neutrinos  $\nu_l$  ( $l = e, \mu, \tau$ ) of the order of the eV can be done through the Seesaw mechanism [154, 155]. This model features heavy Majorana counterparts  $N_l$  ( $l = e, \mu, \tau$ ) to the  $\nu_l$ . The masses of the light and heavy neutrinos are linked through a  $2 \times 2$  mass matrix  $A$  with eigenvalues  $\lambda_{\pm}$  expressed as in Equation 2.10.

$$(2.10) \quad \begin{aligned} A &= \begin{pmatrix} 0 & M \\ M & B \end{pmatrix} \\ \lambda_{\pm} &= \frac{B \pm \sqrt{B^2 + 4M^2}}{2} \end{aligned}$$

The Majorana mass term  $B$  is assumed to be comparable to the Grand Unified Theory scale ( $10^{16}$  GeV) while the Dirac mass term  $M$  is of the order of electroweak scale (246 GeV). In these conditions, the eigenvalue  $\lambda_+$  is almost  $B$  while  $\lambda_-$  is close to the ratio  $-M^2/B$  compatible with very light neutrinos with masses of the order of 1 eV. Studying the left-right symmetric model seeking for the parity violation in weak interactions leads to the incorporation of three additional gauge bosons  $W_R$  and  $Z'$  as a result of the spontaneous symmetry breaking. The processes that are predicted by the model and can be probed at colliders are processes such as  $pp \rightarrow W_R \rightarrow l + N_l + X$  and  $pp \rightarrow Z' \rightarrow N_l + N_l + X$  where the heavy neutrinos decay as  $N_l \rightarrow l + j_1 + j_2$ ,  $j_i$  being jets [156]. Other version of seesaw mechanisms exist to account for the neutrino mass that can also be explained thanks to supersymmetric models [157].

## 2.2 The Large Hadron Collider & the Compact Muon Solenoid

Throughout its history, CERN has played a leading role in high-energy physics. Large regional facilities such as CERN were planned after the second world war in an attempt to increase international scientific collaboration and to allow scientists to share the forever increasing costs of experimental facilities. Indeed, it is necessary to use always more powerful tools to improve the fine understanding of our Universe. The construction of the first CERN accelerators at the end of the 50s, the Synchrocyclotron (SC) and the Proton Synchrotron (PS), was directly followed by the first observation of antinuclei in 1965 [158]. The very first proton-proton collider showing hints of protons not being elementary particles was the Intersecting Storage Rings (ISR). From this experience, the Super Proton Synchrotron (SPS) was built in the 70s to investigate the structure of protons, the preference for matter over antimatter, the state of matter in the early universe or exotic particles, and led to the discovery in 1983 of the W and Z bosons [108–111]. These newly discovered particles and the electroweak interaction were then studied in detail by the Large Electron-Positron (LEP) collider that proved that there only are three generations of elementary particles in 1989 [159]. The LEP was then dismantled in 2000 to allow for the LHC to be constructed in the existing tunnel.

### 2.2.1 LHC, the most powerful particle accelerator

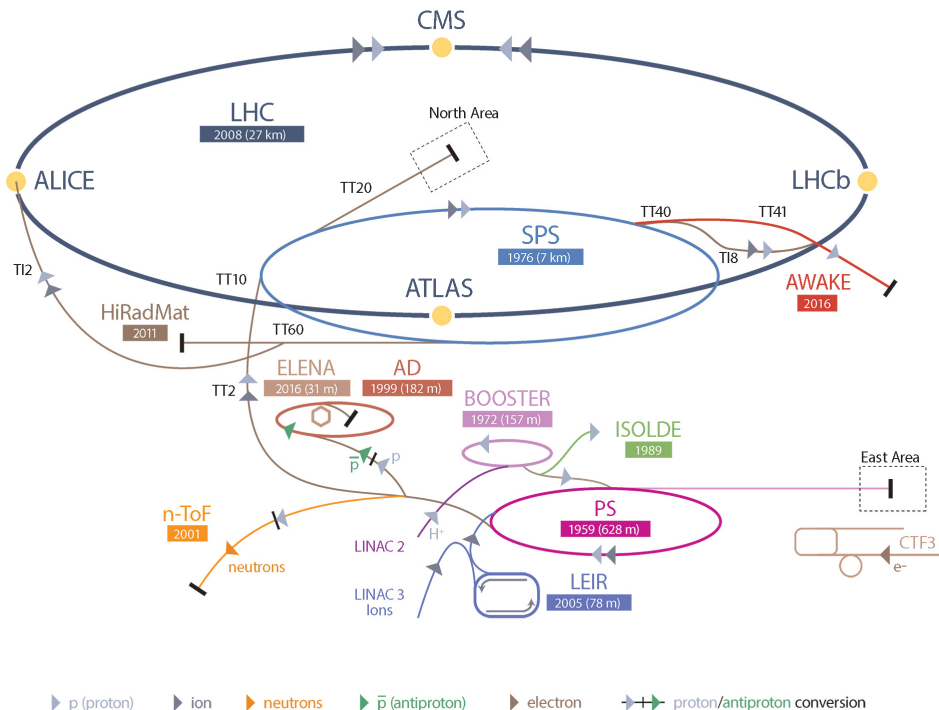


Figure 2.15: CERN accelerator complex.

The different aspects of physics beyond the Standard Model of particle physics and the Standard Model itself can be tested through the use of very energetic and intense hadron and ion colliders. Powerful hadron colliders are suited for searching for strongly interacting particles. The LHC at

1523 CERN is a perfect tool to seek answers to these open questions and the experiments build along its  
 1524 beam lines already started investigating further into the SM and BSM physics.

1525 The LHC has always been considered as an  
 1526 option for the future of CERN. At the moment  
 1527 of the construction of the LEP beneath the border  
 1528 between France and Switzerland, the tunnel was  
 1529 built in order to accommodate what would be a  
 1530 Large Hadron Collider with a dipole field of 10 T  
 1531 and a beam energy in between 8 and 9 TeV [160].  
 1532 In 1985, the creation of a 'Working Group on the  
 1533 Scientific and Technological Future of CERN'  
 1534 took place to investigate such a collider [161].  
 1535 The decision was finally taken almost ten years  
 1536 later, in 1994, to construct the LHC in the LEP  
 1537 tunnel [162] and the approval of the 4 main ex-  
 1538 periments that would take place at the four inter-  
 1539 action points came in 1997 [163] and 1998 [164]:

- 1540 • ALICE [165] has been designed for the  
 1541 purpose of studying the confinement of  
 1542 quarks through exploration of the quark-  
 1543 gluon plasma that is believed to have been  
 1544 a state of matter that existed in the very first  
 1545 moment of the universe.
- 1546 • ATLAS [166] and CMS [167] are general  
 1547 purpose experiments that have been de-  
 1548 signed with the goal of continuing the ex-  
 1549 ploration of the Standard Model and the in-  
 1550 vestigation of new physics.
- 1551 • LHCb [168] has been designed to investi-  
 1552 gate the preference of matter over antimat-  
 1553 ter in the universe through CP violation.

1554 These large-scale experiments, as well as the  
 1555 full CERN accelerator complex, are displayed in  
 1556 Figure 2.15. The LHC is a 27 km long hadron  
 1557 collider and the most powerful accelerator used  
 1558 for particle physics since 2008 [169]. The LHC  
 1559 is designed to collide protons at a center-of-  
 1560 mass energy of 14 TeV and luminosity of  $10^{34}$   
 1561  $\text{cm}^{-2}\text{s}^{-1}$ , as well as  $Pb$  ions at a center-of-mass  
 1562 energy of 2.8 TeV/A with a peak luminosity of  
 1563  $10^{27} \text{ cm}^{-2}\text{s}^{-1}$ . The collider is the last of a long  
 1564 series of accelerating devices. Indeed, before be-  
 1565 ing accelerated by the LHC, the particles need to pass through different acceleration stages. All

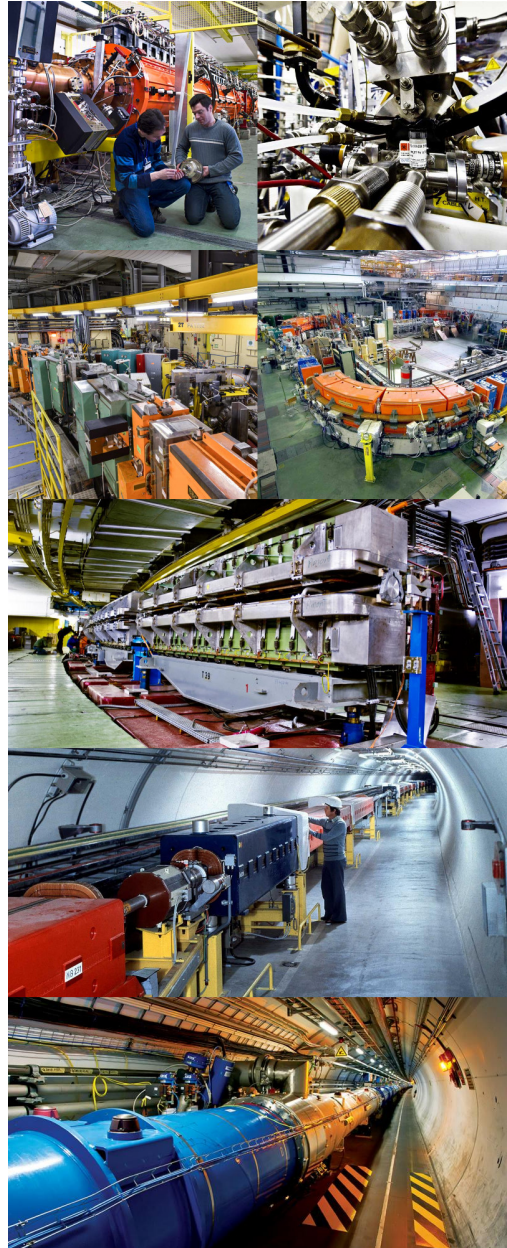


Figure 2.16: Pictures of the different accelerators. From top to bottom: first the LINAC 2 and the Pb source of LINAC 3. Then the Booster and the LEIR. Finally, the PS, the SPS and the LHC.

these acceleration stages are visible on Figure 2.15 and pictures of the accelerators are shown in Figure 2.16.

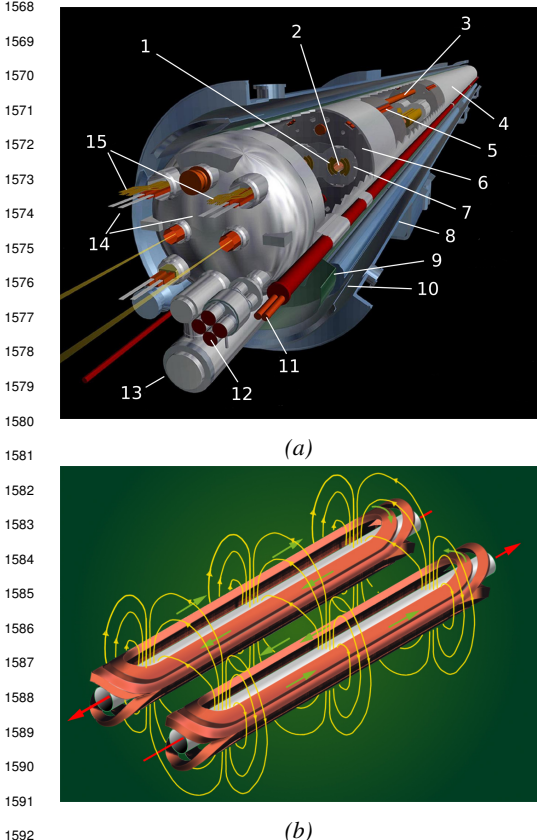


Figure 2.17: Figure 2.17a: schematics of the LHC cryodipoles. 1: Superconducting Coils, 2: Beam pipe, 3: Heat exchanger Pipe, 4: Helium-II Vessel, 5: Superconducting Bus-bar, 6: Iron Yoke, 7: Non-Magnetic Collars, 8: Vacuum Vessel, 9: Radiation Screen, 10: Thermal Shield, 11: Auxiliary Bus-bar Tube, 12: Instrumentation Feed Throughs, 13: Protection Diode, 14: Quadrupole Bus-bars, 15: Spool Piece Bus-bars. Figure 2.17b: magnetic field and resulting motion force applied on the beam particles.

The story of accelerated protons at CERN starts with a bottle of hydrogen gas injected into the source chamber of the linear particle accelerator *LINAC 2* in which a strong electric field strips the electron off the hydrogen molecules only to keep their nuclei, the protons. The cylindrical conductors then accelerate the protons to an energy of 50 MeV. When exiting the *LINAC 2*, the protons are divided into four bunches and injected into the four superimposed synchrotron rings of the *Booster* where they are then accelerated to reach an energy of 1.4 GeV before being injected into the *PS*. The four proton bunches are hence sent as one to the *PS* where their energy eventually reaches 26 GeV. The *PS* not only accelerates protons. It also accelerates heavy ions from the *Low Energy Ion Ring (LEIR)*. Lead is first injected into the dedicated linear collider *LINAC 3*, that accelerates the ions. Electrons are stripped off the lead ions all along the acceleration process and eventually, only bare nuclei are injected in the *LEIR* whose goal is to transform the long ion pulses received into short dense bunches for *LHC*. Ions injected and stored in the *PS* were accelerated by the *LEIR* from 4.2 MeV to 72 MeV. Directly following the *PS*, is finally the last acceleration stage before the *LHC*, the 7 km long *SPS*. The *SPS* accelerates the protons to 450 GeV and inject them in both *LHC* accelerator rings that will increase their energy up to 7 TeV. When the *LHC* runs with heavy lead ions for *ALICE* and *LHCb*, ions are injected and accelerated to reach the energy of 2.8 TeV/A.

The *LHC* beams are not continuous but are rather organised in bunches of particles. When in *pp*-collision mode, the beams are composed of 2808 bunches of  $1.15 \times 10^{11}$  protons separated by

25 ns. When in *Pb*-collision mode, the 592 *Pb* bunches are on the contrary composed of  $2.2 \times 10^8$  ions separated by 100 ns. The two parallel proton beams of the *LHC* are contained in a single twin-bore magnet due to the space restriction in the *LEP* tunnel. Indeed, building two completely separate accelerator rings next to each other was impossible. The dipoles of the 1232 twin-bore magnets are shown in Figure 2.17 alongside the magnetic field generated along the dipole section to accelerate the particles. The dipoles generate a nominal field of 8.33 T, needed to give protons and lead nucleons their nominal energy. Some 392 quadrupoles, presented in Figure 2.18, are also used to focus to the beams, as well as other multipoles to correct smaller imperfections.

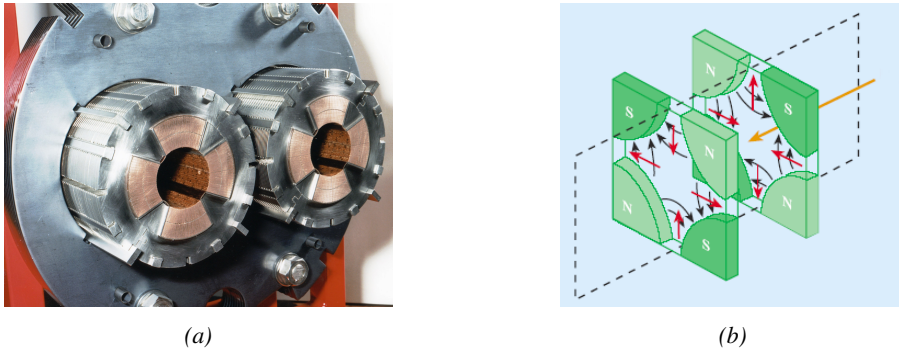


Figure 2.18: The LHC quadrupoles (Figure 2.18a) showed together with the magnetic fields and resulting focussing force applied on the beam by two consecutive quadrupoles (Figure 2.18b).

## 2.2.2 Timeline of operation

1613 LHC accelerated its first proton in September 2008 but the first collisions only started one year later  
1614 in November 2009. At this moment the LHC machine officially became the world's most powerful  
1615 particle accelerator and entered its Physics Run 1 that lasted until February 2013. During Run 1  
1616 of the LHC program, the center-of-mass energy was only half of the nominal LHC energy. Never-  
1617 theless, the energy and luminosity displayed during Run 1 were enough for both CMS and ATLAS  
1618 to discover the Higgs boson [112, 113] as showed in Figure 2.19 and for LHCb to discover pen-  
1619 taquarks [170] and confirm the existence of tetraquarks [171]. During this period, ALICE also re-  
1620 ported a successful observation of the quark-gluon plasma aimed at studying the early universe [172],  
1621 ATLAS reported the observation of a new particle before the discovery of the Higgs [173] and a first  
1622 test of super-symmetric models was performed [174].

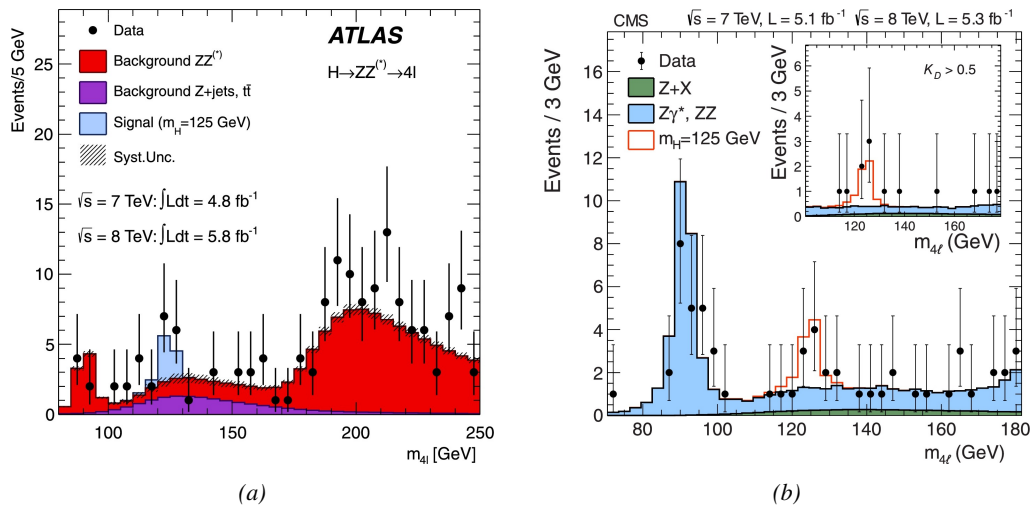


Figure 2.19: Distribution of the four-lepton invariant mass for the  $ZZ \rightarrow 4l$  analysis as presented by both ATLAS [112] and CMS [113] in 2012.

Run 1 was brought to an end with the start of the First Long Shutdown, an almost two years technical stop aimed at increasing the energy of the center-of-mass collisions to  $\sqrt{s} = 13$  TeV

as well as the instantaneous luminosity. This maintenance stop was also effectively used by the experiments which upgraded part of their detection systems. Run 2 then started in 2015 and lasted until end of 2018 where the activities ended with a last heavy ion run. During the operation, the instantaneous was successfully brought to a value of  $1.7 \times 10^{34} \text{ cm}^{-2} \text{ s}^{-1}$  exceeding the design value. Run 2 has been the occasion to acquire more data to study the properties of the Higgs boson with more precision. The boson discovered in the first physics run seems to be consistent with the SM Higgs boson [114].

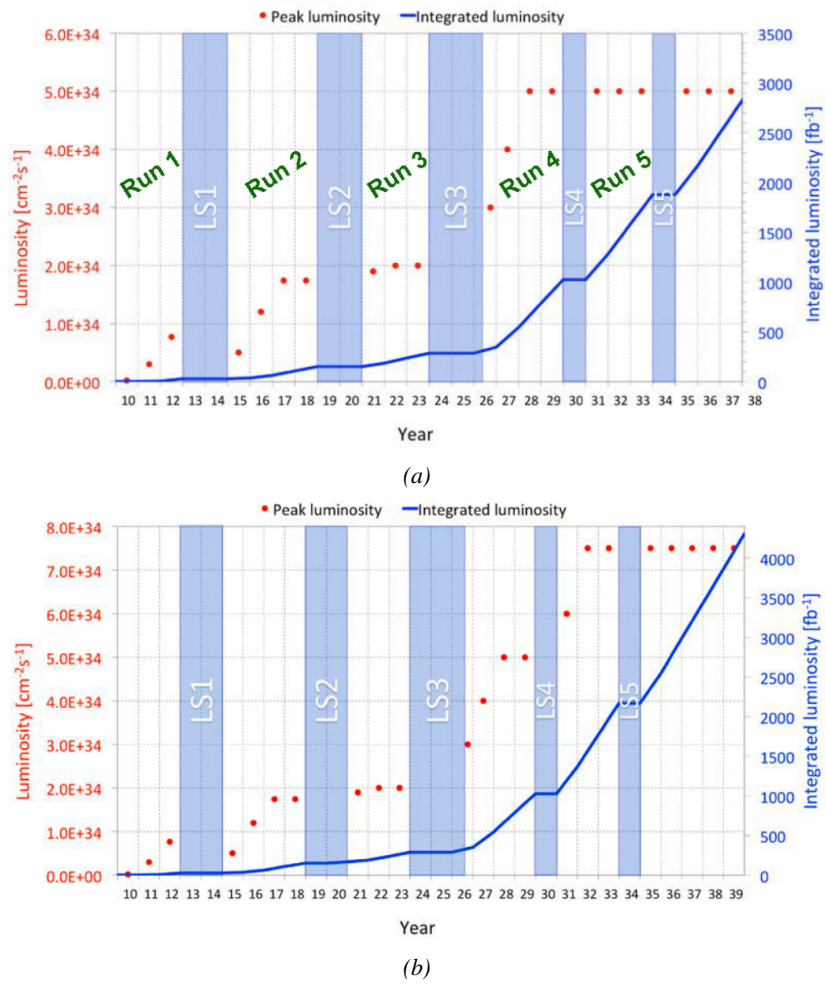


Figure 2.20: Detailed timeline projection of LHC and HL-LHC operation until 2039 showing the evolution of the instantaneous and integrated luminosity as designed (Figure 2.20a) and in the ultimate case where the instantaneous luminosity is increased to  $7.5 \times 10^{34} \text{ cm}^{-2} \text{ s}^{-1}$  thanks to a new increase of instantaneous luminosity during Run 5 (Figure 2.20b) [175–177].

From the end of 2018 to early 2021 the Second Long Shutdown will take place. This second maintenance stop will be the occasion to boost once again the beam energy to finally reach the design energy of LHC, 14 TeV. On the side of the maintenance work, preliminary work for the High Luminosity LHC will be performed. The preparations will consist of detector, on the side of the

1636 experiments, and beam machine upgrades, on the side of LHC. In 2021, the physics program will  
 1637 be resumed with an instantaneous luminosity fixed at  $2 \times 10^{34} \text{ cm}^{-2} \text{ s}^{-1}$ . During these 3 years of  
 1638 run, the LHC will deliver as much integrated luminosity as what was brought during the almost 7  
 1639 years of both Run 1 and 2 of data taking. Phase-1 will end with an overall  $300 \text{ fb}^{-1}$  delivered. The  
 1640 timeline so far described is summarized through the evolution of the instantaneous luminosity and  
 1641 of the corresponding integrated luminosity provided in Figure 2.20.

1642 After the Third Long Shutdown (2024-2026) that will close the activities of Run 3, the accel-  
 1643 erator will enter the HL-LHC configuration [175], increasing the instantaneous luminosity to an  
 1644 unprecedented level of  $5 \times 10^{34} \text{ cm}^{-2} \text{ s}^{-1}$  for  $pp$ -collisions ( $4.5 \times 10^{27} \text{ cm}^{-2} \text{ s}^{-1}$  for  $Pb$ -collisions),  
 1645 boosting the discovery potential of the LHC. The HL-LHC phase should last at least another 10 years  
 1646 depending on the breakthrough this machine would lead to. Already a new accelerating device, the  
 1647 FCC, as been proposed and is being investigated to prepare the future of high-energy physics after  
 1648 the LHC.

### 1649 2.2.3 High Luminosity LHC

1650 After approximately fifteen years of operation, the LHC will undergo a new series of upgrades during  
 1651 the LS3 in order to boost its discovery potential as previously discussed. The period after LS3 is  
 1652 what is referred to HL-LHC or Phase-2. The goal is to aim for a luminosity 5 to 7 times stronger  
 1653 than the nominal one trying to reach even 10 times this value if possible [175, 176]. Increasing  
 1654 the luminosity means that the beam size at the collision points needs to be reduced to boost the  
 1655 number of collisions per bunch crossing. For this purpose, new focusing and bending magnets and  
 1656 collimators will be installed at the collision points as well as newly developed "*crab cavities*" that  
 1657 will tilt the particle bunches just prior to the collisions by giving them transverse momentum and  
 1658 thus increasing their meeting area. In addition, the full proton injection line will be upgraded.

1659 On the experiments side, the pile-up (PU) will be increased up to 150 to 200 interactions per  
 1660 bunch crossing in ATLAS and CMS, making necessary a strong upgrade of the trigger system and  
 1661 of the inner trackers and of the calorimeters. Both ATLAS and CMS will also need to upgrade the  
 1662 muon trigger at the level of their endcaps mainly focusing on the coverage near the beam line in  
 1663 order to increase the detection acceptance and event selection. Moreover, the increased luminosity  
 1664 will also lead to an increased background rate and a faster ageing of the detectors.

1665 The end of 2018 marked the beginning of LS2 and the start of Phase-2 upgrade activities. From  
 1666 the HL-LHC period onwards, i.e. past LS3, the performance degradation due to integrated radiation  
 1667 as well as the average number of inelastic collisions per bunch crossing will rise substantially. This  
 1668 has become a major challenge for all of the LHC experiments, like CMS, that were forced to address  
 1669 an upgrade program for Phase-2 [177]. Dealing with the data from the muon detectors will force to  
 1670 upgrade the detectors and electronics towards the most recent technologies.

### 1671 2.2.4 The Compact Muon Solenoid experiment

1672 Among the four main LHC experiments is the Compact Muon Solenoid used as a multipurpose  
 1673 tool to investigate the SM and the physics beyond its scope. The CMS apparatus in itself is the  
 1674 heaviest detector ever built starring a 15 m diameter and a 29 m length for a total weight of 14 kT.  
 1675 A thick 4 T solenoid magnet located at the beam interaction point hosts trackers and calorimeters.  
 1676 Extending in all directions around the magnet, heavy iron return yokes are installed to extend the  
 1677 magnetic field and support a muon system. The apparatus consists of a barrel, referring to the magnet

and the detectors contained in it and the part of the muon system built directly in the cylinder around the magnet, and of two endcaps in the forward and backward region of the detector that closes the apparatus and complete the detection coverage along the beam line. A front view on the barrel is provided in Figure 2.21 while a detailed view of the apparatus is given in Figure 2.22.

In order to efficiently detect all long living particles and measure their properties with good precision, the CMS detector uses an onion like layout around of the interaction point in order to maximize the covered solid angle. As detailed in Figure 2.23, in the innermost region of the detector, closest to the interaction point, the silicon tracker records the trajectory of charged particles. Around it, the electromagnetic calorimeter (ECAL) stops and measures the energy deposition of electrons and photons. In the next layer, the hadron calorimeter (HCAL), hadrons are stopped and their energy measured. These layers are contained inside of the magnet of CMS, the superconducting solenoid. Outside of the magnet are the muon chambers embedded into iron return yokes used to control the magnetic field and gives muons, the only particles traveling completely through the whole detector, a double bending helping in reconstructing their energy and trajectory. Note that photons and neutral hadrons are differentiated from electrons and charged hadrons in the calorimeters by the fact that they don't interact with the silicon tracker and are not influenced by the magnetic field, as can be seen in Figure 2.23.

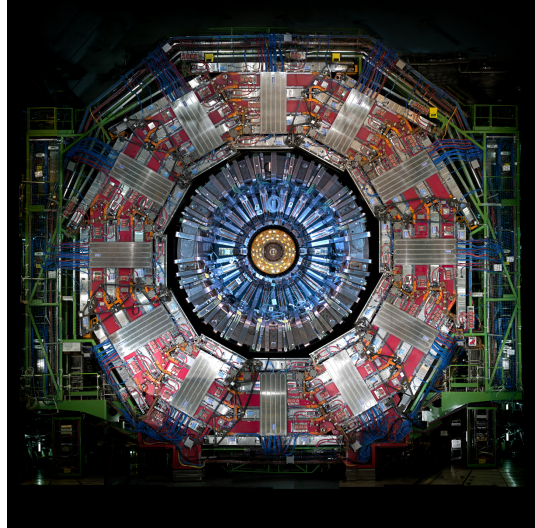


*Figure 2.21: Picture of the CMS barrel. The red outer layer is the muon system hosted into the red iron return yokes. The calorimeters are the blue cylinder inside in magnet solenoid and the tracker is the inner yellow cylinder built around the beam pipe.*

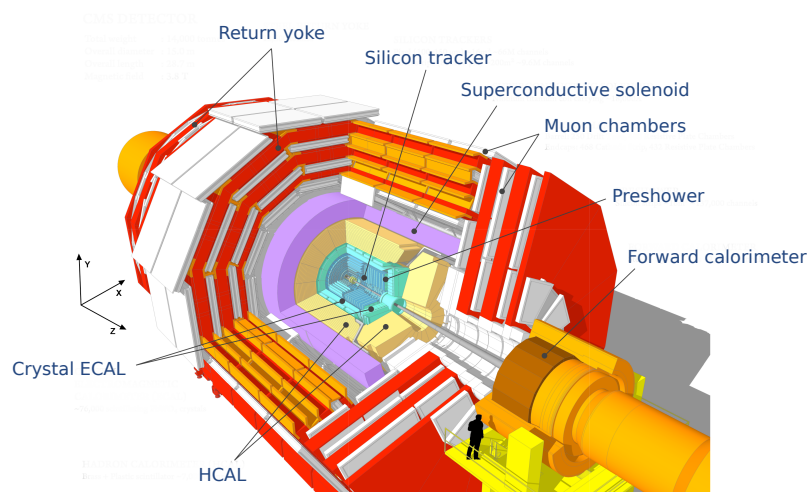


*Figure 2.22: View of the CMS apparatus and of its different components.*

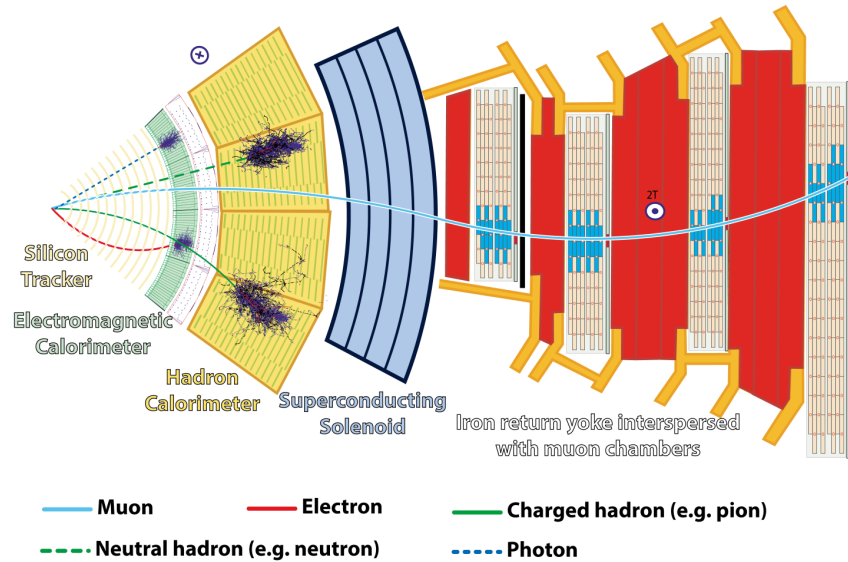


Figure 2.23: Slice showing CMS sub-detectors and how particles interact with them.

#### 1707 2.2.4.1 The silicon tracker

1708 The silicon tracker visible in  
 1709 Figure 2.24 is divided into two  
 1710 different sub-systems: the *pixel*  
 1711 *detector* at the very core and  
 1712 the *microstrip detector* around  
 1713 it. This system is composed  
 1714 of 75 million individual read-  
 1715 out channels with up to 6000  
 1716 channels per squared centime-  
 1717 ter for the pixels making it the  
 1718 world's biggest silicon detec-  
 1719 tor. This density allows for  
 1720 measurements of the particle  
 1721 tracks with a precision of the  
 1722 order of  $10\ \mu\text{m}$ . This is neces-  
 1723 sary to reconstruct all the dif-  
 1724 ferent interaction vertices with precision and have a precise measure of the curvature of the charged  
 1725 particles traveling through the magnetic field to estimate their charge and momentum.

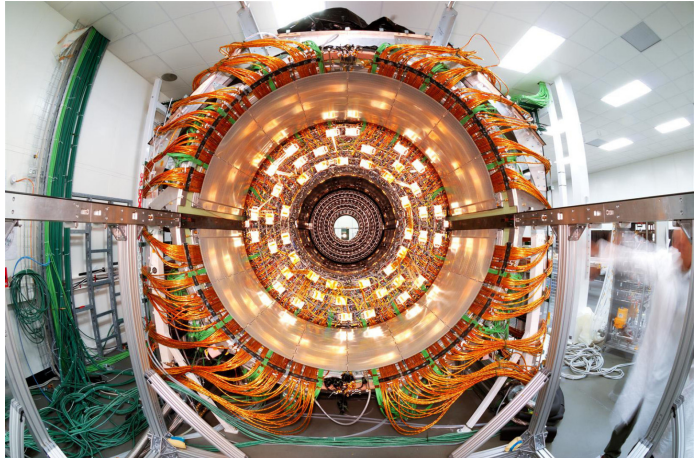
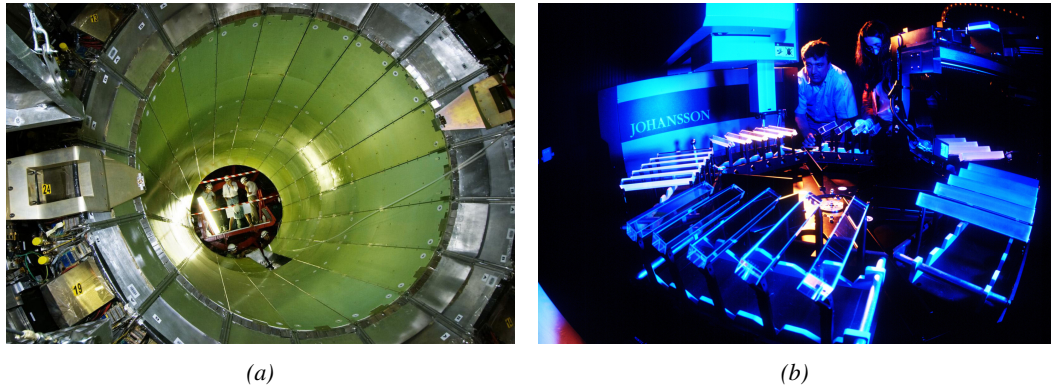


Figure 2.24: The CMS tracker.

#### 1726 2.2.4.2 The calorimeters

1727 The ECAL directly surrounding the tracker is composed of crystals of lead tungstate,  $\text{PbWO}_4$ , a  
 1728 very dense but optically transparent material used to stop high-energy electrons and photons. These  
 1729 crystal blocks basically are extremely dense scintillators which scintillate in fast, short light bursts  
 1730 proportionally to the energy deposition. The light is contained at 80% in the corresponding 25 ns

1731 lasting bunch crossing. Each crystal is isolated from the other by the carbon fiber matrix they are  
 1732 embedded in.



*Figure 2.25: Figure 2.25a: The electromagnetic calorimeter. Figure 2.25b: The lead tungstate crystals composing the ECAL.*

1733 The ECAL is composed of a barrel containing more than 60,000 crystals and of closing  
 1734 endcaps containing another 15,000 crystals.  
 1735 In front of the ECAL endcap is installed  
 1736 a preshower detector made out of two layers  
 1737 of lead and silicon strip detectors to increase  
 1738 the spatial resolution close to the beam line  
 1739 for pion-photon and single-double photon dis-  
 1740 crimination purposes. Figure 2.25 shows the  
 1741 calorimeter inside of the magnet and the crys-  
 1742 tals.  
 1743

1744 The next layer is the HCAL. The role of  
 1745 these forward calorimeters, made using steel  
 1746 and quartz fibers, is to precisely measure the momentum very energetic hadrons. Several layers  
 1747 of brass or steel are interleaved with plastic scintillators readout by photodiodes using wavelength-  
 1748 shifting fibers. The HCAL is also composed of a barrel, shown in Figure 2.26 and of endcaps. It  
 1749 also features forward calorimeters on both sides of CMS in the region very close to the beam line at  
 1750 high pseudorapidity ( $3.0 < |\eta| < 5.0$ ).

#### 1751 **2.2.4.3 The muon system**

1752 Finally, in the outer region of the apparatus, a muon system is used to trigger on potentially interest-  
 1753 ing event by identifying muons. Three different subsystems compose the muon system as shown in  
 1754 Figure 2.27 in which a quadrant of the CMS detector focuses on muon system. Drift Tubes (DTs)  
 1755 are found in the barrel region covering the low pseudorapidity region where particles transverse  
 1756 momentum is lower and Cathode Strip Chambers (CSCs) are found in the endcap region covering  
 1757 higher pseudorapidity region closer to beam line where particles have a stronger momentum. The  
 1758 redundancy of the system is insured by Resistive Plate Chambers (RPCs) in both the barrel and end-  
 1759 cap. Nevertheless, the region closest to the beam line ( $|\eta| > 1.8$ ) was not equipped with RPCs. This



*Figure 2.26: The CMS hadron calorimeter barrel.*

lack of redundancy in the high pseudo rapidity region will be solved during LS2, the following Year End Technical Stop (YETS) in 2021 and 2022, and LS3 where the necessary services, detectors and Link System, that collects the data and synchronizes them, will be installed.

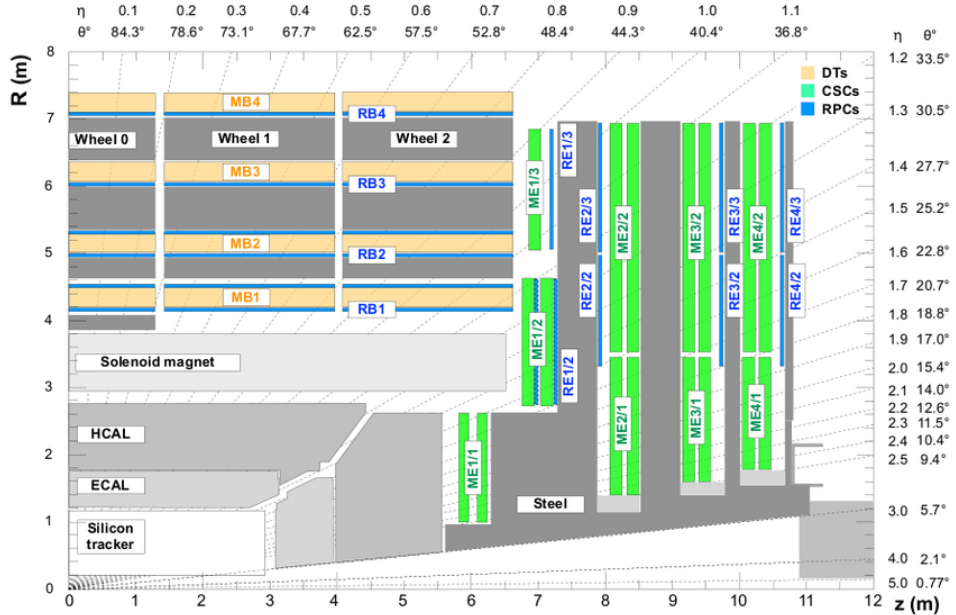


Figure 2.27: A quadrant of the muon system, showing DTs (yellow), RPCs (blue), and CSCs (green).



# 3

1763

1764

## Muon Phase-2 Upgrade

1765 In the previous chapter, the timeline of the LHC has been described and the upcoming High Lumi-  
1766 nosity LHC was introduced. LS3 has now started and the first HL-LHC related upgrade of CMS will  
1767 take place. In order to understand the context in which the work of this thesis was performed as well  
1768 as its motivations, it is necessary to give more insight into the reasons behind the increased instantan-  
1769 eous luminosity of LHC. In a first section of the chapter, these motivations will be discussed.

1770 The muon system of CMS will then be presented in greater details than what was done in the  
1771 previous chapter in order to have a better understanding of the need for upgrades of its different sub-  
1772 systems in the perspective of HL-LHC. Most of the detectors will require new electronics to adapt  
1773 to the new data flow and be integrated into a more robust trigger. Moreover, the redundancy of the  
1774 muon system in the endcaps will need to be improved. This will be achieved by the addition of new  
1775 detectors.

1776 Finally, some insight will be given on ecofriendly gas studies for the specific case of Resistive  
1777 Plate Chambers. These studies don't fall into the scope of the HL-LHC upgrades but the necessity  
1778 of operating the detectors with gas mixtures that are more respectful of the environment is real. The  
1779 European union is starting to press the scientific community for solutions and the research institutes  
1780 are investing time into finding replacements to the gases used while maintaining similar working  
1781 performances.

### 1782 **3.1 Motivations for HL-LHC and the upgrade of CMS**

1783 As detailed in Section 2.2.2, the first data taking period, during which the LHC was only operated  
1784 at a center-of-mass energy of 7 TeV, took place until the start of LS1. It has been sufficient to  
1785 claim the discovery of a new  $125 \text{ GeV}/c^2$  particle compatible with the Higgs boson by both CMS  
1786 and ATLAS in July 2012 and hence achieve a major milestone in the history of science towards the  
1787 understanding of the fundamental nature of the universe. Nevertheless, the LHC machine holds the  
1788 potential to go further and help unravel the remaining mysteries the High-Energy Physics (HEP)  
1789 community is facing.

Over its full lifetime, the HL-LHC is expected to deliver an outstanding integrated luminosity of  $3000 \text{ fb}^{-1}$ , nearly an order of magnitude higher than what will be delivered by LHC until LS3 starts, as shown in Figure 2.20. In the case of Higgs studies, this will lead to measuring the couplings of the boson to a precision of 2 to 5%. Thanks to the estimated 15 millions of Higgs bosons created every year, a more precise measurement of potential deviations from the theoretical predictions is expected. The properties of the boson will hence be tested and compared to the SM Higgs neutral boson. SUSY and heavy gauge boson studies would also see their mass range limits pushed away by at least 1 TeV and could lead to a new breakthrough. Many of the Standard Model extensions discussed in Section 2.1.3 yield Heavy Stable Charged Particles (HSCPs), i.e. heavy long-lived particles. These particles would be produced at the LHC with a high momentum but a velocity significantly lower than the speed of light ( $\beta < 0.9$ ) [178–182] and/or a charge that differs from the elementary charge ( $|Q| = e$ ,  $|Q| < e$  or  $|Q| > e$ ) [181–186]. Depending on the model considered, HSCPs could be lepton-like heavy particles or on the contrary R-hadron, i.e. particles composed of a supersymmetric particle and at least one quark [181].

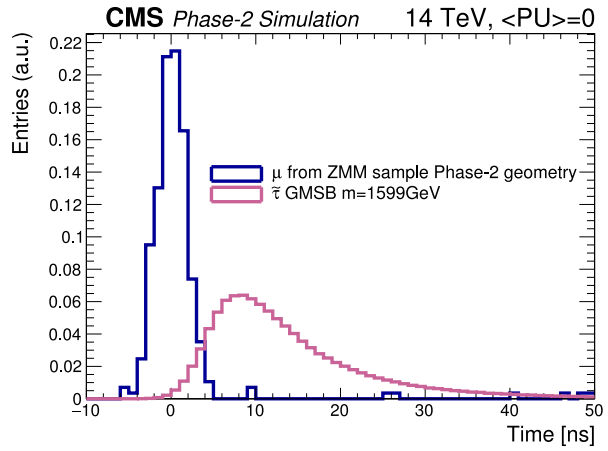


Figure 3.1: The measured transit time of an HSCP in CMS is compared to the transit time of a particle traveling at near the speed of light [177].

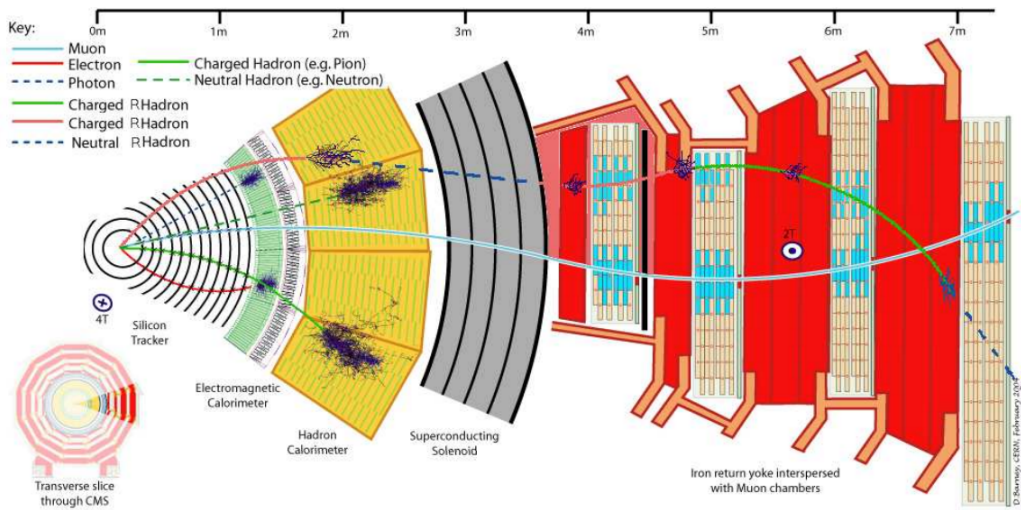


Figure 3.2: Slice of the CMS detector showing examples of passage of SM particles and R-hadrons. On the one hand, lepton-like HSCPs will appear to behave like slow and heavy muons. On the other hand, R-hadrons are likely to convert into other kind of charged or neutral R-hadrons due to interactions inside the detector volume.

1816 Due to lifetimes of the order of a few ns,  
 1817 HSCPs would travel for long enough distances  
 1818 to cross through entire typical collider detec-  
 1819 tors while appearing almost stable. Because  
 1820 of their low velocity, they can be reconstructed  
 1821 and assigned to bunch crossings different to  
 1822 the ones they effectively have been produced,  
 1823 as shown in Figure 3.1, if reconstructed at  
 1824 all. Indeed, the trigger algorithms in use at  
 1825 CMS were not designed for such slow parti-  
 1826 cles, and they assume most particles of inter-  
 1827 est will have a velocity close to the speed of  
 1828 light [182, 187].

1829 As HSCPs are long-lived particles, their  
 1830 identification would be possible thanks to the  
 1831 muon system. The main background will con-  
 1832 sist of wrongly measured muons which should  
 1833 have a lower transverse momentum, a near to  
 1834 speed-of-light velocity and a low ionisation  
 1835 energy loss. An example of passage of HSCPs  
 1836 through a slice of the CMS detector is showed  
 1837 in Figure 3.2. The tracks associated to the  
 1838 HSCPs would then have to be reconstructed in  
 1839 both the silicon detectors, for precise  $dE/dx$   
 1840 measurement, and the muon system detectors. In this case, the muon system will be used to perform  
 1841 Time-of-flight (ToF) measurements to discriminate between near speed-of-light particles and slower  
 1842 ones. The full reconstruction will then look for useful signatures such as the large transverse mo-  
 1843 mentum of the candidates, or their large ionisation energy loss alongside the low velocity accurately  
 1844 measured thanks to the muon system as depicted in Figure 3.3. The ToF measurement to identify  
 1845 beyond the Standard Model particles will mostly rely on the time information provided by the Drift  
 1846 Tubes, in the barrel region of the detector, and Cathode Strip Chambers, in the endcaps. From CMS  
 1847 point of view, it will then become necessary to increase the acceptance and redundancy of the end-  
 1848 caps toward higher pseudo-rapidity as the pseudo-rapidity region  $1.6 < |\eta| < 2.5$  is only covered  
 1849 by CSCs.

1850  
 1851 A natural consequence of the higher instantaneous luminosity will be the increase of collisions  
 1852 per bunch crossing. It is estimated that the pile-up will rise from the approximate average of 40  
 1853 collisions per bunch crossing in 2017 and 2018, presented in Figure 3.4, to 140 to 200 depending on  
 1854 the scenario considered [188]. The trigger rate will then be affected in the same way putting a lot  
 1855 of stress on the trigger algorithms. Upgrading the electronics of some of the detectors and working  
 1856 on the data flow within the experiment would help going through HL-LHC with keeping similar  
 1857 performance than during Phase-1. On the other hand, the impact of the increased background will  
 1858 become problematic in many ways and will force for upgrades or many sub-systems of CMS. The  
 1859 main effects will be a large increase of the irradiation of the detectors, mainly close to the beam  
 1860 line. Both the detectors already installed and the new detectors that will extend the coverage of the

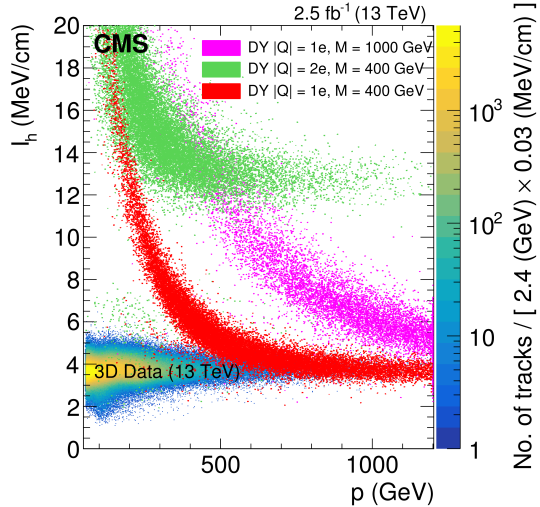


Figure 3.3: Distribution of the energy-loss  $dE/dx$  as described by Bethe-Bloch formula through the estimator  $I_h$  with increasing particle momentum for tracks in the 13 TeV data. The estimator depends on the charge deposition of the particles per unit length in the silicon detectors of CMS which is related to their energy loss as explained in a publication by the CMS Collaboration [181]. The simulated HSCPs are singly or multiply charged particles with masses of 400 and 1000 GeV.

muon system toward higher pseudo-rapidity need to be certified for the irradiation levels they will be subjected to until the end of HL-LHC. Simulations of the expected distribution of absorbed dose in the CMS detector under HL-LHC conditions show, in Figure 3.5, that detectors placed close to the beam line will have to withstand high irradiation, the radiation dose being of the order of a few tens of Gy.

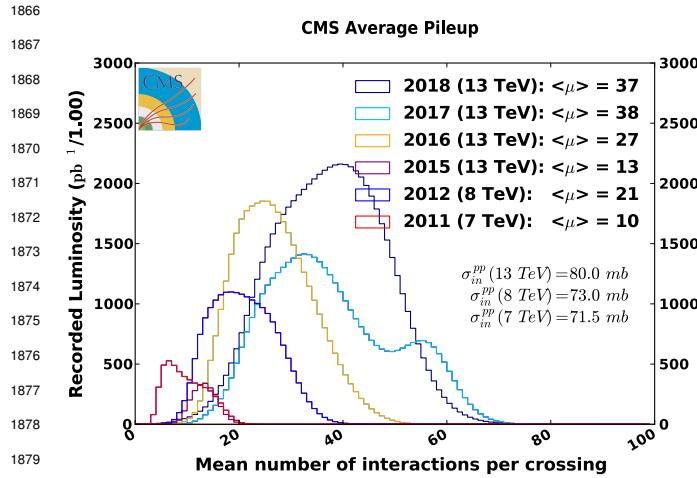


Figure 3.4: Distribution of the average number of interactions per crossing (pileup) for pp-collisions in 2011 (red), 2012 (blue), 2015 (purple), 2016 (orange), 2017 (light blue), and 2018 (navy blue). The overall mean values and the minimum bias cross sections are also shown [189].

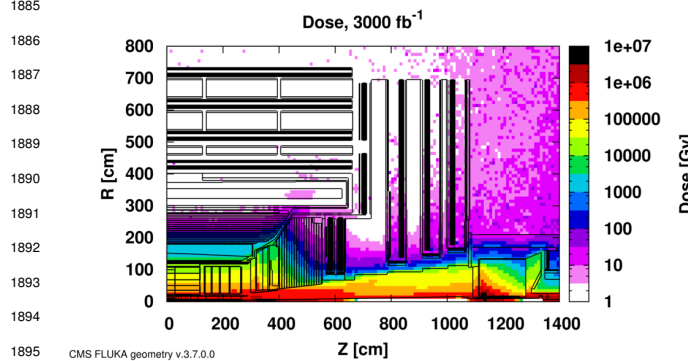


Figure 3.5: Absorbed dose in the CMS Cavern after an integrated luminosity of  $3000 \text{ fb}^{-1}$ . Using the interaction point as reference,  $R$  is the transverse distance from the beamline and  $Z$  is the distance along the beamline [177].

and measurement of their energy with reasonable precision only using the tracker is nearly impossible. Thus, this increased tracker coverage range needs to be put in parallel with a matching muon detector and will open doors to multi-lepton final states in which leptons are likely to have a low transverse momentum and to be found near the beam line.

Finally, as the muon system is composed only of gaseous detectors, strong environmental concerns have risen over the last years as the European directives will restrict the use of fluorine based

Improving this situation will come with the increase of hit numbers recorded along the particle track to reduce the ambiguity on muon versus background detection. Moreover, the measurement of small production cross-section and/or decay branching ratio processes, such as the Higgs boson coupling to charge leptons, and in particular to muons, or the  $B_s \rightarrow \mu^+ \mu^-$  decay, is of major interest. Such considerations give more weight to the upgrade of the forward regions to maximize the physics acceptance to the largest possible solid angle.

To ensure proper trigger performance within the present coverage, the muon system will be completed with new chambers, and the electronics of the present system will need to be upgraded. A first step into this direction will be taken by installing new gaseous detectors in each endcap layer and extend the coverage up to  $|\eta| = 2.8$ . Nevertheless, the region beyond  $|\eta| > 2.8$  and extending to  $|\eta| = 5.0$  only is covered by the forward HCAL detectors and lack redundant muon detector coverage. Extensions of the tracker in the context of HL-LHC will increase its coverage up to  $|\eta| = 4.0$  but the identification of muons

<sup>1907</sup> gas mixtures. Both the CSC and RPC subsystems, using  $CF_4$ ,  $C_2H_2F_4$ , or  $SF_6$ , will need to adapt  
<sup>1908</sup> their working gas in order to strongly reduce the greenhouse potential of the mixtures released into  
<sup>1909</sup> the atmosphere due to gas leaks.

## <sup>1910</sup> 3.2 Description of the muon system

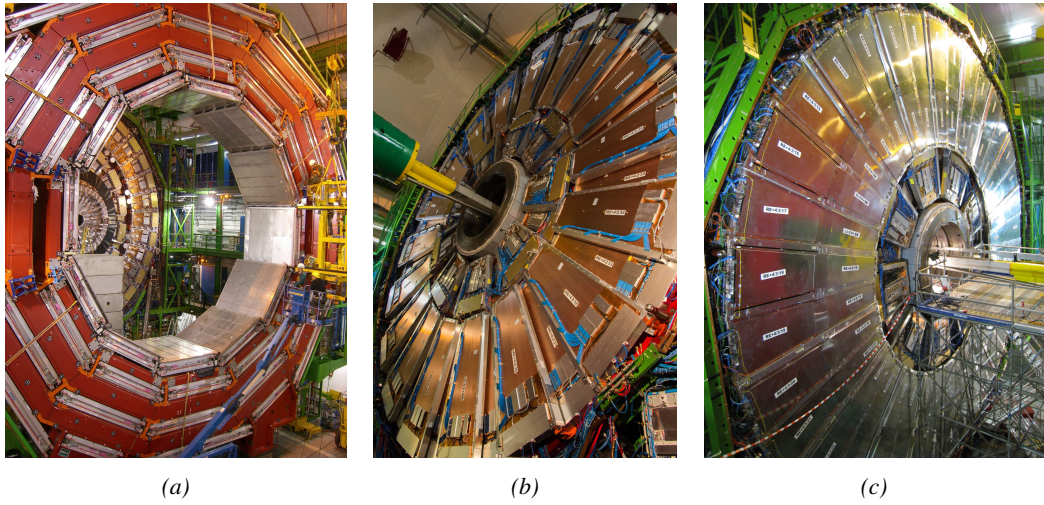


*Figure 3.6: Figure 3.6a: Barrel wheel with its detector rings and return yokes. Figure 3.6b: CSC endcap disk with the two CSC stations. The outer station is made of 10 deg detectors while the inner station is made of 20 deg detectors. Figure 3.6c: RPC endcap disk. The inner station is not equipped, leaving the inner CSC station visible.*

<sup>1911</sup> The barrel region is divided into five *wheels* made out of four *rings* of detectors with iron return yokes  
<sup>1912</sup> in between them whereas the endcaps are made out of four disks, each divided into pseudorapidity  
<sup>1913</sup> stations, two for CSCs (except for the first disk where three stations are equipped) and three for  
<sup>1914</sup> RPCs, although only two RPCs stations are equipped at present. The wheels and disks are shown  
<sup>1915</sup> in Figure 3.6. So far, each subsystem was dedicated to a particular task. DTs, in the barrel, and  
<sup>1916</sup> CSCs, in the endcaps, are used mainly for their spatial resolution. Indeed, DTs' resolution is of  
<sup>1917</sup> the order of  $100\text{ }\mu\text{m}$  along both the  $(r - \phi)$  and  $(r - z)$  components while the resolution of CSCs  
<sup>1918</sup> is similar but varies in a range from  $50\text{ }\mu\text{m}$  to  $140\text{ }\mu\text{m}$  depending on the distance to the beamline.  
<sup>1919</sup> On the other hand, RPCs are used as redundant detection system in the whole muon system. They  
<sup>1920</sup> display a very good intrinsic time resolution of  $1.5\text{ ns}$  although the electronics only provide bunch  
<sup>1921</sup> crossing information with a time resolution of  $25\text{ ns}$ .

### <sup>1922</sup> 3.2.1 The Drift Tubes

<sup>1923</sup> The 250 CMS DTs, found in the barrel covering the pseudorapidity region  $0 < |\eta| < 1.2$  and  
<sup>1924</sup> whose structure is shown in Figure 3.7, are composed of three *superlayers* of DT cells. Two of  
<sup>1925</sup> these superlayers are dedicated to measuring the  $\phi$  coordinate of the muons and while the last one  
<sup>1926</sup> measures the  $\eta$  (or  $z$ ) coordinate. Each superlayer consists on four layers of 60 to 70 DT cells  
<sup>1927</sup> arranged in quincunx to allow for a precise reconstruction of the muon path through the DT layers.

1928 Each DT cell is a rectangular aluminium gas volume with a central anode wire. Cathode strips are  
 1929 placed on the narrow surface of the cells and electrode strips are placed on the wide surface to help  
 1930 shaping the electric field to ensure a consistent drift velocity of electrons in the drift volume. These  
 1931 detectors are operated using a 85/15 mixture of Ar and CO<sub>2</sub>. Outside the gas volume of each DT  
 1932 chamber is attached a Minicrate electronics (MiC) that hosts both read-out and trigger electronics.

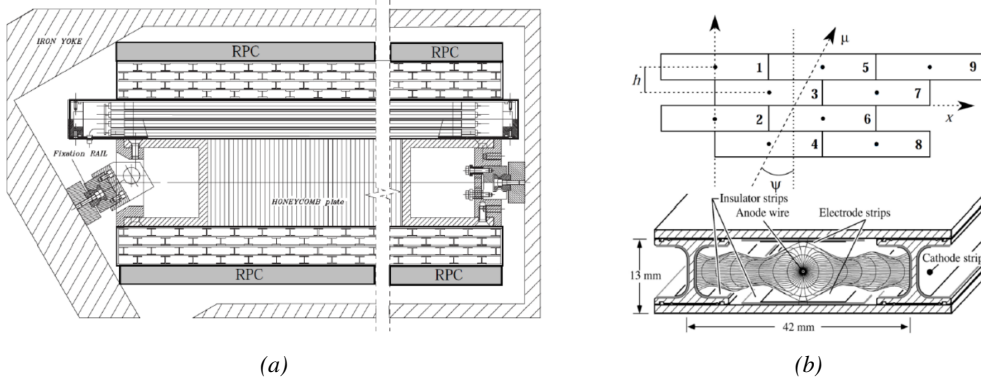


Figure 3.7: Figure 3.7a: Cross section of a DT module showing the two superlayers measuring the  $\phi$  coordinate, perpendicular to the cross section plane, and the superlayer measuring the  $\eta$  coordinate, placed in between the two others with a honeycomb plate and parallel to the cross section plane. The DT detector is sandwiched in between 2 RPCs whose readout strips are perpendicular to the cross section plane, measuring the  $\phi$  coordinate. Figure 3.7b: A DT cell is shown together with its electric field. The path of a muon through a superlayer is shown.

### 3.2.2 The Cathode Strip Chambers

1933 The 540 CMS CSCs are found in the endcaps covering the pseudorapidity region  $0.9 < |\eta| < 2.5$   
 1934 and described through Figures 3.8 and 3.9. Each module is composed of six panels of CSC, each  
 1935 panel consisting in a wide gas volume of 9.5 mm (7 mm in the case of ME1/1 station) containing  
 1936 anode wires and whose surfaces are cathodes. The top cathode is a wide copper plane of the size of  
 1937 the gas volume. The bottom cathode is divided into thin trapezoidal copper strips radially arranged  
 1938 to measure the azimuthal coordinate  $\phi$  with a pitch ranging from 8 to 16 mm. The 0.50  $\mu\text{m}$  anode  
 1939 wires are placed perpendicularly to the strips to measure radial coordinate  $r$  and are grouped by  
 1940 ten to fifteen with a wire to wire space of 3.2 mm. In the specific case of ME1/1 placed against  
 1941 the HCAL endcap, the 0.30  $\mu\text{m}$  anode wires have a wire to wire distance of 2.5 mm and are not  
 1942 disposed perpendicularly to the strips but slightly tilted by an angle of 29 deg to compensate for the  
 1943 lorentz force due to the very strong local magnetic field of 4 T. These detectors are operated with a  
 1944 40/50/10 mixture of Ar, CO<sub>2</sub> and CF<sub>4</sub>. Combining the information of the multiple CSC panels, the  
 1945 detectors achieve a very precise measurement of the muon track. The read-out of the cathode strip  
 1946 signals is performed by cathode front-end boards (CFEBs) mounted on the detectors. The boards  
 1947 are used to collect and digitize the charge of the signals and transfer it to off-chamber electronics  
 1948 called Data acquisition mother boards (DMBs). In parallel, the data from the CFEBs together with  
 1949 the data from the anode wires, after treatment by on-chamber electronics called Anode local charged  
 1950 track boards (ALCTs), is used to build a fast trigger information which is sent other off-chamber  
 1951 electronics called Trigger mother boards (TMBs).

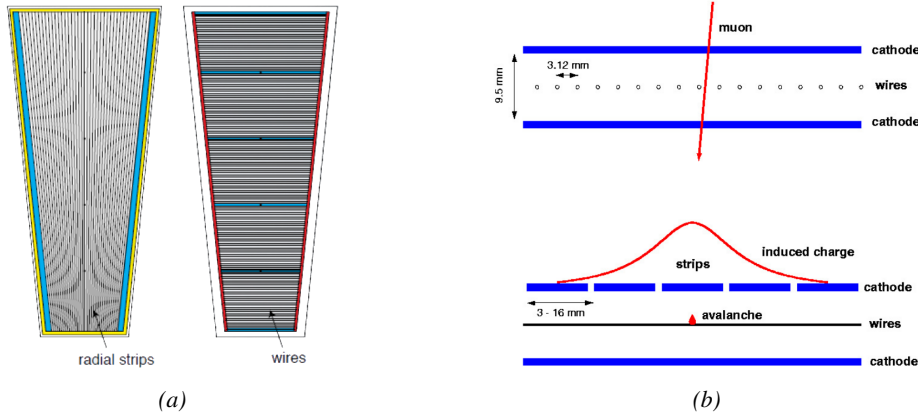


Figure 3.8: Figure 3.8a: Cathode strips and anode wire layout of a CSC panel. Figure 3.8b: Avalanche development and charge collection by anode wires and induction on cathode strips inside of a CSC panel.

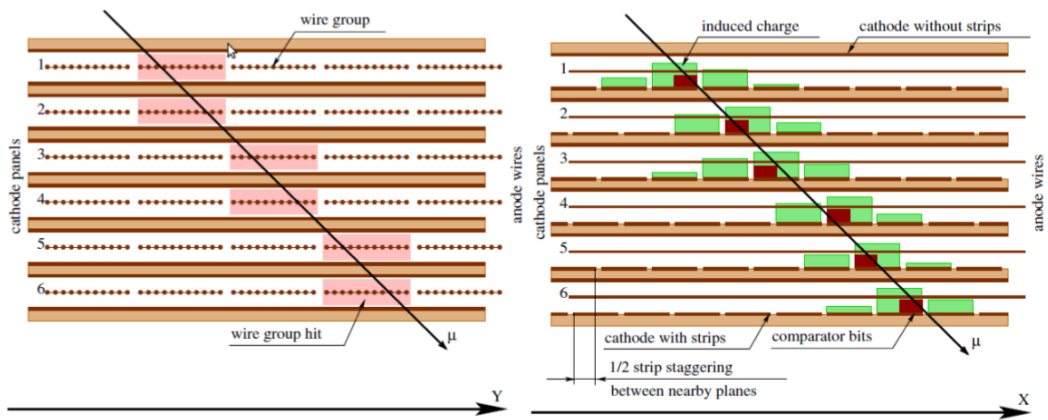


Figure 3.9: Muon track reconstruction through the six panels of a CMS CSC using the information of anode wire groups and cathode strip charge distribution combined with comparator bits to decide on which half strip the muon is more likely to have passed.

### 3.2.3 The Resistive Plate Chambers

Despite their excellent spatial resolution, the wire chambers (DTs and CSCs) are limited in terms of time resolution by the fact that the charge needs to drift towards the anode wire and be collected before having the confirmation that a particle was detected as the drift volume is not used to develop avalanches. Indeed, the stronger electric field close to the anode wire triggers the avalanche and the gain of the detector. Due to the drift, the time resolution is thus limited at best to approximately 2 to 3 ns. In addition, even though the intrinsic time resolution of the tracking chambers is rather good compared to the 25 ns in between successive collisions, the processing time of the trigger system doesn't allow for very fast triggering as it provides a time precision of only 12.5 ns. Thus, detectors fully dedicated to timing measurement have been installed as a redundant system. These detectors are RPCs, also gaseous detectors but that use current induction instead of charge collection allowing for a time resolution of the order of 1 ns only. Theoretically, depending on the design used, RPCs

1965 could reach a time resolution of the order of 10 ps but in the context of LHC where bunch crossing  
 1966 happen every 25 ns, a time resolution of 1 ns is sufficient to accurately assign the right bunch crossing  
 1967 to each detected muon.

1968 The 1056 RPCs equip the  
 1969 CMS muon system both in  
 1970 the barrel and endcap regions  
 1971 and cover the pseudorapidity  
 1972 region  $0 < |\eta| < 1.6$ .  
 1973 They are composed of two  
 1974 layers of RPC *gaps* as de-  
 1975 scribed in Figure 3.10. Each  
 1976 gap consists in two resis-  
 1977 tive electrodes made out of  
 1978 2 mm thick Bakelite enclos-  
 1979 ing a 2 mm thick gas volume con-  
 1980 taining a 95.2/4.5/0.3 mixture  
 1981 of  $C_2H_2F_4$ ,  $i - C_4H_{10}$  and  $SF_6$ . Due to this geometry, the electric field inside of a gap is ho-  
 1982 mogeneous and linear at every point in the gas translating into a uniform development of avalanches  
 1983 in the gas volume as soon as a passing muon ionises the gas. The two gaps sandwich a readout  
 1984 copper strip plane. A negative voltage is applied on the outer electrodes, used as cathodes, and the  
 1985 inner electrodes, the anodes, are simply connected to the ground as well as the readout panel that  
 1986 picks up the current induced by the accumulated charge of the growing avalanches in one or both  
 1987 of the gas gaps. This OR system allows for a lower gain (i.e. a lower electric field) on both gaps to  
 1988 reach the maximal efficiency of such a detector.

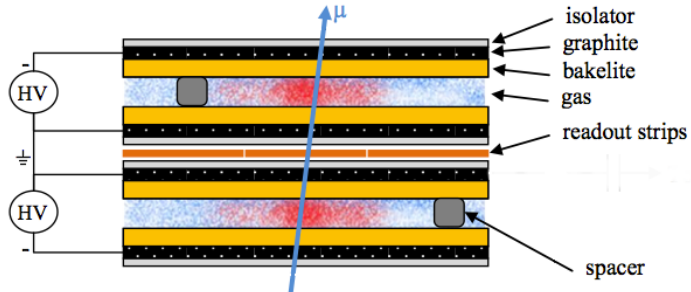


Figure 3.10: Double-gap layout of CMS RPCs. Muons passing through the gas volumes will create electron-ions pairs by ionising the gas. This ionisation will immediately translate into a developing avalanche.

### 1989 3.3 Necessity for improved electronics

1990 Drift Tubes and Cathode Strip  
 1991 Chambers are important compo-  
 1992 nents used to identify and measure  
 1993 muons, especially thanks to their  
 1994 spatial resolution of the order of  
 1995  $100 \mu\text{m}$ . Nevertheless, the lumi-  
 1996 nosity and irradiation during HL-  
 1997 LHC will cause serious event loss  
 1998 and ageing on the electronics of  
 1999 these subsystems that will comprise  
 2000 the triggering and data transferring  
 2001 needs of CMS. Thus, electronics up-  
 2002 grade is foreseen to address these  
 2003 expected problems. While only  
 2004 the RPCs' electronic system is able  
 2005 to operate under Phase-2 require-  
 2006 ments [190], DTs and CSCs will  
 2007 need to improve their trigger acceptance rate and latency to ensure that the Level-1 trigger thresh-

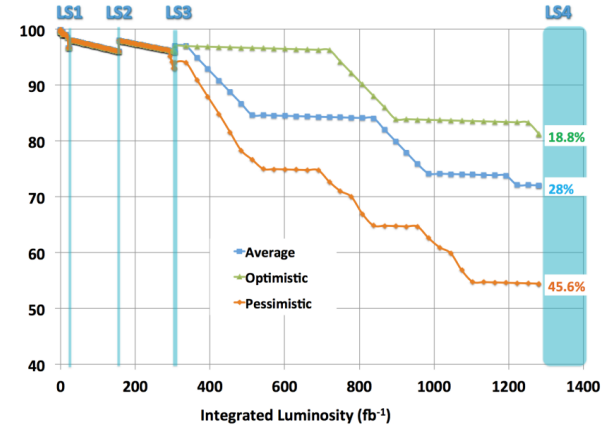
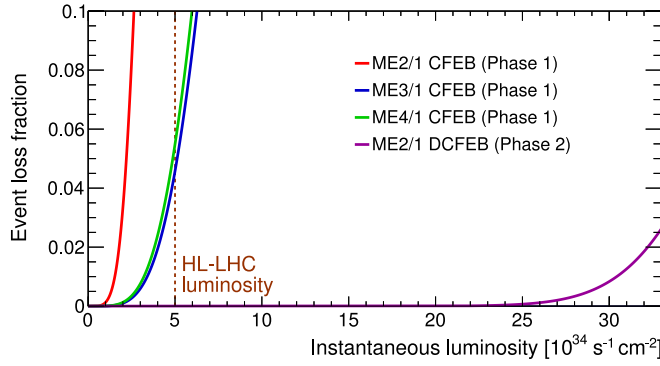


Figure 3.11: Extrapolated fraction of failing channels of the present DT MiC1 electronics as a function of the integrated luminosity for different scenarios until LS4 [177].

old can stay at the same level [191]. The Level-1 trigger consists of custom hardware processors receiving data from the calorimeters and the muon system. In return, they generate a trigger signal within  $3\ \mu\text{s}$ , with a maximum rate of 100 kHz. In the perspective of HL-LHC, each subsystem needs to achieve a minimum rate of 500 kHz with a latency not greater than  $12.5\ \mu\text{s}$ . DTs and CSCs will also need to improve their Data Acquisition (DAQ) transfer rate to reach a minimum near 1 Tbit/s. The foreseen upgrades are expected to exceed the requirements.



*Figure 3.12: The event loss fractions as a function of the instantaneous luminosity is compared for CFEBs (Phase-1) and DCFEBs (Phase-2) at different CSC locations. HL-LHC luminosity is marked with the dashed line [177].*

and High Voltage (HV) modules will not need any replacement. On the other hand, CSCs showed that their electronics would be able to live through the 10 years of Phase-2, but the limited buffer depth might cause memory overflows and read-out inefficiencies with a fraction of event loss ranging from 5 to more than 10% at an instantaneous luminosity similar to which of HL-LHC depending on the expected background. The replacement of CSCs' CFEBs by digital ones, DCFEBs, with a deeper buffer would permit to make event loss negligible and satisfy HL-LHC requirements as can be seen in Figure 3.12. All these new DT and CSC electronics will be connected to the trigger electronics via optical links to ensure a faster communication [177].

The upgrade on the side of Resistive Plate Chambers will not be done at the level of the electronics but rather that of the Link System located in the service cavern of CMS. RPC Link System connects the front-end electronics data of RPCs into CMS trigger processors. The main motivation for such an upgrade is that the electronic board composing the link system are built using ob-

The first version of Mini-crake electronics (MiC1) used by DTs don't allow for high enough trigger rate. In addition to this problem, it was shown that these electronics contain components that are not radiation hard enough to sustain HL-LHC conditions and hence, a too large number of channels may fail due to radiations as showed in Figure 3.11. The MiC1 will be replaced on each detector by an improved version referred to as MiC2 while Front-End Electronics (FEE)

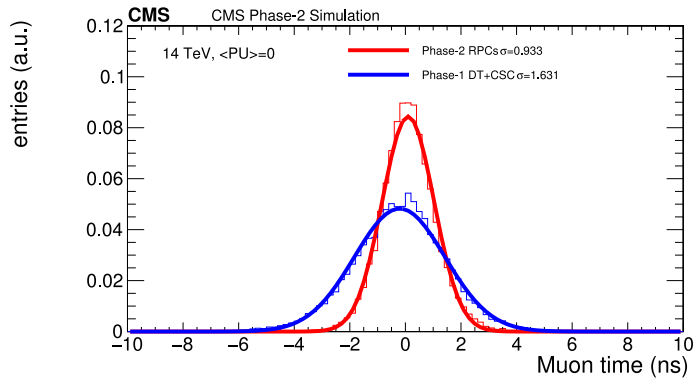


*Figure 3.13: Comparison of the simulated time residuals in between reconstructed and true muon times without (blue) and with (red) the upgraded RPC link system [177].*

solete and/or weak components that can easily suffer from the electromagnetic noise. These components may become the source of failing channels throughout Phase-2. Moreover, these link boards were originally designed only to match RPC digitized signals with the corresponding bunch crossing. Due to this feature, the time resolution of the full RPC chain is hence limited to 25 ns and does not make use of the full time resolution of the detectors. The time resolution foreseen after the upgrade can be seen through Figure 3.13 and is of the order of 1 ns. The exploitation of the full time resolution would make the synchronization of the RPC system easier and allow to have a finer offline out-of-time background removal within the 25 ns between consecutive bunch crossings. Moreover, this would greatly improve the trigger and reconstruction on HSCPs. Using the TOF information in between consecutive RPC stations, the minimal particle velocity than could be probed will drop from approximately 0.6 to 0.25 times the speed of light as showed in Figure 3.14.

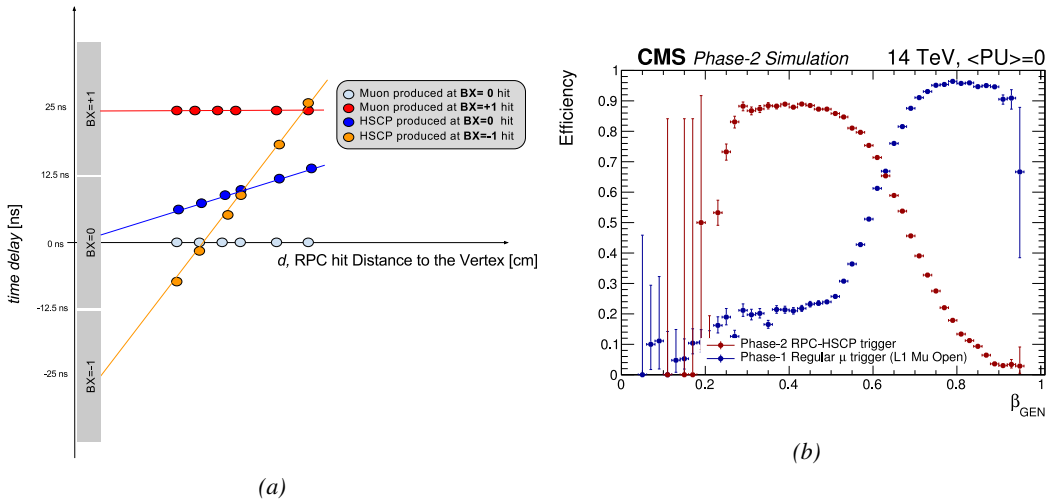


Figure 3.14: Figure 3.14a: Time delay with respect to a particle traveling at the speed of light measured at consecutive RPC stations for particles originating at different bunch crossings and traveling at different velocities [177]. Figure 3.14b: In blue is showed the standard Level-1 muon trigger efficiency as a function of  $\beta$  and in blue is showed the RPC-HSCP trigger efficiency after upgrade of the RPC Link System [177].

Upgrading RPC link system will require the installation of 1376 new link boards and 216 control boards. The new boards will make use of the recent progress made with fast FPGAs and will be a great improvement to the ASICs formerly used as they will be able to process signals from several detectors in parallel.

### 3.4 New detectors and increased acceptance

In the present muon system, the redundancy is assured by RPCs used for their robust bunch crossing assignments. The extension of the muon system towards higher pseudo-rapidity in an effort to complete the redundancy and to contribute to the precision of muon momentum measurements will require muon chambers with a spatial resolution less or comparable to the multiple scattering muons are subjected to while traveling through the detector volume [192].

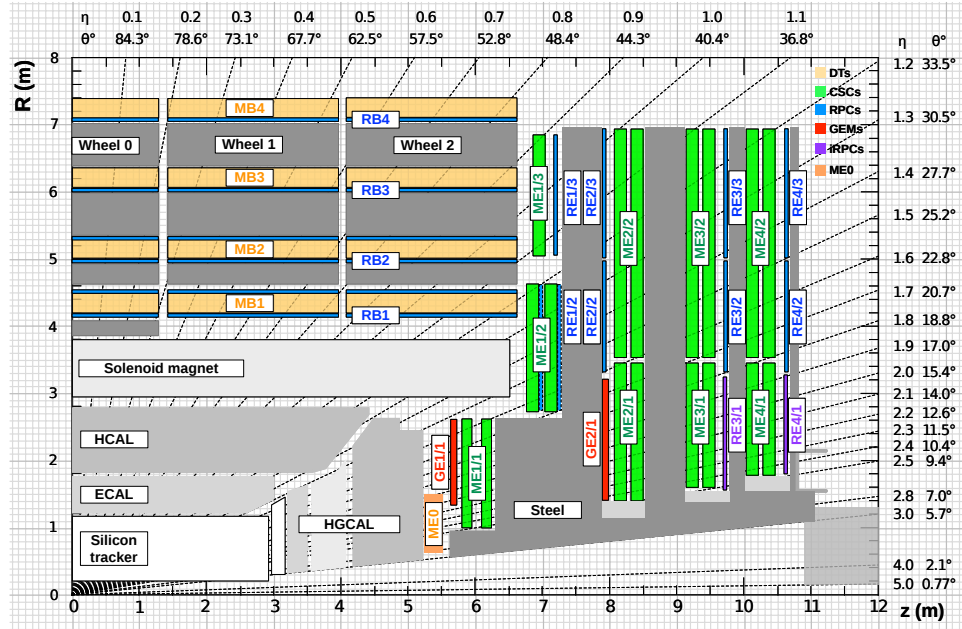


Figure 3.15: A quadrant of the muon system, showing DTs (yellow), RPCs (blue), and CSCs (green). The locations of new forward muon detectors for Phase-2 are contained within the dashed box and indicated in red for GEM stations (ME0, GE1/1, and GE2/1) and dark blue for improved RPC (iRPC) stations (RE3/1 and RE4/1).

Figure 3.15 shows a similar quadrant of CMS than the one presented in Figure 2.27 with the addition of Gas Electron Multiplier (GEM) (ME0, GE1/1 and GE2/1) and improved RPC (iRPC) (RE3/1 and RE4/1) in the pseudo-rapidity region  $1.6 < |\eta| < 2.4$ . The completion of the redundancy was already scheduled in the original CMS Technical Proposal [193] but never addressed. The coming Phase-2I is then the occasion to equip the region with the newest GEM and RPC technology. In order to match CMS requirements, a spatial resolution of  $\mathcal{O}(\text{few mm})$  will be necessary for the proposed new RPC stations while the GEMs will need a resolution better than 1 mm, as showed by the simulation in Figure 3.16. Indeed, most of the plausible physics will be covered only considering muons with  $p_T < 100 \text{ GeV}$ .

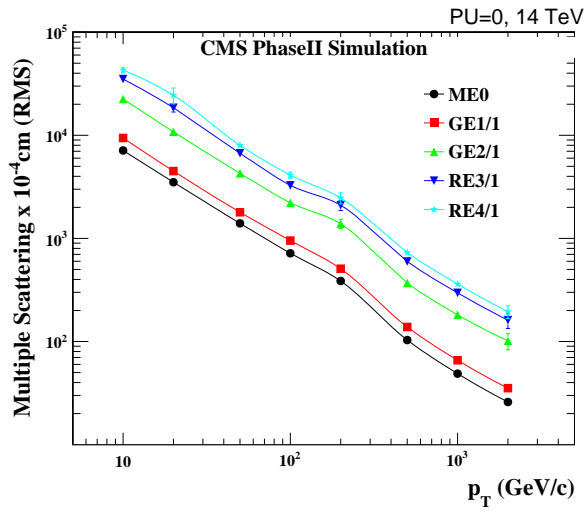


Figure 3.16: RMS of the multiple scattering displacement as a function of muon  $p_T$  for the proposed forward muon stations. All of the electromagnetic processes such as bremsstrahlung and magnetic field effect are included in the simulation.

### 2097 3.4.1 Gas electron multipliers

2098 In the region closer to the interaction point  
 2099 where the spatial resolution is requested for  
 2100 the new detectors to be better than 1 mm (at  
 2101 least for ME0 and GE1/1 according to Fig-  
 2102 ure 3.16) and where the background rate will  
 2103 be the highest for muon detectors, the choice  
 2104 has been made to use triple GEMs, micro pat-  
 2105 tern gaseous detectors, instead of the origi-  
 2106 nally planned RPCs. The GE1/1 project has  
 2107 been the first to be approved and demonstra-  
 2108 tors have been installed in CMS already during  
 2109 LS1. The rest of the detectors will be installed  
 2110 during LS2 while the GE2/1 and ME0 projects  
 2111 are still under development. ME0, GE1/1 and  
 2112 GE2/1 will be installed respectively close to  
 2113 the HCAL endcap, on the first and on the sec-  
 2114 ond muon endcap disks as can be seen from  
 2115 Figure 3.15.

2116 Gas Electron Multipliers are gaseous de-  
 2117 tectors [194] whose gas volume is confined be-  
 2118 tween two planar electrodes, the anode serv-  
 2119 ing as read-out panel. The gas volume is di-  
 2120 vided in two or more regions by a single or  
 2121 multiple *GEM foils* as showed in Figure 3.17.  
 2122 These foils are very thin, of the order of a few  
 2123 tens of  $\mu\text{m}$ , and are pierced with holes as can  
 2124 be seen in Figure 3.18. Both surfaces of the  
 2125 GEM foils are clad with copper in order to ap-  
 2126 pply a strong electric field in between each side  
 2127 that will generate very strong potentials in the  
 2128 holes. The gas region contained in between  
 2129 the cathode and the GEM foil is called the drift  
 2130 region as the electric field is not strong enough  
 2131 to cause avalanches and thus start an amplifi-  
 2132 cation. The primary electrons drift toward the  
 2133 foil and are accelerated and amplified by the  
 2134 very high potential within the holes, as showed  
 2135 in Figure 3.18. Then the electrons reach the  
 2136 second drift region where they will induce a  
 2137 signal on the read-out located on the anode.  
 2138 By restraining the amplification process at the  
 2139 level of the holes, the electrons can stay con-  
 2140 fined in a very little space and thus induce a  
 2141 very localized current, providing the GEMs

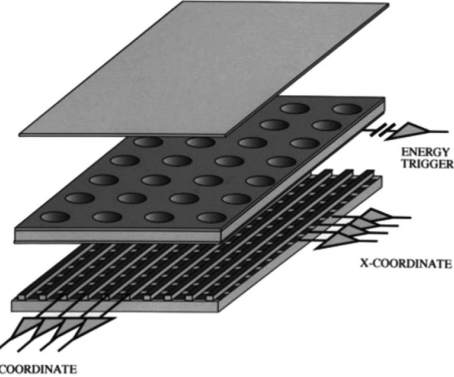


Figure 3.17: Schematics of a GEM. On top is the cathode and on the bottom, the anode on which a 2D readout is installed. Finally, the GEM foil separates the gas volume into the drift region, in between the cathode and the foil, and the induction region, in between the foil and the anode. A negative voltage is applied on the cathode. The anode is connected to the ground.

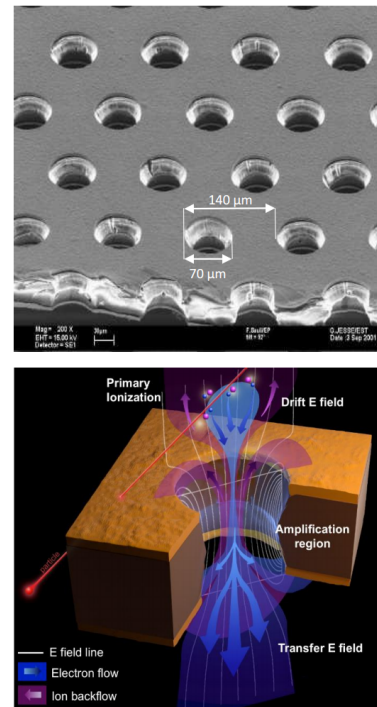


Figure 3.18: Top: Picture of a CMS GEM foil provided by a scanning electron microscope. Bottom: Representation of the electric field in a GEM hole and of the amplification electrons and ions undergo due to the very intense electric field.

2142 with a very good spatial resolution.

2143 The process can be re-  
 2144 peated several times in a row,  
 2145 in order to achieve a stronger  
 2146 amplification. The GEMs that  
 2147 will be used in CMS are triple-  
 2148 GEM detectors operated with a  
 2149 70/30 gas mixture of  $Ar/CO_2$ .  
 2150 They contain three GEM foils  
 2151 and hence three electron am-  
 2152 plifications, as can be seen  
 2153 in Figure 3.19. The GEM  
 2154 foils used in CMS are 50  $\mu m$   
 2155 foils clad with 5  $\mu m$  of copper  
 2156 on each side. The foils are  
 2157 pierced with double-canonical  
 2158 holes which inner and outer  
 2159 diameters are respectively 50  
 2160 and 70  $\mu m$  which are placed  
 2161 140  $\mu m$  from each other in a  
 2162 hexagonal pattern, as showed in Figure 3.18. These detectors have a time resolution better than  
 2163 10 ns and reach very good spatial resolutions of less than 200  $\mu rad$  as indeed the position of the  
 2164 hits is not measured along the strips but following the azimuthal angle granularity of the radially  
 2165 organized trapezoidal strips.

2166 The GEM Upgrade project started with GE1/1 [195]. GE1/1 detectors will already be installed  
 2167 during LS2. GE2/1 and ME0, on the other hand, will profit of the R&D knowledge and skills  
 2168 developed for GE1/1 while the requirements for each subsystem are different as they are not placed  
 2169 at the same distance from the interaction point. In this very forward region, a different position with  
 2170 respect to the center of the detector can dramatically change the conditions in which the detectors  
 2171 will have to be operated. In terms of rate capability, GE2/1, which is the furthest, is required to  
 2172 withstand 2.1 kHz/cm<sup>2</sup> while GE1/1 needs to be better than 10 kHz/cm<sup>2</sup> and ME0, better than  
 2173 150 kHz/cm<sup>2</sup>. In terms of ageing with respect to charge deposition, ME0 needs to be certified to  
 2174 840 mC/cm<sup>2</sup>, GE1/1 to 200 mC/cm<sup>2</sup> and GE2/1 only to 9 mC/cm<sup>2</sup>. All 3 detectors need to have a  
 2175 time resolution better than 10 ns and an angular resolution better than 500  $\mu rad$ .

2176 On each GE1/1 ring, 36 super chambers, consisting of two single GEM layers and spanning 10°,  
 2177 will be installed covering the pseudo-rapidity region  $1.6 < |\eta| < 2.2$  together with ME1/1 CSCs.  
 2178 The reach of the muon system will be improved thanks to the GE2/1 that will overlap with the GE1/1  
 2179 and cover a region from  $|\eta| > 1.6$  to  $|\eta| < 2.4$  and complete the redundancy of ME2/1. The super  
 2180 chambers, built with two triple-GEM layers each consisting of four single GEM modules due to  
 2181 the rather large surface of the GE2/1 chambers, that will be installed on the first ring of the second  
 2182 endcap will span 20° each. Hence, a total of 72 chambers will be assembled to equip the muon  
 2183 system. Finally, the ME0 installed near the HCAL endcap will cover the region  $2.0 < |\eta| < 2.8$ .  
 2184 This subsystem will consist in super modules of six layers of triple-GEM detectors covering an  
 2185 azimuthal angle of 20° leading to the construction of 216 single detectors.

2186 Adding the GEMs into the forward region of the muon system will allow to strongly enhance  
 2187 the Level-1 Trigger performance as shown in Figure 3.20. In the region  $1.6 < |\eta| < 2.4$ , the trigger

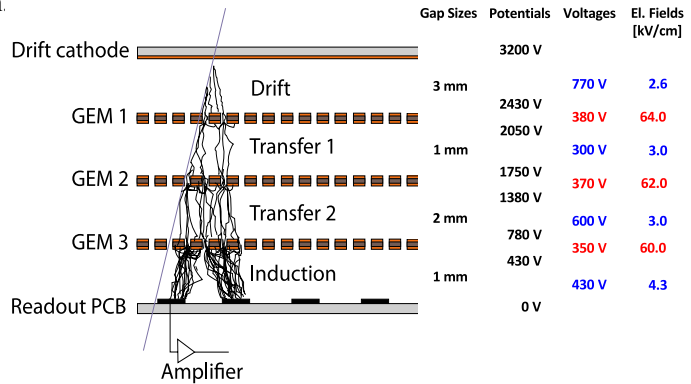


Figure 3.19: Schematic representation of CMS triple-GEMs. The gas volume is divided into four areas. The drift area is the region where the primary electrons are created before being amplified a first time while passing through the first GEM foil. Then the process of drift and amplification is repeated twice in following two transfer areas and GEM foils. Finally, the charges have been amplified enough to induce current in the read-out strips while in the last drift area. The typical dimensions, potentials and electric fields are provided.

efficiency of the current system would lie between 80 and 90% under HL-LHC conditions. The installation of GEMs would bring the efficiency to a consistent 92 to 94% on the entire region. At the same time, the trigger rate is expected to fluctuate from 3 to 10 kHz with the current system alone. The addition of detectors to complete the redundancy would allow keeping the rate mostly under 2 kHz. Moreover, benefiting from the good spatial and angular resolution of the GEMs, the precision into the muon measurement will also be improved by an order of magnitude thanks to the addition of GEMs as can be seen from the simulation presented in Figure 3.21.

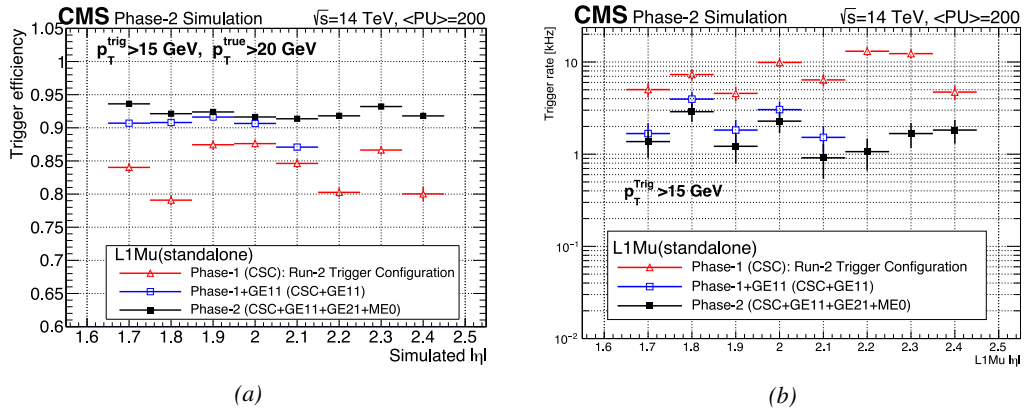


Figure 3.20: Simulated efficiency and rate of the standalone Level-1 muon trigger using tracks reconstructed in CSCs and all GEM stations compared with Phase-1 values in the case where only CSCs are used or CSCs+GE11. The zones of inefficiency of the CSC subsystem are compensated by the addition of GEMs during Phase-2 and the trigger rates is kept from increasing due to the high luminosity [177].

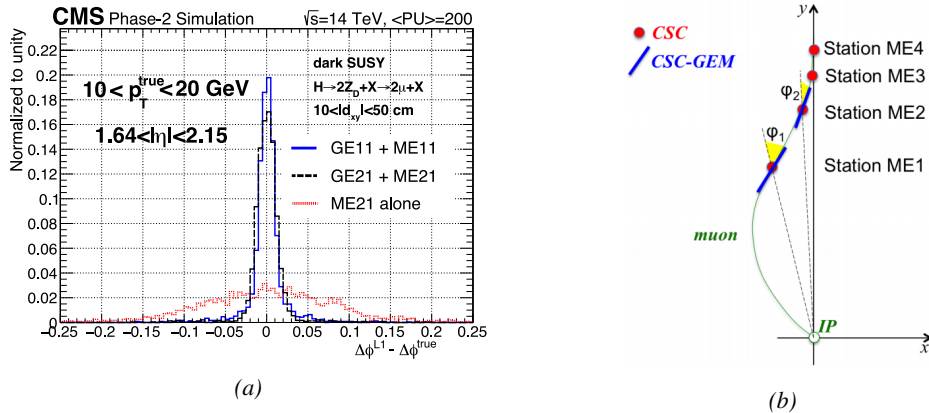


Figure 3.21: Figure 3.21a: Simulated resolution of the muon direction measurement  $\Delta\phi$  with Phase-2 conditions. In the second endcap station, the resolution is compared in the case of CSCs (ME2/1) alone and CSCs+GEMs (GE2/1+ME2/1) while a similar resolution measurement is given in the case of the first station (GE1/1+ME1/1) [177]. Figure 3.21b: The addition of GEM detectors on stations 1 and 2 (ME0 is considered to contribute to station 1) as redundant system to CSCs allows improving the muon momentum improvement through a more accurate measurement of the local bending angles  $\phi_1$  and  $\phi_2$  [177].

### 2195 3.4.2 Improved forward resistive plate chambers

2196 Figure 3.15 shows that the iRPCs that will equip the third and fourth endcap disks in position RE3/1  
 2197 and RE4/1 will finally be the partners of the CSCs in position ME3/1 and ME4/1. They will complete  
 2198 Phase-1 plans by bringing the needed upgrades in the perspective of Phase-2 as the older chambers  
 2199 are not suitable to equip the forward region of CMS due to HL-LHC rates and charge deposition.  
 2200 By completing the redundancy, more hits along the muon track will be available and the lever arm  
 2201 will be improved. The benefits from extending the redundancy of the muon system with iRPCs to  
 2202 the forward most region is shown in Figure 3.22 in which the trigger efficiency is presented with and  
 2203 without RPCs. It is possible to see that the efficiency of the CMS muon trigger with the complete  
 2204 redundancy is consistently improved to a level above 95% in the region  $|\eta| > 1.8$  as the iRPCs help  
 2205 filling the holes in the CSC system.

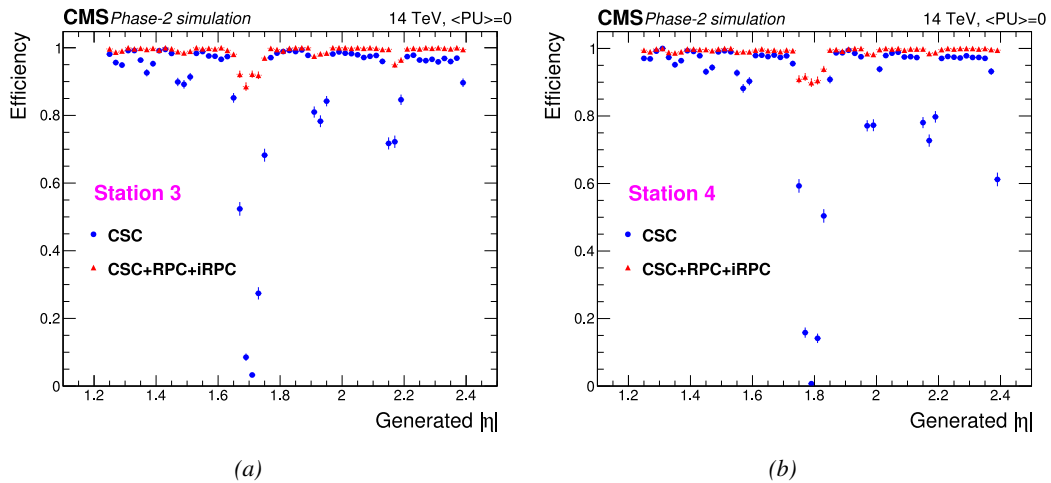
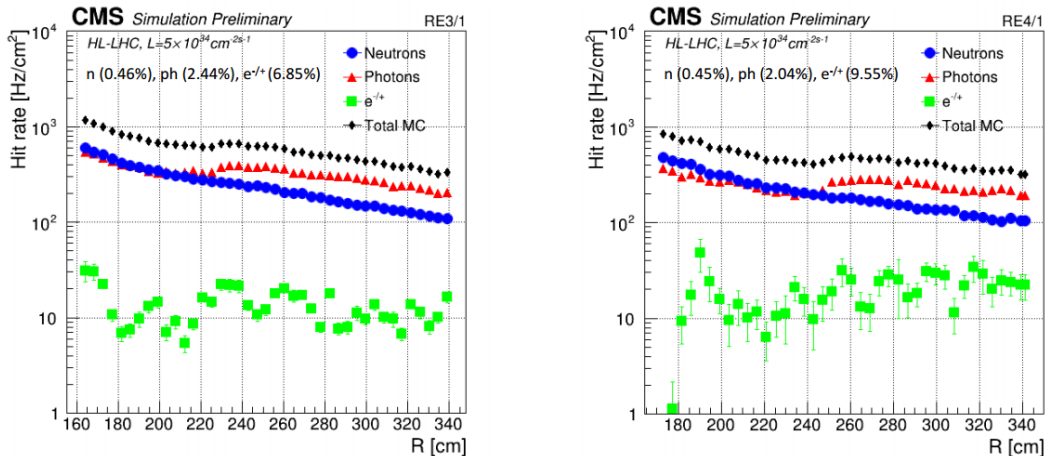


Figure 3.22: Simulation of the impact of RPC hit inclusion onto the local trigger primitive efficiency in station 3 (Figure 3.22a) and station 4 (Figure 3.22b) [177]. The contribution of iRPC starts above  $|\eta| = 1.8$ .

2206 The detectors that will be installed in the coming years will have similarities with the already  
 2207 existing RPC system. 18 of the new chambers, each spanning  $20^\circ$  in  $\varphi$  around the beam axis with  
 2208 96 radially oriented trapezoidal read-out strips, will cover each muon endcap disk leading to the  
 2209 production of 72 iRPCs. The main difference with the old RPC detectors will be found at the level  
 2210 of the read-out panels. Indeed, the new chambers will not feature read-out strips segmented in  $\eta$   
 2211 but rather will favor a read-out on both strip ends to determine the position of the hits along the  
 2212 chamber. By using fast front-end electronics a radial spatial resolution of the order of 2 cm could  
 2213 be achieved to contribute to the better reconstruction of muons in the forward region where the  
 2214 bending due to the magnetic field is low. This technical choice is motivated by the fact that, in  
 2215 the case a  $\eta$  segmentation were to be used, at least five pseudo-rapidity partitions would have been  
 2216 necessary to reach the minimal radial spatial resolution ( $\approx 20$  cm). Having only one strip along the  
 2217 chamber read-out from both ends reduces by 60% the total number of channels and the necessary  
 2218 cabling, and allows for a better spatial resolution. The strip pitch will range from 6.0 mm (5.9 mm)  
 2219 on the high pseudo-rapidity end to 12.3 mm (10.9 mm) on the low one on position RE3/1 (RE4/1).  
 2220 The spatial resolution in the direction perpendicular to the strips should reach approximately 3 mm,  
 2221 better than the minimal needed resolution (Figure 3.16). Finally, the overall time resolution of the

new installation will be equally 1 ns, as for the present due to the same link system being used even though the detector itself can achieve a time resolution of less than 100 ps, necessary for a spatial reconstruction of the hits with a resolution of 2 cm or less along the strip length.

Having only a single strip instead of pseudo-rapidity segmentation will increase the probability of double hits in the same channel. The probability was estimated to be low enough as it shouldn't exceed 0.7%. This estimation was made assuming an average hit rate per unit area of  $600 \text{ Hz/cm}^2$  in the iRPCs (see Figure 3.23), a cluster size (average number of strips fired per muon) of 2, a strip active area of  $158.4 \times 0.87 \text{ cm}^2$  and a safety factor 3. The corresponding rate per strip is estimated to be 380 kHz leading to an average time interval in between two consecutive hits of 2600 ns. This is compared to the minimal time interval of 16 ns necessary to avoid ambiguities. Indeed, a maximum of 10 ns is spent by the signal traveling through the strip to reach the electronics to which can be added 1 ns of dead time and 2 Time-to-Digital Converter (TDC) clock cycles of 2.5 ns to convert the signal arrival time into a digital value in the FEEs. The probability of having ambiguous double hits in a strip is then the ratio between the minimal time interval in between two consecutive hits and the average time interval estimated from the rate the detectors would be subjected to.



*Figure 3.23: Expected hit rate due to neutrons, photons, electrons and positrons at HL-LHC instantaneous luminosity of  $5 \times 10^{34} \text{ cm}^{-2}\text{s}^{-1}$  in RE3/1 and RE4/1 chambers [196, 197]. The sensitivities of iRPCs used in the simulation for each particle are reported and differ from one endcap disk to another as the energies of the considered particles varies with the increasing distance from the interaction point.*

The instantaneous luminosity at HL-LHC being very high, the rates at the position of the new chambers needed to be simulated in order to understand the necessary requirements for these detectors. The simulated results for different background components (neutrons, photons, electrons and positrons) are shown in Figure 3.23 assuming known sensitivities to these particles. It is shown that on average over the iRPC areas the rates would be of the order of  $600 \text{ Hz/cm}^2$  ( $600 \text{ Hz/cm}^2$  seen in RE3/1 and  $480 \text{ Hz/cm}^2$  in RE4/1) [196, 197]. Thus, taking into account a safety factor of about 3, it was decided that improved RPCs should at least be certified for rates reaching  $2 \text{ Hz/cm}^2$  which will be achieved thanks to several improvements on the design and on the electronics. The detectors design will be based on the existing RPCs as they will also feature double RPC gaps. Similarly to the existing RPC system, the electrode material will be HPL although the thickness of the electrodes and of the gas gap will be reduced to 1.4 mm as a thinner gas gap leads to a decrease

of deposited charge per avalanche as showed in Figure 3.24. The charge deposition in the case of 1.4 mm thick electrodes is reduced by a factor greater than 5 when compared to 2 mm electrodes at a similar electric field. The smaller the gas gap, the more the detector becomes sensitive to gap non-uniformities across the electrode planes, making a gap of 1.4 mm a good compromise in between these two competing factors.

A lower charge deposition inside of the detector volume means a slower ageing and a longer lifetime for detectors subjected to high irradiation. But, in order to take advantage of the lower detector gain, more sensitive electronics are required such that part of the gain that was formerly achieved in the gas volume can be moved to the electronics. Achieving this with the technology developed more than ten years ago for the present system is not possible as the signal over noise ratio of such electronics doesn't allow to detect charges as low as 10 fC. Moreover, the new front-end electronics will need to be radiation hard to survive more than ten years of HL-LHC conditions. The new technology that has been chosen is based on the PETIROC ASIC manufactured by OMEGA and is a 64-channel ASIC called CMS RPCROC[177, 198, 199]. The properties of these electronics will be discussed in Chapter 6.

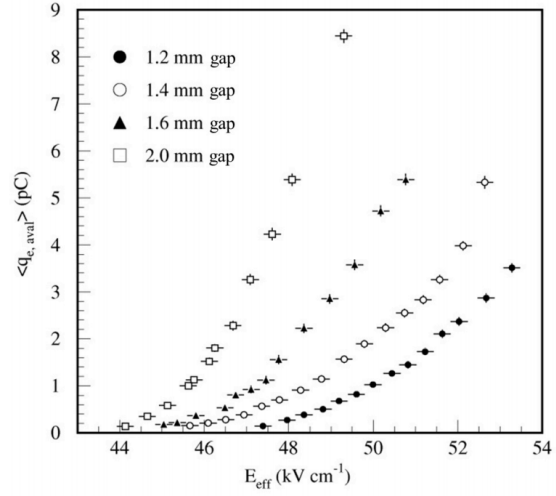


Figure 3.24: Measured average charge per avalanche as a function of the effective electric field for different gas gap thickness in double-gap RPCs using HPL electrodes [177].

The properties of these electronics will be discussed in Chapter 6.

### 3.5 Impact on Level-1 Trigger and physics performance

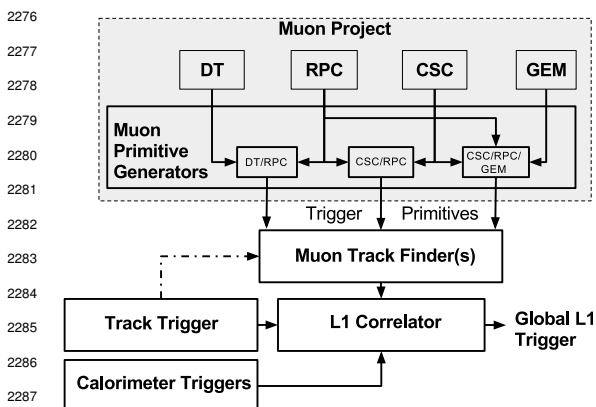


Figure 3.25: Level-1 Trigger data flow during Phase-2 operations [177].

The upgrades of the different subsystems will have a subsequent impact on the Level-1 Trigger. Indeed, although its main scheme will not be affected, the efficiency of the trigger in identifying muons and provide the DAQ with good and fast trigger that can cope with HL-LHC instantaneous luminosity is a major improvement. In addition to the upgrade of the muon system in terms of trigger accept rate and latency, the Level-1 Trigger will get extra information by including the Tracker Trigger into its Muon Track Finder logic and combine the L1 Muon Trigger with Tracker and Calorimeter Triggers to generate a Global L1 Trigger, as shown in Figure 3.25. Using the

track candidates of both the muon system and the tracker in spatial coincidence will allow for a much better momentum resolution thanks to better identified muons and, hence, better measured transverse impulsion as described in reference [177].

In terms of muon trigger, three regions are considered due to their different track finding logic: the Barrel Muon Track Finder (BMTF), the Endcap Muon Track Finder (EMTF) for both the barrel and endcap regions, and finally the Overlap Muon Track Finder (OMTF) which concerns the pseudo-rapidity region in which there is a common coverage by both the barrel and endcap muon systems. This region can be seen in Figure 3.15 for  $0.9 < |\eta| < 1.2$  and requires a specific more complex logic to provide an efficient reconstruction of muons due to the different orientation of the detectors and of the more complex magnetic field of this region. The development of a track finder specific to the overlap region was achieved during the Phase-1 upgrade of the L1-Trigger [200].

The upgraded RPC link system, allowing to take profit of the full 1 ns resolution of the detectors, will help reducing the neutron induced background, slightly improve the bunch crossing assignment, and help increasing the trigger efficiency in every sector. The upgrade of DT electronics is also to take into account as the trigger primitive generator will be renewed through the use of TDCs that will send the digitized signals directly to common DT/RPC back-end electronics instead of having an on-detector trigger logic as it will be the case until the end of Phase-1. The combination of RPC hits together with DT primitives will bring extra improvement in the bunch crossing assignment in the barrel and overlap regions and improve the efficiency of the trigger between the wheels were the quality of DT primitives is the poorest.

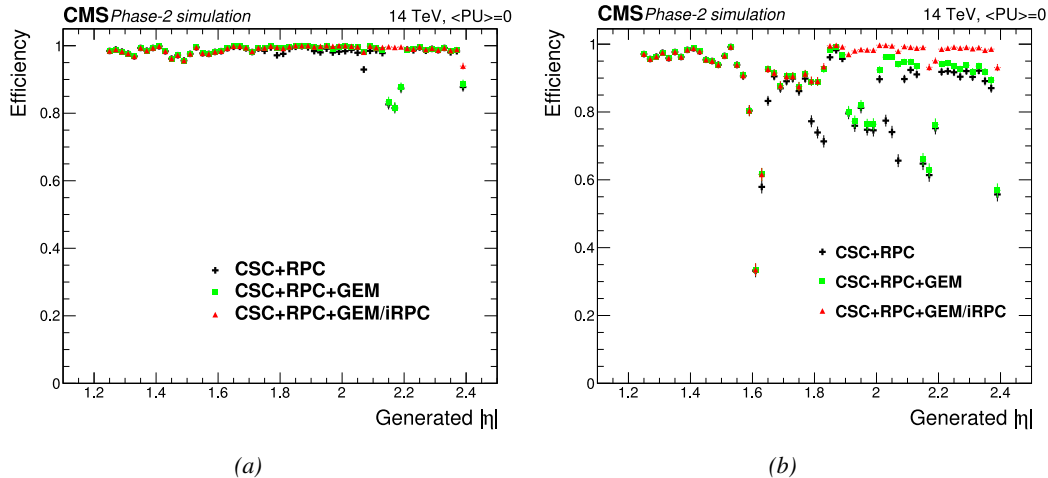


*Figure 3.26: Efficiency of the L1 trigger in the endcap region after Phase-2 upgrade in the case CSC/GEM/RPC hits are requested in at least two stations out of four (3.26a) and in all four stations (3.26b) [177].*

The current EMTF already uses more sophisticated algorithms by combining together RPC hits and CSC primitives. The GEMs, in stations 1 and 2, and the iRPCs, in stations 3 and 4, will be added into the EMTF algorithm. Both these contributions will help increase the efficiency of the L1 trigger in the endcap region in one hand, as showed by Figure 3.26, and help lowering the L1 trigger rate in the other hand, especially in the most forward region. Similarly to the RPC/CSC algorithms, data from both CSCs and GEMs are combined into the Optical TMBs (OTMBs) to build on each station, GEM/CSC primitives matching space and time information from both subsystems. The efficiency

improvement and rate reduction close to the beam line will be naturally enhanced by the addition of more hits along the muon tracks, as can be seen from Figure 3.27 that focuses especially in the most challenging pseudo-rapidity region. Indeed, the contribution from the GEMs to the lever arm of each track thanks to their high angular resolution will be a great asset in achieving such results, as can be seen in Figure 3.28. The rate will be partly reduced in the forward region thanks to the better spatial resolution of iRPCs, with respect to the current RPC system. The ambiguity brought by multiple local charged tracks in CSCs will be reduced, as explained through Figure 3.29. Indeed, as the rates will increase, the probability to record more than a single local charged track will greatly increase. This is due to the fact that the trigger algorithm uses information from three consecutive bunch crossings to find muon tracks. It is estimated that with iRPCs operated at 95% efficiency the resolution of ambiguous events would be of the order of 99.7%.

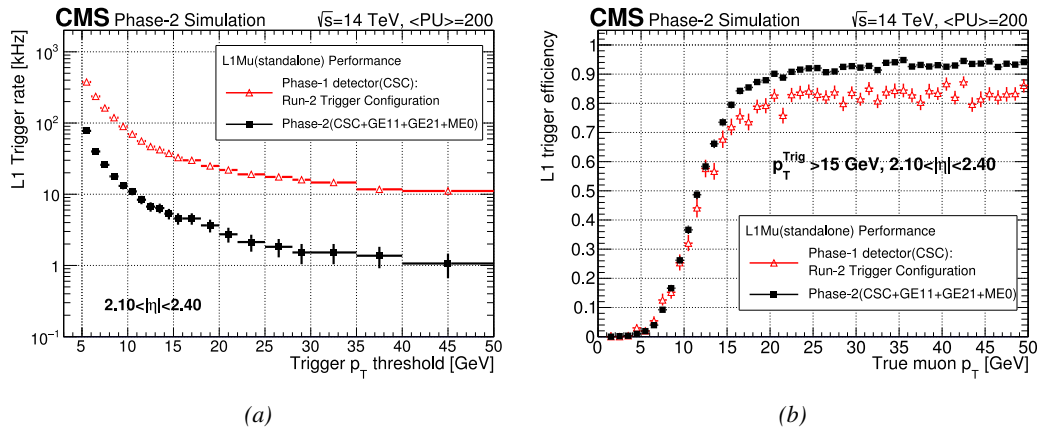


Figure 3.27: Comparison of L1 trigger performances for prompt muons with and without the addition of GEMs in the region  $2.1 < |\eta| < 2.4$  at Phase-2 conditions [177]. GEMs would allow a reduction of the trigger accept rate by an order of magnitude (Figure 3.27a) while increasing the trigger efficiency (Figure 3.27b).

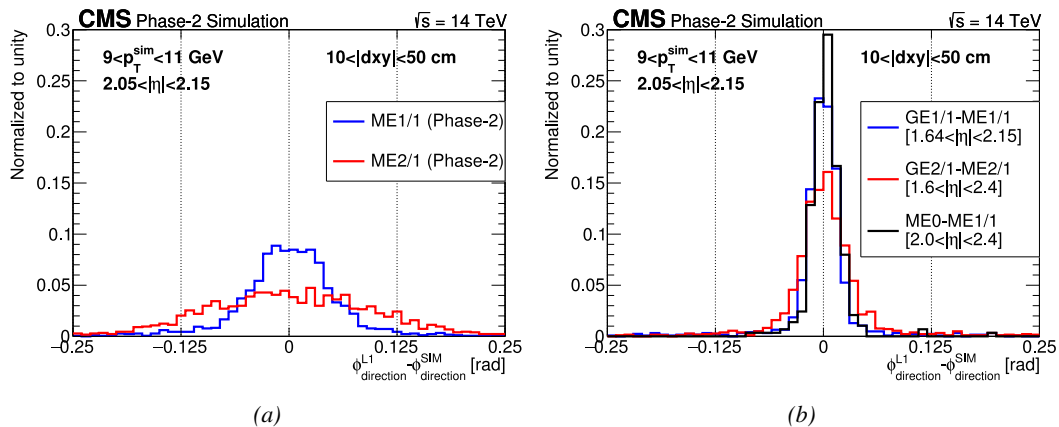
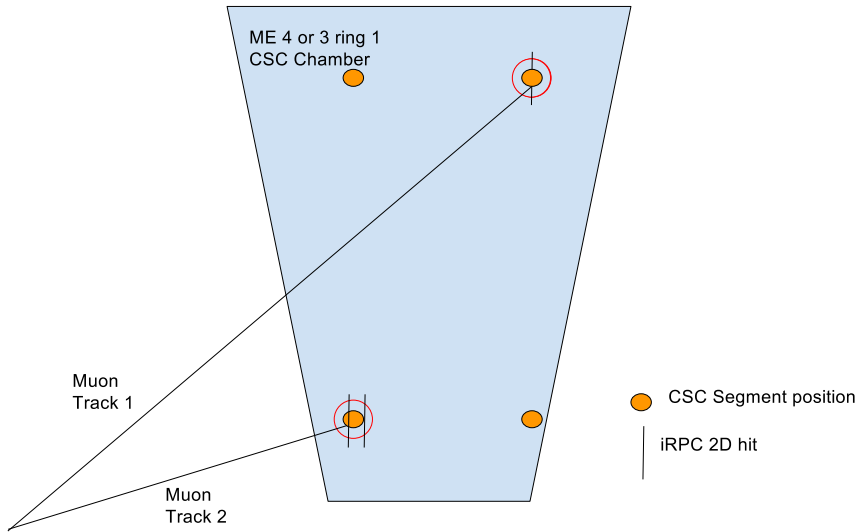


Figure 3.28: The angular resolution on reconstructed muon tracks in the GEM overlap region  $2.0 < |\eta| < 2.15$  is compared for Phase-2 conditions in the case CSC are alone (Figure 3.28a) and in the case the GEMs' data, including ME0, is combined to which of CSCs (Figure 3.28b) [177].



*Figure 3.29: Resolution of the LCT ambiguous events thanks to the combination of CSC and iRPC readout data. Using CSCs only, two pairs of hits are possible [177].*

## 3.6 Ecofriendly gas studies

The European Commission adopted a new "F-gas regulation" in 2014 [201] with the goal to strongly control and reduce the use of fluorinated gases with high Global Warming Potential (GWP). Using  $CF_4$ ,  $C_2H_2F_4$  and  $SF_6$ , both CSC and RPC subsystems will need to address this problem by finding new gas mixture for the operation of their detectors. Finding a replacement for these gas components that were used for very specific reasons is a great challenge. Indeed, CSCs use  $CF_4$  in order to enhance the longevity of the detectors, increase the drift velocity of electrons and quench photons with a non-flammable gas mixture. RPCs use a mixture mainly composed of  $C_2H_2F_4$ , or  $R134a$ , that features a high effective Townsend coefficient and the great average fast charge allowing for operations with a high threshold. The mixture also contains a small fraction of  $SF_6$  that is used for its electronegative properties that prevents the development of delta-rays in the gas volume that might trigger multiple ionization and avalanches.

	CSC	RPC
Greenhouse gases used	$CF_4$	$C_2H_2F_4$ and $SF_6$
Greenhouse gases fraction in the gas mixture	10%	95.2% and 0.3%
Global Warming Potential (relative to $CO_2$ )	6500	1300 and 23900
Gas mixture re-circulation	Yes, 90%	Yes, 85%
Gas mixture replenishing rate (l/hr)	700	1100
F-gas recuperation	Yes, $\approx 40\%$	No
F-gas venting rate (l/hr)	42	1047 and 3.3
$CO_2$ -equivalent rate ( $m^3/h$ )	273	1440
Relative impact (entire muon system = 100%)	16%	84%

*Table 3.1: Details of the greenhouse fluorinated gases used in CMS and of their GWP [177].*

Nevertheless, all these gases have a very high GWP, as reported in Table 3.1, and only few

options are left. The subsystems need to work on strongly decreasing the loss of these gases due to leaks in the gas system or need to completely change their gas mixture for more ecofriendly ones. Reducing the amount of F-gas released in the atmosphere due to leaks on the current gas system will require installation of a F-gas recuperation system on RPCs side and an upgrade of CSCs existing one in addition to the repair of existing leaks. With such measures, it is expected that the total rate of greenhouses gas vented in the atmosphere would represent only 1.6% of the current levels [177]. In the most critical case the F-gas were to be banned, it would be necessary to have replacement mixtures to operate CMS. CSC is presently investigating replacement for  $CF_4$  such as  $CF_3I$ ,  $C_4F_6$ ,  $IC_3F_6$ ,  $C_3F_8$  or  $CHF_3$ . RPCs, in collaboration with the ATLAS RPC group which uses the same gas mixture, have identified  $CF_3I$  ( $GWP \leq 1$ ) and  $C_3H_2F_4$  ( $GWP \sim 6$ ), referred to as *HFO-1234ze*, as potential candidates with mixtures containing  $CO_2$ .  $CO_2$  is already widely used by various RPC experiments in mixtures with argon. More R&D needs to be conducted for both subsystems before concluding on the best alternative. Finding no good alternative to the present mixtures will require very efficient abatement system in CMS to burn and convert the greenhouse gases into less harmful ones. This way, the air pollution would be strongly reduced.

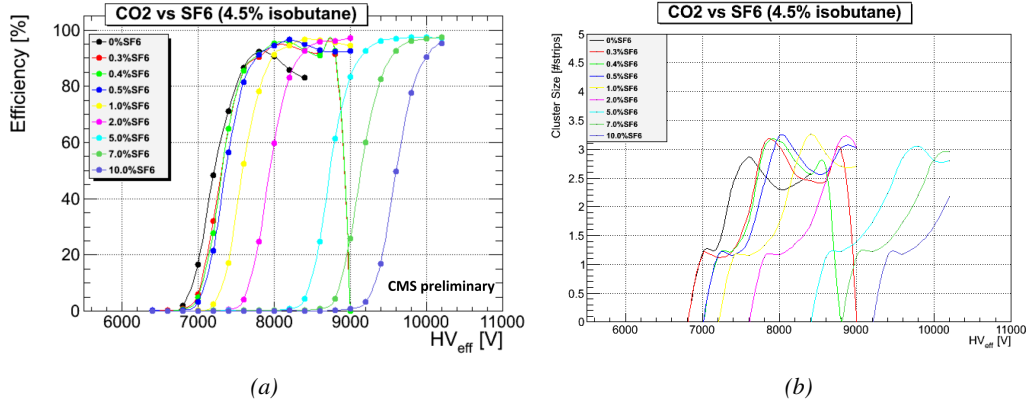


Figure 3.30: Efficiency (Figure 3.30a [202]) and cluster size (Figure 3.30b) of a standard double-gap RPC operated with  $CO_2$  mixtures for different ratios of  $SF_6$ .

Preliminary studies conducted in Ghent confirmed that  $CO_2$  alone would require more than 1% of  $SF_6$  to reach full efficiency, as presented in Figure 3.30. Even though the results obtained in Ghent don't show the streamer probability (the probability to have very large avalanches whose induced charge is greater than 20 pC), the variation of the cluster size indicates that the streamers become predominant before the efficiency plateau is reached. Then, a very first test with an *HFO/CO<sub>2</sub>* was performed. Only one ratio was tested as can be seen from Figure 3.31 that displays a good efficiency with a plateau located at a similar high voltage than with *R134a* based mixtures

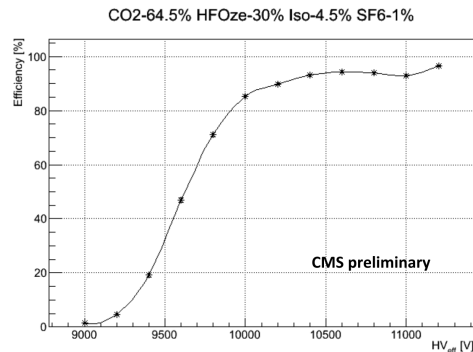
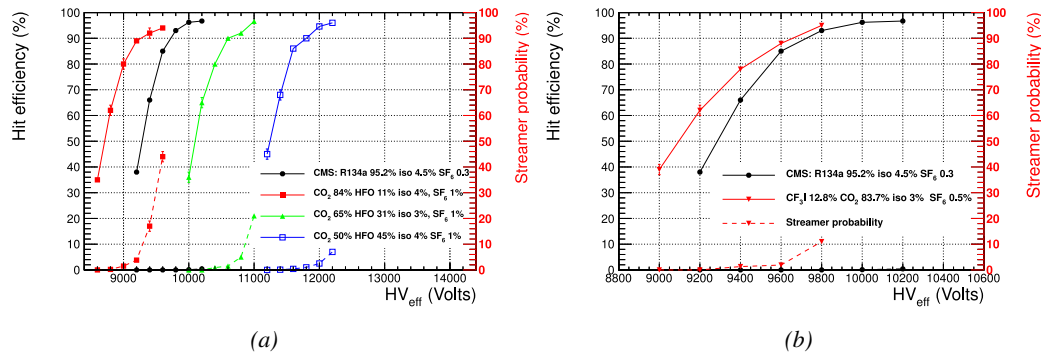


Figure 3.31: Efficiency of a CMS double-gap RPC operated with 30% of  $HFO$ , 4.5% of  $iC_4H_{10}$ , 1% of  $SF_6$  and 64.5% of  $CO_2$  [202].

(Figure 3.32). The status of RPC studies is presented in Figure 3.32 in which the performance (efficiency and streamer probability) of a CMS double-gap RPC operated with alternative gas mixtures is compared to the present CMS RPC mixture. Although the efficiency of detectors operated with mixtures containing  $CO_2/CF_3I$  or  $CO_2/HFO$  as a replacement for  $C_2H_2F_4$  seems to reach similar levels than which of the detectors operated with the present mixture, the new gas mixtures feature a streamer probability that far exceeds which of the present fluorinated mixture. The  $SF_6$  doesn't seem to prevent the formation of streamers as efficiently even when used at levels more than three times higher than with the standard CMS RPC mixture. Nevertheless, it is important to note that these results were obtained with a single-gap RPC while the use of a double-gap RPC reduces the operation voltage by 200 to 300 V, lowering the induced charge. A compromise in between good efficiency and acceptable level of streamer probability, and the fine-tuned composition of potential replacement gas mixtures will be kept on being studied using a standard double-gap CMS RPC.



**Figure 3.32:** The efficiency (solid lines) and streamer probability (dashed lines) of  $HFO/CO_2$  (Figure 3.32a) and  $CF_3I/CO_2$  (Figure 3.32b) based gas mixtures as a function of the effective high-voltage are compared with the present CMS RPC gas mixture represented in black [177, 202]. The detector used for the study is a single-gap RPC with similar properties than CMS RPCs. The streamer probability is defined as the proportion of events with a deposited charge greater than 20 pC.

Although the technology certification was conducted with the standard CMS gas mixture which is a known reference, the iRPCs will need to be operated with new environmental-friendly gas mixtures. Studies have then been conducted with iRPCs, assuming that the  $HFO/CO_2$  mixture containing an almost equal level of both components was the most likely candidate to replace the standard mixture. In this purpose, an iRPC prototype has been built to be tested with an  $HFO/CO_2$  gas mixture. The mixture, referred to as "eco-gas" in Figure 3.33, contained 50% of  $HFO$ , 4.5% of  $iC_4H_{10}$ , 0.3% of  $SF_6$  and 45.2% of  $CO_2$ . In Figure 3.33 is presented a result consistent with the blue curve obtained with 45% of  $HFO$ , 4% of  $iC_4H_{10}$ , 1% of  $SF_6$  and 50%

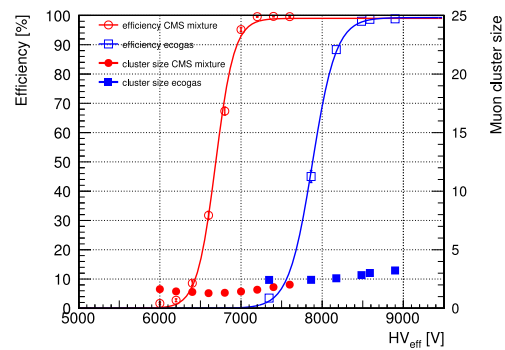


**Figure 3.33:** Efficiency (open symbols) and cluster size (full symbols) of an iRPC as a function of the effective voltage for the standard CMS gas mixture and an environmental-friendly gas mixture [177].

<sup>2401</sup> of  $CO_2$  flushed into a standard double-gap RPC. Instead of the streamer probability, the cluster size  
<sup>2402</sup> is shown. The average number of hits generated by a muon passing through the chamber seem to  
<sup>2403</sup> have increased by 1 at the level of the knee of the sigmoid plateau using the ecogas.



# 4

2404

2405

## Physics of Resistive plate chambers

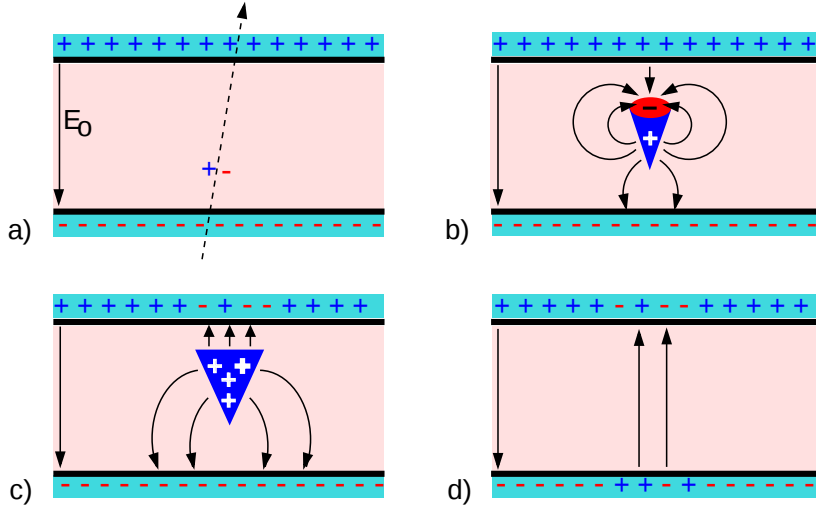
2406 A Resistive Plate Chamber (RPC) is a gaseous detector used in high-energy physics experiments  
2407 as described in Chapter 3. It has been developed in 1981 by Santonico and Cardarelli [203], under  
2408 the name of *Resistive Plate Counter*, as an alternative to the local-discharge spark counters pro-  
2409 posed in 1978 by Pestov and Fedotovich [204, 205]. Working with spark chambers implied using  
2410 high-pressure gas and high mechanical precision which the RPC simplified by formerly using a gas  
2411 mixture of argon and butane flowed at atmospheric pressure and a constant and uniform electric  
2412 field propagated in between two parallel electrode plates. Moreover, a significant increase in rate  
2413 capability was introduced by the use of electrode plate material with high bulk resistivity, preventing  
2414 the discharge from growing throughout the whole gas gap. Indeed, the effect of using resistive elec-  
2415 trodes is that the constant electric field is locally canceled out by the development of the discharge,  
2416 limiting its growth.

2417 Through its development history, different operating modes [206–208], gas mixtures [203, 208–  
2418 213] and new detector designs [214–216] have been discovered, leading to further improvement of  
2419 the rate capability of such a detector. The low developing costs and easily achievable large detection  
2420 areas offered by RPCs, as well as the wide range of possible designs, made them a natural choice  
2421 to as muon chambers and/or trigger detectors in multipurpose experiments such as CMS [192] or  
2422 ATLAS [217], time-of-flight detectors in ALICE [218], calorimeter with CALICE [219] or even  
2423 detectors for volcanic muography with ToMuVol [220].

### 2424 4.1 Principle

2425 RPCs are ionisation detectors composed of two parallel resistive plate electrodes in between which  
2426 a constant electric field is set. The space in between the electrodes, referred to as *gap*, is filled with  
2427 a dense gas that is used to generate primary ionization into the gas volume. The free charge carriers  
2428 (electrons and cations) created by the ionization of the gas molecules are then accelerated towards the  
2429 electrodes by the electric field, as shown in Figure 4.1 [221]. RPCs being passive detectors, a current  
2430 on pick-up copper read-out placed outside of the gas volume is induced by the charge accumulation

2431 during the growth of the avalanche resulting from the acceleration of the charge carriers. As a  
 2432 consequence, the time resolution of the detector is substantially increased as the output signal is  
 2433 generated while the electrons are still in movement. The advantage of a constant electric field, over  
 2434 multi-wire proportional chambers, is that the electrons are being fully accelerated from the moment  
 2435 charge carriers are freed and feel the full strength of the electric field that doesn't depend on the  
 2436 distance to the readout and that the output signal doesn't need for the electrons to be physically  
 2437 collected.



2438 *Figure 4.1: Different phases of the avalanche development in the RPC gas volume subjected to a constant  
 2439 electric field  $E_0$ . a) An avalanche is initiated by the primary ionisation caused by the passage of a charged  
 2440 particle through the gas volume. b) Due to its growing size, the avalanche starts to locally influence the electric  
 2441 field. c) The electrons, lighter than the cations reach the anode first. d) The ions reach the cathode. While  
 2442 the charges have not recombined, the electric field in the small region around the avalanche stays affected and  
 2443 locally blinds the detector.*

2438 After an avalanche developed in the gas, a time long compared to the development of a discharge  
 2439 is needed to recombine the charge carriers in the electrode material due to their resistivity. This  
 2440 property has the advantage of affecting the local electric field and avoiding sparks in the detector  
 2441 but, on the other hand, the rate capability is intrinsically limited by the time constant  $\tau_{RPC}$  of the  
 2442 detector. Using a quasi-static approximation of Maxwell's equations for weakly conducting media,  
 2443 it can be shown that the time constant  $\tau_{RPC}$  necessary to the charge recombination at the interface  
 2444 in between the electrode and the gas volume is given by the Formula 4.1 [222].

$$(4.1) \quad \tau_{RPC} = \frac{\epsilon_{electrode} + \epsilon_{gas}}{\sigma_{electrode} + \sigma_{gas}}$$

2445 A gas can be assimilated to vacuum, leading to  $\epsilon_{gas} = \epsilon_0$  and  $\sigma_{gas} = 0$ , and the electrodes  
 2446 permittivity and conductivity can be written as  $\epsilon_{electrode} = \epsilon_r \epsilon_0$  and  $\sigma_{electrode} = 1/\rho_{electrode}$ ,  
 2447 showing the strong dependence of the time constant to the electrodes resistivity in Formula 4.2.

$$(4.2) \quad \tau_{RPC} = (\epsilon_r + 1)\epsilon_0 \times \rho_{electrode}$$

Very few materials with a low enough resistivity exist in nature. The resistivity targeted to build RPCs ranges from  $10^9$  to  $10^{12} \Omega \cdot \text{cm}$ . The most common RPC electrode materials are displayed in Table 4.1. When the doped glass and ceramics can offer short time constants of the order of 1 ms, the developing cost of such materials is quite high due to the very low demand. Thus, High-pressure laminate (HPL) is often the choice for high-rate experiments using very large RPC detection areas. Other experiments working at cosmic muon fluxes can safely operate with ordinary float glass.

Material	$\rho_{\text{electrode}} (\Omega \cdot \text{cm})$	$\epsilon_r$	$\tau_{\text{RPC}} (\text{ms})$
Float glass	$10^{12}$	$\sim 7$	$\sim 700$
High-pressure laminate	$10^{10}$ to $10^{12}$	$\sim 6$	$\sim 6$ to 600
Doped glass (LR S)	$10^9$ to $10^{11}$	$\sim 10$	$\sim 1$ to 100
Doped ceramics (SiN/SiC)	$10^9$	$\sim 8.5$	$\sim 1$
Doped ceramics (Ferrite)	$10^8$ to $10^{12}$	$\sim 20$	$\sim 0.2$ to 2000

Table 4.1: Properties of the most used electrode materials for RPCs.

## 4.2 Rate capability and time resolution of Resistive Plate Chambers

The electrode material plays a key role in the maximum intrinsic rate capability of RPCs. R&D is continuously being done to develop at always cheaper costs material with lower resistivity. Nevertheless, the amount of charge released, i.e. the size of the discharge, if reduced leads to a smaller blind area in the detector, increasing the rate capability of the detector. On the other hand, the drift velocity of electrons in the gas volume being quite stable with the applied electric field, the design of a detector and the associated read-out and pulse-processing electronics will be a major component of the time resolution of RPCs. Moreover, the sensitivity of the electronics will also help increasing the rate capability by lowering the gain the gas volume needs to be operated at, increasingly lowering the gas volume in which the signals will develop.

### 4.2.1 Operation modes

Being a gaseous detector using an accelerating electric field to amplify the signal of primary charge carriers, the RPC can be operated into different modes as the electric field intensity varies. Each mode offers different performances for such a detector, and it will be showed that the operating mode corresponding to the lowest electric field possible is best suited for high-rate detectors working in collider experiments.

RPCs where developed early 1980s. At that time it was using an operating mode now referred to as *streamer mode*. Streamers are large discharges that develop in between the two electrodes enough to locally discharge the electrodes. If the electric field inside of the gas volume is strong enough, with electrons being fast compared to ions, a large and dense cloud of positive ions will develop nearby the anode and extend toward the cathode while the electrons are being collected, eventually leading to a streamer discharge due to the increase of the field seen at the cathode. The field is then strong enough so that electrons are pulled out of the cathode. Electrodes, though they are a unique volume of resistive material, can be assimilated to capacitors. At the moment an electric field is applied in between their outer surfaces, the charge carriers inside of the volume will start moving leading to a situation where there is no voltage across the electrodes and a higher density

of negative charges, i.e. electrons, on the inner surface of the cathode. Finally, when a streamer discharge occurs, these electrons are partially released in the gas volume contributing to increase the discharge strength until the formation of a conductive plasma, the streamer. This can be understood through Figure 4.2 [206]. Streamer signals are very convenient in terms of read-out as no further amplification is required with output pulses amplitudes of the order of a few tens to few hundreds of mV as can be seen on Figure 4.3.

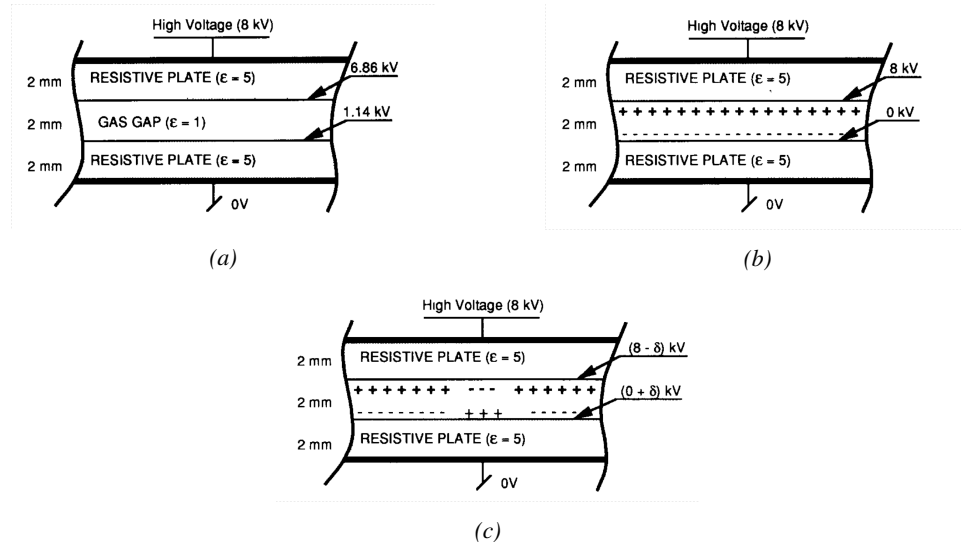


*Figure 4.2: Movement of the charge carriers in an RPC. Figure 4.2a: Voltage across an RPC whose electrodes have a relative permittivity of 5 at the moment the tension is applied. Figure 4.2b: After the charge carriers moved, the electrodes are charged and there is no voltage drop over the electrodes anymore. The full potential is applied on the gas gap only. Figure 4.2c: The streamer discharge initiated by a charged particle transports electrons and cations towards the anode and cathode respectively.*

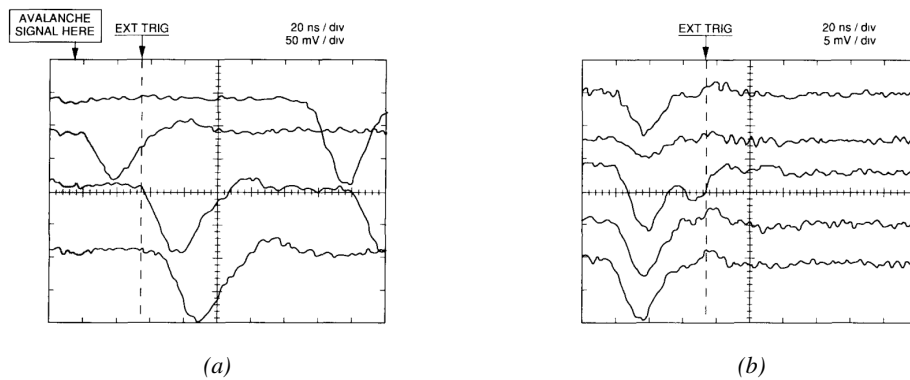


*Figure 4.3: Typical oscilloscope pulses in streamer mode (Figure 4.3a) and avalanche mode (Figure 4.3b). In the case of streamer mode, the very small avalanche signal is visible.*

Though, when the electric field is reduced, the electronic gain is small until the electrons get close enough to the anode and the positive ion cloud is much smaller. The electric field cannot rise

2489 to the point a field emission of electrons on the cathode is possible. The resulting signal is weak,  
 2490 of the order of a few mv as shown on Figure 4.3, and requires amplification. This is the *avalanche*  
 2491 mode of RPC operation. This mode offers a higher rate capability by providing smaller discharges  
 2492 that don't affect the electrodes charge and are more locally contained in the gas volume as was  
 2493 demonstrated by Crotty with Figure 4.4 [206]. The detector only stays locally blind the time the  
 2494 charge carriers are recombined and there is no need for electrode recharge which is a long process  
 2495 affecting a large portion of the detector. Another advantage of avalanche signals over streamer is  
 2496 the great time consistency. Figure 4.3 shows very clearly that avalanche signals have a very small  
 2497 time jitter. Thus, using such a mode is a natural choice for experiments in which the detectors are  
 2498 required to have a high detection rate.

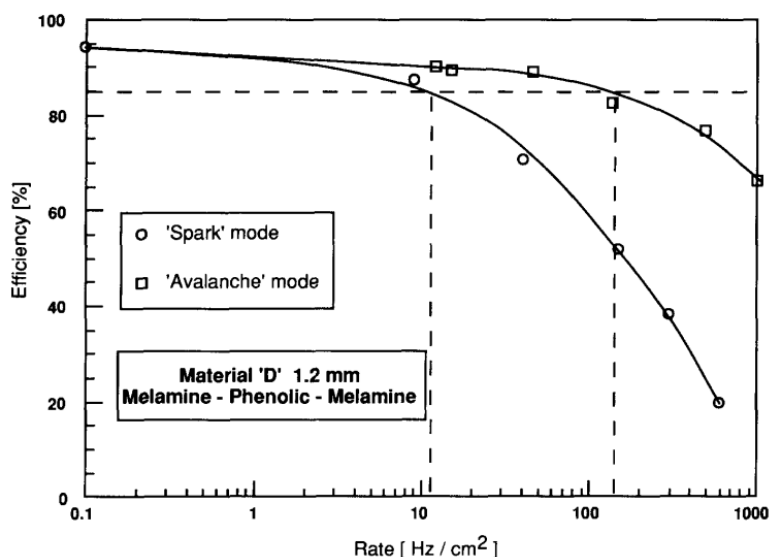
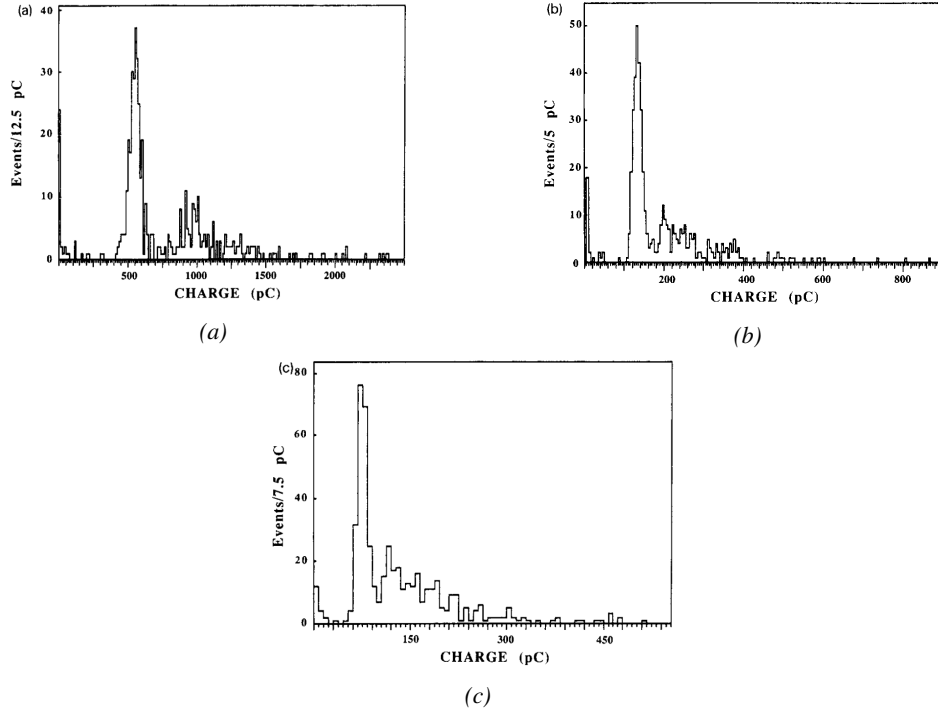


Figure 4.4: Rate capability comparison for the streamer and avalanche mode of operation. An order of magnitude in rate capability for a maximal efficiency drop of 10% is gained by using the avalanche mode over the streamer mode.

#### 2499 4.2.2 Standard gas mixture for RPCs operated in collider experiments

2500 The first RPC working in streamer mode was operated with a 50/50 mixture of argon and butane [203],  
 2501 a standard mixture used at that time in multi-wire proportional chambers, taking profit of  
 2502 the good effective Townsend coefficient of argon to maximize the number of primary charge carriers  
 2503 freed in the gas by ionizing particles and of the quenching properties of butane. Before the discovery  
 2504 of the avalanche mode of RPC operation and concerned about the rate capability of RPCs operated  
 2505 in streamer mode, the performance improvement of the detectors through the increase of fast charge  
 2506 ratio in the signal development, decreasing the charge induced per avalanche as can be seen through  
 2507 Figure 4.5, was studied by adding Freon based gases, such as  $CF_3Br$ , into the typical  $Ar/C_4H_{10}$   
 2508 gas mixture was studied and showed that a lower induced charge could lead to an improvement the  
 2509 rate capability [209]. This consideration led to the discovery of the avalanche mode which confirmed  
 2510 that the smaller the induced charge, the better the rate capability of the RPCs [206]. This discovery  
 2511 could be made thanks to the increased number of lower induced charge events allowed by adding a

2512 fraction of strong quencher in the gas mixture.



*Figure 4.5: Comparison of the charge distribution of signals induced by cosmic muons in an RPC operated with a gas mixture of argon, butane and bromotrifluoromethane ( $CF_3Br$ ). The  $Ar/C_4H_{10}$  is kept constant at 60/40 in volume while the total amount of  $CF_3Br$  in the mixture is varied: 0% (Figure 4.5a), 4% (Figure 4.5b) and 8% (Figure 4.5c) [209].*

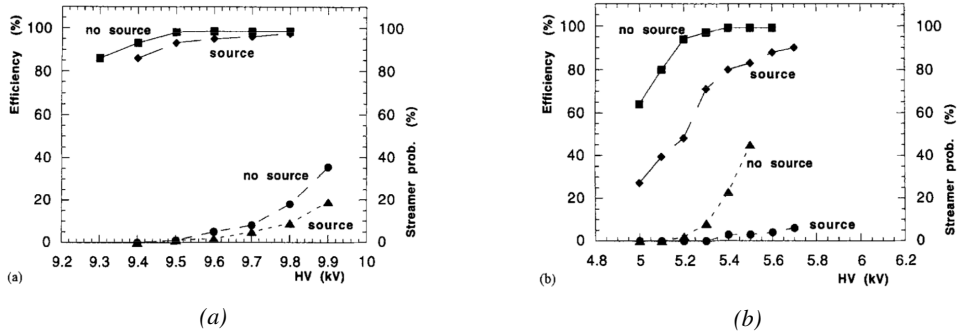


*Figure 4.6: Comparison of the efficiency and streamer probability, defined as the fraction of events with an induced charge 10 times larger than that of the average avalanche, with and without irradiation by a 24 GBq  $^{137}Cs$  source of an RPC successively operated with a 90/10 mixture  $C_2H_2F_4/i-C_4H_{10}$  (Figure 4.6a) and a 70/5/10/15 mixture of  $Ar/i-C_4H_{10}/CO_2/C_2H_2F_4$  (Figure 4.6b) [210].*

2513 From this moment onward, more and more studies were conducted in order to find a gas mixture  
2514 that would allow for the best suppression of streamers for the benefit of low charge avalanches. Most

R&D groups working with narrow gaps started using freon-based gas mixtures while users of wide gap RPCs kept using  $Ar/CO_2$  based mixtures. The differences in between narrow and wide gaps will be later discussed in Section 4.2.3. The  $CF_3Br$  having a high GWP, tetrafluoroethane was preferred to it as more suitable ecofriendly gas in the middle of the 90s. An advantage of this new freon component is that it featured a high primary ionization and a low operating voltage, as reported by Cardarelli [208]. Thus, the new gas mixtures used were mainly composed of tetrafluoroethane alone with lower content of isobutane in order to reduce the flammability of the mixtures in the case it were to be used in accelerator experiments for safety reasons. Performance and models about such mixtures were discussed in papers of Abbrescia [210, 211] and showed a better suitability of such a gas mixture, with respect to argon based ones, for operations with high radiation backgrounds leading to a need for high-rate capability of the detectors, as can be seen from Figures 4.6 and 4.7. Indeed, although the operating voltage of a tetrafluoroethane based mixture is higher than which of an argon based mixture but the efficiency under irradiation is more stable, the voltage range with negligible streamer probability is much wider, and the fast charge ratio available is much greater, providing with more stable operation of the detector.

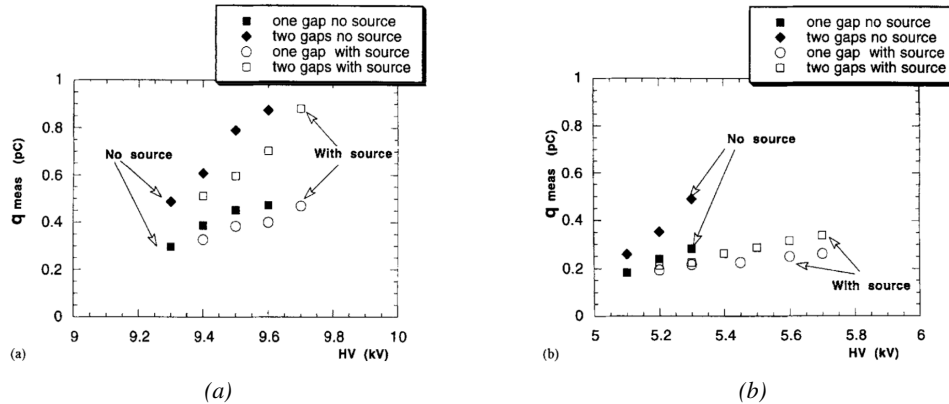


Figure 4.7: Comparison of the fast charge ratio with and without irradiation by a 24 GBq  $^{137}Cs$  source of an RPC successively operated with a 90/10 mixture  $C_2H_2F_4/i-C_4H_{10}$  (Figure 4.7a) and a 70/5/10/15 mixture of  $Ar/i-C_4H_{10}/CO_2/C_2H_2F_4$  (Figure 4.7b). The results are provided for both single-gap and double-gap operation [210].

Aside of the improvement of the rate capability through linseed oil surface treatment of HPL electrodes, which allowed for a lower intrinsic noise rate and dark current of the detectors by improving the smoothness of the electrodes surface [223], it was later found that the streamers could be further suppressed by adding an electronegative compound into the gas mixture. The benefits of adding  $SF_6$  in order to push the transitions from avalanche to streamers towards high voltages has been discussed in 1998 [212, 213] and eventually the high-rate RPC destined to be used in accelerator physics would unanimously start using this compound into RPC gas mixtures. Being able to control the creation of streamers allows for slower ageing of the detector and lower power consumption as the currents driven by the electrodes consecutively to the induced charges would be smaller. In summary, the typical gas mixture RPCs are operated with is generally composed of the following 3 gas compounds, although as mentioned in Chapter 3.6, research is being conducted into new more ecofriendly gas mixture using gases with a much lower Global Warming Potential:

- Tetrafluoroethane ( $C_2F_4H_2$ ), also referred to as *Freon* or *R134a*, is the principal compound

2543 of the RPC gas mixtures, with a typical fraction above 90%. It is used for its high effective  
 2544 Townsend coefficient and the great average fast charge that allows to operate the detector  
 2545 with a high threshold with respect to argon, for example, that has similar effective Townsend  
 2546 coefficient but suffers from a lower fast charge. To operate with similar conditions, argon  
 2547 would require a higher electric field leading to a higher fraction of streamers, thus limiting the  
 2548 rate capability of the detector [210, 211].

- 2549
- 2550 • Isobutane ( $i\text{-C}_4\text{H}_{10}$ ), only present in a few percent in the gas mixtures, is used for its UV  
 2551 quenching properties [224] helping to prevent streamers due to UV photon emission during  
 the avalanche growth.
  - 2552 • Sulfur hexafluoride, ( $\text{SF}_6$ ), simply referred to as  $\text{SF}_6$ , is used in very little quantities for its  
 2553 high electronegativity. Any excess of electrons is absorbed by the compound and streamers  
 2554 are suppressed [212, 213]. Nevertheless, a fraction of  $\text{SF}_6$  higher than 1% will not bring  
 2555 any extra benefit in terms of streamer cancellation power but will lead to higher operating  
 2556 voltage [212], as can be understood through Figure 4.8.

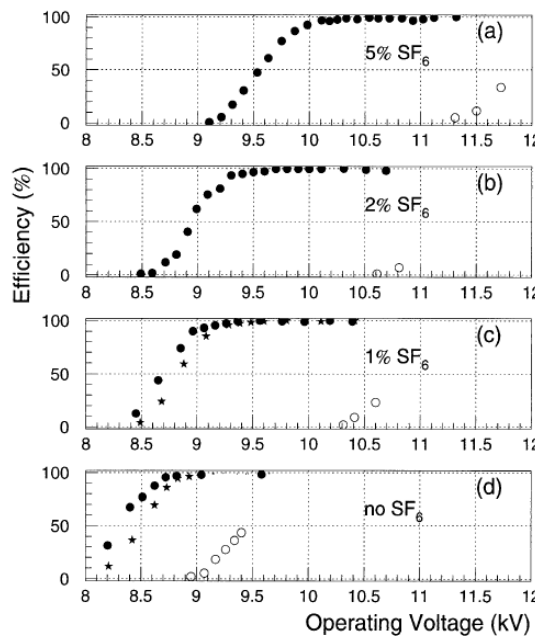
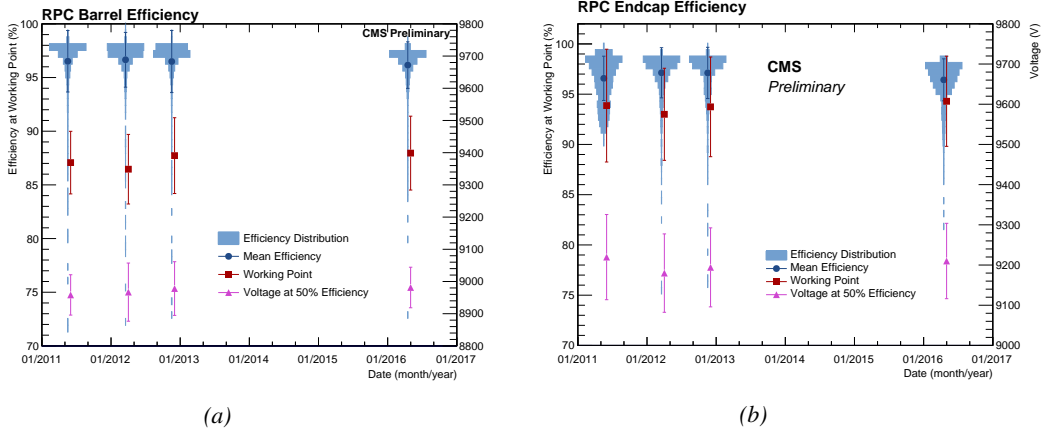


Figure 4.8: Efficiency (circles and stars with 30 mV and 100 mV thresholds respectively) and streamer probability (open circles) as function of the operating voltage of a 2 mm single-gap HPL RPC flushed with a gas mixture containing (a) 5%, (b) 2%, (c) 1% and (d) no  $\text{SF}_6$  [212].

2557 In the last steps of R&D, the gas mixture of CMS RPCs was foreseen to be a 96.2/3.5/0.3 compo-  
 2558 sition of  $\text{C}_2\text{H}_2\text{F}_4$ / $i\text{-C}_4\text{H}_{10}$ / $\text{SF}_6$  [225] but finally it was slightly changed into a 95.2/4.5/0.3 mixture  
 2559 of the same gases [226]. A summary of the operation performance of the RPCs since the start of  
 2560 LHC and of CMS data taking is given in Figure 4.9 [227]. The performance of the detectors is  
 2561 regularly monitored and the operating voltages updated in order to obtain a very stable performance  
 2562 through time. Nevertheless, the detectors will face new challenges during Phase-II during which they

will exposed to more extreme radiation conditions. Description of the longevity tests with extreme irradiation and the conclusions regarding the operation of the present RPC system will be given in Chapter 5.



*Figure 4.9: Evolution of the efficiency, working voltage, and voltage at 50% of maximum efficiency for CMS Barrel (Figure 4.9a) and Endcap (Figure 4.9b) RPCs obtained through yearly voltage scans since 2011. The working voltage of each RPC is updated after each voltage scan to ensure optimal operation [227].*

It was already discussed that in the future, it is likely that the use of freon gases could be banned. As potential replacement for tetrafluoroethane was proposed the trifluoriodomethane ( $CF_3I$ ), a molecule with similar properties than  $CF_3Br$  which was replaced by the tetrafluoroethane, and the 1,3,3,3-tetrafluoropropene ( $C_3H_2F_4$  or HFO-1234re), a molecule with similar properties than the actual tetrafluoroethane and proposed as a replacement in refrigerating and air conditioning systems [228]. These two gases have stronger quenching properties than  $C_2H_2F_4$  which means a much stronger electric field needs to be applied on the parallel electrodes of the RPCs in order to reach full efficiency. But the power supply system of CMS RPC is limited to 15 kV and so is ATLAS power supply system which is participating in a joined R&D. As can be seen from Figure 3.32, reducing the working voltage was achieved by mixing the potential replacements together with  $CO_2$ . Introducing carbon dioxide into the mixture while keeping similar levels of isobutane and  $SF_6$  increases the streamer probability and the best candidate identified for a compromise in between low enough working voltage and acceptable levels of streamers corresponds to a mixture containing 50% of HFO, 4.5% of  $iC_4H_{10}$ , 0.3% of  $SF_6$  and 45.2% of  $CO_2$  but is not yet considered satisfactory. On the other hand, no good replacement for  $SF_6$  has yet been identified. With its very high Global Warming Potential (23900), even small fraction of this gas in the mixture (it only represents 0.3% of CMS standard mixture but more than 5% of its overall GWP) substantially increase the danger for the environment. Although finding a replacement for this gas is less critical than for the tetrafluoroethane composing more than 90% of usual RPC standard mixtures, the problem will need to be addressed.

### 4.2.3 Detector designs and performance

Different RPC designs have been used, and each of them presents its own advantages. Historically, the first type of RPC to have been developed is what is now referred to as *narrow gap* RPC [203,

2589 229].

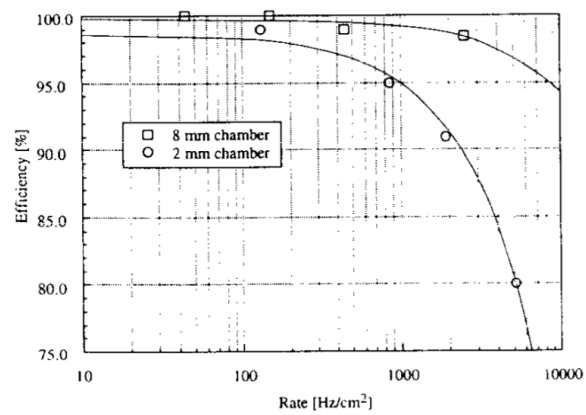


Figure 4.10: Comparison of the rate capability of 8 mm and 2 mm wide RPCs. The lines are linear fits on the data [229].

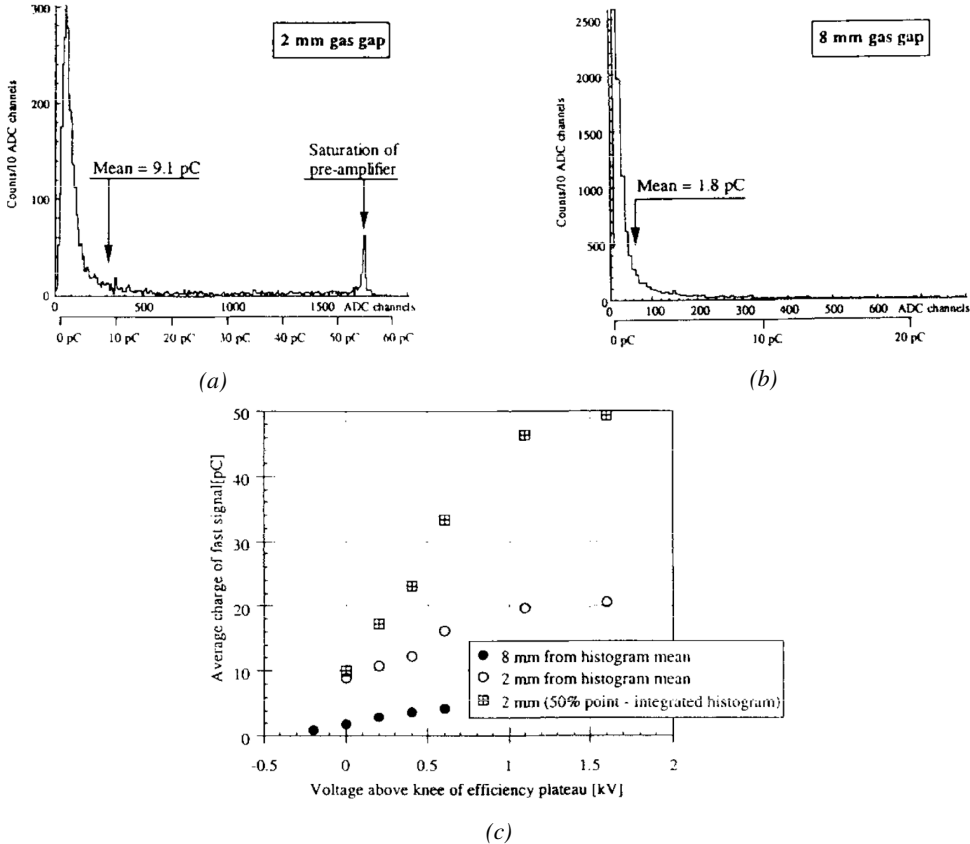
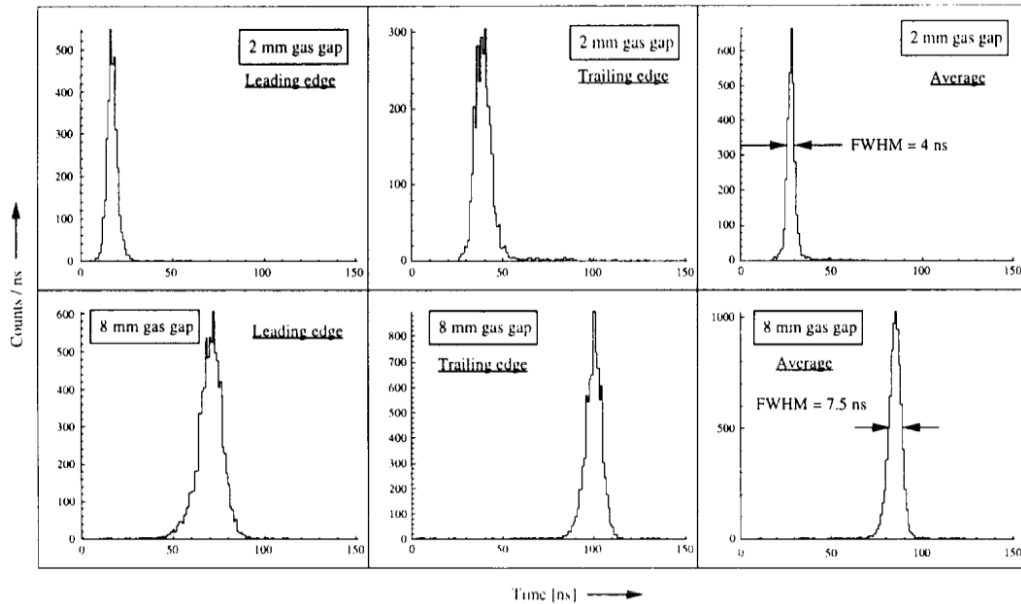


Figure 4.11: Distributions of the induced charge of fast signals on 2 mm (Figure 4.11a) and 8 mm (Figure 4.11b) RPCs exposed to a radiation rate of  $100 \text{ Hz/cm}^2$ . Average induced charge of fast signals as a function of the high voltage applied on 2 mm and 8 mm RPCs (Figure 4.11c). In the case of the 2 mm RPC, a saturation of the pre-amplifier was observed. The average of the distribution is underestimated, and the median is showed together with the average to account for this bias [229].

After the avalanche mode has been discovered [206], it has been shown that increasing the width of the gas gap lead to higher rate capability, due to lower charge deposition per avalanche, and lower power dissipation [229], as is showed in Figures 4.10 and 4.11. The distance in between the electrode being greater, a weaker electric field can be applied and a lower gain used as a longer gas volume will contribute to the signal induction on the read-out circuit. Nevertheless, by increasing the gas gap width, the time resolution of the detector decreases. This is a natural result if the increase of active gas volume in the detector is taken into account. Indeed, for a given detection threshold on the induced charge per signal, only the small fraction of gas closest to the cathode will provide enough gain to have a detectable signal. In the case of a wider gas volume, the active region is then larger and a larger time jitter is introduced with the variation of starting position of the avalanche, as discussed in [214] and showed in Figure 4.12.



*Figure 4.12: Time distributions of the leading, trailing, and average of both leading and trailing edges for 2 mm (top row) and 8 mm (bottom row) RPCs exposed to a  $100 \text{ Hz/cm}^2$  radiation rate. The data was collected with RPCs operated at the voltage corresponding to the knee of the efficiency distribution, defined as the point where 95% of the maximum efficiency is obtained [229].*

2601 To improve both the time resolution and the rate capability, different methods were used trying  
 2602 to take advantage of both narrow and wide gap RPCs into a single design. Thus, double-gap  
 2603 RPCs, combining two narrow gaps into a single detector to increase the effective sensitive volume,  
 2604 and multigap RPCs, which divided the large volume of a wide gap RPC into thinner sub-gaps by  
 2605 adding intermediate electrodes in between the cathode and anode to improve the time resolution by  
 2606 mimicking narrow gap RPCs, were developed starting from the middle of the 90s.

#### 2607 4.2.3.1 Double-gap RPC

2608 Made out of two narrow RPC detectors stacked on top of each other as shown in Figure 4.13, this  
 2609 detector layout, popularized by the two multipurpose experiments CMS [192] and ATLAS [217] at  
 2610 LHC, can be used as an OR system in which each individual chamber participates in the output signal  
 2611 and increases the overall sensitive volume of the detector apparatus. Keeping the copper strip read-  
 2612 out system at the ground, CMS and ATLAS, due to different goals, have chosen different designs as  
 2613 CMS RPCs possess a 1D read-out while ATLAS RPCs offer a 2D read-out. The difference comes  
 2614 from placing the read-out in between the gaps, the anodes facing each other, or to have both RPC  
 2615 gaps in between two layers of read-out panels, one along the X-axis and one along the Y-axis, the  
 2616 cathodes facing each other.

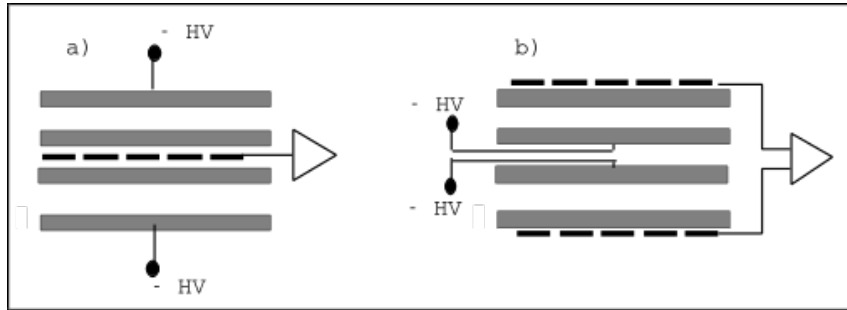


Figure 4.13: Possible double-gap RPC layouts: a) "standard" 1D double-gap RPC, as used in CMS experiment, where the anodes are facing each other and a 1D read-out plane is sandwiched in between them, b) double read-out double-gap RPC as used in ATLAS experiment, where the cathodes are facing each other and 2 read-out planes are used on the outer surfaces. This last layout can offer the possibility to use a 2D reconstruction by using orthogonal read-out planes.

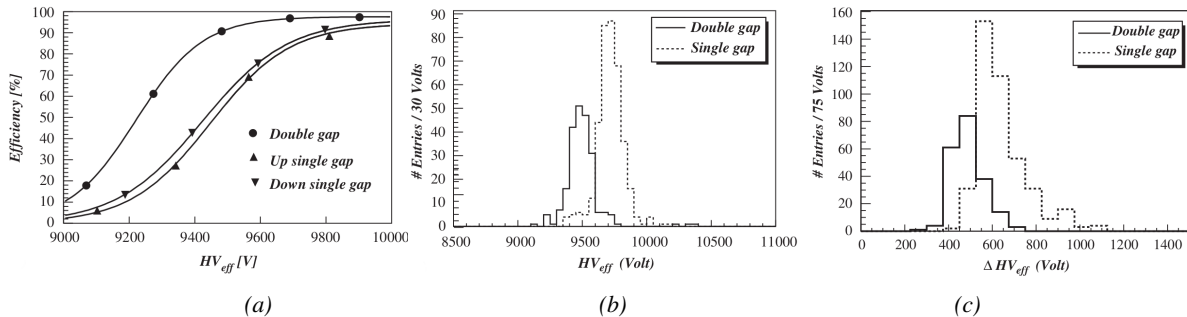
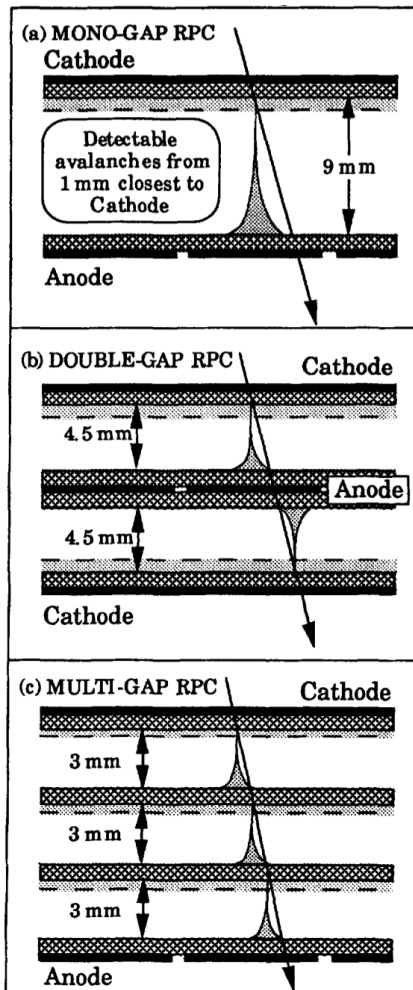


Figure 4.14: Comparison of performance of CMS double and single-gap RPCs using cosmic muons [225].  
Figure 4.14a: Comparison of efficiency sigmoids. Figure 4.14b: Voltage distribution at 95% of maximum efficiency. Figure 4.14c:  $\Delta_{10\%}^{90\%}$  distribution.

The gain of such a detector is reduced by a factor 2 with respect to single-gap RPCs with an efficiency plateau reached at lower voltage, as visible on Figure 4.14, due to the two gas gaps contributing to the signal formation and offering a dynamic range closer to that of a wide gap RPC. A double-gap is then fully efficient while the individual RPC gaps composing it are only 70 to 80% efficient. Naturally, by operating the double-gap at a lower voltage, the rate capability is found to be increased as the induced charge per gap is then lower than in the case of a single-gap detector also leading to a reduction of the streamer probability and a better extraction of the fast charge of the total signal as could be seen through previously presented Figure 4.7.

#### 4.2.3.2 Multigap RPC (MRPC)

MRPCs are layouts in which floating sub electrode plates are placed into a wide gap RPC to divide the gas volume and create a sum of narrow gaps [214, 215]. Similarly to the double-gap RPC for which the gain could be reduced by increasing the dynamic range, the multigap reduces the gain while keeping a total dynamic range similar to that of a wide gap RPC by reducing the size of each individual sub-gap composing the detector. The dynamic range, associated to the sensitive volume, and the comparison of each detector layout to the wide gap RPC is showed in Figure 4.15.



*Figure 4.15: Representation of different RPC layouts (wide gap on Figure (a), double-gap on Figure (b) and multigap on Figure (c)), of the corresponding sensitive volume in gray, and of the associated avalanche size [215].*

2632 By operating the detector with thinner gaps, the time resolution is improved. Comparatively to  
 2633 the time resolution presented in Figure 4.12 for the wide gap RPC of 8 mm, a complementary study  
 2634 was conducted on multigaps using two 4 mm and four 2 mm subgaps and showed, via Figure 4.16,  
 2635 an improvement of the time resolution with the reduction of the gap width and of the number of gaps  
 2636 while the same sensitive volume was kept [215].

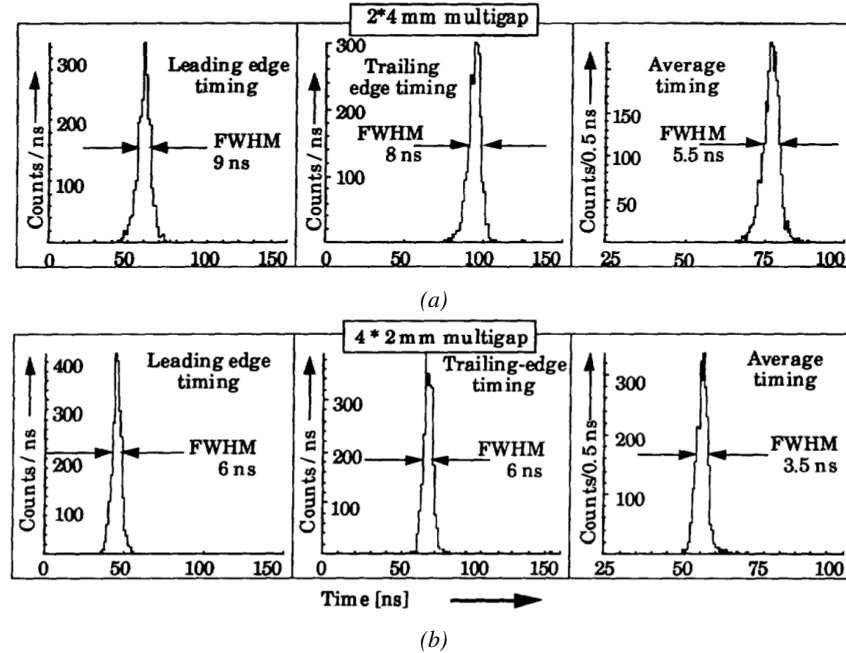


Figure 4.16: Time distributions of the leading, trailing, and average of both leading and trailing edges for multigap RPCs consisting in two 4 mm (Figure 4.16a) and four 2 mm (Figure 4.16b) exposed to a 100 Hz/cm<sup>2</sup> radiation rate. The data was collected with RPCs operated at the voltage corresponding to the knee of the efficiency distribution, defined as the point where 95% of the maximum efficiency is obtained [215].

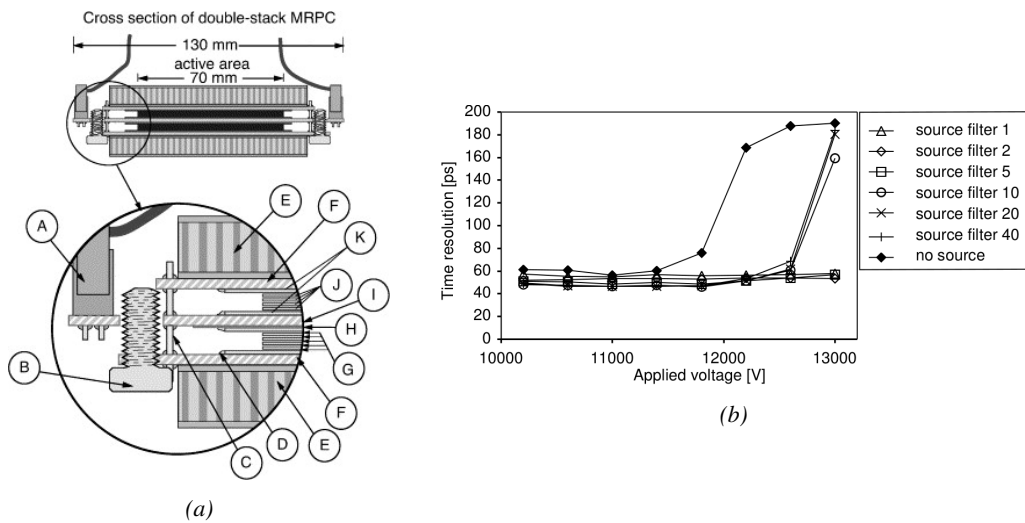


Figure 4.17: Presentation of a study of a possible ALICE MRPC cell using 250 µm gas gaps, 620 µm outer glass electrodes, and 550 µm inner floating electrodes (Figure 4.17a), and of its time resolution performance as a function of the applied high voltage for different radiation levels referred through different filter settings of the 740 GBq  $^{137}\text{Cs}$  source the former CERN GIF facility [230].

2637 After the problem of streamers was solved by adding  $\text{SF}_6$  into the gas mixture, the size of the

2638 MRPCs decreased as the research groups started applying the concept of dividing the gas volume  
 2639 into subvolumes to the narrow gap RPCs leading to the, now, widely used micro gap MRPCs. The  
 2640 time resolution of such a detector can reach of few tens of ps, with gas gaps of the order of a few  
 2641 hundred  $\mu\text{m}$  as showed in Figure 4.17 representing a single cell of ALICE Time-of-flight (ToF)  
 2642 system consisting of double MRPCs, as it was studied in the early 2000s [230].

2643 Sometimes used as a double multigap RPC, taking advantage of the OR of double-gap RPCs to  
 2644 both be able to operate a higher number of gaps while keeping a reasonable high voltage applied  
 2645 in between the cathode and anode and to further reduce the gain, the MRPC is mainly used as ToF  
 2646 detector [230–234] due to its excellent timing properties that allow to perform particle identification  
 2647 as explained by Williams in [235]. The principle of particle identification using ToF is simply the  
 2648 measurement of the velocity of a particle. Indeed, particles are defined by their mass (for the parameter  
 2649 of interest here, their electric charge being measured using the bending angle of the particles  
 2650 traveling through a magnetic field) and this mass can be calculated by measuring the velocity  $\beta$  and  
 2651 momentum of the particle:

$$(4.3) \quad \beta = \frac{p}{\sqrt{p^2 + m^2}}$$

2652 Intuitively, it is trivial to understand that 2 different particles having the same momentum will  
 2653 have a different velocity due to the mass difference and thus a different flight time  $T_1$  and  $T_2$  through  
 2654 the detector and this is used to separate and identify particles. The better the time resolution of the  
 2655 ToF system used, the stronger will the separation be:

$$(4.4) \quad T = \frac{L}{v} = \frac{L}{c \cdot \beta}, \quad \Delta T = T_1 - T_2 = \frac{L}{c} \left( \sqrt{1 + m_1^2/p^2} - \sqrt{1 + m_2^2/p^2} \right) \cong (m_1^2 - m_2^2) \frac{L}{2cp^2}$$

2656 An example of particle identification is given for the case of STAR experiment in Figure 4.18.

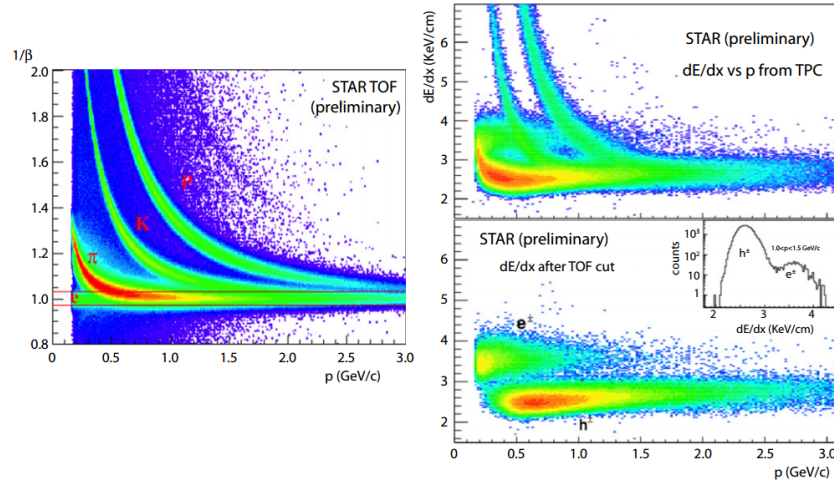


*Figure 4.18: Particle identification applied to electrons in the STAR experiment. The identification is performed combining ToF and  $dE/dx$  measurements [235].*

2657 Taking into account the distortion effect on the electric field inside of an MRPC built using micro  
 2658 gaps due to the exposition to irradiation, distortion that can be understood by monitoring the current  
 2659 drawn by the detector which should stay constant at constant electric field, another benefice of using  
 2660 such small gas gaps is the strong reduction of the average avalanche volume and thus of the blind  
 2661 spot on MRPCs leading to an improved rate capability. Multigaps can sustain backgrounds of several  
 2662 kHz/cm<sup>2</sup> as demonstrated in Figure 4.19.

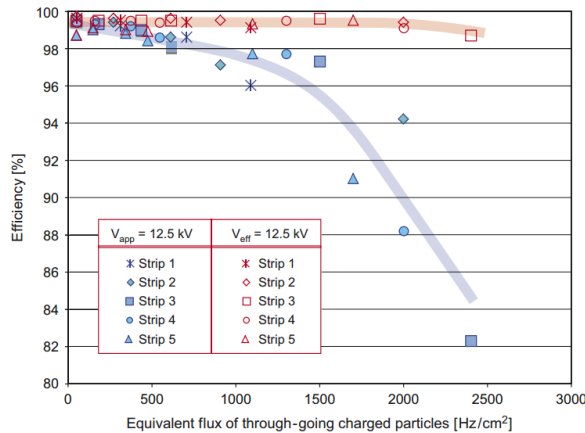


Figure 4.19: Comparison of the detector performance of ALICE ToF MRPC [236] at fixed applied voltage (in blue) and at fixed effective voltage (in red). The effective voltage is kept fixed by increasing the applied voltage accordingly to the current drawn by the detector.

#### 2663 4.2.3.3 Charge distribution and performance limitations

2664 [This part could be moved in the next section of the chapter and deepened using the perspective  
 2665 of the avalanche physics.]

2666 The direct consequence of the different RPC layouts is a variation of intrinsic time resolution of  
 2667 the RPC as the gap size decreases and of the rate capability when the deposited charge per event is  
 2668 spread over a larger number of amplification volumes, allowing for a reduction of the overall gain of  
 2669 the detectors which is replaced by an on-electronics pre-amplification of the signals. In this sense,  
 2670 an advantage is given to multigaps whose design use sub-millimeter gas volumes providing very  
 2671 consistent signals.

2672 From the charge spectrum point of view, each layout has its own advantages. When the double-  
 2673 gap has the highest induced-over-drifting charge ratio, as seen in Figure 4.20, the multigap has a  
 2674 charge spectrum strongly detached from the origin, as visible in Figure 4.21. A high induced-over-  
 2675 drifting charge ratio means that the double-gap can be safely operated at a high threshold or that at  
 2676 a similar threshold it can be operated with a twice smaller drifting charge, meaning a higher rate  
 2677 capability if operated with sensitive enough electronics. On the other hand, the strong detachment  
 2678 of the charge spectrum from the origin in the MRPC case allows reaching a higher efficiency with  
 2679 increasing threshold as most of the induced charge is not low due to the convolution of several  
 2680 single-gap spectra. The range of stable efficiency increases with the number of gaps, as presented in  
 2681 Figure 4.22.

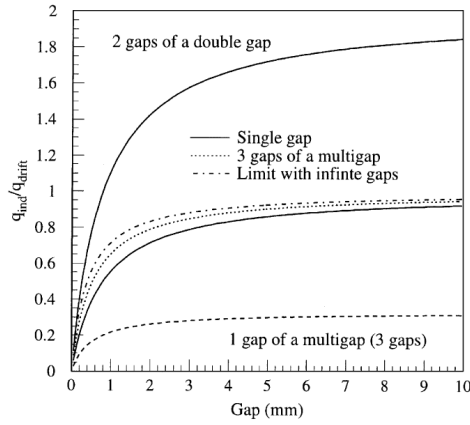


Figure 4.20: Ratio between total induced and drifting charge have been simulated for single-gap, double-gap and multigap layouts [237]. The total induced charge for a double-gap RPC is a factor 2 higher than for a multigap.

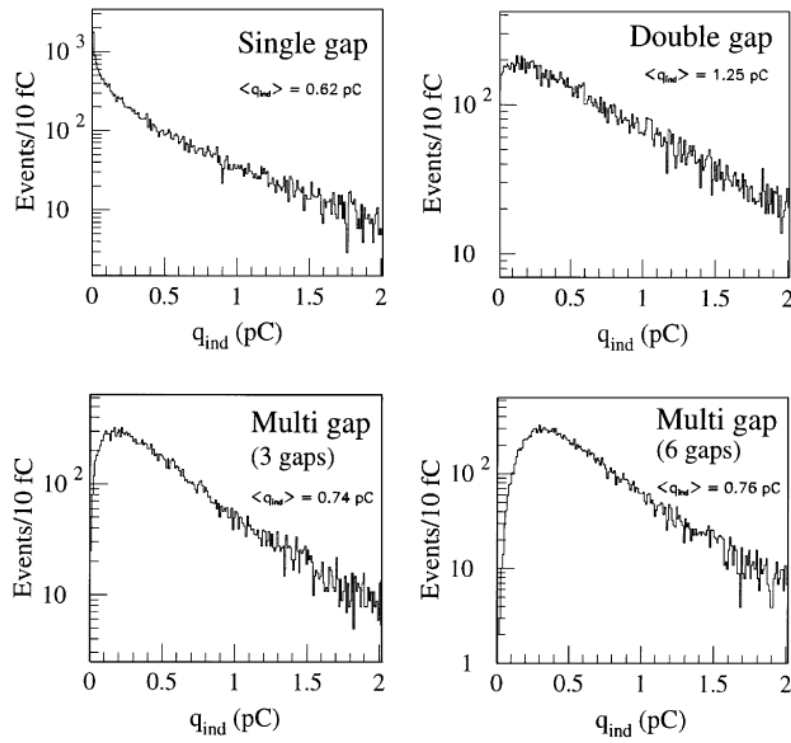


Figure 4.21: Charge spectra have been simulated for single-gap, double-gap and multigap layouts [237]. It appears that when single-gap shows a decreasing spectrum, double and multigap layouts exhibit a spectrum whose peak is detached from the origin. The detachment gets stronger as the number of gaps increases.

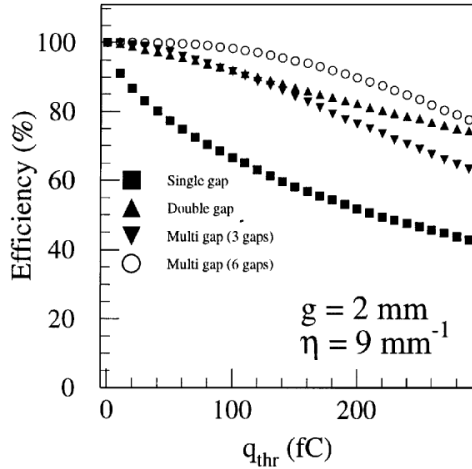


Figure 4.22: The maximal theoretical efficiency is simulated for single-gap, double-gap and multigap layouts [237] at a constant gap thickness of 2 mm and using an effective Townsend coefficient of  $9 \text{ mm}^{-1}$ .

### 4.3 Signal formation

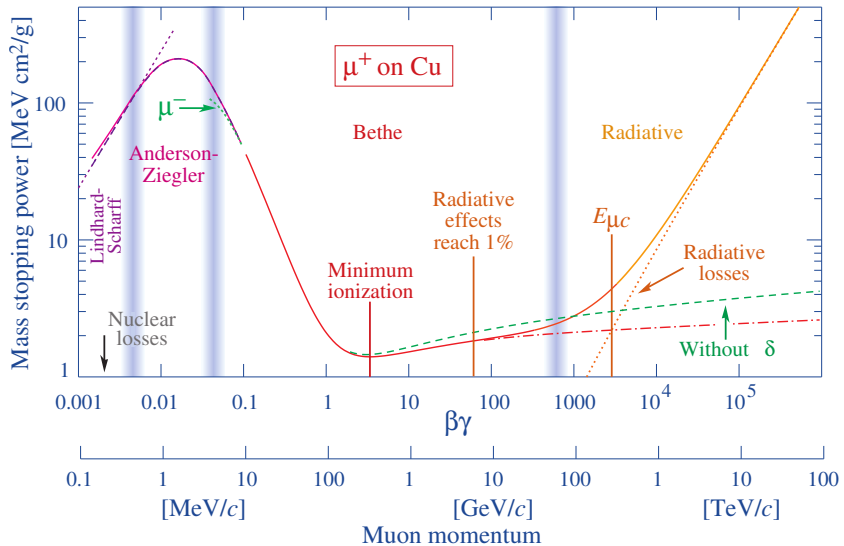


Figure 4.23: Mass stopping power as a function of  $\beta\gamma = p/Mc$  for positive muons in copper [115]. The total stopping power is indicated with a solid line and local components with dashed lines. The vertical bands are used to indicate boundaries between different approximations used at different energy range.

The physics of Resistive Plate Chambers still is far from being fully understood and work is regularly being accomplished in trying to model these detectors the best way possible by phenomenological models using well-defined physics [221, 238, 239]. These theoretical works have nevertheless led to a better understanding of the key principles that account for RPCs signal formation. As previously

discussed, the typical mixture of such a detector is in great majority composed by a ionizing gas with some quenching properties and a low ionization potential to easily produce electrons, with the addition of UV quencher and electronegative compounds. The electronic avalanche formation will be triggered by a charged particle passing through the gas, typically a muon in the case of most uses of RPCs. The production of electrons in the gas of a detector is related to the energy lost by the incoming particle traveling through a material medium. The example of the mass stopping power of copper on muons is given in Figure 4.23 on which the different energy loss mechanisms at different energy ranges are visible. Once primary electrons have been freed in the gas volume, the electric field applied in between the electrodes of the RPC will make the charges move and there will be a competition in the gas in between the Townsend and attachment coefficient which describe the evolution of the number of electrons in an avalanche. While drifting through the gas, the electrons are also subjected to diffusion that will affect the evolution of the avalanches. Finally, when the avalanche is big enough, the accumulation of negative (electrons) and positive (ions) charges in the gas volume will start affecting the local electric field. This effect is known as space charge effect.

### 4.3.1 Energy loss at intermediate energies

Intuitively, a particle traveling through a medium will interact with its components, losing energy. When a muon travels through the gas of a gaseous detector, at the energy range usually observed, it interacts with the molecules of the gas leading to dissipation of the transferred energy in the form of inelastic diffusion or ionization. The photons and electron-ion pairs resulting from these interactions can trigger avalanches in the gas which will contribute to feed the avalanche growth thanks to the strong electric field applied in between the two electrodes of an RPC.

The mass stopping power of moderately relativistic ( $0.1 \lesssim \beta\gamma \lesssim 1000$ ) heavy particles ( $M \gg m_e$ ) traveling through a medium via excitation and ionization processes was studied by Bethe in 1930 [240] and is well described by the so called the Bethe Formula given in Equation 4.5.

$$(4.5) \quad \left\langle -\frac{dE}{dx} \right\rangle = K z^2 \frac{Z}{A} \frac{1}{\beta^2} \left( \frac{1}{2} \ln \frac{2m_e c^2 \beta^2 \gamma^2 W_{max}}{I^2} - \beta^2 - \delta(\beta\gamma) \right)$$

The different parameters used in this equation are

$E$	-	incident particle energy $\gamma Mc^2$	MeV
$x$	-	mass per unit area	$\text{g cm}^{-2}$
$N_A$	-	Avogadro's number	$6.022\ 140\ 857(74) \times 10^{23} \text{ mol}^{-1}$
$c$	-	speed of light in vacuum	$299\ 792\ 458 \text{ m s}^{-1}$
$\mu_0$	-	permeability of free space	$4\pi \times 10^{-7} \text{ N A}^{-2}$
$\epsilon_0$	-	permittivity of free space $\epsilon_0 = 1/\mu_0 c^2$	$8.854\ 187\ 817\dots \times 10^{-12} \text{ F m}^{-1}$
$\alpha$	-	fine structure constant $\alpha = e^2/4\pi\epsilon_0\hbar c$	$1/137.035\ 999\ 139(31)$
$r_e$	-	classical electron radius $r_e = e^2/4\pi\epsilon_0 m_e c^2$	$2.817\ 940\ 3227(19) \text{ fm}$
$e$	-	elementary charge of the electron	$-1.6021766208(98) \times 10^{-19} \text{ C}$
$m_e c^2$	-	electron mass $\times c^2$	$0.510\ 998\ 9461(31) \text{ MeV}$
$K$	-	constant defined as $K = 4\pi N_A r_e^2 m_e c^2$	$0.307\ 075 \text{ MeV mol}^{-1} \text{ cm}^2$
$z$	-	charge number of incident particle	
$Z$	-	atomic number of absorbing medium	
$A$	-	atomic mass of absorbing medium	$\text{g mol}^{-1}$
$\beta$	-	velocity of particle $\beta = v/c$	
$\gamma$	-	Lorentz factor $\gamma = (1 - \beta^2)^{-1/2}$	

$W_{max}$	-	maximum energy transfer through a single collision	MeV
$I$	-	mean excitation energy of absorbing medium	eV
$\delta(\beta\gamma)$	-	density effect correction to ionization energy loss	

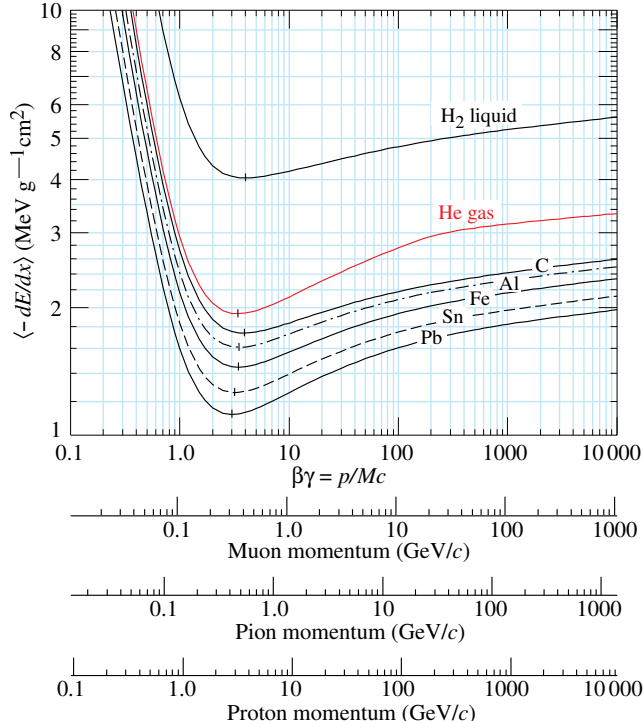


Figure 4.24: Mean mass stopping power for liquid hydrogen, as used in bubble chambers, gaseous helium, carbon, aluminum, iron, tin, and lead without the inclusion of radiative effect at higher  $\beta\gamma$  necessary for pions and muons in denser materials [115].

In this equation, the maximum energy transfer  $W_{max}$  is defined as function of the incident particle mass  $M$ , expressed in MeV/c<sup>2</sup>

$$(4.6) \quad W_{max} = \frac{2m_e c^2 \beta^2 \gamma^2}{1 + 2\gamma m_e / M + (m_e / M)^2}$$

and the mean excitation energy  $I$  depends on the absorber. Its determination is non-trivial but recommendations are given by the International Commission on Radiation Units & Measurements (ICRU) based on experimental measurements and interpolations as showed in Figure 4.25.

For the case of copper, the mean stopping power is visible in Figure 4.23. The mean stopping power corresponding only to the Bethe range for other materials is given in Figure 4.24 and shows that  $\langle -dE/dx \rangle$  is similar for each material with a slow decrease with  $Z$ . The factor affecting the equation the most is  $\beta$  as the dependence on  $M$  is introduced at higher energies in the logarithm via the max transfer energy per single collision but in most practical cases, only the dependence on  $\beta$  is considered as most of the relativistic particles are closest to the lowest mean energy loss rate and are

referred to as minimum ionizing particles (mip's). The almost logarithmic relation in between the mean energy loss rate for minimum ionizing particles and  $Z$  is showed in Figure 4.26.

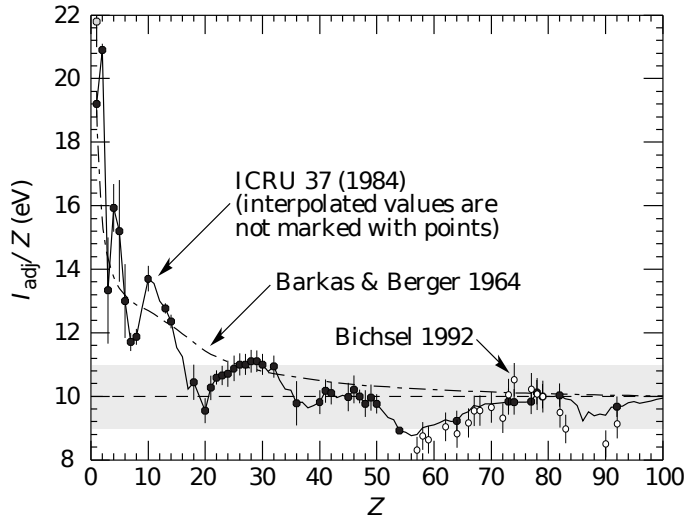


Figure 4.25: Mean excitation energies normalized to the atomic number as adopted by the ICRU [115, 241, 242].

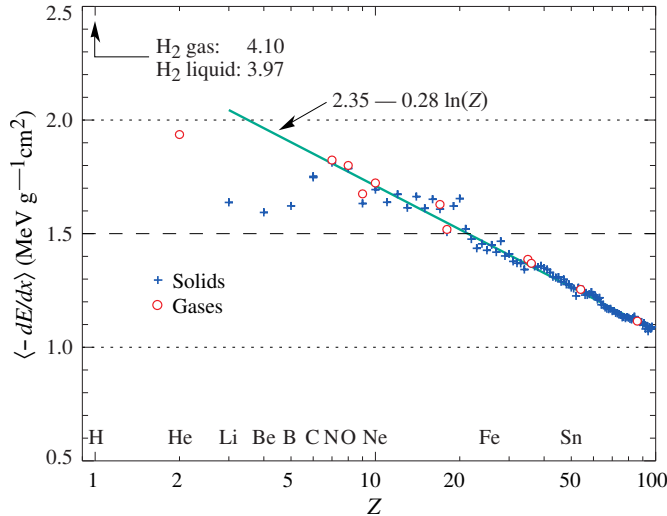


Figure 4.26: Mean mass stopping power at minimum ionization as a function of the atomic number [115].

Finally, the term  $\delta(\beta\gamma)/2$  corresponds to the density effect correction introduced to account for the polarization of a real media that limits the spatial extension of the electric field of relativistic particles. Indeed, as the energy of a particle increases, the associated electric field will flatten and extend. Due to this effect, the distant collision contribution to Equation 4.5 will increase as  $\ln(\beta\gamma)$  but the polarization of the media truncates this rise. At high energies, the correction is given by

2730 Equation 4.7

$$(4.7) \quad \delta/2 \longrightarrow \ln(\hbar\omega_p/I) + \ln(\beta\gamma) - 1/2$$

2731 where  $\hbar\omega_p$  represents the plasma energy that depends on the electron density of the media and  
 2732 the electron mass and can be calculated as  $\sqrt{\rho\langle Z/A\rangle} \times 28.816$  eV. The introduction of this cor-  
 2733 rection term reduces the increase of the mean stopping power at higher energies as can be seen in  
 2734 Figure 4.23. Moreover, due to poorer electron density, the effect is less visible on gases than on  
 2735 liquids and solids has can be seen from Figure 4.24.

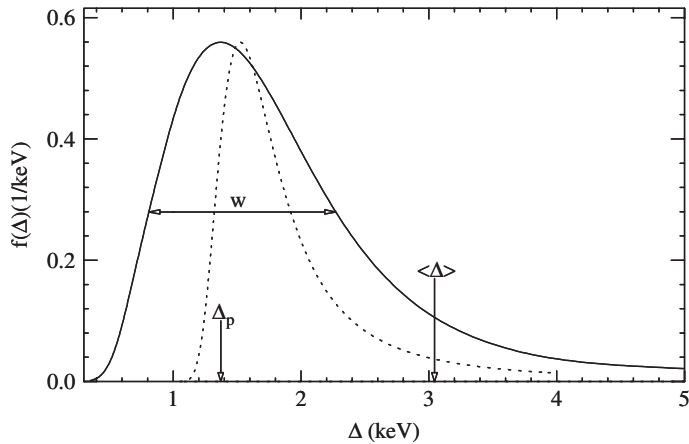


Figure 4.27: Example of straggling function  $f(\Delta)$  of particles passing through 1.2 cm of Argon gas with a  $\beta\gamma$  of 3.6 and represented with a solid line. The original Landau distribution is showed with a dashed line [243].

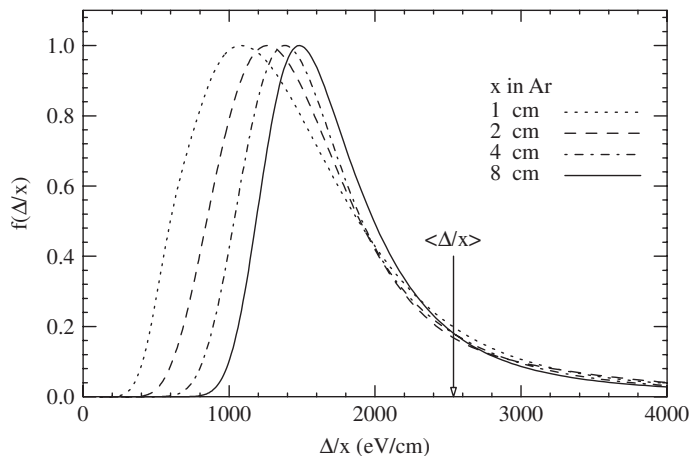


Figure 4.28: Evolution of straggling functions  $f(\Delta)$  of particles passing through a volume of Argon gas with a  $\beta\gamma$  of 3.6 with increasing thickness  $x$  [243].

2736 The mean energy loss per collision can be difficult to measure for low data samples but is not  
 2737 always representative of the energy loss distribution for a given incident particle energy. Hence, it is

2738 easier to access the most probable energy loss which is a lower value than than the average loss due  
 2739 to the distribution of the energy transfer. This value is well described by a highly skewed Landau  
 2740 distribution for detectors with "moderate" thickness  $x$ , expressed in g mol $^{-1}$ . But for gas volumes,  
 2741 a Landau distribution greatly underestimates the width  $w$  of the distribution and only succeeds to  
 2742 provide with a correct value for the most probable energy loss, as showed in Figure 4.27. Thus,  
 2743 the energy loss distribution is better represented by its most probable energy loss  $\Delta_p$  and its full-  
 2744 width-at-half-maximum (FWHM)  $w$ . As showed by Figure 4.28, the distribution is affected by  
 2745 the thickness of the gas volume and the most probable energy loss normalized to the thickness is  
 2746 increased and the width decreased, converging towards the Landau distribution, whereas the mean  
 2747 energy loss is unchanged. Corrections are brought to the original Landau equation in order to account  
 2748 better for the number of collisions leading to an increased width of the energy loss distribution [243].

2749 In the case of gas mixtures, composed of several elements, using Bragg additivity it can be  
 2750 understood that the mean energy loss of the mixture is the sum of the mean energy losses in each  
 2751 individual element  $j$  layer of weight  $w_j$ .

$$(4.8) \quad \left\langle \frac{dE}{dx} \right\rangle = \sum w_j \left\langle \frac{dE}{dx} \right\rangle_j$$

### 2752 4.3.2 Primary ionization

2753 Using Bethe formula to understand the mean energy transfer of charged particles when traveling  
 2754 through a gas volume give an intuition of the physics that affect the particle but doesn't provide a  
 2755 detailed enough information about the individual ionizations along its tracks at a microscopic level.  
 2756 In order to simulate efficiently an RPC and hence understand the processes governing avalanches  
 2757 creation and growth, knowledge on the ionization process is necessary.

2758 To convert the energy loss rate into a number of primary ionizations was developed in 1980 the  
 2759 Photo-Absorption Ionisation (PAI) model [244] based on the cross section of ionization of gas atoms  
 2760 to real photons and the dielectric constant of the medium through which the charged particles are  
 2761 going. Indeed, the interaction of charged particles with the gas molecules being of electromagnetic  
 2762 nature, it is mediated by quasi-real photons and, hence, the cross section to photon ionization is  
 2763 important to understand. This approach is nevertheless semi-classical as it relies on classical elec-  
 2764 trodynamics and it only gives access to the energy transfer to the gas atoms and no information on  
 2765 the energy dissipation and secondary emissions is available on the output of the model. The energy  
 2766 transferred to the medium is not all used for ionization. For an energy deposition  $\Delta$ , the number of  
 2767 electron-ion pairs produced is:

$$(4.9) \quad \Delta = n_i W$$

2768  $W$  corresponds to the mean work per pair production that depends on the medium and is greater  
 2769 than the ionization potential leading to the conclusion that part of the transferred energy is dissipated  
 2770 through other processes [239, 245]. In order to understand the energy dissipation and the secondary  
 2771 emissions, the fine structure of each atom is taken into account. Through the PAI model, the incident  
 2772 charged particle interacts is assumed to interact with the full atom rather than with a single electron.

2773 Although, considering that the particle interacts with a single electron, leads to the possibility to  
 2774 study the excited state of the atom once the photo-electron has been emitted with an energy corre-  
 2775 sponding to the transferred energy minus the binding energy of the electronic shell. The resulting

vacancies in the electronic shell will be filled through emission of photons or Auger electrons and can contribute to further ionization or excitation in the gas volume. Fluorescence photons are usually not considered as they only constitute a very small fraction of secondary emissions [246]. Assuming that the transferred energy is absorbed in its totality by a single electronic shell, the PAI model was modified to include relaxations and constitute the new Photo-Absorption Ionisation with Relaxation (PAIR) model [246]. In this model, the cross section corresponding to the whole atom is re-expressed using a sum of partial cross sections corresponding to the different electronic shells. When one or more electrons are knocked out of the atom, the vacancies are filled by electrons of the shell above with relaxation by Auger electron emission. These processes happen in cascade from the inner shell to the outer one until all the vacancies are filled and the energy has been released.

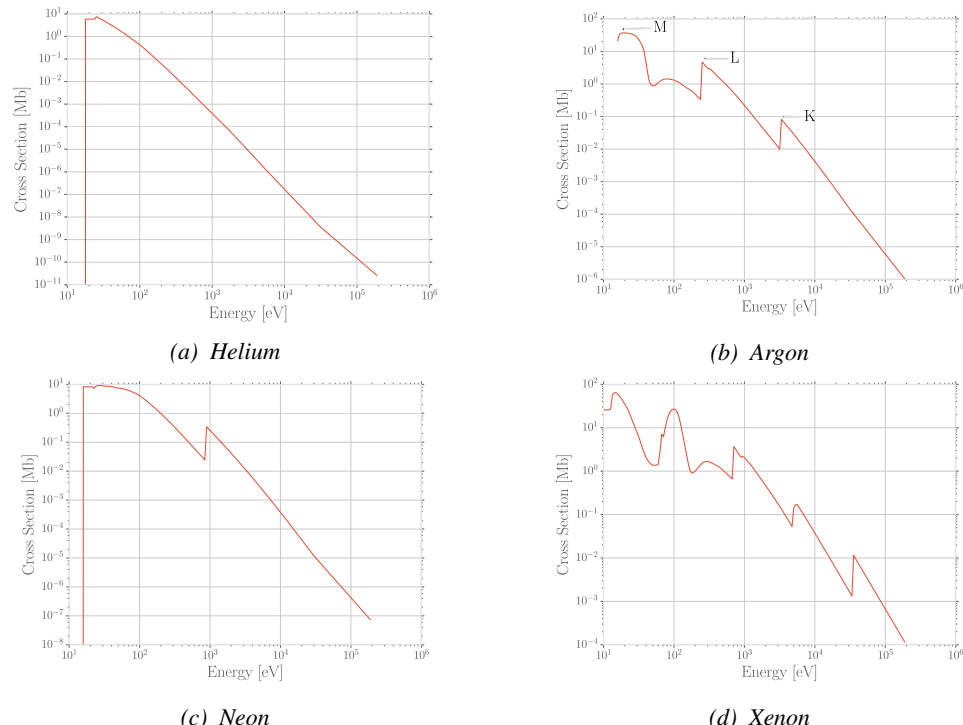


*Figure 4.29: Photoabsorption cross section as computed by HEED for noble gases with different electric shell numbers [239].*

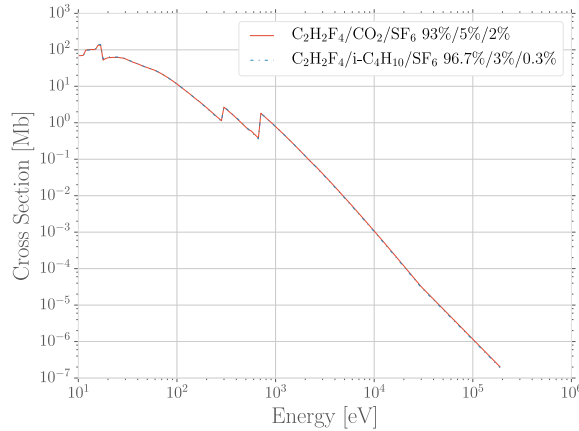


Figure 4.30: Photoabsorption cross section as computed by HEED for typical RPC gas mixtures [239]. The RPC mixture with CO<sub>2</sub> corresponds to the mixture used by CALICE SDHCAL [247] while the other one was foreseen for the experiment ATLAS [248] but has been changed since then.

This model is included in the program HEED developed at CERN [249] and called by Garfield, a program developed for the simulation of gaseous detectors. The results for the cross section for a few noble gases are given in Figure 4.29. It can be seen that for each shell, the cross section is increased. More complex patterns are seen with bigger atoms such as Xenon on Figure 4.29d. For gas mixtures, like the typical RPC mixtures, the cross section is showed in Figure 4.30. Both mixtures being mainly composed of C<sub>2</sub>H<sub>2</sub>F<sub>4</sub>, the variations in between the 2 cross section profiles are very subtle and depends on the concentration of the other compounds.

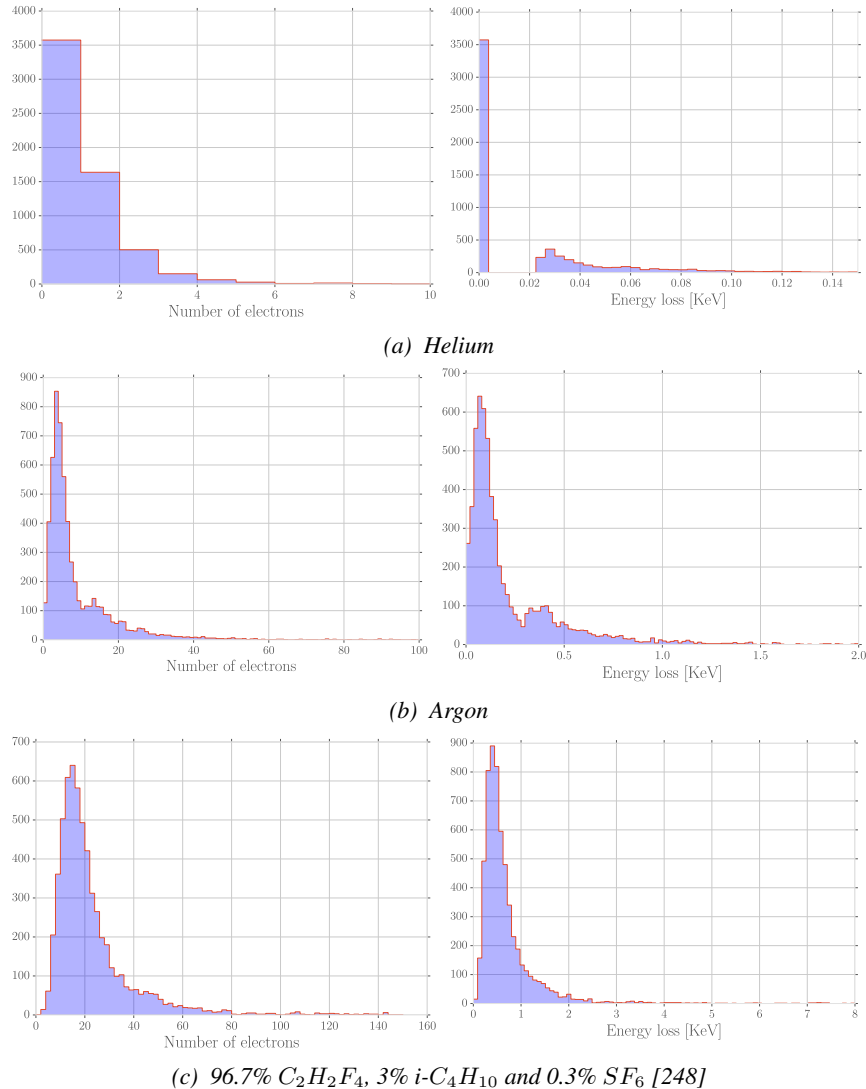


Figure 4.31: Distributions of number of electrons (left) and energy loss (right) for a 5 GeV/c muon passing through 1.2 mm of Helium (Figure 4.31a), Argon (Figure 4.31b) or a typical RPC gas mixture (Figure 4.31c) [239].

Once the cross section of interaction is known, it is possible to extract the distribution of energy loss and of the number of produced electrons, as showed in Figure 4.31 for Helium, Argon, which is used in gaseous detectors, and for a typical RPC mixture [239]. The distributions are computed using HEED and show typical straggling function profiles with some complex structures that can be related to interaction of the incoming particle with the different electronic shells. Helium does not have a great photoabsorption cross-section according to Figure 4.29a and a muon will not be likely to lose a lot of energy and to create a lot of electrons whereas in a more complex atom like Argon, the cross-section is greater and will lead to a greater energy loss of muons and more electron produced. Finally, a complex gas mixture used in RPCs will offer an even greater cross-section, a wider energy loss distribution and will be able to produce more electrons. The same information is seen by looking

at the evolution of the mean number of clusters as a function of the lorentz factor associated to muons showed in Figure 4.32a. Indeed, the greater photoabsorption cross-section of RPC mixtures allows for a much greater number of clusters to be created by charged particles. The size of these clusters is studied through Figure 4.32b which shows that, in most of the cases ( $\approx 80\%$ ), the clusters only are composed of a single electron which is consistent with minimum ionizing particles.

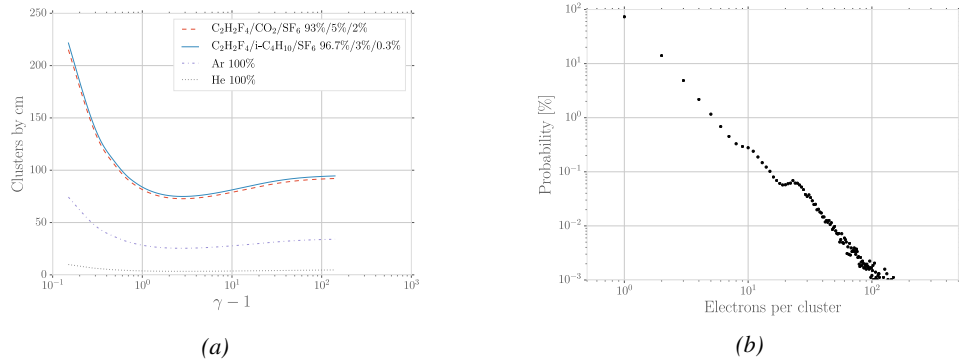


Figure 4.32: Figure 4.32a: Mean cluster density for muons through different gas volumes [239]. Figure 4.32b: Distribution of the number of electrons per cluster for a 5 GeV/c muon traveling through a mixture of 96.7%  $C_2H_2F_4$ , 3%  $i-C_4H_{10}$  and 0.3%  $SF_6$  [239, 248].

### 4.3.3 Development and propagation of avalanches

From the clusters released in the gas volume by the charged particles, free electrons will start drifting due to the electric applied in between the electrodes of the RPC. Gaining velocity and energy, these electrons in their turn will be able to ionize the gas. This process being repeated by all the produced electrons will trigger an avalanche to develop.

The growth of the avalanche can be intuitively understood as a competition between two effects. Due to their increasing energy, electrons have a probability to trigger new ionizations by interacting with gas molecules. On the other hand, before the minimal amount of energy is reached, the electrons can get attached to a gas molecule instead. These two effects can be described using a simple model in which the multiplication and attachment processes are given by the Townsend coefficient  $\alpha$  and the attachment coefficient  $\eta$ , assuming that the history of previous interactions in the gas does not influence new interactions. This model simply takes into account probabilities to have at the gas depth  $z$ , for a given number  $n$  of free electrons in the gas,  $n+1$  or  $n-1$  electrons at the depth  $z+dz$  (respectively  $n\alpha dz$  and  $n\eta dz$ ). Then, the mean number of electrons  $\bar{n}$  and cations  $\bar{p}$  can be written for single compound gases as

$$(4.10) \quad \frac{d\bar{n}}{dz} = (\alpha - \eta)\bar{n}, \quad \frac{d\bar{p}}{dz} = \alpha\bar{n}$$

which, assuming the initial conditions  $\bar{n}(0) = 1$  and  $\bar{p}(0) = 0$ , lead to the mean number of electrons and cations at a depth  $z$

$$(4.11) \quad \bar{n}(z) = e^{(\alpha-\eta)z}, \quad \bar{p}(z) = \frac{\alpha}{\alpha-\eta} \left( e^{(\alpha-\eta)z} - 1 \right)$$

2825 The Townsend and attachment coefficient as a function of the applied electric field are given in  
 2826 Figure 4.33 for a standard RPC gas mixture using Magboltz [250].

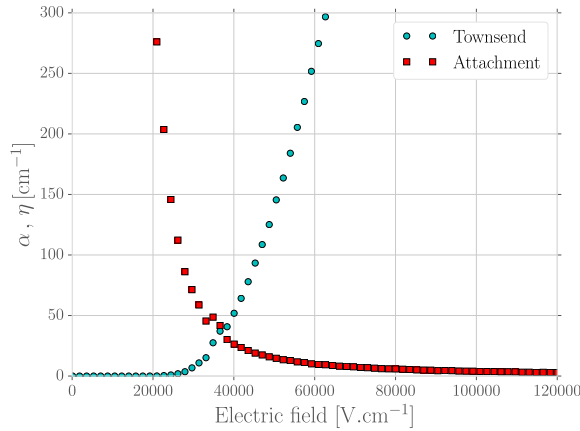


Figure 4.33: Townsend and attachment coefficient for a typical 96.7/3/0.3 mixture of  $C_2H_2F_4/i-C_4H_{10}/SF_6$ , at a temperature  $T = 296.15\text{ K}$  and a pressure  $P = 1013\text{ hPa}$  [239, 248].

2827 Nevertheless, there are more to the avalanche growth than simply these two factors. Throughout  
 2828 the 20<sup>th</sup> century, models have been developed to better understand the physics of discharges in gas.  
 2829 In 1937, Furry developed a model to describe electromagnetic cascades [251] that would be used for  
 2830 electron avalanches in gas during the 1950s. Furry realized that the use of a Poisson law to describe  
 2831 the distribution of shower sizes could not be accurate as he understood that the events occurring in  
 2832 the development of a cascade are not independent from each other, as a Poisson law would suggest.  
 2833 Indeed, part of the particles produce others and this process depends on both their original energy  
 2834 and energy lost. Experimental results showed excess of small showers and an under estimate of very  
 2835 large ones. To solve this problem, Furry proposed a distribution of sizes of following the likelihood  
 2836 described in Equation 4.12, in which  $\bar{n} = e^{\alpha z}$ , compared with a Poisson law in Figure 4.34.

$$(4.12) \quad P(n, \bar{n}) = \bar{n}^{-1}(1 - \bar{n}^{-1})^{n-1}$$

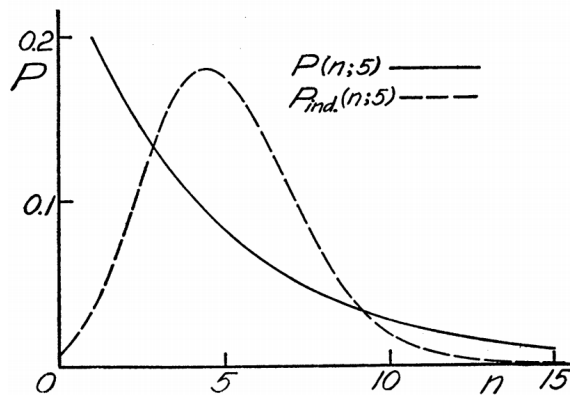


Figure 4.34: Comparison of the distribution law of Furry and the Poisson law for  $\bar{n} = 5$  [251].

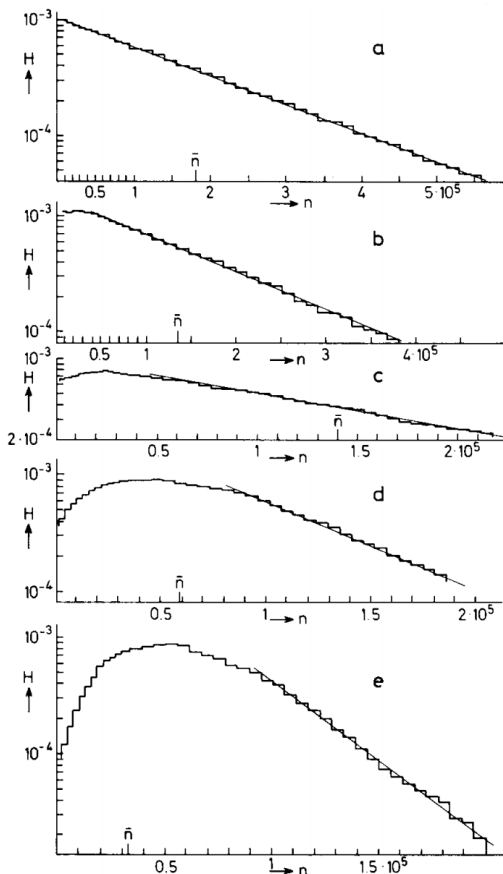


Figure 4.35: Single-electron avalanche size distribution in a proportional counter filled with methylal at different  $E/p$  values. (a) 70, (b) 76.5, (c) 105, (d) 186.5, (e) 426V/cm torr [252].

In this model, no extra energy is brought to the electrons in the showers, contrary to the case of a gaseous detector such as an RPC where an electric field accelerates them. Using the Furry model, Genz studied the fluctuations in electron avalanches in gaseous detectors [252]. Collisions leading to ionizations leave electrons with an energy much smaller than the ionization energy  $eU_i$ , where  $U_i$  is the ionization potential of a gas molecule. Hence, the electrons need to travel a distance  $s = U_i/E$  along the electric field  $E$  to acquire a high enough energy to trigger a new ionization. For the probability of a new ionization to be independent from the path followed by the electrons since the previous ionization, the mean free path  $1/\alpha$  of electrons in the gas has to be large compared to  $s$  and thus  $E/\alpha \gg U_i$ . The Townsend coefficient is related to the gas pressure leading to conditions on the value of  $E/p$ . Avalanches in gas are large compared to the showers Furry has studied in his original paper. For very large avalanche sizes, Equation 4.12 can be written as an exponential, as showed in Equation 4.13.

$$(4.13) \quad P(n, \bar{n}) = \bar{n}^{-1} e^{-n/\bar{n}}$$

This exponential behaviour is showed through Figure 4.35. In practice, to fully understand the avalanche growth, taking into account the path followed by electrons from one ionization to another

will become necessary. In the same paper, Genz then discusses models using Polya distributions to estimate the multiplication by looking at the size of the avalanche it self. Indeed, the number of charge carriers in the avalanche might become important enough to have an effect on the multiplication process. To account for this, it was proposed to use a varying Townsend coefficient such as described by Equation 4.14 depending on the position  $x$  in which  $\theta$  is an empirical parameter leading to the probability distribution of Equation 4.15. In the limit case where  $\theta$  goes to 0, the formula describes again the Furry model. But the data deviates from this model as well at large  $n$  values. Moreover, the introduction of an empirical parameter makes the model hard to interpret physically.

$$(4.14) \quad \alpha(n, x) = \alpha(x) \left(1 + \frac{\theta}{n}\right), \quad n > 0$$

$$(4.15) \quad P(n, x) = \frac{1 + \theta}{\bar{n}} \frac{1}{\theta!} \left(\frac{n(1 + \theta)}{\bar{n}}\right)^{\theta} e^{-\frac{n(1 + \theta)}{\bar{n}}}$$

In order to have a model that describes reality better, the introduction of the attachment into the model is an important step. Despite its limitations, the Furry model had the advantage to well describe avalanches occurring when the attachment could be ignored. This is only natural that this model was then extended to included attachment. This was done by Riegler, Lippmann and Veenhof [248] which showed that what was important was to consider both the Townsend coefficient describing the multiplication *and* the attachment coefficient, not only the effective multiplication coefficient  $\bar{\alpha} = \alpha - \eta$ . The probability to see an avalanche started by a single electron grow to a size  $n$  after having traveled a distance  $z$  through the gas is given by Equation 4.16.

$$(4.16) \quad \begin{aligned} P(n, z) = & P(n-1, z) (n-1)\alpha dz (1 - (n-1)\eta dz) \\ & + P(n, z) (1 - n\alpha dz) (1 - n\eta dz) \\ & + P(n, z) n\alpha dz n\eta dz \\ & + P(n+1, z) (1 - (n+1)\alpha dz) (n+1)\eta dz \end{aligned}$$

The first term of this probability that from a state with  $n-1$  electrons, only 1 multiplies while the others don't get attached. Both the second and third terms describes the probability that from a state with already  $n$  electrons the total number of electrons stay the same. On the second term, no electron gets attached nor multiplies while on the third term, 1 electron gets multiplied and 1 gets attached to compensate. Finally, the fourth term describes the probability to fall from a state with  $n+1$  to a state with  $n$  electrons due to the attachment of a single electron. At the first order, the evaluation of the previous expression leads to Equation 4.17 which general solution is given in Equation 4.18 in which are introduced the variables  $\bar{n}(z)$ , defined as in Equation 4.11, and  $k = \eta/\alpha$  making explicit the fact that the distribution does not depend on the effective Townsend coefficient only.

$$(4.17) \quad \frac{dP(n, z)}{dz} = -P(n, z)n(\alpha + \eta) + P(n-1, z)(n-1)\alpha + P(n+1, z)(n+1)\eta$$

$$(4.18) \quad P(n, z) = \begin{cases} k^{\frac{\bar{n}(z)-1}{\bar{n}(z)-k}}, & n = 0 \\ \bar{n}(z) \left(\frac{1-k}{\bar{n}(z)-k}\right)^2 \left(\frac{\bar{n}(z)-1}{\bar{n}(z)-k}\right)^{n-1}, & n > 0 \end{cases}$$

The example given through Figure 4.36 shows the importance of each individual process in the growth of avalanches and the fluctuation of their size. The values of  $\alpha$  and  $\eta$  will influence the probability distribution, as can be seen from Figure 4.36a. Then, Figure 4.36b shows that the fluctuation really takes place within the very first interactions. Indeed, when the avalanche contains a large enough number of charge carriers (a few hundreds), its size then increases like  $e^{z(\alpha-\eta)}$ .

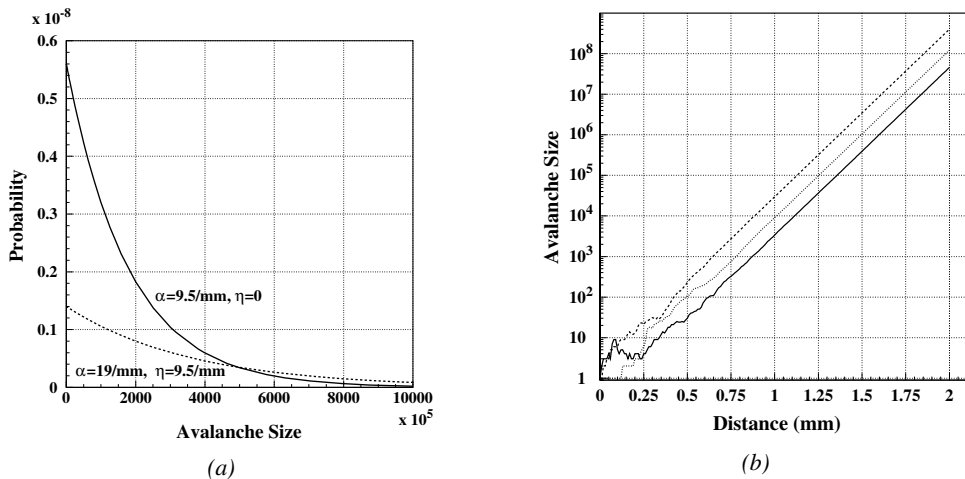


Figure 4.36: Figure 4.36a: Comparison of avalanche size distributions for different values of Townsend and attachment coefficients. The effective Townsend coefficient is the same for both distributions. Figure 4.36b: Fluctuation in avalanche size for avalanche started by a single electron with  $\alpha = 13 \text{ mm}^{-1}$  and  $\eta = 3.5 \text{ mm}^{-1}$  [248].

#### 4.3.4 Drift and diffusion of the electron cloud

During the growth of avalanches, an electron cloud drifting along the electric field through the gas will undergo thermal diffusion due to random collisions with the gas molecules. This phenomenon can be studied using Maxwell-Boltzmann distribution whose mean is defined by the thermal energy of the cloud  $\langle E \rangle = 3/2kT$  with an extra component coming from the constant drift motion. The drift of electrons along the field lines is usually observed on a macroscopic scale through which the speed can be assimilated to a constant  $v_D$  which corresponds to the mean drift speed over a large number of collisions in the gas.

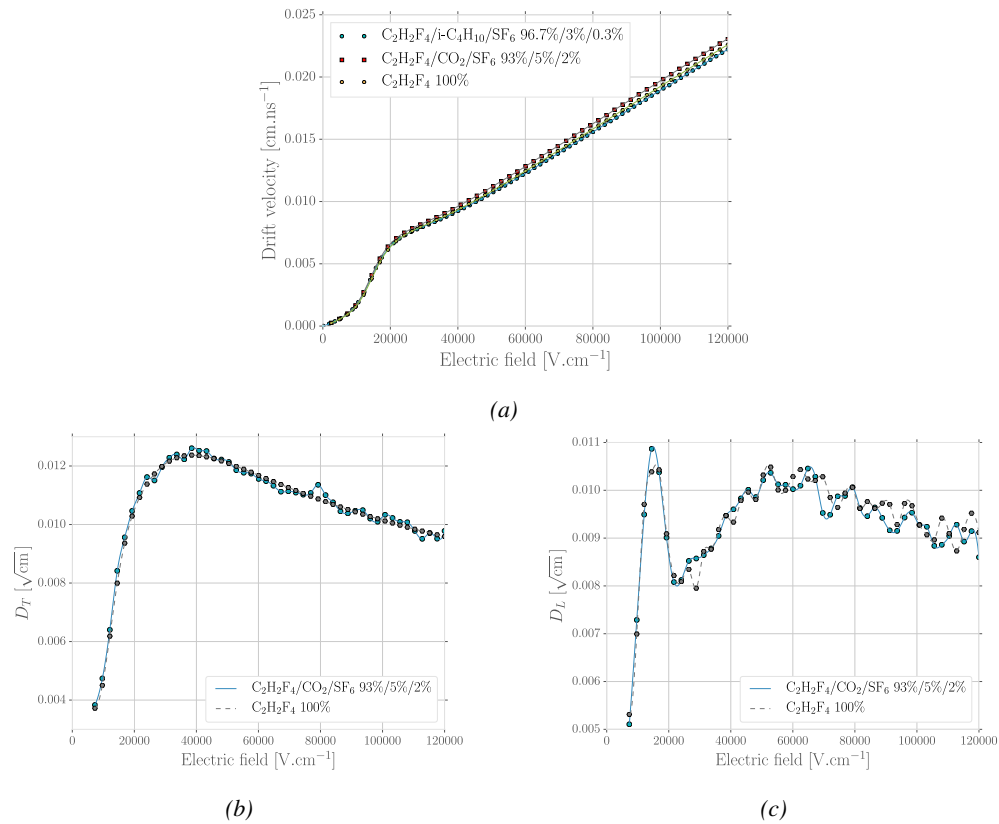


Figure 4.37: Figure 4.37a: Electrons mean drift velocity  $v_D$  in pure  $C_2H_2F_4$  and typical RPC gas mixtures. Figure 4.37b: Transverse diffusion coefficient in pure  $C_2H_2F_4$  and a typical RPC gas mixture. Figure 4.37c: Longitudinal diffusion coefficient in pure  $C_2H_2F_4$  and a typical RPC gas mixture. All results are given with a pressure  $P = 760$  Torr and a temperature  $T = 296.15$  K [239].

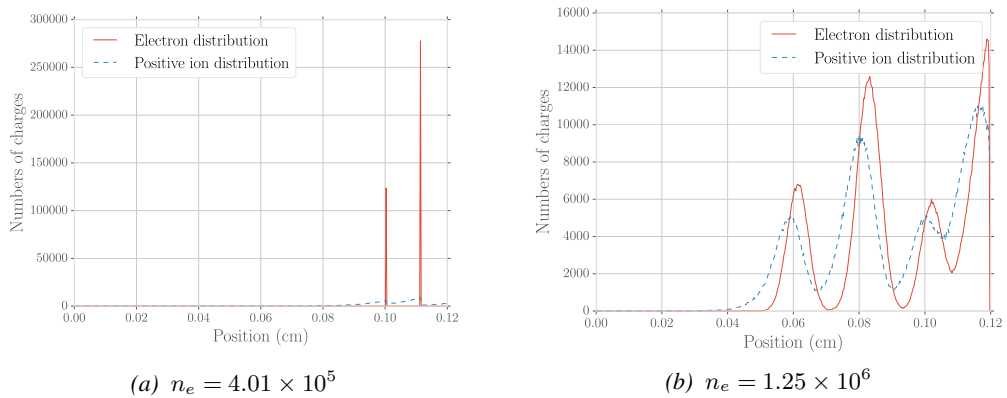


Figure 4.38: Comparison of the free charge carriers in the gas after a time  $t = 7.90$  ns in the case where no diffusion is taken into account to simulate the avalanche (Figure 4.38a) and in the case where the diffusion is implemented (Figure 4.38b) [239].

Indeed, at the microscopic scale, the electrons are drifting over a distance  $\delta z$  while acquiring the corresponding kinetic energy  $T = e_0 |\vec{E}| \delta z$  until they are slowed down by a collision in which they lose part of their energy. This process is repeated as long as electrons are free carriers. Starting from a point-like electron cloud, the Gaussian density distribution at  $\vec{r}_0$  will be described by Formula 4.19 in which the width of the isotropic distribution is  $\sigma = 2\bar{D}t$ , with  $\bar{D}$  being a diffusion coefficient expressed in  $\text{m}^2/\text{s}$  [221].

$$(4.19) \quad \varphi(\vec{r}, t) = \frac{1}{(\sqrt{2\pi}\sigma(t))^3} \exp\left(-\frac{(\vec{r} - \vec{r}_0)^2}{2\sigma^2(t)}\right)$$

Now, if the constant drifting motion is added, the distribution is anisotropic and can be divided onto transversal (Formula 4.20) and longitudinal (Formula 4.21) terms,  $\varphi(r, z, t) = \varphi_T(r, t)\varphi_L(z, t)$ , with a cylindrical symmetry around the field axis [221]. The variables  $t$  and  $\sigma_{T,L}(t)$  can be hidden to the profit of the diffusion coefficients by using the relations  $v_D = l/t$  and  $\sigma_{T,L}^2(t) = 2\bar{D}_{T,L}l/v_D$  and introducing new diffusion coefficients  $D_{T,L} = \sqrt{2\bar{D}_{T,L}/v_D}$  in order to explicitly show the dependence of the Gaussian width in drifted distance  $l$ .

$$(4.20) \quad \varphi_T(r, t) = \frac{1}{D_T^2 l} \exp\left(-\frac{(r - r_0)^2}{2D_T^2 l}\right)$$

$$(4.21) \quad \varphi_L(z, t) = \frac{1}{\sqrt{2\pi l} D_L} \exp\left(-\frac{(z - z_0)^2}{2D_L^2 l}\right)$$

These coefficients, as well as the drift velocity of the electrons, can be calculated thanks to Magboltz as showed in Figure 4.37. The influence of the diffusion on the distribution of charge carriers throughout the gas volume is depicted in Figure 4.38. From very localised electron clusters in the gas in Figure 4.38a, a Gaussian diffusion is then visible in Figure 4.38b. Due to the interactions with gas molecules during the drift, diffusions can occur in the forward and backward direction. Electrons diffused backward will effectively drift over a longer distance and multiply more than electrons diffused forward that will see a shorter drift length. As an effect, the avalanche develops over a longer time and extends over a greater gas volume than in the case the electron cloud is considered as point like and without diffusion. Moreover, as a side effect to the longer growth of the avalanche due to backward longitudinal diffusion, the total production of electrons is increased.

### 4.3.5 Space charge effect & streamers

Now that has been considered the basic processes that influence the development of avalanches in a gaseous detector in the previous sections, it is now important to consider the influence of the charge carriers present in the avalanche on the electric field seen by the avalanche. Indeed, each charged particle induces an electric field and it is only natural that the increasing density of electrons and ions in the detector volume will affect the electric field. Thus, parameters such as the Townsend and attachment coefficients, drift velocity or diffusion coefficients will find themselves to be modified along the gas gap length due to this effect referred to as *space charge effect*. Figure 4.39 is a more detailed version of Figure 4.1 (b) in which three electric regions are distinguished [221]. When compared to the linear electric field of strength  $E_0$  that is developed in between the detector's electrodes, the

accumulation of negative charges (electrons) on the front of the avalanche will reinforce the effective electric field in between the anode and the avalanche front. Deeper in the gas volume, the positive charges (cations) slowly drift towards the cathode and can induce together with the avalanche front opposite electric field loops. Finally, due to the density of positive charges, the electric field seen in between the ions tails and the cathode charged with negative charges is on average stronger than  $E_0$  and compensate for the locally reversed field  $E_2$ . Lippmann roughly estimated by considering that  $10^6$  charges were contained in a sphere of radius  $r_d = 0.1$  mm that the space charge effect could change the electric field by 3% and the Townsend and attachment coefficient up to 14% [221, 239].

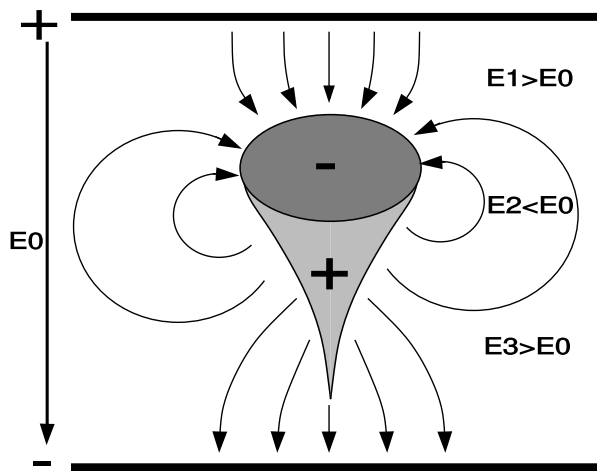


*Figure 4.39: Schematic representation of an avalanche and of the electric field deformation it causes due to the local concentration of charge carriers [221].*

To account for the space charge effect, the electric potential and field of free charges are solved and applied to each charge in the avalanche [221, 239]. As discussed by Français who has been working on simulating RPCs similar to that used by the SDHCAL project of ILC, the computation of these equations for each individual charge carrier to dynamically know the space charge field at every stage of an avalanche development is a difficult task and would require far too much computation time and a solution is to pre-compute an interpolation table keeping an adequately large number of values of the space charge field for each position in space thanks to which the values stored in the interpolation table become very close to the analytic solution and allow for a much faster simulation.

The study of space charge effect through simulation shows that it can lead to a saturation of the avalanche growth due to the deformation of the electric field, as showed through Figure 4.40. Additionally, a more precise understanding of the space charge effect is given through Figure 4.41 which looks at the distribution of charges and the distortion of the electric field at different steps of the evolution of an avalanche in a RPC. At the moment a 5 GeV muon ionizes the gas, electron-ion pairs are created in the gas in different clusters (Figure 4.41a). Later, the first clusters have reached the anode while the clusters that were created closest to the cathode are now big enough to start influencing the electric field in the gap (Figure 4.41b). When a cluster is big enough, the electric field in front of it locally increases a lot and contributes to a stronger but very localised multiplication. At the same moment, the positive ions right behind the cluster avalanche front decrease the electric field, saturating the electron multiplication on the tail of the electron cloud (Figure 4.41c).

2949 Finally, when all the electrons have reached the anode and are relaxing, the electric field still is very  
 2950 deformed by the distribution of both positive and negative ions in the gas volume closest to the anode  
 2951 (Figure 4.41d).

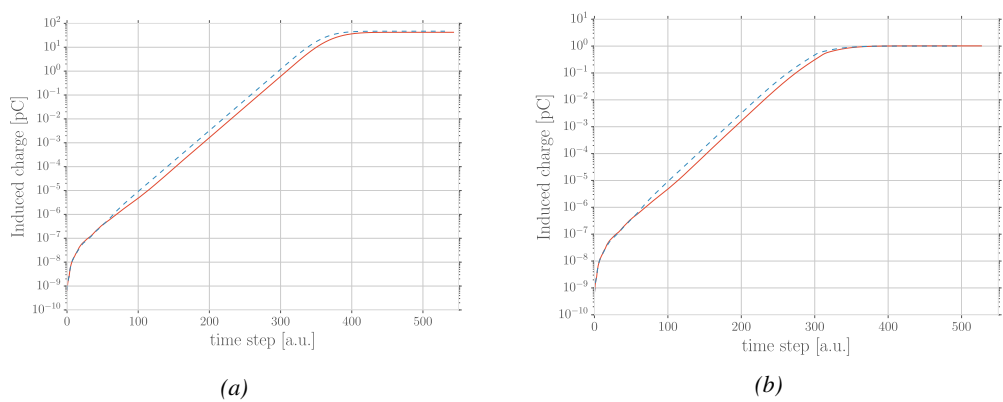


*Figure 4.40: Evolution of the charge induced by an avalanche started by a single electron in a 1.2 mm thick RPC with an applied electric field of 54 kV/cm in the case space charge is not taken into account (Figure 4.40a) and in the case it is implemented into the simulation (Figure 4.40b). The total induced charge is correlated to the size of the avalanche [239].*

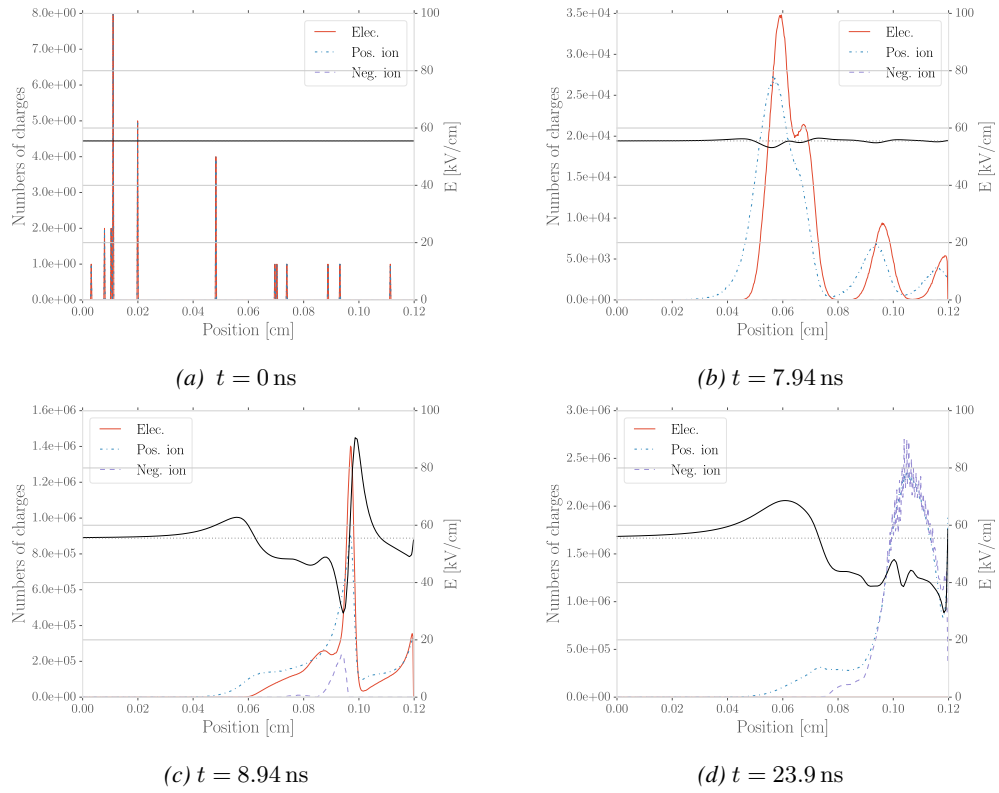


Figure 4.41: Distributions of charge carriers within the gas volume of a 1.2 mm thick RPC and the corresponding deformation of the electric field at different time steps with an applied electric field of 55.5 kV/cm [239].

2952        The electric field following the development of an avalanche can stay perturbed for a long time  
 2953        with respect to the avalanche development due to the slow drift of the much heavier ions. This can  
 2954        result in powerful secondary avalanches triggered by the fluctuation of the electric field together with  
 2955        the emission of UV-photons leading to emission of electrons at the surface of the electrode. This is  
 2956        a slow phenomenon compared to the development of avalanches. Experimentally, it is observed that  
 2957        the stronger the electric field applied over the gap, the sooner after the avalanche, referred to as *pre-*  
 2958        *cursor signal* in this context, and the stronger will the secondary avalanche be, possibly reaching the  
 2959        streamer regime. This could be due to the amount of UV-photons emitted by the growing precursor.  
 2960        These photons will be able to trigger new avalanches in a radius of a few mm around the precursor  
 2961        by knocking electrons from the cathode by photoelectric effect. The strong distortions of the electric  
 2962        field due to a large avalanche will be more likely to emit UV-photons as the electric field at the front  
 2963        of the precursor avalanche will be large, providing the electrons with a larger energy. Eventually, the  
 2964        new avalanches can grow to form streamers.

## 2965 4.4 Effect of atmospherical conditions on the detector's performance

2966

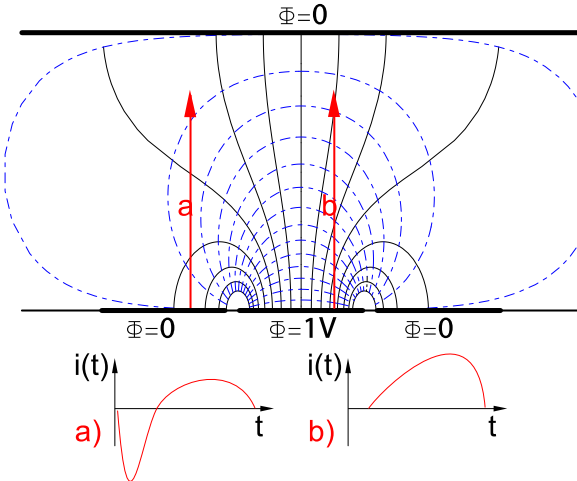


Figure 4.42: Representation of the weighting field in the volume of an RPC and the resulting induced current in the strip placed at 1 V and its neighbour connected to the ground. The induced current corresponds, as can be understood from Formula 4.22 [221].

2967 Accordingly to Ramo's theorem, the movement of charge carriers, and in particular, the movement  
 2968 of a dense electron cloud toward the anode induces a current signal on one or more of the readout  
 2969 electrodes (strips or pads). The ions on the other hand induce only a very small current as their  
 2970 movement is much slower than which of the electrons. The current induced by  $n_C l$  clusters of  $N_j(t)$   
 2971 charge carriers drifting at velocities  $\vec{v}_{Dj}(t) = \vec{x}_j(t)$  at a time  $t$  is given by Formula 4.22 in which  $e_0$   
 2972 is the unit charge and  $\vec{E}_w$  is the weighting field.

$$(4.22) \quad i(t) = \sum_{j=1}^{n_C l} \vec{E}_{wj}(\vec{x}_j(t)) \cdot \vec{v}_{Dj}(t) e_0 N_j(t)$$

2973 The weighting field, that has been schematized in Figure 4.42, corresponds to the electric field  
 2974 that would be observed in the gas gap if a readout electrode is placed at a potential of 1 V while  
 2975 keeping all the other electrodes grounded. Then the induced charge in the readout can be simply  
 2976 obtained by integrating Formula 4.22 over the duration  $T$  of the signal, as given by Formula 4.23.

$$(4.23) \quad Q(t) = \int_0^T \sum_{j=1}^{n_C l} \vec{E}_{wj}(\vec{x}_j(t)) \cdot \vec{v}_{Dj}(t) e_0 N_j(t)$$

2977 The signal induced in the readout of RPCs operated in avalanche mode is then sent into Front-  
 2978 End Electronics in which they will be pre-amplified and discriminated. The discrimination and  
 2979 digitization of signals in CMS FEE are described through Figure 4.43. On a first stage, analogic  
 2980 signals are amplified, following the curve given on Figure 4.44, and then sent to the Constant Frac-  
 2981 tion Discriminator (CFD) described in Figure 4.45. At the end of the chain, 100 ns long pulses are

sent in the LVDS output. The digital signals are both used as trigger for CMS and to evaluate the performance of the detectors. The performance will depend on the applied HV, i.e. on the electric field inside of the gas volume, but also on the threshold applied on the CFDs. Indeed, in order to reduce the probability to measure noise, the threshold is set to a level where the noise is strongly suppressed while the signals are not too affected. Typically, CMS FEEs are set to a threshold of 215 mV after pre-amplification, corresponding to an input charge of about 140 fC.

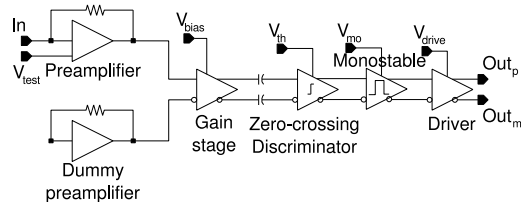


Figure 4.43: Schematics of CMS RPC FEE logic.

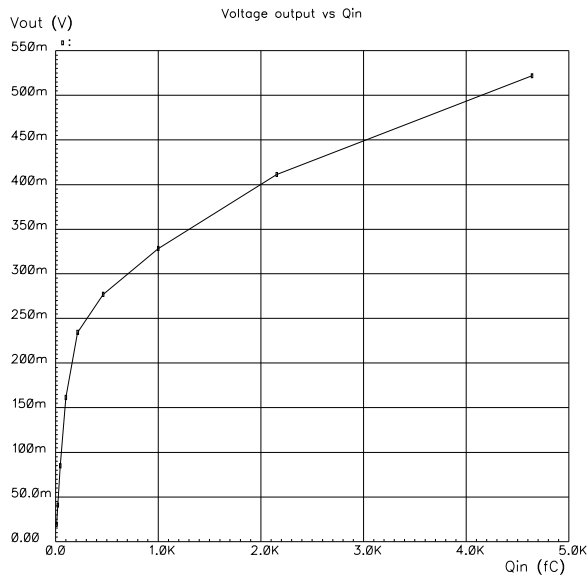
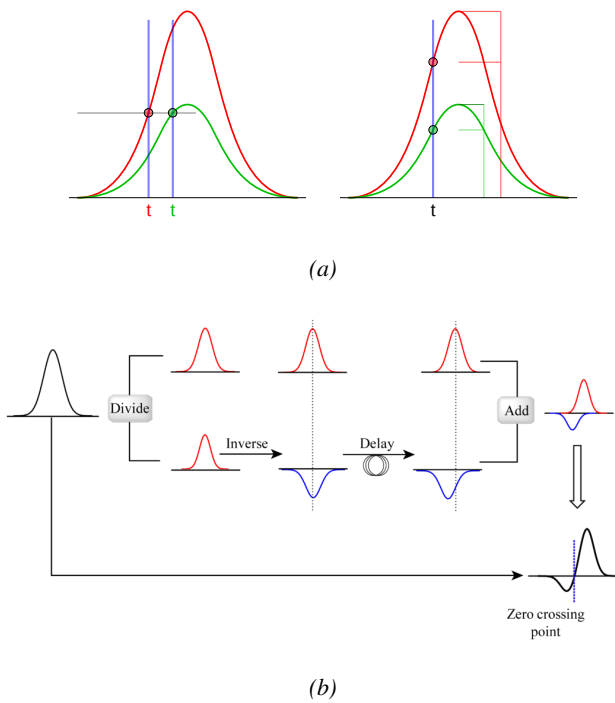


Figure 4.44: Equivalence in between the charge of the induced signal in input of the CMS FEE and the signal strength on the output of the pre-amplifier.



*Figure 4.45: Description of the principle of a CFD. A comparison of threshold triggering (left) and constant fraction triggering (right) is shown in Figure 4.45a. Constant fraction triggering is obtained thanks to zero-crossing technique as explained in Figure 4.45b. The signal arriving at the input of the CFD is split into three components. A first one is delayed and connected to the inverting input of a first comparator. A second component is connected to the noninverting input of this first comparator. A third component is connected to the noninverting input of another comparator along with a threshold value connected to the inverting input. Finally, the output of both comparators is fed through an AND gate.*

The performance of a detector is then simply measured relatively to which of a reference detector used as trigger as the ratio in between the number of events recorded in coincidence in the detector and the reference and the total number of trigger events,  $\epsilon = n_{events}/n_{triggers}$ . An example of efficiency measured as a function of the effective voltage  $HV_{eff}$  is given in Figure 4.46 and can be fitted thanks to a sigmoidal function described as in Formula 4.24 and where  $\epsilon_{max}$  is the maximal efficiency of the detector,  $\lambda$  is proportional to the slope at half maximum and  $HV_{50}$  is the value of the voltage when the efficiency reaches half of the maximum.

$$(4.24) \quad \epsilon(HV_{eff}) = \frac{\epsilon_{max}}{1 + e^{-\lambda(HV_{eff} - HV_{50})}}$$

CMS RPC also define two points on this sigmoid that called *knee* and *working point*. The corresponding voltages  $HV_{knee}$  is defined as the voltage at 95% of the maximum efficiency, and  $HV_{WP}$  is defined as in Formula 4.25.

$$(4.25) \quad HV_{WP} = HV_{knee} + \begin{cases} 100V & (\text{barrel}) \\ 150V & (\text{endcap}) \end{cases}$$

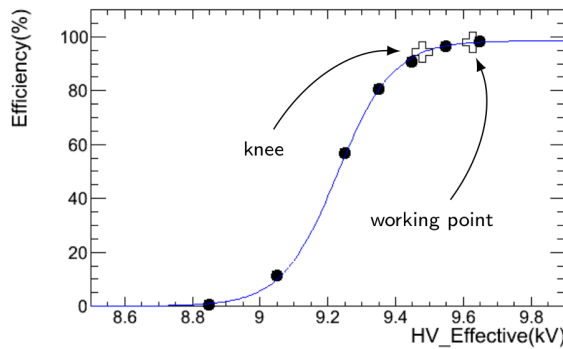


Figure 4.46: Typical efficiency sigmoid of a CMS RPC detector. The black dots correspond to the data, the blue line to the sigmoid fit and the opened cross to the knee and working extracted from the fit line.

Nevertheless, the voltage applied on a detector may vary due to a change in environmental conditions. Indeed, the variation of temperature and/or pressure will have effect on the gas density and the electrodes' resistivity which can be overcome by changing the electric field accordingly. The variation in temperature and pressure are depicted respectively in Figure 4.47 and Figure 4.48. A standard procedure to correct for temperature and pressure variations is to keep the factor  $HV \cdot T/P$  constant using Formula 4.26 [253, 254] with reference values for  $T_0$  and  $P_0$ . For example, CMS uses  $T_0 = 293.15$  K and  $P_0 = 965$  hPa.

$$(4.26) \quad HV_{app} = HV_{eff} \frac{P_0}{P} \frac{T}{T_0}$$

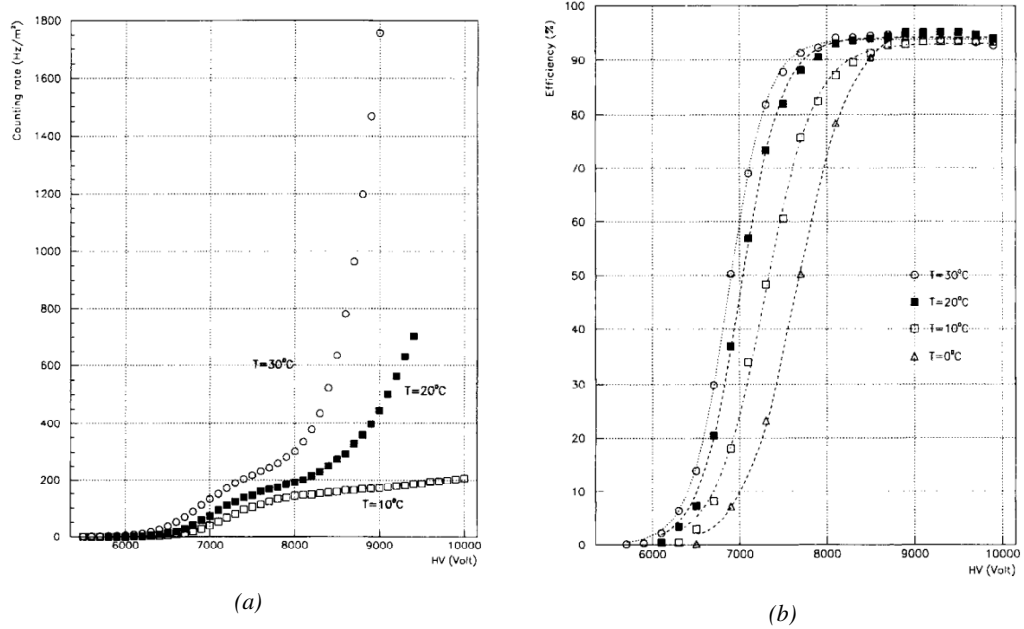
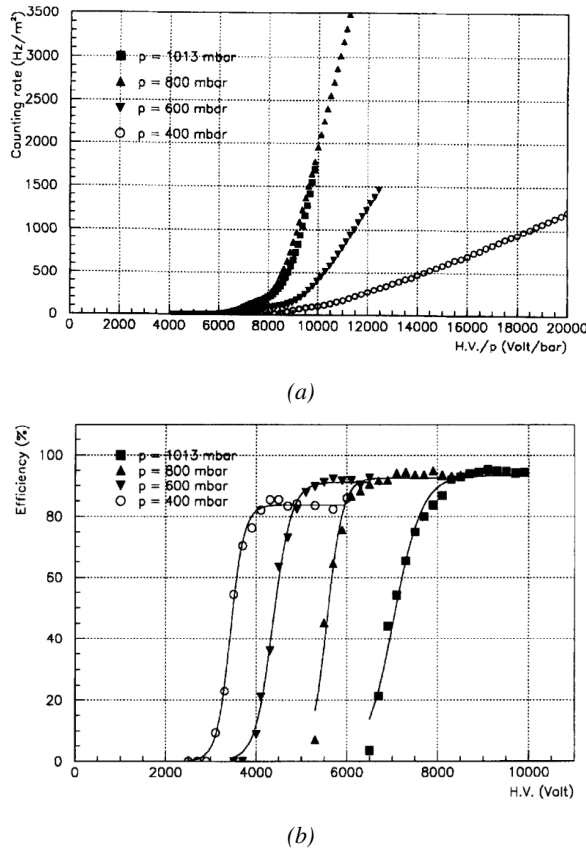


Figure 4.47: Effect of the temperature variation on the rate (Figure 4.47a) and the efficiency (Figure 4.47b) of an RPC [253].



*Figure 4.48: Effect of the pressure variation on the rate (Figure 4.48a) and the efficiency (Figure 4.48b) of an RPC [254].*

It was actually found that such a simple procedure would overcorrect the applied voltage in the case the variations of temperature or pressure were too important [255–258]. CMS, considering that the temperature variations in the detector cavern were very small, decided only to improve the pressure correction, giving rise to Formula 4.27 [255] while on the other hand, ATLAS decided to have a more robust correction for both parameters and uses Formula 4.28 instead [258]. The coefficients  $\alpha$ , in the case of CMS, and  $\alpha, \beta$ , in the case of ATLAS, are extracted from fit on available dataset obtained during the operation of the detectors.

$$(4.27) \quad HV_{app} = HV_{eff} \left( 1 - \alpha + \alpha \frac{P_0}{P} \right) \frac{T}{T_0}, \quad \alpha = 0.8$$

$$(4.28) \quad HV_{eff} = HV_{app} \left( 1 + \alpha \frac{\Delta T}{T_0} \right) \left( 1 - \beta \frac{\Delta P}{P_0} \right), \quad \alpha = 0.5, \beta = 0.71$$



# 5

3012

3013

3014

## Longevity studies and Consolidation of the present CMS RPC subsystem

3015 The RPC system, located in both barrel and endcap regions, provides a fast, independent muon trigger  
3016 with a looser  $p_T$  threshold over a large portion of the pseudo-rapidity range ( $|\eta| < 1.6$ ). During  
3017 HL-LHC operations the expected conditions in terms of background and pile-up will make the iden-  
3018 tification and correct  $p_T$  assignment a challenge for the muon system. The goal of RPC upgrade is to  
3019 provide additional hits to the Muon System with more precise timing. All this information will be  
3020 elaborated by the Trigger System in a global way enhancing the performance of the trigger in terms  
3021 of efficiency and rate control. The RPC Upgrade is based on two projects: an improved Link Board  
3022 System and the extension of the RPC coverage up to  $|\eta| = 2.4$ .

3023 The Link Board System is responsible for the processing, the synchronization and the zero-  
3024 suppression the signals coming from the RPC FEBs. The Link Board components have been pro-  
3025 duced between 2006 and 2007 and will be subjected to ageing and failure on a long term scale. An  
3026 upgraded Link Board System will overcome the ageing problems and will allow for a more precise  
3027 timing information to the RPC hits from 25 to 1.5 ns.

3028 In order to develop an improved RPC that fulfills CMS requirements, an extensive R&D program is  
3029 being conducted. The benefits of adding two new RPC layers in the innermost ring of stations 3 and  
3030 4 will be mainly observed in the neutron-induced background reduction and efficiency improvement  
3031 for both trigger and offline reconstruction.

3032 The coverage of the RPC System up to higher pseudo-rapidity  $|\eta| = 2.1$  was part of the original  
3033 CMS TDR. Nevertheless, the expected background rates being higher than the certified rate capabili-  
3034 ty of the present CMS RPCs in that region and the budget being limited, RPCs were restricted to a  
3035 shorter range. Even though the iRPC technology that will equip the extension of the Muon System  
3036 will be different than the current CMS RPC technology, it is necessary to certify the rate capability  
3037 and longevity of the existing detectors as the radiation level will increase together with the increase  
3038 of instantaneous luminosity of the LHC. For this purpose, spare RPC detectors built but not installed  
3039 in CMS have been installed in different irradiation facilities, first of all, to certify the detectors to the

3040 new levels of irradiation they will be subjected to and, finally, to study their ageing and certify their  
 3041 good operation throughout the HL-LHC program.

## 3042 5.1 Testing detectors under extreme conditions

3043 The upgrade from LHC to HL-LHC will increase the peak luminosity from  $10^{34} \text{ cm}^{-2} \text{ s}^{-1}$  to reach  
 3044  $5 \times 10^{34} \text{ cm}^{-2} \text{ s}^{-1}$ , increasing in the same way the total expected background to which the RPC  
 3045 System will be subjected to. Mainly composed of low energy gammas, neutrons, and electrons and  
 3046 positrons from  $p\text{-}p$  collisions, but also of low momentum primary and secondary muons, punch-  
 3047 through hadrons from calorimeters, and particles produced in the interaction of the beams with  
 3048 collimators, the background will mostly affect the regions of CMS that are the closest to the beam  
 3049 line, i.e. the RPC detectors located in the endcaps.

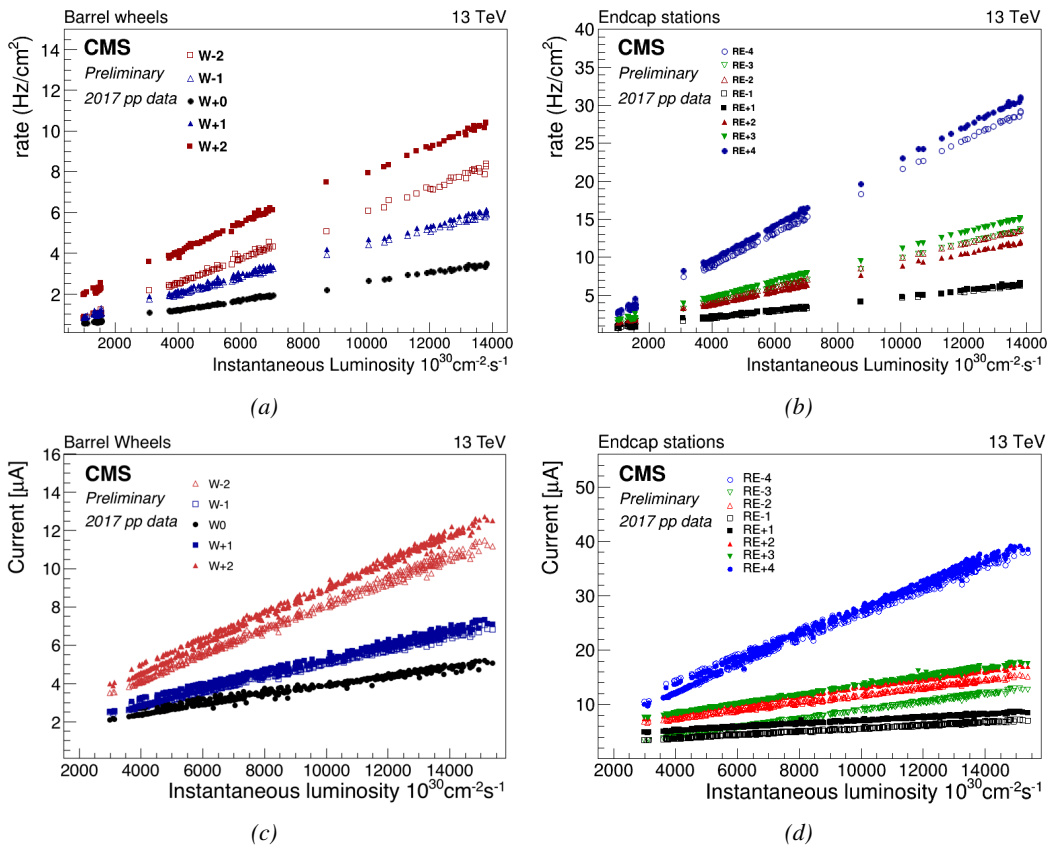


Figure 5.1: Mean RPC Barrel (left column) and Endcap (right column) rate (top row) and current (bottom row) as a function of the instantaneous luminosity as measured in 2017  $p\text{-}p$  collision data.

3050 Data collected over 2017, presented through Figure 5.1, allows to study the values of the back-  
 3051 ground rate in all the RPC System. This was achieved thanks to a monitoring of the rates in each  
 3052 RPC rolls, where rolls correspond to the pseudo-rapidity partitioning of the readout electronics, and  
 3053 of the current in each HV channel. A linear dependence in between the mean rate or current with

instantaneous luminosity is showed in selected runs with identical LHC running parameters. In Figure 5.2, a linear extrapolation of the distribution of the background hit rate per unit area as well as the integrated charge is showed at a HL-LHC condition. The maximum rate per unit area in the endcap detectors at HL-LHC conditions is expected to be of the order of  $600 \text{ Hz/cm}^2$  while the charge deposition should exceed  $800 \text{ mC/cm}^2$ . The detectors will then be certified up to an irradiation of  $840 \text{ mC/cm}^2$ . These extrapolations are provided with a required safety factor 3 for the certification study.

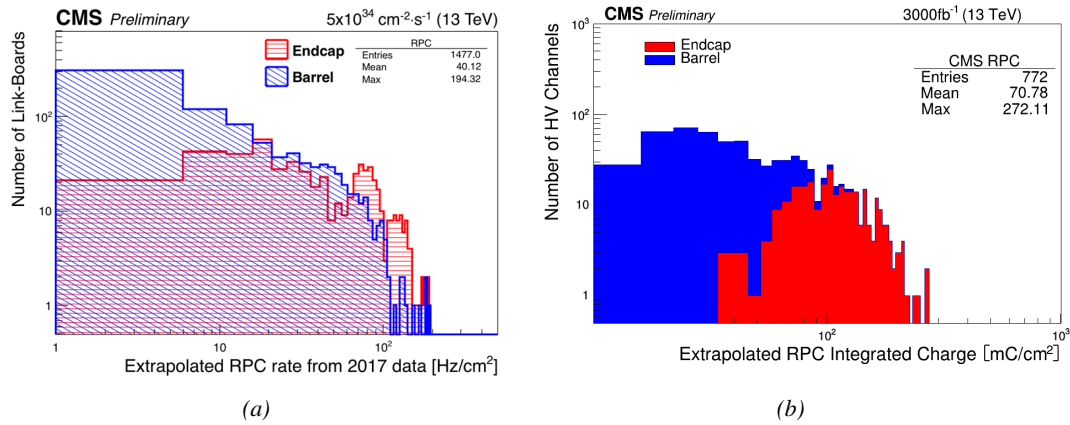


Figure 5.2: Figure 5.2a: The hit rate per region (Barrel, Endcap) is linearly extrapolated to HL-LHC highest instantaneous luminosity ( $5 \times 10^{34} \text{ cm}^{-2} \text{ s}^{-1}$ ) using the rate as a function of instantaneous luminosity recorded by RPCs in 2017 showing a linear dependence. Figure 5.2b: The integrated charge per region (Barrel, Endcap) is extrapolated to HL-LHC integrated luminosity ( $3000 \text{ fb}^{-1}$ ) using the data accumulated in 2016 in every HV channel.

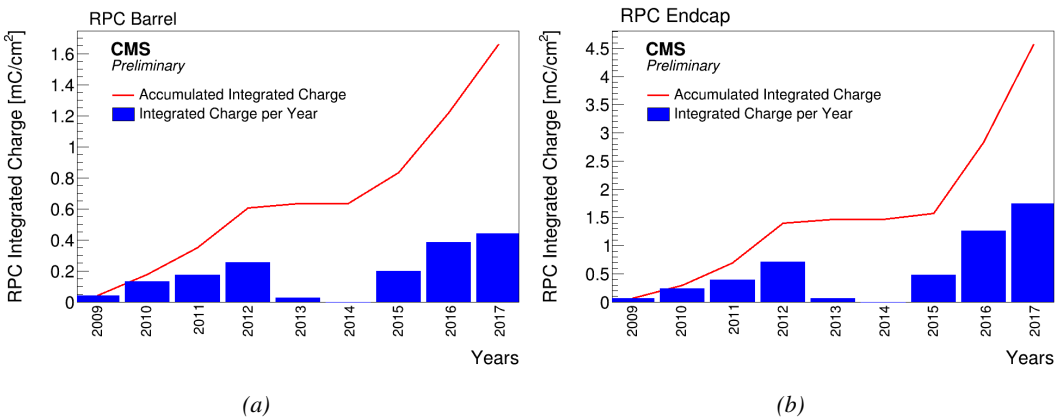


Figure 5.3: CMS RPC mean integrated charge in the Barrel region (Figure 5.3a) and the Endcap region (Figure 5.3b). The integrated charge per year is shown in blue. The red curve shows the evolution of the accumulated integrated charge through time. The blank period in 2013 and 2014 corresponds to LS1. The total integrated charge for the entire operation period (Oct.2009 - Dec.2017) is estimated to be about  $1.66 \text{ mC/cm}^2$  in the Barrel and  $4.58 \text{ mC/cm}^2$  in the Endcap.

In the past, extensive long-term tests were carried out at several gamma and neutron facilities

certifying the detector performance. Both full size and small prototype RPCs have been irradiated with photons up to an integrated charge of  $\sim 0.05 \text{ C/cm}^2$  and  $\sim 0.4 \text{ C/cm}^2$  respectively and were certified for rates reaching  $200 \text{ Hz/cm}^2$  [259, 260]. Since the beginning of Run-I until December 2017, the RPC system provided stable operation and excellent performance and did not show any ageing effects for a maximum integrated charge in a detector of the order of  $0.01 \text{ C/cm}^2$  - the average being of the order of  $2 \text{ mC/cm}^2$  in the Barrel and  $5 \text{ mC/cm}^2$  in the Endcap, closer to the beam line, as can be seen from Figure 5.3 - and a peak luminosity reaching  $1.4 \times 10^{34} \text{ cm}^{-2} \text{ s}^{-1}$  during 2017 data taking period.

To perform the necessary studies on the present CMS RPC detectors, facilities offering the possibility to irradiate the chambers are necessary in order to recreate HL-LHC conditions or stronger and study their performance through time. Such facilities exist at CERN and were exploited to conduct this study. A first series of preliminary studies was conducted in the former gamma facility of CERN (GIF) before its dismantlement. This preliminary study was used as a stepping stone towards the building of a more powerful irradiation fully dedicated to longevity studies of CMS and ATLAS subsystems in the perspective of HL-LHC. The period of preliminary work has also been a key moment in the elaboration and improvement of data acquisition, offline analysis and online monitoring tools that are extensively used in the new gamma irradiation facility.

### 5.1.1 GIF

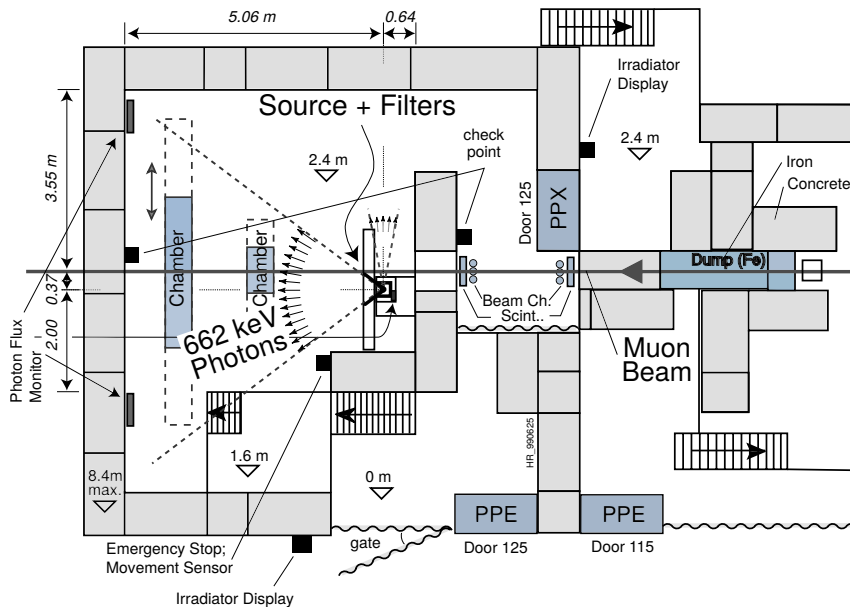


*Figure 5.4: Layout of the test beam zone called X5c GIF at CERN. Photons from the radioactive source produce a sustained high rate of random hits over the whole area. The zone is surrounded by 8 m high and 80 cm thick concrete walls. Access is possible through three entry points. Two access doors for personnel and one large gate for material. A crane allows installation of heavy equipment in the area.*

Located in the SPS West Area at the downstream end of the X5 test beam, the Gamma Irradiation Facility (GIF) was a test area in which particle detectors were exposed to a particle beam in presence of an adjustable gamma background [261]. Its goal was to reproduce background conditions these

detectors would suffer in their operating environment at LHC. GIF layout is showed in Figure 5.4. Gamma photons are produced by a strong  $^{137}\text{Cs}$  source installed in the upstream part of the zone inside a lead container. The source container includes a collimator, designed to irradiate a  $6 \times 6 \text{ m}^2$  area at 5 m maximum to the source. A thin lens-shaped lead filter helps providing with a uniform out-coming flux in a vertical plane, orthogonal to the beam direction. The photon rate is controlled by further lead filters allowing the maximum rate to be limited and to vary within a range of four orders of magnitude. Particle detectors under test are then placed within the pyramidal volume in front of the source, perpendicularly to the beam line in order to profit from the homogeneous photon flux. Adjusting the background flux of photons can then be done by using the filters and choosing the position of the detectors with respect to the source.

As described on Figure 5.5, the  $^{137}\text{Cs}$  source emits a 662 keV photon in 85% of the decays. An activity of 740 GBq was measured on the 5<sup>th</sup> of March 1997. To estimate the strength of the flux in 2014, was considered the nuclear decay through time associated to the Cesium source whose half-life is well known ( $t_{1/2} = (30.05 \pm 0.08) \text{ y}$ ). The GIF tests were done in between the 20<sup>th</sup> and the 31<sup>st</sup> of August 2014, i.e. at a time  $t = (17.47 \pm 0.02) \text{ y}$  resulting in an attenuation of the activity from 740 GBq in 1997 to 494 GBq in 2014.

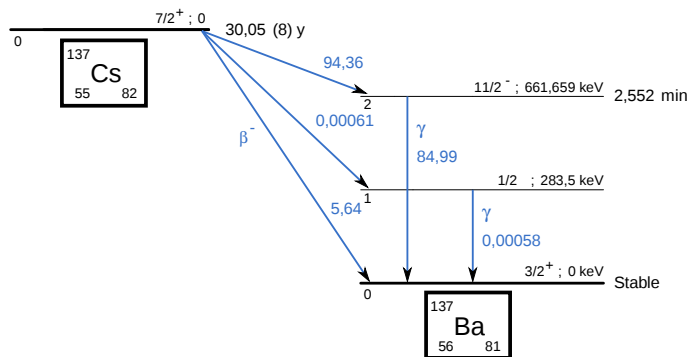


Figure 5.5:  $^{137}\text{Cs}$  decays by  $\beta^-$  emission to the ground state of  $^{137}\text{Ba}$  (BR = 5.64%) and via the 662 keV isomeric level of  $^{137}\text{Ba}$  (BR = 94.36%) whose half-life is 2.55 min.

### 5.1.2 GIF++

The new Gamma Irradiation Facility (GIF++), located in the SPS North Area at the downstream end of the H4 test beam, has replaced its predecessor during LS1 and has been operational since spring 2015 [262]. Like GIF, GIF++ features a  $^{137}\text{Cs}$  source of 662 keV gamma photons, their fluence being controlled with a set of filters of various attenuation factors. The source provides two separated large irradiation areas for testing several full-size muon detectors with homogeneous irradiation, as presented in Figure 5.6.

The source activity was measured to be about 13.5 TBq in March 2016. The photon flux being far greater than HL-LHC expectations, GIF++ provides an excellent facility for accelerated ageing tests of muon detectors. The source is situated in a bunker designed to perform irradiation test along a muon beam line, the muon beam being available during selected periods throughout the year. The H4 beam, providing the area with muons with a maximum momentum of about 150 GeV/c, passes through the GIF++ zone and is used to periodically study the performance of the detectors placed under long term irradiation. Its flux is of  $104 \text{ particles/s/cm}^2$  focused in an area similar to

3113  $10 \times 10 \text{ cm}^2$ . Therefore, with properly adjusted filters, one can simulate the background expected at  
 3114 HL-LHC and study the performance and ageing of muon detectors in HL-LHC environment.

3115

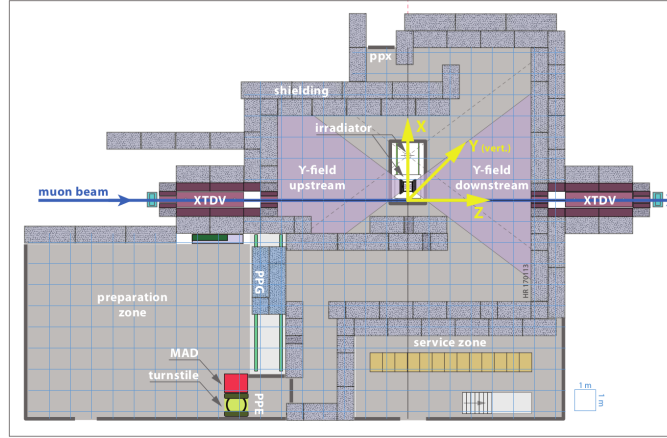


Figure 5.6: Floor plan of the *GIF++* facility. When the facility downstream of the *GIF++* takes electron beam, a beam pipe is installed along the beam line ( $z$ -axis). The irradiator can be displaced laterally (its center moves from  $x = 0.65 \text{ m}$  to  $2.15 \text{ m}$ ), to increase the distance to the beam pipe.

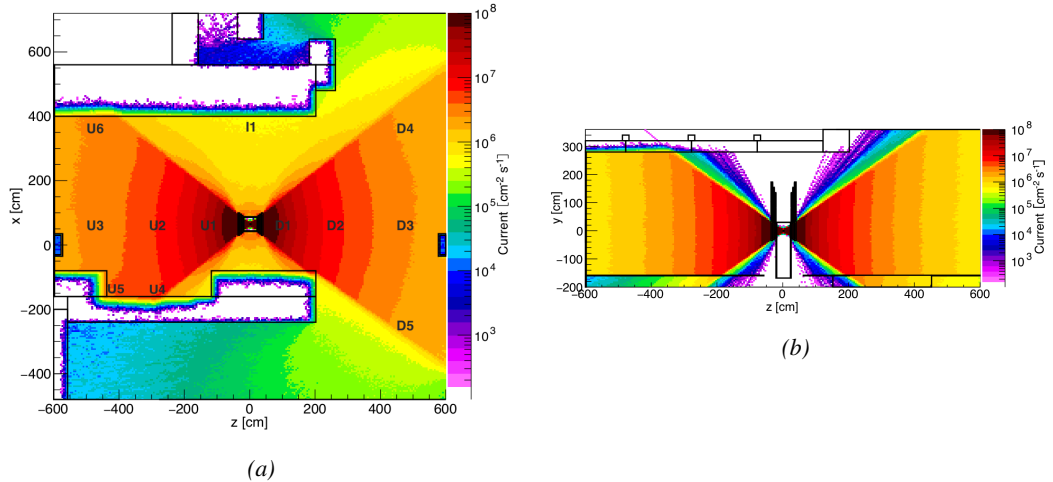


Figure 5.7: Simulated unattenuated current of photons in the  $xz$  plane (Figure 5.7a) and  $yz$  plane (Figure 5.7b) through the source at  $x = 0.65 \text{ m}$  and  $y = 0 \text{ m}$  [263]. With angular correction filters, the current of 662 keV photons is made uniform in  $xy$  planes.

3116 The gamma current as simulated with GEANT4 is presented in Figure 5.7 in which the labels  
 3117 UN, DN, with  $N \in [1 : 5]$  and I1 correspond to the position of different Radiation Monitoring  
 3118 (RADMON) sensors dedicated to measuring the irradiation in the bunker area [263]. According to  
 3119 the simulation results, that agree within 12% to the doses measured with the RADMONs, the RPCs  
 3120 that will be tested in *GIF++* can expect a maximal gamma current of the order of  $2$  to  $5 \times 10^6$

3121  $\text{cm}^{-2} \text{s}^{-1}$  assuming they will always stay in a region in between sensor U5 and the back wall of the  
 3122 upstream area.

## 3123 5.2 Preliminary studies at GIF

### 3124 5.2.1 RPC test setup

3125 During summer 2014, preliminary tests have been conducted in the GIF area on an endcap chamber  
 3126 of type RE4/2 and labeled RE-4-2-BARC-161 produced for the extension of the endcap with a  
 3127 fourth disk in 2013. This chamber has been placed into a trolley covered with a tent. The positions  
 3128 of the RPC inside the tent and of the tent with respect to the source in the bunker are described in  
 3129 Figure 5.8. The goal of the study was to have a preliminary understanding of the rate capability  
 3130 of the present technology used in CMS. It was decided to measure the efficiency of the RPC under  
 3131 irradiation at detecting cosmic muons as, at the time of the tests, the beam not operational anymore.  
 3132 Three different absorber settings were used and compared to the case where the detector was not ir-  
 3133 radated in order to study the evolution of the performance of the detector with increasing exposition  
 3134 to gamma radiation. First of all, measurements were done with the fully opened source. To complete  
 3135 this preliminary study, the gamma flux has been attenuated by a factor 2, a factor 5 and finally the  
 3136 source was shut down. The efficiency of the RPC at detecting the cosmic muons in coincidence with  
 3137 a cosmic trigger as well as the background rate as seen by the detectors were measured.

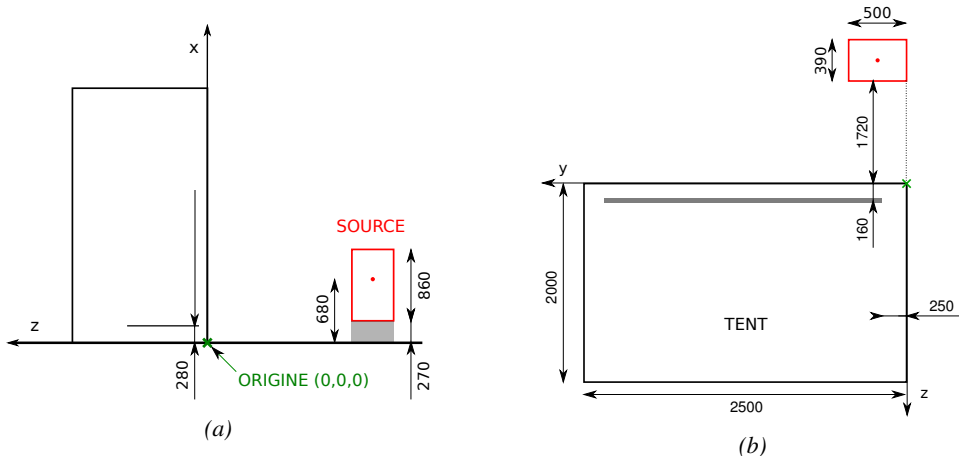


Figure 5.8: Description of the RPC setup. Dimensions are given in mm. A tent containing RPCs is placed at 1720 mm from the source container. The source is situated in the center of the container. RE-4-2-BARC-161 chamber is 160 mm inside the tent. This way, the distance between the source and the chambers plan is 2060 mm. Figure 5.8a provides a side view of the setup in the xz plane while Figure 5.8b shows a top view in the yz plane.

3138 The trigger system was composed of two plastic scintillators and was placed in front of the setup  
 3139 with an inclination of  $10^\circ$  with respect to the detector plane in order to look at cosmic muons. Using  
 3140 this particular trigger layout, showed in Figure 5.9, leads to a cosmic muon hit distribution into the  
 3141 chamber similar to the one of Figure 5.10. Measured without gamma irradiation, two peaks can  
 3142 be seen on the profile of readout partition B, centered on strips 52 and 59. Section 5.2.2 will help  
 3143 us understand that these two peaks are due respectively to forward and backward coming cosmic

<sup>3144</sup> particles where forward coming particles are first detected by the scintillators and then the RPC  
<sup>3145</sup> while the backward coming muons are first detected in the RPC.



*Figure 5.9: RE-4-2-BARC-161 chamber is inside the tent as described in Figure 5.8. In the top right, the two scintillators used as trigger can be seen. This trigger system has an inclination of 10° relative to horizontal and is placed above half-partition B2 of the RPCs. PMT electronics are shielded thanks to lead blocks placed in order to protect them without stopping photons from going through the scintillators and the chamber.*

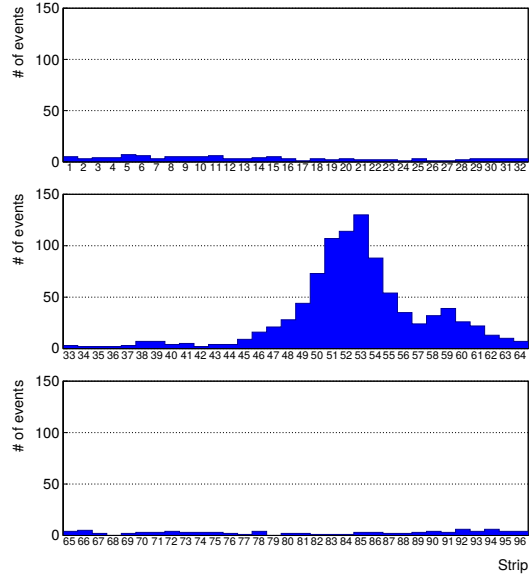


*Figure 5.10: Hit distributions over all three partitions of RE-4-2-BARC-161 chamber is showed. Top, middle and bottom figures respectively correspond to partitions A, B, and C. The profiles show that some events still occur in other half-partitions than B2, which corresponds to strips 49 to 64, in front of which the trigger is placed, contributing to the inefficiency of detection of cosmic muons. In the case of partitions A and C, the very low amount of data can be interpreted as noise. On the other hand, it is clear that a little portion of muons reach the half-partition B1, corresponding to strips 33 to 48.*

3146 The data taking is then performed thanks to a CEAN TDC module of type V1190A [264] to  
 3147 which is connected the digitized output of the RPC Front-End Board, as described in Figure 5.11a  
 3148 and the trigger signal from the telescope. The communication with the computer is performed thanks  
 3149 to a CAEN communication module of type V1718 [265]. In order to control the rates recorded by  
 3150 the detector, the digitized RPC signals are also sent to scalers as described in Figure 5.11b. The  
 3151 C++ DAQ software used in GIF was developed as an early attempt towards the understanding of  
 3152 the CAEN libraries and the data collected by the TDCs was saved into .dat files is analysed with  
 3153 an algorithm computing parameters such as efficiency, hit profile, cluster size, or gamma and noise  
 3154 rates which was developed with C++ as well. Finally, histograms and curves are produced using  
 3155 ROOT.

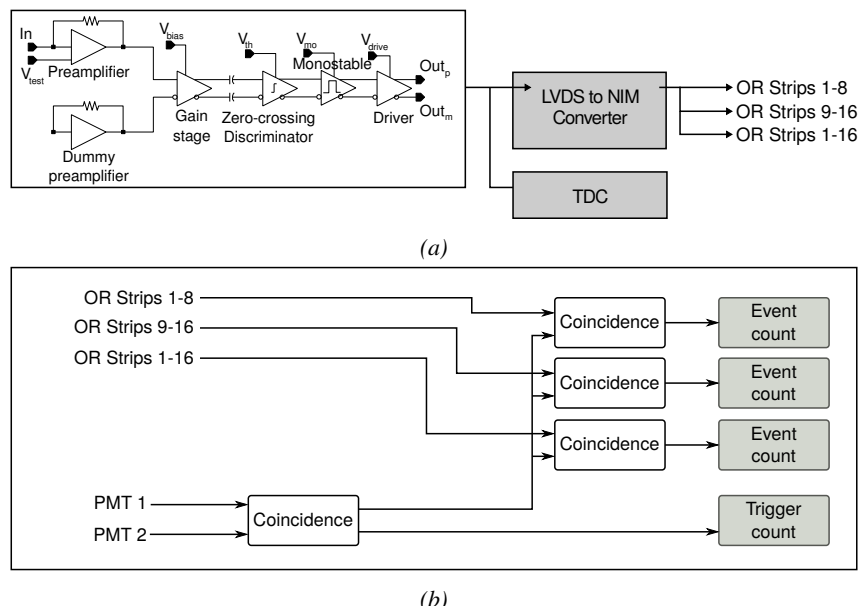


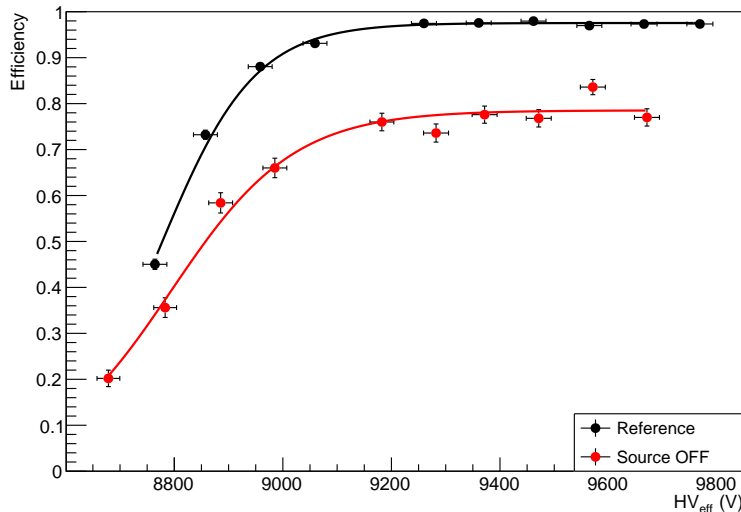
Figure 5.11: Signals from the RPC strips are shaped by the FEE described on Figure 5.11a. Output LVDS signals are then read-out by a TDC module connected to a computer or converted into NIM and sent to scalers. Figure 5.11b describes how these converted signals are put in coincidence with the trigger.

### 3156 5.2.2 Geometrical acceptance of the setup layout to cosmic muons

3157 In order to profit from a constant gamma irradiation, the detectors inside of the GIF bunker need  
 3158 to be placed in a plane orthogonal to the beam line. The muon beam that used to be available was  
 3159 meant to test the performance of detectors under test. This beam being not active anymore, another  
 3160 solution to test detector performance had to be used. Thus, it has been decided to use cosmic muons  
 3161 detected through a telescope composed of two scintillators. Lead blocks were used as shielding to  
 3162 protect the photomultipliers from gammas as can be seen from Figure 5.9.

3163 An inclination of  $\sim 10^\circ$  has been given to the cosmic telescope to maximize the muon flux. A  
 3164 good compromise had to be found between good enough muon flux and narrow enough hit distribution  
 3165 to be sure to contain all the events into only one half partitions as required from the limited  
 3166 available readout hardware. It was then foreseen to detect muons and read them out only from  
 3167 half-partition B2, the last 16 channels of readout partition B (i.e. strips 49 to 64). Nevertheless,

3168 a consequence of the misplaced trigger, that can be seen as a loss of events in half-partition B1  
 3169 (strips 33 to 48) in Figure 5.10, is an inefficiency. The observed inefficiency of approximately 20%  
 3170 highlighted in Figure 5.12 by comparing the performance of chamber RE-4-2-BARC-161 as mea-  
 3171 sured prior to the study at GIF and at GIF without irradiation seems too important, compared to the  
 3172 12.7% of data contained into the first 16 strips observed on Figure 5.10, to only be explained by the  
 3173 geometrical acceptance of the setup itself. Simulations have been conducted to show how the setup  
 3174 brings inefficiency.



3175 *Figure 5.12: Results are derived from data taken on half-partition B2 only. On the 18<sup>th</sup> of June 2014, data  
 has been taken on chamber RE-4-2-BARC-161 at CERN building 904 (Prevessin Site) with cosmic muons  
 providing us a reference efficiency plateau of  $(97.54 \pm 0.15)\%$  represented by a black curve. A similar  
 measurement has been done at GIF on the 21<sup>st</sup> of July with the same chamber giving a plateau of  $(78.52 \pm 0.94)\%$   
 represented by a red curve.*

### 3175 5.2.2.1 Description of the simulation layout

3176 The layout of GIF setup has been reproduced, only roughly using Figure 5.9 due to the lack of  
 3177 measures, and incorporated into a C++ Monte Carlo (MC) simulation to study the geometrical ac-  
 3178 ceptance of the telescope projected onto the readout strips [266]. A 3D view of the simulated layout  
 3179 is given into Figure 5.13. Muons are generated randomly in a horizontal plane located at a height  
 3180 corresponding to the lowest point of the PMTs. This way, the needed size of the plane in order to  
 3181 simulate events happening at very large azimuthal angles (i.e.  $\theta \approx \pi$ ) can be kept relatively small  
 3182 while the total number of muon tracks to propagate is kept relatively small. The muon flux is de-  
 3183 signed to follow the usual  $\cos^2\theta$  distribution for cosmic particles. The goal of the simulation is to  
 3184 look at muons that pass through the telescope composed of the two scintillators and define their dis-  
 3185 tribution onto the RPC read-out plane. During the reconstruction, the read-out plane is then divided  
 3186 into read-out strips and each muon track is assigned to a strip.

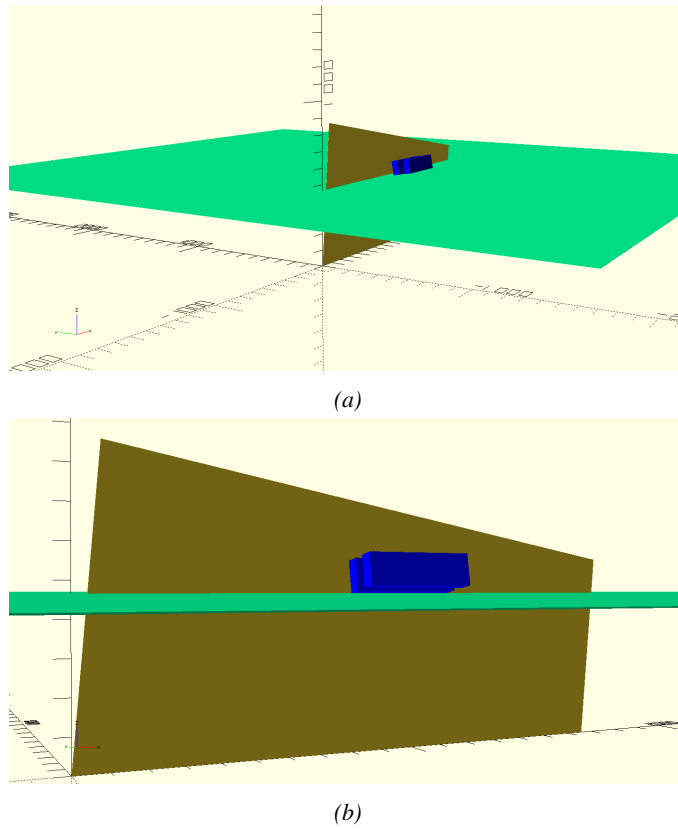


Figure 5.13: Representation of the layout used for the simulations of the test setup. The RPC read-out plane is represented as a yellow trapezoid while the two scintillators as blue cuboids looking at the sky. The green plane corresponds to the muon generation plane within the simulation. Figure 5.8a shows a global view of the simulated setup. Figure 5.8b shows a zoomed view that allows to see the two scintillators as well as the full RPC plane.

### 5.2.2.2 Simulation procedure

3187     $N_\mu = 10^8$  muons are randomly generated inside the muon plane with an azimuthal angle  $\theta$  chosen  
 3188    to follow a  $\cos^2\theta$  distribution. Infinite planes are associated to each surface of the scintillators.  
 3189    Knowing the muon position into the muon generation plane and its direction allows, by assuming  
 3190    that muons travel in a straight line, to compute the intersection of the muon track with these planes.  
 3191    Applying conditions to the limits on the contours of the scintillators' faces then gives an answer to  
 3192    whether or not the muon passed through the scintillators. In the case the muon was not *detected* into  
 3193    both scintillators, the simulation discards the muon and generates a new one.  
 3194

3195    On the contrary, if the muon is labeled as good, its position within the RPC read-out plane  
 3196    is computed and the corresponding strip, determined through geometrical tests, gets a *hit*. Muon  
 3197    hits fill different histograms whether they are associated to forward or backward coming muons.  
 3198    A discrimination is performed according to their direction components. An  $(x, y, z)$  position into  
 3199    the generation plane as well as a  $(\theta; \phi)$  pair are associated to each generated muon providing with  
 3200    information on the direction the track follows. This way, muons satisfying the condition  $0 \leq \phi < \pi$   
 3201    are labeled as *backward* coming muons while muons satisfying  $\pi \leq \phi < 2\pi$  as *forward* coming

3202 muons.

3203 **5.2.2.3 Results and limitations**

3204 The output from the simulation is given in Figure 5.14 in which the distribution is showed for all  
 3205 muons but also for the separate contributions of forward and backward coming muons. The strip  
 3206 number is here given in a range of 1 to 32 corresponding to the 32 strips contained in each RPC  
 3207 read-out partition, without taking into account the fact that partition B of an RPC correponds, by  
 3208 convention, to strips 33 to 64. Comparing the number of muons recorded respectively in the first 16  
 3209 strips and the in all of the 32 strips of the RPC read-out panel, it can be established than, out of the  
 3210 total amount of muons that have passed through the telescope and reached the RPC, 16.8% where to  
 3211 be detected in the 16 first strip of the read-out plane corresponding to half partition B1. This brings  
 3212 a geometrical inefficiency of the same amount that can then be used to correct the data by scaling up  
 3213 by a factor  $c_{geo} = 1/(1 - 0.168)$  the maximum efficiency measured during data taking.

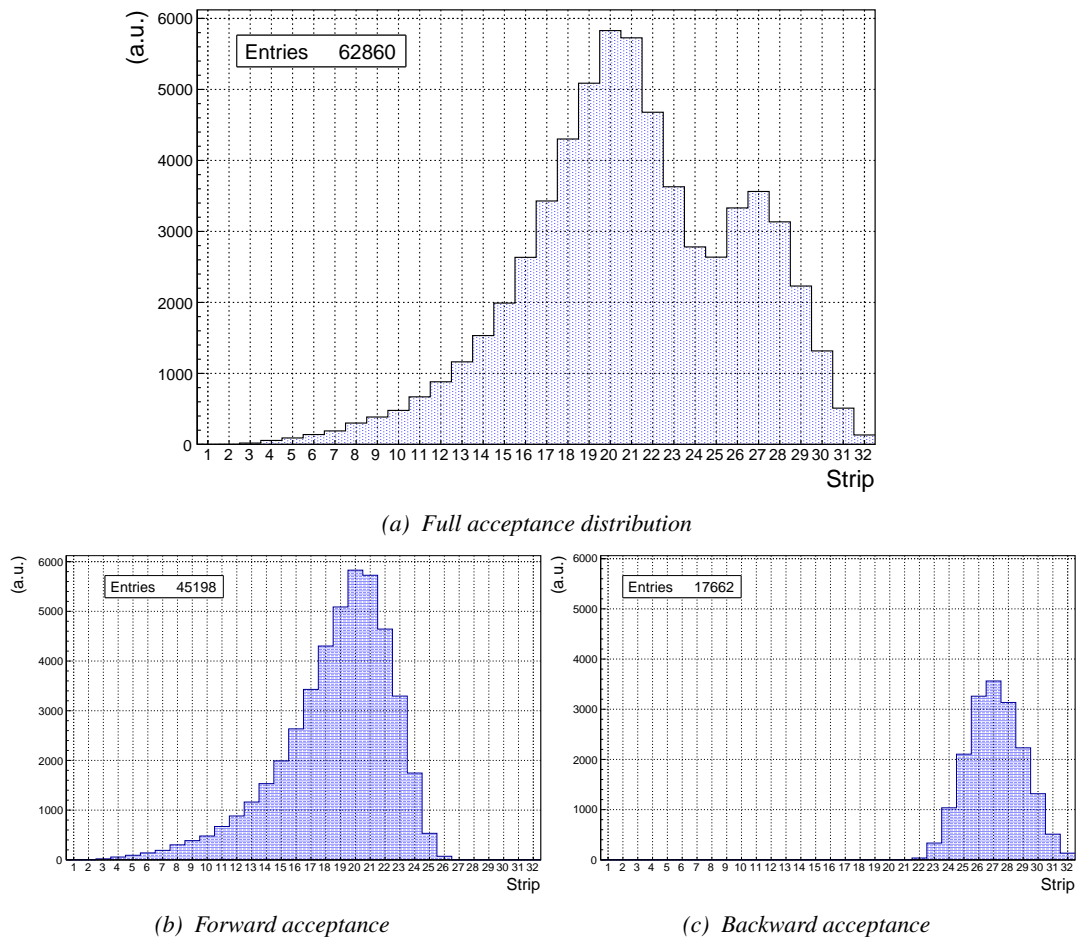


Figure 5.14: Geometrical acceptance distribution as provided by the Monte Carlo simulation.

3214 Nevertheless, it is difficult to evaluate a systematic uncertainty on this geometrical correction for

3215 different reasons. First of all, even though the dimensions of the scintillators and of the RPC are well  
 3216 known, the position of each element of the setup with respect to one another was not measured. It was  
 3217 then necessary, using known dimensions, to extract the positions of each element from Figure 5.9  
 3218 with unknown uncertainty. The inclination is also roughly measured to be  $10^\circ$  and even if the  
 3219 position of each peak, distant in the simulation of 7 strips, tends to confirm this assumption, the  
 3220 geometrical inefficiency would be affected by a variation of the inclination angle. Introducing in the  
 3221 simulation an error of  $\pm 2^\circ$  would lead to a correction factor  $c_{geo} = 1.20^{+0.04}_{-0.03}$  that allows for a good  
 3222 improvement of the efficiency measured in GIF, as can be seen from Figure 5.15. GIF measurement  
 3223 is in agreement with the reference curve within statistical errors.

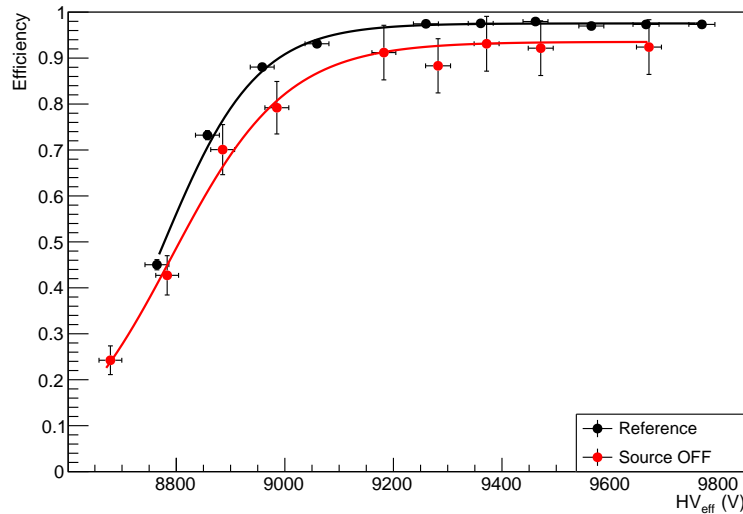
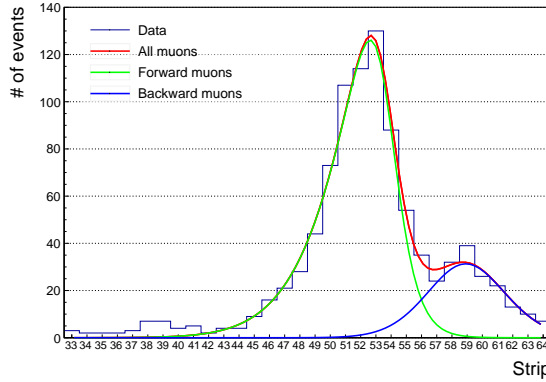


Figure 5.15: Correction of the efficiency without source. The efficiency after correction gets much closer to the Reference measurement performed before the study in GIF by reaching a plateau of  $(93.52 \pm 2.64)\%$ .

3224 Further corrections could be also be brought as it can easily be understood that the distribution  
 3225 showed through Figure 5.14a differs from the measured hit profile showed in Figure 5.10. The  
 3226 contributions of forward and backward muon indicate that 28.1% of the total geometrical acceptance  
 3227 should contribute to detecting backward muons whereas it is measured that the hit profile contains  
 3228 22.0% of backward data only. This estimation of the backward versus forward content in the data was  
 3229 done through a fit using a sum of two skew distribution, one acting on the forward muon peak while  
 3230 the other acts on the backward muon fit, as showed in Figure 5.16. Although a skew distribution  
 3231 lacks physical interpretation, it allows fitting easily such kind of data. A description of a skew  
 3232 distribution, as the product of a gaussian and a sigmoid (Formula 5.1), is given through Formula 5.2.

$$(5.1) \quad g(x) = A_g e^{\frac{-(x-\bar{x})^2}{2\sigma^2}}, \quad s(x) = \frac{A_s}{1 + e^{-\lambda(x-x_i)}}$$

$$(5.2) \quad sk(x) = g(x) \times s(x) = A_{sk} \frac{e^{\frac{-(x-\bar{x})^2}{2\sigma^2}}}{1 + e^{-\lambda(x-x_i)}}$$



*Figure 5.16: Hit distributions over read-out partition B of RE-4-2-BARC-161 chamber together with skew distribution fits corresponding to forward and backward coming muons.*

From the obvious difference in between geometrical simulation and data, it is necessary to realize that the geometrical acceptance and the hit profile are two distinct information. When the geometrical acceptance only provides with the information about what the detector can expect to see in a perfect world where all muons are detected in the exact same way independently from their energy, angle of incidence, fluctuation of the detector gain due to complex avalanche development, thresholds applied on the scintillators and on the RPC FEEs to reduce the noise, the cross-talk and corresponding spread of the induced charge observed on the read-out strips, the hit profile provides the final product of all the previously mentioned contributions and can greatly differ from purely geometrical considerations. A full physics analysis involving softwares such as GEANT would be required to further refine the correction on the measured efficiency at GIF.

### 5.2.3 Photon flux at GIF

In order to understand and evaluate the  $\gamma$  flux in the GIF area, simulations had been conducted at the time GIF was opened for research purposes [261]. Table 5.1 presented in this article gives the  $\gamma$  flux for different distances  $D$  to the source. The simulation was done using GEANT and a Monte Carlo N-Particle (MCNP) transport code, and the flux  $F$  is given with the estimated error from these packages expressed in %.

Nominal ABS	Photon flux $F$ [ $\text{cm}^{-2} \text{s}^{-1}$ ]			
	at $D = 50 \text{ cm}$	at $D = 155 \text{ cm}$	at $D = 300 \text{ cm}$	at $D = 400 \text{ cm}$
1	$0.12 \times 10^8 \pm 0.2\%$	$0.14 \times 10^7 \pm 0.5\%$	$0.45 \times 10^6 \pm 0.5\%$	$0.28 \times 10^6 \pm 0.5\%$
2	$0.68 \times 10^7 \pm 0.3\%$	$0.80 \times 10^6 \pm 0.8\%$	$0.25 \times 10^6 \pm 0.8\%$	$0.16 \times 10^6 \pm 0.6\%$
5	$0.31 \times 10^7 \pm 0.4\%$	$0.36 \times 10^6 \pm 1.2\%$	$0.11 \times 10^6 \pm 1.2\%$	$0.70 \times 10^5 \pm 0.9\%$

*Table 5.1: Total photon flux ( $E\gamma \leq 662 \text{ keV}$ ) with statistical error predicted considering a  $^{137}\text{Cs}$  activity of 740 GBq at different values of the distance  $D$  to the source along the x-axis of irradiation field [261].*

The simulation does not provide with an estimated flux at the level of the RPC under test. First of all, it is necessary to extract the value of the flux from the available data contained in the original paper and then to estimate the flux in 2014 at the time the experimentation took place. In the case of a pointlike source emitting isotropic and homogeneous gamma radiations, the gamma flux  $F$  at a

3253 distance  $D$  from the source with respect to a reference point situated at  $D_0$  where a known flux  $F_0$   
 3254 is measured will be expressed like in Formula 5.3, assuming that the flux decreases as  $1/D^2$ , where  
 3255  $c$  is a fitting factor that can be written from Formula 5.3 as Formula 5.4. Finally, using Equation 5.4  
 3256 and the data of Table 5.1, with  $D_0 = 50$  cm as reference point, Table 5.2 can be built. It is interesting  
 3257 to note that  $c$  for each value of  $D$  doesn't depend on the absorption factor.

$$(5.3) \quad F^{ABS} = F_0^{ABS} \times \left( \frac{cD_0}{D} \right)^2$$

$$(5.4) \quad c = \frac{D}{D_0} \sqrt{\frac{F^{ABS}}{F_0^{ABS}}} , \quad \Delta c = \frac{c}{2} \left( \frac{\Delta F^{ABS}}{F^{ABS}} + \frac{\Delta F_0^{ABS}}{F_0^{ABS}} \right)$$

Nominal ABS	Correction factor $c$		
	at $D = 155$ cm	at $D = 300$ cm	at $D = 400$ cm
1	$1.059 \pm 0.70\%$	$1.162 \pm 0.70\%$	$1.222 \pm 0.70\%$
2	$1.063 \pm 1.10\%$	$1.150 \pm 1.10\%$	$1.227 \pm 0.90\%$
5	$1.056 \pm 1.60\%$	$1.130 \pm 1.60\%$	$1.202 \pm 1.30\%$

Table 5.2: Correction factor  $c$  is computed thanks to Formula 5.4 taking as reference  $D_0 = 50$  cm and the associated flux  $F_0^{ABS}$  for each absorption factor available in table 5.1.

3258 For the range of  $D/D_0$  values available, it is possible to use a simple linear fit to get the evolution  
 3259 of  $c$  that can be expressed as  $c(D/D_0) = aD/D_0 + b$ . Using Formula 5.5, but neglecting the  
 3260 uncertainty on  $D$  that will only be used when extrapolating the values for the position of the RPC  
 3261 under test whose position is not perfectly known, the results showed in Figure 5.17 is obtained.  
 3262 Figure 5.17b confirms that using only a linear fit to extract  $c$  is enough as the evolution of the rate  
 3263 that can be obtained superimposes well on the simulation points.

$$(5.5) \quad F^{ABS} = F_0^{ABS} \left( a + \frac{bD_0}{D} \right)^2 , \quad \Delta F^{ABS} = F^{ABS} \left[ \frac{\Delta F_0^{ABS}}{F_0^{ABS}} + 2 \frac{\Delta a + \Delta b \frac{D_0}{D} + \Delta D \frac{bD_0}{D^2}}{a + \frac{bD_0}{D}} \right]$$

3264 In the context of the 2014 GIF tests, the RPC read-out plane is located at a distance  $D = 206$  cm  
 3265 from the source. Moreover, to estimate the strength of the flux in 2014, it is necessary to consider the  
 3266 nuclear decay through time associated to the Cesium source whose half-life is well known ( $t_{1/2} =$   
 3267  $(30.05 \pm 0.08)$  y). The very first source activity measurement has been done on the 5<sup>th</sup> of March  
 3268 1997 while the GIF tests were done in between the 20<sup>th</sup> and the 31<sup>th</sup> of August 2014, i.e. at a time  
 3269  $t = (17.47 \pm 0.02)$  y resulting in an attenuation of the activity from 740 GBq in 1997 to 494 GBq in  
 3270 2014. All the needed information to extrapolate the expected flux through the detector at the moment  
 3271 of GIF preliminary tests has now been assembled, leading to Table 5.3. By assuming a sensitivity of  
 3272 the RPC to  $\gamma$  of  $2 \times 10^{-3}$ , the order of magnitude of the expected hit rate per unit area would be of  
 3273 the order of the kHz for the fully opened source, as reported in the last column of the table.

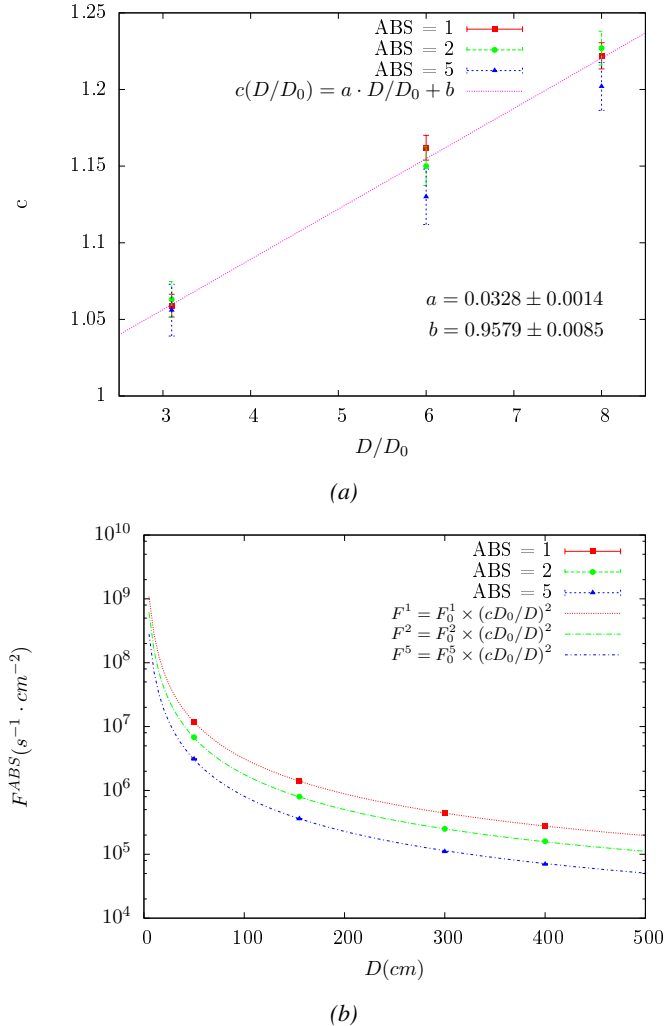


Figure 5.17: Figure 5.17a shows the linear approximation fit performed on data extracted from table 5.2. Figure 5.17b shows a comparison of Formula 5.5 with the simulated flux using  $a$  and  $b$  given in figure 5.17a in formulae 5.3 and the reference value  $D_0 = 50\text{ cm}$  and the associated flux for each absorption factor  $F_0^{ABS}$  from table 5.1.

Nominal ABS	Photon flux $F$ [ $\text{cm}^{-2} \text{s}^{-1}$ ]			Rate [ $\text{Hz}/\text{cm}^2$ ] at $D^{2014} = 206\text{ cm}$
	at $D_0^{97} = 50\text{ cm}$	at $D^{97} = 206\text{ cm}$	at $D^{2014} = 206\text{ cm}$	
1	$0.12 \times 10^8 \pm 0.2\%$	$0.84 \times 10^6 \pm 1.2\%$	$0.56 \times 10^6 \pm 1.2\%$	$1129 \pm 14$
2	$0.68 \times 10^7 \pm 0.3\%$	$0.48 \times 10^6 \pm 1.2\%$	$0.32 \times 10^6 \pm 1.2\%$	$640 \pm 8$
5	$0.31 \times 10^7 \pm 0.4\%$	$0.22 \times 10^6 \pm 1.2\%$	$0.15 \times 10^6 \pm 1.2\%$	$292 \pm 4$

Table 5.3: The data at  $D_0$  in 1997 is taken from [261]. Using Formula 5.5, the flux at  $D$ , including an error of 1 cm, can be estimated in 1997. Then, taking into account the attenuation of the source activity, the flux at  $D$  can be estimated at the time of the tests in GIF in 2014. Assuming a sensitivity of the RPC to  $\gamma$  s =  $2 \times 10^{-3}$ , an estimation of the hit rate per unit area is obtained.

3274 The goal of the study will be to have a good measurement of the intrinsic performance without  
 3275 source irradiation. Then, taking profit of the two working absorbers, at absorption factors 5 (300 Hz)  
 3276 and 2 ( $\sim 600$  Hz) the goal will be to show that the detectors fulfill the performance certification of  
 3277 CMS RPCs. Finally, a first idea of the performance of the detectors at higher backgrounds will be  
 3278 provided with absorption factor 1 (no absorption and  $>1$  kHz)).

### 3279 5.2.4 Results and discussions

3280 The data taking at GIF has been conducted in between the 21<sup>st</sup> and the 31<sup>st</sup> of August, 2014. Data  
 3281 has been collected with source both ON and OFF using three different absorber settings (ABS 5, 2  
 3282 and 1) in order to vary the irradiation on the RPC. For each source setting, two HV scans have been  
 3283 performed with two different trigger settings. During a first scan the trigger sent to the TDC module  
 3284 was the coincidence of the two scintillators composing the telescope while during a second scan the  
 3285 trigger was a pulse coming from a pulse generator in order to measure the noise or gamma rate seen  
 3286 by the chamber. Indeed, using a pulse allows to trigger at moments not linked to any physical event  
 3287 and, hence, to obtain a *RANDOM* trigger on noise and gamma events to measure the associated rates,  
 3288 the probability to have a pulse in coincidence with a cosmic muon being negligible.

3289 From the cosmic trigger scans, a summary of the efficiencies and corresponding cluster sizes is  
 3290 showed in Figure 5.18. The efficiency curves with Source ON show a shift with respect to the case  
 3291 without irradiation. With ABS 5, the general shape of the efficiency curve stays unchanged whereas  
 3292 a clear alteration of the performance is observed at ABS 2 and ABS 1. From the cluster size results,  
 3293 a reduction of the cluster size under irradiation can be observed at equivalent efficiency. This effect  
 3294 can be due to the perturbation of the electric field by the strong rate of gamma particles starting  
 3295 avalanches in the gas volume of the detector.

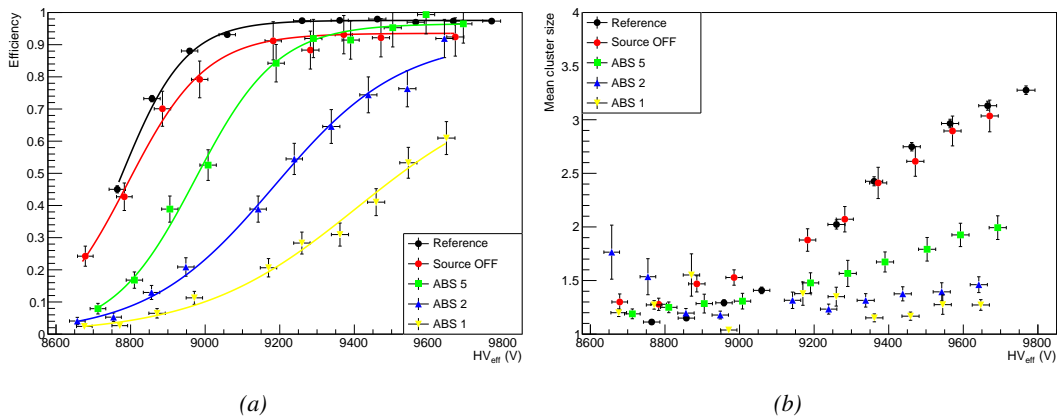
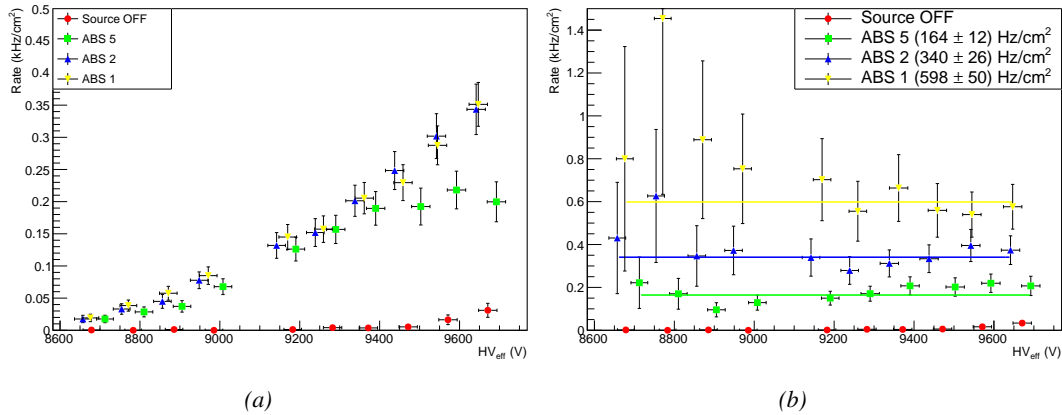


Figure 5.18: Efficiency (Figure 5.18a) and cluster size (Figure 5.18b) of chamber RE-4-2-BARC-161 measured at GIF with Source OFF (red) and Source ON using different absorber settings: ABS 5 (green), ABS 2 (blue) and ABS 1 (yellow). The results are compared to the Reference values obtained with cosmics.

3296 It is necessary to study the evolution of the performance of the chamber with the increasing rate.  
 3297 In Figure 5.19a, the noise rate when the source is OFF stays low but increases at voltages above  
 3298 9500 V. The rise of the noise rate in the detector can be related to the increased streamer probability  
 3299 observed with such a large electric field. The rates with source ON measured at GIF all show a

similar behaviour until a high voltage of approximately 9400 V at which the rate of ABS 5 saturates, corresponding to the chamber reaching full efficiency. It is important to note that, even though the rates look similar independently from the gamma flux, relatively to the efficiency of the chamber, the rate actually increases with increasing flux at equivalent efficiency. A rough way to measure the rate effectively observed by the detector for each source setting would be to normalize the measured rates to the efficiency of the detector. This exercise was done with Figure 5.19b from which constant fits where done on Source ON data in order to extract the rate the chamber was subjected to.



*Figure 5.19: Rates in chamber RE-4-2-BARC-161 measured at GIF with Source OFF (red) and Source ON using different absorber settings: ABS 5 (green), ABS 2 (blue) and ABS 1 (yellow). On Figure 5.19b, the rates of Figure 5.19a were normalized to the measured efficiency, and constant fits are performed on Source ON data showing the gamma rate in the chamber.*

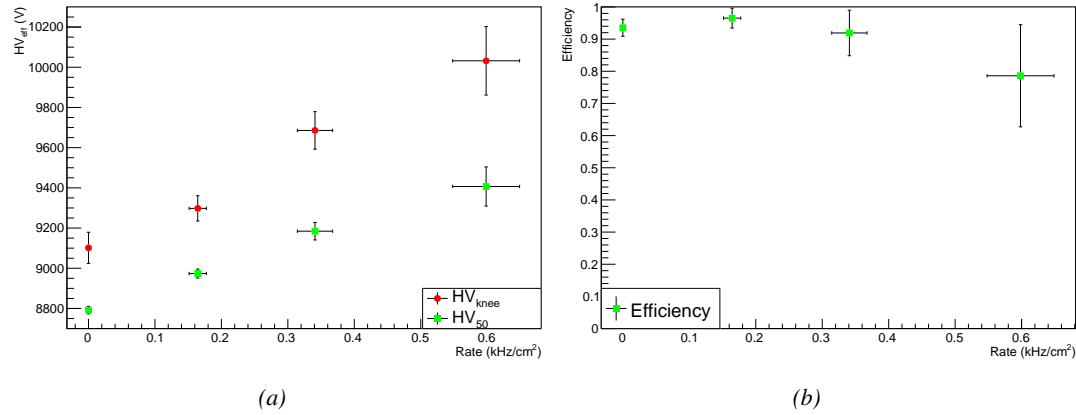


*Figure 5.20: Evolution of the voltages at half maximum and at 95% of the maximum efficiency (Figure 5.20a), and of the maximum efficiency (Figure 5.20b) as a function of the rate in chamber RE-4-2-BARC-161. The data is extracted from the fits in Figures 5.18a and 5.19b.*

The results need to be taken with care as a better estimation of the rate would have been to push the detector towards higher voltages to reach the efficiency plateau for each absorber configuration

and only then extract the measured rate at working voltage, defined as in Formula 4.25. Nevertheless, using this method to estimate the rate to which the chamber is subjected, it is possible to look at the evolution of the  $HV_{50}$  and  $HV_{knee}$  (the working voltage being defined to be 150 V above the knee in the endcap) as a function of the increasing rate as showed in Figure 5.20. The results from GIF suggest that at a rate of 600 Hz/cm<sup>2</sup> the working voltage of the chamber is increased by a thousand V while the efficiency is reduced to approximately 80%, although the result still is consistent with an efficiency better than 90% due to the large error on the measurement. Moreover, it is likely that the rates obtained through fitting on normalized values is underestimated. Indeed, monitoring the current in the three gaps composing a CMS endcap RPC (Figure 5.21) while knowing the rate, the charge deposition per avalanche  $q_\gamma$  can be computed.

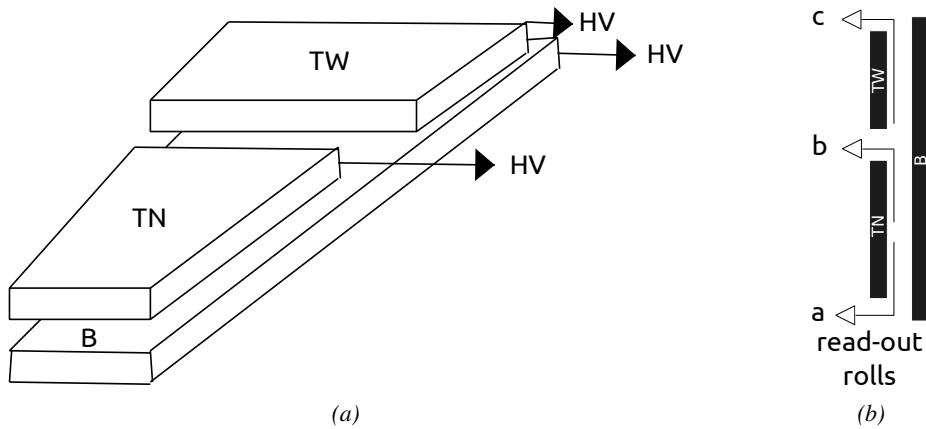


Figure 5.21: Presentation of a double-gap endcap RPC with its three RPC gaps. Due to the partitioning of the read-out strips into three rolls, the TOP layer of gap is divided into two gaps: TOP NARROW (TN) and TOP WIDE (TW). The BOTTOM (B) only consists in one gap.

A charge is expressed in C which is consistent with a current density, expressed in A/cm<sup>2</sup>, divided by a rate per unit area, expressed in Hz/cm<sup>2</sup>. The current driven by the RPC is assumed to be due to the irradiation, hence, to the avalanches developing in the gas volume due to the photons of the Cesium source. On the other hand, the rate is supposed to be a measure of the number of photons interacting with the detector. This way, it comes that the charge deposition per avalanche is expressed like  $q_\gamma = J_{mon}/R_\gamma$ ,  $J_{mon}$  being the monitored current density and  $R_\gamma$  the measured  $\gamma$  rate. The current density is computed as the sum of the current density measured on the top gap layer and of which measured in the bottom gap layer,  $J_{mon} = (I_{mon}^{TW} + I_{mon}^{TN})/(A_{TW} + A_{TN}) + I_{mon}^B/A_B$ ,  $A_{B,TN,TW}$  being the active area and  $I_{mon}^{B,TN,TW}$  the monitored currents of the gaps. According to Figure 5.22, the charge deposition per avalanche consistently converges to a value of the order of 50 pC for each absorber setting which corresponds to a value more than twice greater than what reported in literature for CMS detectors [267, 268] indicating that the rates could have been wrongly evaluated during the short study performed at GIF. An increase of the  $\gamma$  rate by a factor 2 would be consistent with the expected rates calculated in Table 5.3, assuming the sensitivity to  $\gamma$  to be of the order of  $2 \times 10^{-3}$ .

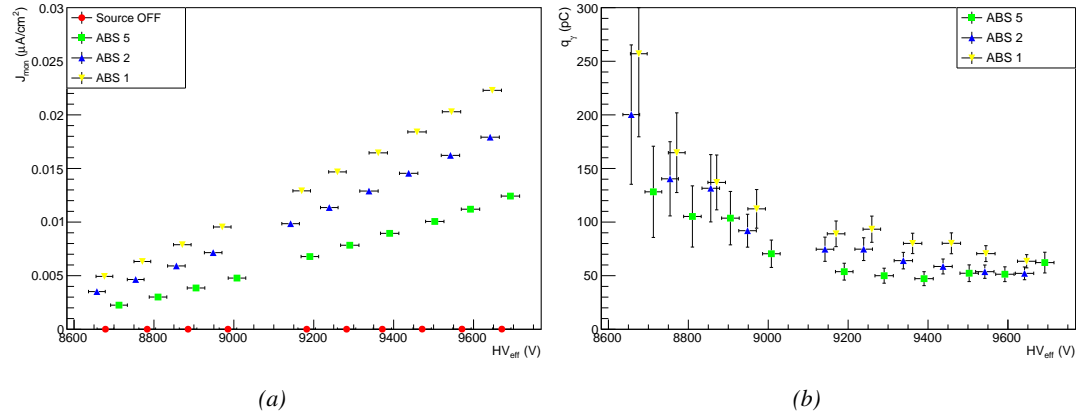


Figure 5.22: Current density and charge deposition per gamma avalanche, defined as the current density normalized to the measured rate taken from Figure 5.19a as a function of the effective high voltage in chamber RE-4-2-BARC-161 measured at GIF with Source ON using different absorber settings: ABS 5 (green), ABS 2 (blue) and ABS 1 (yellow).

Overall, working at GIF has been a rewarding experience as it offered CMS RPC R&D team the possibility to start developing the necessary skills and tools that would become the core of GIF++ experiment. The quality of the results can be argued both due to the little robustness of the experimental setup and the lack of available statistics to draw conclusions from, bringing large errors on the final result. The confrontation of the data to known results pointed to a failure in correctly measuring the  $\gamma$  rate at working voltage and, hence, to an overestimation of the charge per avalanche and of the drift of working voltage with increasing rate. Nevertheless, the prototypes of DAQ and offline analysis tools proved to be reliable.

### 5.3 Longevity tests at GIF++

#### 5.3.1 Selection and characterization of CMS RPCs for longevity at GIF++

First proposed in 2009 [269], the new Gamma Irradiation Facility of CERN was thought in the perspective of future upgrades of LHC that would bring detectors to be operated in a high irradiation environment. GIF++ would thus provide all LHC R&D teams working on behalf of the different LHC experiment with a facility to perform longevity studies using a very intense Cesium gamma source.

In the specific case of CMS RPC, the longevity studies imply a constant irradiation of selected detectors in order to accumulate a charge equivalent to what is expected during HL-LHC, i.e. a charge of  $0.8 \text{ C}/\text{cm}^2$  according to Figure 5.2 including a safety factor 3, while other detectors are left non-irradiated to be used as references. Throughout the irradiation campaign, the performance of the irradiated and reference detectors will be periodically probed using the high intensity H4 muon beam. Dedicated test beam periods will be used to measure the efficiency and  $\gamma$  rate at the level of the detectors with different source absorber settings to have access to the rate capability of CMS RPCs, that needs to be certified above  $600 \text{ Hz}/\text{cm}^2$ , and to identify signs of ageing in the case the performance of the irradiated detectors diverges from those of the reference detectors with increasing accumulated charge. Other than the performance of the detectors, signs of ageing

3359 could come from increasing dark current that would be related to local ageing of the electrodes  
 3360 triggered by the hydrofluoric acid ( $HF$ ) production in an irradiated environment.  $HF$  is produced  
 3361 by the decomposition of  $C_2H_2F_4$  molecules during the charge multiplication process and leads to  
 3362 increased dark current and noise in Bakelite RPCs treated with linseed oil. This effect is strongly  
 3363 reinforced by the presence of UV photons [270, 271]. A close monitoring of the current driven by  
 3364 the detectors will then be necessary as well as dedicated periodical electrode resistivity measurement  
 3365 and chromatography measurement on the gas exhaust.

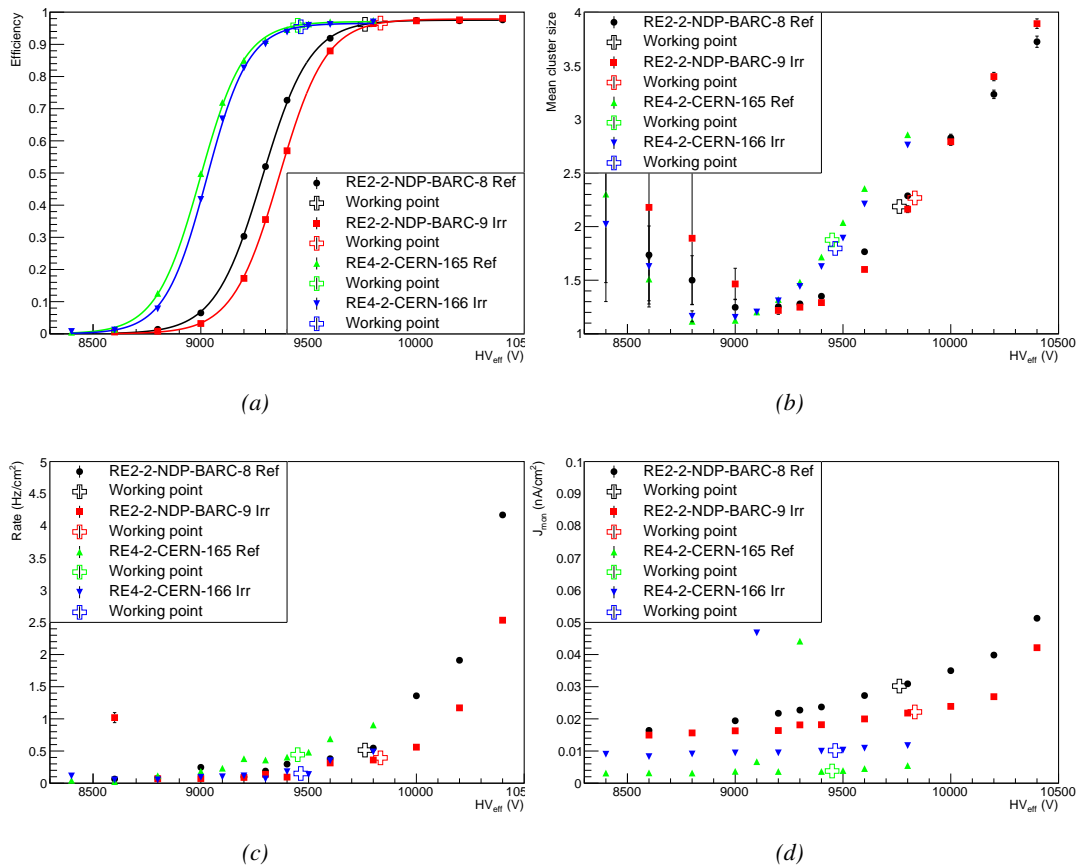


Figure 5.23: Characterization of CMS RPC detectors foreseen to be used at Gif++ for longevity studies of the present system. Using cosmic muons, efficiency (Figure 5.23a) and cluster size (Figure 5.23b) were measured as well as noise rate (Figure 5.23c) and current density (Figure 5.23d). For each detector, the working voltage, defined as in Formula 4.25, was extracted from sigmoid fits performed in Figure 5.23a and the values of efficiency, cluster size, noise rate and current density at this voltage are reported using open crosses.

3366 As the maximum background is found in the endcap, the choice naturally was made to focus  
 3367 the Gif++ longevity studies on endcap chambers. Most of the RPC system was installed in 2007.  
 3368 Nevertheless, the large chambers in the fourth endcap (RE4/2 and RE4/3) have been installed during  
 3369 LS1 in 2014. The Bakelite of these two different productions having different properties, four spare  
 3370 chambers of the present system were selected. From the original CMS RPC system, two RE2/2  
 3371 spares were selected along two RE4/2 spares from the newest detectors. Having two chambers of

3372 each type allows to always keep one of them non-irradiated as reference. Due to the limited gas  
 3373 flow in GIF++, the RE4 chamber remained non-irradiated until end of November 2016 where the  
 3374 longevity studies could finally be started on those chambers.

3375 The performance of the chambers prior to the start of the longevity campaign has been char-  
 3376 acterized in Ghent before being shipped to CERN to be installed in GIF++. The results of the  
 3377 characterization are showed in Figure 5.23 and summarized in Table 5.4. A clear difference in per-  
 3378 formance for both types of chambers is observed as the working voltages of the newest chambers,  
 3379 of type RE4, are 300 to 400 V lower to the older chambers indicating that the gap thickness of RE4  
 3380 detectors could be thinner. This conclusion could as well be supported by the lower cluster size at  
 3381 working voltages that also are smaller in RE4 chambers. Even though the measured currents are  
 3382 low, RE4 detectors draw less current without irradiation than RE2 detectors pointing to a difference  
 3383 in electrode resistivity that were produced at different moments. Efficiency and noise rate levels are  
 3384 of the same order of magnitude for both type of RPCs.

RPC	RE2-2-NPD-BARC-08	RE2-2-NPD-BARC-09	RE4-2-CERN-165	RE4-2-CERN-166
Used as	Reference	Irradiation	Reference	Irradiation
$HV_{WP}$ [V]	(9762 ± 6)	(9833 ± 6)	(9449 ± 5)	(9464 ± 5)
Efficiency at WP	(96.2 ± 0.3)	(96.6 ± 0.3)	(95.9 ± 0.3)	(95.5 ± 0.3)
Cluster size at WP	(2.19 ± 0.04)	(2.27 ± 0.05)	(1.88 ± 0.04)	(1.80 ± 0.04)
Noise at WP [Hz/cm <sup>2</sup> ]	(0.51 ± 0.01)	(0.39 ± 0.01)	(0.44 ± 0.00)	(0.15 ± 0.01)
$J^{WP}$ [pA/cm <sup>2</sup> ]	(30.1 ± 0.1)	(22.2 ± 0.1)	(3.8 ± 0.0)	(10.2 ± 0.0)

Table 5.4: Summary of the characterization measurement performed in Ghent on CMS RPC detectors foreseen to be used at GIF++ for longevity studies of the present system. For each detector, the working voltage, defined as in Formula 4.25, was extracted from sigmoid fits performed in Figure 5.23a and the values of efficiency, cluster size, noise rate and current density at this voltage are reported.

### 5.3.2 RPC test setup

3386 For an easy manipulation of the detectors, a trolley with a structure containing slots in which the  
 3387 RPCs can be slid vertically and referred to as T1 was used. In this position, each chamber is in a  
 3388 plane perpendicular to the beam line and the source flux as can be seen through Figure 5.24, receiving  
 3389 a uniform irradiation. Moreover the trolley allows for easy movement of the system. Indeed, the  
 3390 position of the trolley varies according to the period of the year.

3391 During the dedicated test beam periods during which GIF++ longevity experiments are in control  
 3392 of the muon beam, the trolley is placed in the upstream region of the bunker, in the beam line, as  
 3393 described through Figure 5.24a. The CMS RPC detectors are the ones being farther away from the  
 3394 source on this side of the source as other detectors need to be certified at higher background rates. An  
 3395 additional trolley, reffered to as T3, containing iRPCs and tracking RPCs is placed in between the  
 3396 source and the trolley containing present CMS RPCs. Indeed, iRPCs need to be certified at higher  
 3397 rates and thus need to be placed closer to the source to receive a stronger irradiation using the same  
 3398 absorber settings. The space on T1 being limited, the tracking RPCs used for extra offline informa-  
 3399 tion during the analysis are placed on the same trolley than iRPCs and are kept at full efficiency at  
 3400 all time to reconstruct muon tracks in correlate them with hits recorded in T1 chambers. The beam  
 3401 trigger system is composed of 2 scintillators placed outside on each side of the bunker and of a third  
 3402 scintillator placed in between T1 and the wall of the bunker along the beam line.

3403 However, most of the year, T1 is placed in the so called *ageing position* corresponding to the

furthest position from the source outside of the beam line, which needs to stay clear during periods where GIF++ doesn't have the control of the beam so that a beam tube can be installed through the bunker, as can be seen in Figure 5.24b. The reason for placing the chambers as far as possible from the source comes from the too high irradiation delivered by the source during the irradiation periods where all the other experiment having placed detectors into the bunker requires to integrate as much charge as possible. Hence, the source is operated with any absorbers. On the contrary, during the test beam periods, all the groups working in GIF++ are interested in operating the source using various absorber settings to study the performance of their detectors under different irradiation conditions. The time spent with a source fully opened and during which the RPCs of T1 are kept at a standby voltage of 6500 V much lower than what necessary to grow avalanches in the gas is then small compared to the time spent with other source settings and during which data can be taken.

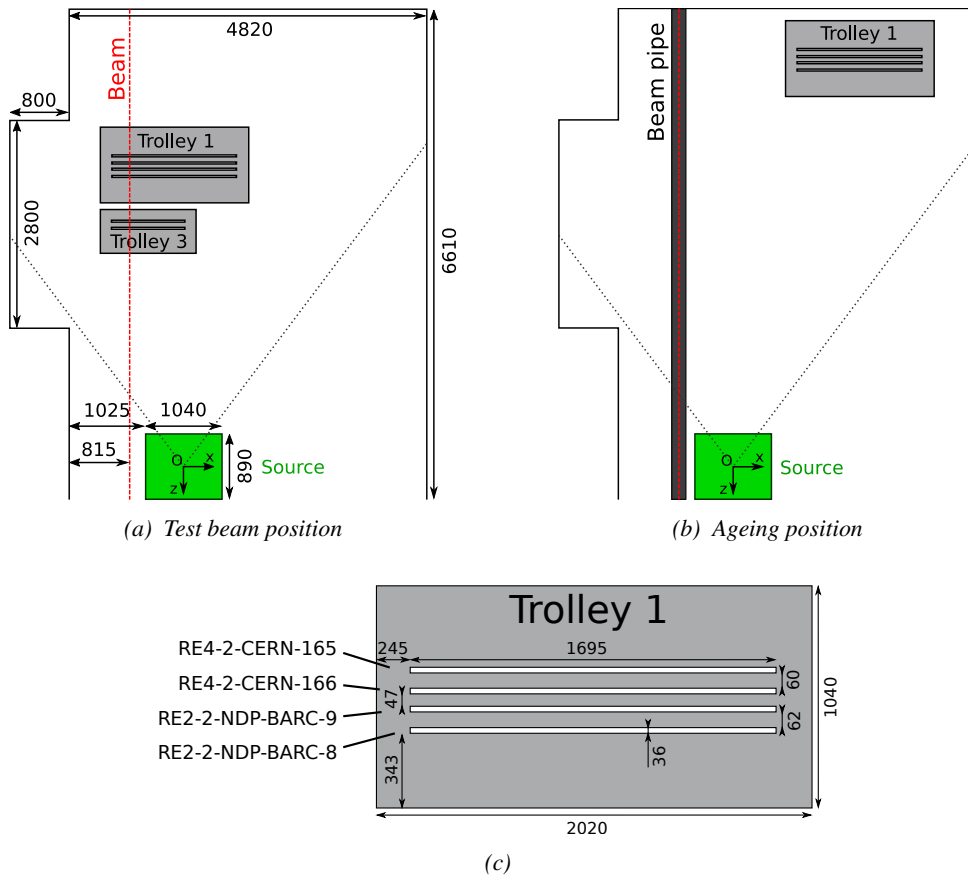


Figure 5.24: CMS RPC setup inside of GIF++ bunker during test beam (Figure 5.24a) and ageing periods (Figure 5.24b). The space in between the RPCs and the source is usually used by other detectors while the space in between T1 and the upstream wall is not filled. Due to the presence of the beam pipe, the trolley is moved away from the beam line during irradiation periods and placed farther away from the source for less intense irradiation. The position of the trolley can vary due to the use of the space by other setups and is then not exact. In the contrary, the position of the chambers in the trolley is fixed and given in Figure 5.24c.

From the bunker area, the detectors are connected to the service area, visible in Figure 5.6, through the wooden floor thanks to long cable. The service area hosts all the high and low voltage

3417 power supplies, the TDCs and computers used for data acquisition and preliminary offline analysis  
 3418 used to fill the Detector Control Software (DCS) webpage, referred to as WebDCS, with Data Quality  
 3419 Monitoring (DQM) histograms useful for the shifters on duty in the control room located farther in  
 3420 the building, away from the beam lines, as well as the gas system required for the gaseous detectors  
 3421 installed in GIF++ [272]. The detectors read-out is, as in the case of GIF, connected to V1190A  
 3422 VME TDCs communicating with the DAQ computer thanks to a V1718 VME bridge manufactured  
 3423 by CAEN. Moreover, a constant monitoring of all the environmental parameters, in different points  
 3424 of the bunker area, gas parameters, to control its composition, temperature and pressure, and of the  
 3425 voltages and currents delivered by the power supplies is performed and displayed on the homepage  
 3426 of the WebDCS interface.

### 3427 5.3.3 GIF++ data flow

3428 At GIF++, the CMS RPC R&D experiment collects different types of data coming from the detectors  
 3429 monitored parameters, such as voltage and currents, the gas, source, and environmental parameters,  
 3430 and, of course, the TDC data in which are collected the actual muon and gamma physics. These  
 3431 different data sources compose three different data flows as presented in Figure 5.25.

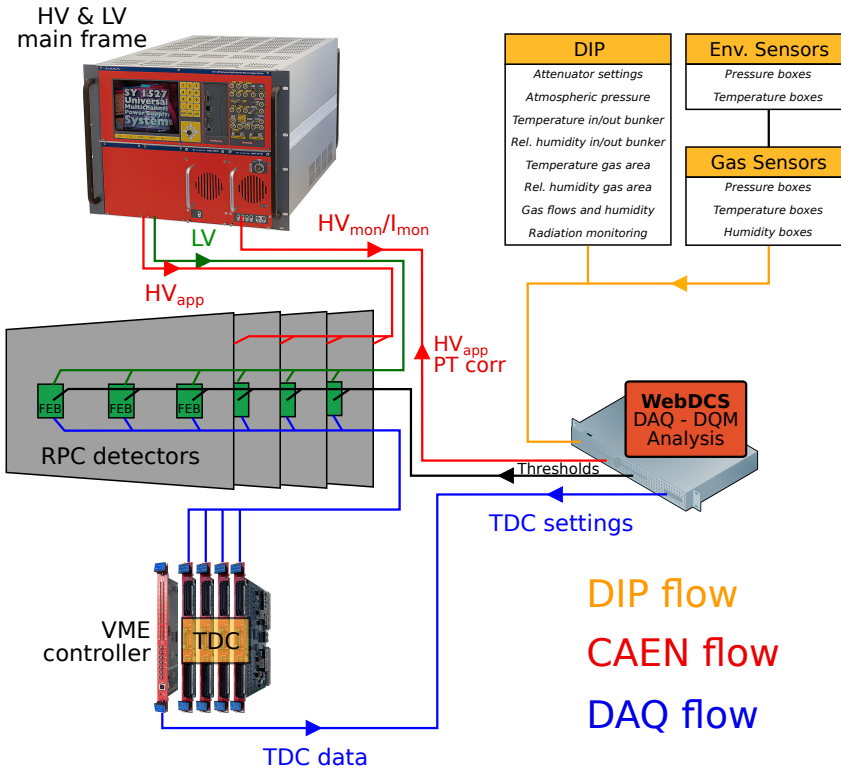


Figure 5.25: Visualisation of the main data flows in GIF++. The yellow flow lines correspond to the DIP flow used for source, environmental and gas information. The red flow lines are for the CAEN flow through which the WebDCS communicates the voltages to be applied on the detectors using pressure and temperature information and retrieves the monitored voltages and currents. Finally, the blue flow lines correspond to the DAQ flow through which the RPC data is collected from the TDCs by the computer.

3432 The *DIP flow*, DIP being a communication system allowing for exchange of real-time information  
 3433 between systems, concerns all the data coming from the gas composition, temperature and humidity, the environmental temperature and pressure, the source settings and the radiation monitoring sensors. The experimental area is in charge of measuring, storing and distributing the data  
 3434 of interest for all of the users of the facility (source settings, radiation monitoring, gas composition  
 3435 at the exit of the gas mixer and general environmental information). Retrieving this data is done by  
 3436 accessing to the database of the experimental hall in which GIF++ is located through DIP communica-  
 3437 tion. More specific data such as gas flow, temperature and humidity at the level of the detectors  
 3438 (upstream and downstream of the detectors) as well as environmental parameters are at the charge  
 3439 of the users. For this reason, several pressure, temperature and humidity sensors were installed on  
 3440 the gas distribution system of the RPC trolleys. The corresponding data flow, although not related  
 3441 to DIP itself, is saved together with the DIP data into the local CMS RPC database and displayed  
 3442 on the front page of the WebDCS together with alerts in the case the values measured are out of  
 3443 optimal working range. The data is particularly important to perform the PT correction described in  
 3444 Section 4.4 of Chapter 4 and keep stable the effective voltage of the detectors. Monitoring history  
 3445 plots are made using JavaScript are also displayed for an easy access to past information, as  
 3446 showed in Figure 5.26.  
 3447

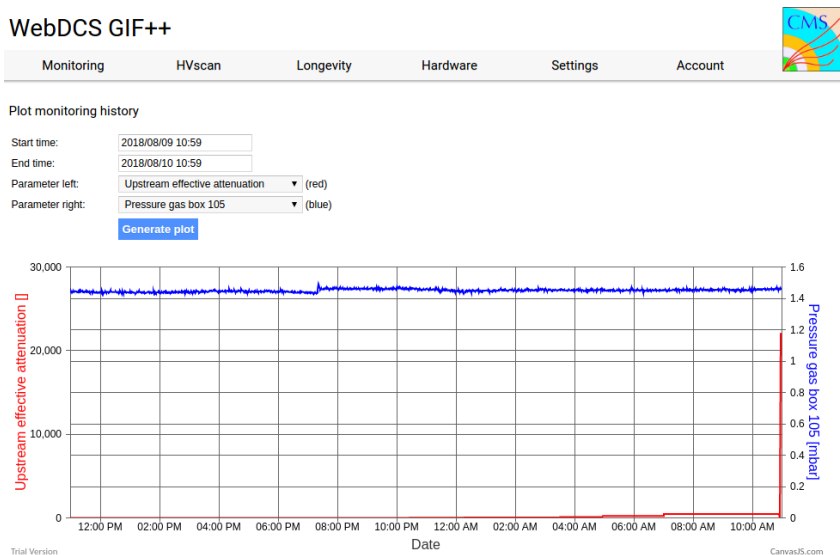


Figure 5.26: *DIP monitoring history accessed through GIF++ WebDCS interface.*

3449 The data flow related to the monitoring of the detector high voltages and currents, referred to  
 3450 as *CAEN flow* as a reference to the manufacturer of power supplies, is retrieved thanks to computer  
 3451 to main frame communications. Indeed, during the operations (irradiation or beam period), these  
 3452 values can be accessed directly through the bus of the main frame hosting the high voltage supplies.  
 3453 Finally, the DAQ flow concerns all data acquired through the use of the TDCs, i.e. all the muon or  
 3454 gamma data recorded by the detectors under test at GIF++.

### 3455 5.3.4 Measurements performed during beam periods

3456 As previously described, two types of measurement are performed on the chambers during beam  
 3457 periods. On one hand, it is interesting to measure the efficiency of the RPCs with increasing voltage  
 3458 with different source absorber settings but on the other hand, it is important to correlate the efficiency  
 3459 information to the gamma rate seen by the chambers at the voltages that were scanned for efficiency.  
 3460 The choice was made to separate efficiency measurements from rate measurements to better manage  
 3461 time and data volume. In both cases, TDC data recorded during so called *HV scans* is divided into  
 3462 *runs*, one for each high voltage point, whose data is stored into ROOT files. The TDC settings  
 3463 used during both these scans as well as the ROOT data structure are detailed in Section A.4.2 of  
 3464 Appendix A.

3465 The goal of both efficiency and rate scans is to measure the rate capability of the detectors but  
 3466 also to monitor any degradation of the performance due to ageing. This way, during test beam  
 3467 periods the efficiency and corresponding gamma background are measured to correlate the evolution  
 3468 of rate capability at different stages of irradiation. In the absence of other signs of ageing, a reduction  
 3469 of the rate capability could be related to an increase of the electrodes resistivity.

#### 3470 5.3.4.1 Efficiency scans

3471 The HV scans performed to specifically measure the muon detection efficiency under different ir-  
 3472 radiation conditions follow a standardized procedure. Data using the DAQ is taken at the same 12  
 3473 HV points for all chambers, ranging from 9 kV to 10.1 kV by steps of 100 V. For each HV run,  
 3474 a minimum of 5000 muon beam triggers, provided by the coincidence of the three scintillators, is  
 3475 required in order to accumulate enough statistics for a reliable computation of the efficiency of the  
 3476 detectors. In addition to the four RPCs held on T1, two tracking RPCs installed on T3 are kept at  
 3477 a fixed voltage of 9.7 kV to provide the analysis software [273] with beam position information to  
 3478 exclude off-track signals. The tracking RPCs, whose design is based on which of CMS RPCs, are  
 3479 double gap detectors featuring 2 mm HPL electrodes and 2 mm gas gaps. Finally, the monitored  
 3480 currents and voltages are recorded in histograms along the TDC data in a different ROOT file for  
 3481 each run.

3482 HV scans are taken for different source settings as the goal is to irradiate all the detectors with a  
 3483 minimal rate of 600 Hz/cm<sup>2</sup>. Usually, a full study of the performance of the detectors is performed  
 3484 with Source OFF, and then with nine absorber settings that attenuate the nominal gamma flux by  
 3485 factors from more than 200 to only 3, settings with fully opened source being avoided with RPCs  
 3486 in test beam position. Adjusting the gamma flux is possible thanks to the three layers of absorbers  
 3487 featured on the Cesium source [274].

#### 3488 5.3.4.2 Rate scans

3489 These background measurements are performed using a similar HV scan procedure than in the case  
 3490 of efficiency measurements. The HV scan in test beam period will be taken fewer HV points than  
 3491 for the efficiency scans as the region of interest is located around the knee and efficiency plateau  
 3492 of the detectors in order to extract through linear interpolation the value of the rate at the working  
 3493 voltage deduced from the efficiency scan. Thus, these scans are performed only on six HV points  
 3494 ranging from 9.5 kV to 10 kV. Rate scans are substantially heavier than efficiency scans. Indeed, a  
 3495 good estimation of the rate requires a long enough integrated time worth of data. The way data is  
 3496 collected, detailed in Appendix A, makes the DAQ search for data stored in the TDC buffers prior to

3497 the trigger signal. The time window from which the data is collected ranges in between only 25 ns  
 3498 to more than 50  $\mu$ s. The Cesium source delivering a consistent gamma flux, it was decided than a  
 3499 total integrated time of 0.2 s would be enough to have a reliable calculation of the  $\gamma$  rate. This is  
 3500 achieved by taking 20,000 random trigger pulses delivered by a pulse generator at a frequency of  
 3501 300 Hz while extracting 10  $\mu$ s of data from the buffers for each trigger.

3502 Separating rate measurements from efficiency measurement was motivated by the inconsistency  
 3503 of the muon beam provided in GIF++. Using periods without beam to measure rates with a good  
 3504 statistics allows for faster study programs. Moreover, depending on the muon strength that can  
 3505 strongly vary due to users placed upstream of GIF++ and using magnets, the number of muon de-  
 3506 livered per beam spill can make the accumulation of 20,000 events too long for the other users of  
 3507 GIF++. Hence, efficiency scans are performed with lower statistics, and the time window from which  
 3508 the data is extracted is strongly reduced (400ns for efficiency scans versus 10  $\mu$ s for rate scans) to  
 3509 keep the data size to its bare minimum.

### 3510 5.3.4.3 Offline analysis and Data Quality Monitoring

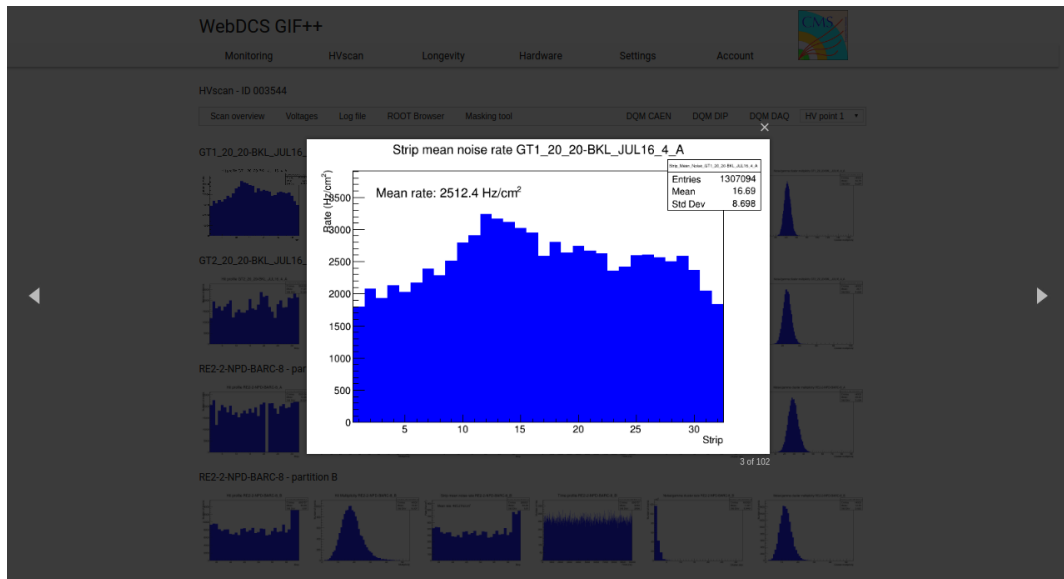
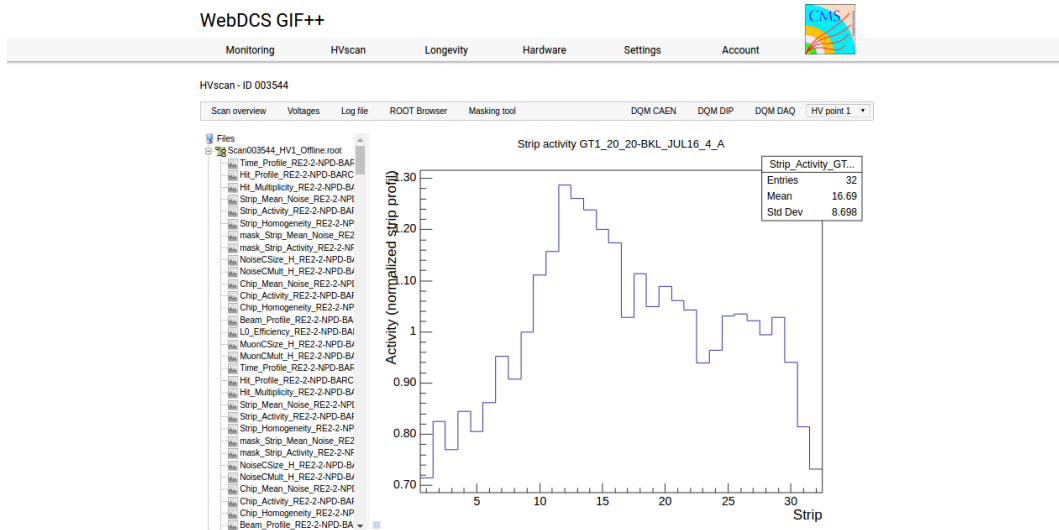


Figure 5.27: Example of DQM page available on CMS RPC WebDCS in GIF++. The rate measured in one of the tracking chambers, namely GT1\_20\_20-BKL\_JUL16\_4, is presented here. The DQM page allows clicking on each histogram to extend its view and to navigate through the histograms thanks to the left and right arrows.

3511 The data recorded during efficiency and rate scans always consist in two ROOT files per run, a run  
 3512 corresponding to a HV point. One of the files corresponds to the TDC data, a collection of hits  
 3513 per active channel on the read-out of the RPCs, while the second is the CAEN main frame data,  
 3514 offering a monitoring of the currents and high voltages. This data is systematically analysed at the  
 3515 end of each scan thanks to the Offline Analysis tool of GIF++, detailed in Appendix B, that produces  
 3516 histograms such as hit, rate and time profiles, hit multiplicities, gamma cluster sizes or multiplicities  
 3517 for the DQM display of the WebDCS, as showed in Figure 5.27. More histograms can be accessed  
 3518 through the ROOT browser included in the WebDCS, as showed in Figure 5.28. Moreover, the

analysis performed thanks to the Offline tool is definitive in the case of evaluating the rates from rate scans. On the contrary, the algorithm for efficiency calculation is kept simple and approximative in the tool as including tracking into the analysis requires manual adjustment for each individual scan.



*Figure 5.28:* Example of DQM ROOT Browser page available on CMS RPC WebDCS in GIF++. The strip activity profile, defined as the rate profile normalized to the mean rate, in one of the tracking chambers, namely GT1\_20\_20-BKL\_JUL16\_4, is presented here. Available ROOT files and histograms can be browsed thanks to the left panel showing the directory and files structures.

### 5.3.5 Measurements performed during irradiation periods

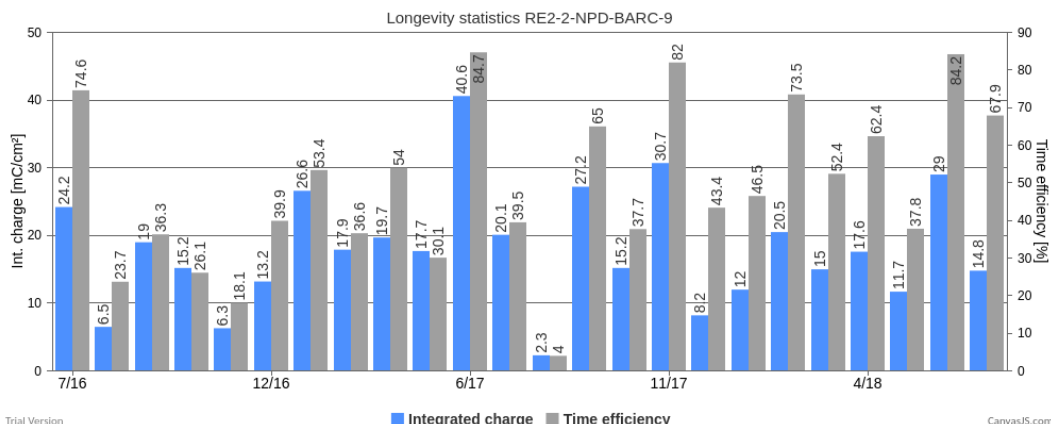


*Figure 5.29:* Longevity statistics of chamber RE2-2-NPD-BARC-9 in GIF++. For each month since July 2017, the integrated charge (in blue) as well as the time efficiency of irradiation (in gray) is reported.

Even though test beam periods are stressful times has an extensive data taking planing needs to be finalized in a short amount of time, the biggest amount of data comes from irradiation periods. Indeed, when T1 is moved back to its ageing position in between each test beam periods, data is recorded at any time the source can be switched ON for irradiation. Indeed, other experiments in the area might prevent the source from staying opened continuously. As an example, the time efficiency of irradiation of CMS RPC detectors in GIF++ is presented in Figure 5.29.

Several types of measurement are performed throughout the irradiation period. Indeed, as long as the detectors are being irradiated, a monitoring of the currents is performed to evaluate the corresponding integrated charge considering the irradiation time. Moreover, the corresponding gamma rates need to be measured on a regular basis. Ageing signs can be understood through an increase of the detector noise correlated with an increased dark current. For this purpose, HV scans are performed to measure the noise with increasing voltage and the dark currents. Another way to highlight ageing is through the loss of rate capability of the detectors. During irradiation periods this can be looked through thanks to HV scans performed at various source settings, which are referred to as *source scans*. The loss in rate capability could be understood by a saturation of the measured at higher gamma flux. This effect could be correlated with an increase of the electrodes resistivity. The resistivity is then measure periodically during the year, generally before or after test beam periods by the use of Argon breakdown technic.

### 5.3.5.1 Longevity scans

The main activity of irradiation periods consists in the *longevity scans* during which the currents of the irradiated chambers are continuously monitored. The two irradiated chambers, RE2–2–NPD–BARC–09 and RE4–2–CERN–166, are both brought to a voltage of 9.8 kV while the source flux can vary depending on the need of experiments using the facility. The currents are recorded on each active gas volume and each gap contribution is then translated into the mean chamber integrated charge as can be seen from Figure 5.30. At the end of each longevity scan the integrated charge accumulated in each chamber is used to update the summary plots providing the collaboration with official results to be spread.

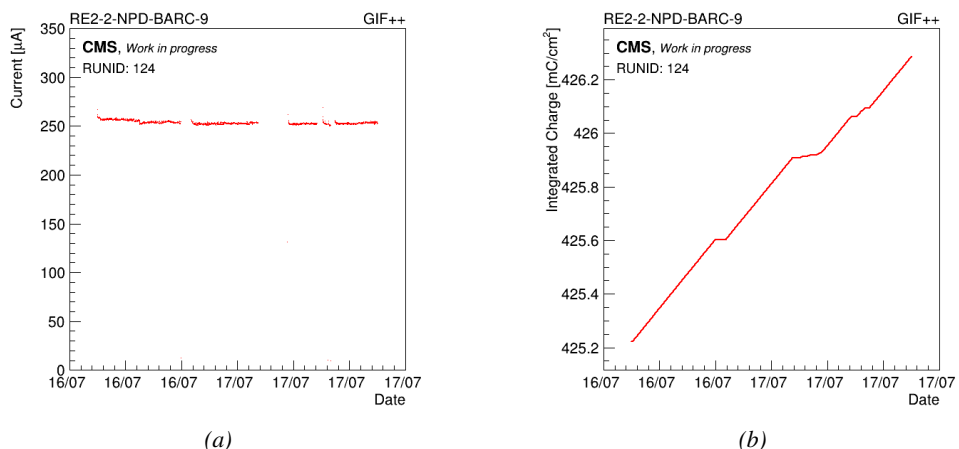


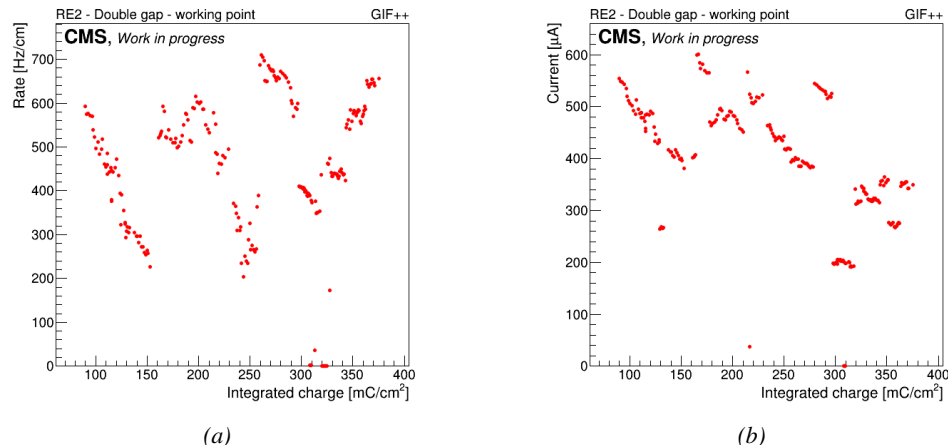
*Figure 5.30: Example of current monitoring (Figure 5.30a) and of corresponding integrated charge (Figure 5.30b) of chamber RE2–2–NPD–BARC–09. The decrease of current is related to a decrease of the voltage due to the daily rate scan procedure or to periods during which the source was turned OFF.*

### 3550 5.3.5.2 Daily rate monitoring scans

3551 Every night during longevity scans, the DAQ is used to perform *daily rate scans*. These scans aim  
 3552 at keeping track of the gamma rate measured in the irradiated RPCs during longevity but is also  
 3553 measured the noise rate at standby voltage and this, for each gap individually. The procedure for  
 3554 these HV scans consist in 9 runs for which 50,000 random triggers are requested, corresponding to  
 3555 0.5 s of total integrated time.

- 3556 1- All gaps are first left at the irradiation voltage of 9.8 kV to measure the  $\gamma$  rate.
- 3557 2- Then all gaps are brought to the standby voltage of 6.5 kV to measure the noise rate of the full  
 detectors.
- 3559 3- Both top gaps (TW and TN) are brought to a voltage equivalent to an OFF status, i.e. 1 kV so  
 3560 that the noise contribution of only the bottom gap at standby voltage can be measured.
- 3561 4- The bottom gaps are ramped up toward the working voltage of 9.8 kV to measure their contri-  
 3562 bution to the gamma rate estimation.
- 3563 5-8 The steps 3 and 4 are repeated on TN and then on TW, keeping the bottom and the top gap  
 3564 which is not of interest at a voltage of 1 kV. This way, the individual contribution to the noise  
 3565 and gamma rates are known.
- 3566 9- Finally, both TW and TN are brought to working voltage while the bottom gap is left at 1 kV  
 3567 to measure the gamma rate for the full top layer at once.

3568 Finally, the voltages of all gaps are brought back to working voltage for the longevity program  
 3569 to continue until the next daily scan.



3570 *Figure 5.31: Example of rate (Figure 5.31a) and current (Figure 5.31b) monitoring of chamber  
 3571 RE2-2-NPD-BARC-09 with increasing integrated charge. The variations of the rate and current are cor-  
 3572 related and corresponds to change of source irradiation, gas flow, gas humidity, or environmental conditions.*

3570 Naturally, as this data is taken using GIF++ DAQ, two ROOT files containing the DAQ data and  
 3571 CAEN data are created for each runs in the exact same way than for efficiency or rate scans taken  
 3572 during test beam periods but while the currents are still monitored by the longevity scan and saved

3573 into GIF++ database for an easy evaluation of the currents to the integrated charge. The Offline  
 3574 Analysis tool provides then the DQM page with histograms and daily values can be assembled in  
 3575 long term monitoring plots to study the variations of rate and current with increasing integrated  
 3576 charge, as presented in Figure 5.31. The rates on every single read-out channel are also tracked to  
 3577 control their activity with increasing integrated charge and, this way, understand the appearance of  
 3578 hot spots through noisy channels, as showed in Figure 5.32.

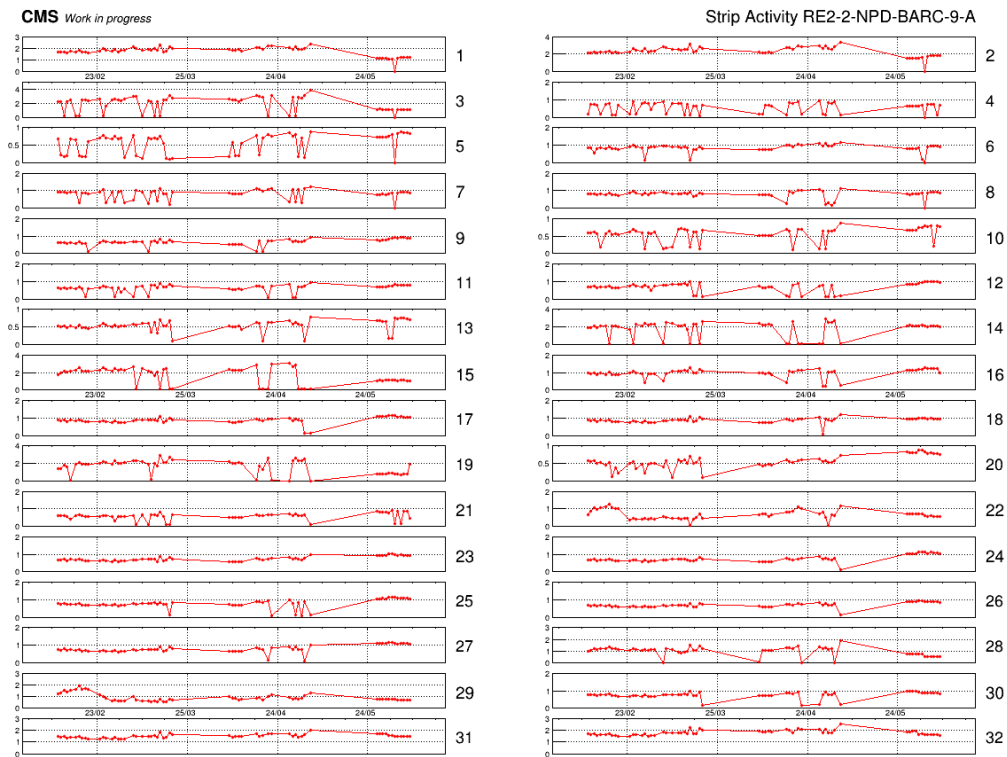


Figure 5.32: Example of strip activity of chamber RE2-2-NPD-BARC-09 monitoring through time. The activity of a strip is defined as the rate of the individual channel normalized to the mean rate measured in the corresponding read-out partition.

### 3579 5.3.5.3 Weekly noise monitoring scans

3580 Once a week, the source is turned OFF for the CMS RPC to make a noise scan, which consist  
 3581 into a HV scan composed of seven runs and involving both the irradiated but also the reference  
 3582 chambers, providing with a weekly monitoring of the evolution of the irradiated chambers noise and  
 3583 dark current. The first run is taken at standby voltage for all chambers while the next 6 runs are taken  
 3584 with voltages ranging from 9.4 to 9.9 kV in order to have for both type of chambers, RE2 and RE4, a  
 3585 coverage of the noise rate in the voltage region in which the efficiency rises and reaches the plateau.

### 3586 5.3.5.4 Weekly source scans

3587 Directly following the weekly noise scans, HV rate scans are organised at three different source set-  
 3588 tings, usually corresponding to ABS 6.8, 4.6 and 3.3. The procedure of these HV scans is strictly

3589 similar to which of weekly noise scans, involving the four RPCs in order to have a weekly com-  
 3590 parison of the values recorded in every chamber. Measuring with all detectors at the same time  
 3591 allows getting rid of potential systematics that might make the rates (noise or gamma) vary from one  
 3592 measurement to another. If such systematic effect occurs, it will be observed in all detectors.

### 3593 5.3.5.5 Weekly current scans

3594 The previously detailed daily rate scans, but also the weekly noise and source scans are interesting  
 3595 tools to look at an increase of noise rates and dark currents or at a loss of rate capability and point  
 3596 to an increase of surface resistivity of the electrodes through the absorption of hydrofluoric acid.  
 3597 Nevertheless, periodically measuring the currents on wider high voltage ranges allows to have access  
 3598 to the ohmic part of the current driven by the detectors related to the electrodes resistance. This is  
 3599 why precise current scans, consisting only in measuring the current driven through the four detectors,  
 3600 are performed each week. The scan procedure consists in 131 high voltage steps in between 500 V  
 3601 and 10 kV by steps of 100 V until the standby voltage of 6.5 kV is reached and then by steps of  
 3602 50 V. The current increase in between 500 V and the voltage where charge multiplication starts to  
 3603 occur is only driven by the resistance of the detector to current and thus increases linearly. A fit on  
 3604 this linear increase of the currents in the range before charge multiplication occurs gives access to  
 3605 the resistance of the system electrodes/gas. If any variation of the electrode resistance occurs, the  
 3606 global resistance will increase and so will the current. Technically, these scans will record a ROOT  
 3607 file per HV step that will have the same format than the CAEN ROOT file saved during other HV  
 3608 scans and is also analysed using the Offline Analysis tool to provide with DQM histograms as well  
 3609 as standardised  $I/V$  tables.

### 3610 5.3.5.6 Resistivity measurements

3611 Aside of the parameters monitored to spot ageing, the resistivity of the HPL planes is measured  
 3612 regularly before or after test beam periods through high voltage scans of the detectors operated  
 3613 with pure Argon. The electric field strength at which Argon breaks down being well known, the  
 3614 breakdown voltage in the detectors is measured and gives an information about the resistance of the  
 3615 electrodes, as above the breakdown voltage Argon turns into a conductive plasma and thus does not  
 3616 offer electric resistance anymore, which then can be used to calculate the resistivity of the electrode  
 3617 material. The Argon line in GIF++ are not kept humid and thus this measurement is not performed  
 3618 too often to make sure the electrodes don't dry out, leading to an increase of the electrode resistivity.

## 3619 5.3.6 Results and discussions

3620 Since 2015, CMS RPCs have been irradiated in GIF++ with the goal to reach a total integrated  
 3621 charge per irradiated detector of  $0.84 \text{ C/cm}^2$  while certifying the detectors to a rate capability of  
 3622  $600 \text{ Hz/cm}^2$ . As of today, the RE2 and RE4 chambers respectively achieved 51 and 26% of the  
 3623 total irradiation program. A few years of irradiation are expected before reaching the end of the  
 3624 longevity study and a final answer on whether the detector will be able to live through HL-LHC or  
 3625 not. A negative answer to this question would probably lead to solutions to replace the detectors  
 3626 before HL-LHC or to improve the shielding of these detectors against background radiation in the  
 3627 experimental cavern, which could be a more sustainable solution.

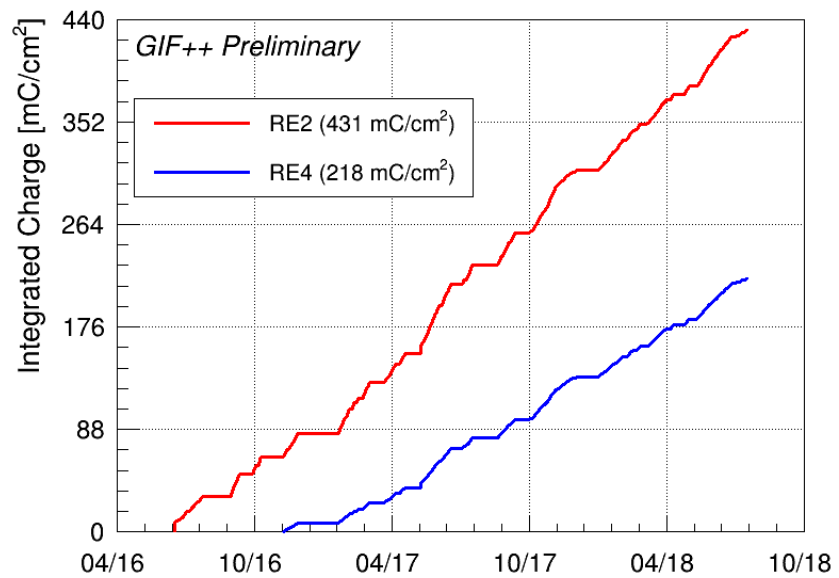


Figure 5.33: Total integrated charge in the irradiated RPCs, RE2–2–NPD–BARC–9 and RE4–2–CERN–165, before starting August 2018 test beam period. The irradiation of the RE2 chamber started in June 2016 while the RE4 chamber couldn't be irradiated before November 2016.



# 6

3628

3629

3630

## Improved RPC investigation and preliminary electronics studies

3631 The extension in the endcap of the RPC sub-system towards higher pseudo-rapidity will bring the  
3632 new detectors to be exposed to much more intense background radiations due to the proximity of  
3633 the detectors with the beam line (Figure 3.5). The challenge will be to produce high counting rate  
3634 detectors with limited ageing rate to ensure a stable operation of the detector over a period longer  
3635 than ten years. In Chapter 4 was discussed the influence of the detector design (number and thickness  
3636 of gas volumes, OR system, etc...) on the charge deposition and rate capability. Nevertheless, this  
3637 question can also be addressed from the electronics point of view as a better signal to noise ratio  
3638 would also mean the possibility to greatly lower the charge threshold on the signals to be detected,  
3639 allowing to use the detector at lower gain, hence lowering the charge deposition per avalanche in the  
3640 gas volume. Cardarelli showed that the production of low-noise fast FEEs could help decreasing the  
3641 charge deposition per avalanche at working voltage by an order of magnitude, virtually increasing  
3642 the life expectancy of such a detector in the same way [275].

### 3643 **6.1 FEE candidate for the production of iRPCs**

3644 The extension of the third or fourth endcap disks with improved RPCs has been presented in  
3645 Chapter 3 together with the expected background levels. An important piece of these iRPCs will be  
3646 the Front-End Electronics that will be equipped on the chambers. A fast, low-jitter and low charge  
3647 sensitive electronics will help in further reducing the charge deposition in the detector by making it  
3648 possible to operate at lower gain.

3649 In the context of the CMS Muon Upgrade, two FEE solutions have been considered to equip the  
3650 iRPCs. The baseline for the RPC upgrade is based on the PETIROC ASIC, initially for Time-of-  
3651 flight (ToF) applications. A back-up solution is also under study and focusses on a new low-noise  
3652 preamplifier designed in INFN laboratories in Rome to replace the preamplification stage of the  
3653 already existing CMS RPC Front-End Board.

The FEEs that are foreseen to equip the new RPCs need to be able to detect charges as small as 10 fC. Not only the new electronics need to be fast and reliable, they also should be able to sustain the high radiation the detectors will be subjected to in the region closest to the beam.

### 6.1.1 CMS RPCROC: the RPC upgrade baseline

Designed by Weeroc, a spin-off company from the french OMEGA laboratory, the PETIROC 2A consists in a fast and low jitter 32-channel ASIC originally developed to read-out Silicon Photomultiplier (SiPM) in ToF applications and that allows for precise time measurements [198, 199]. The ASIC uses an AMS 350 ns SiGe technology. The block diagram of the ASIC is showed on Figure 6.1. A 10-bit DAC allows to adjust the trigger level in a dynamical range spanning from 0.5 to a few tens of photoelectrons and a 6-bit DAC to adjust the response of each individual channel to similar a level.

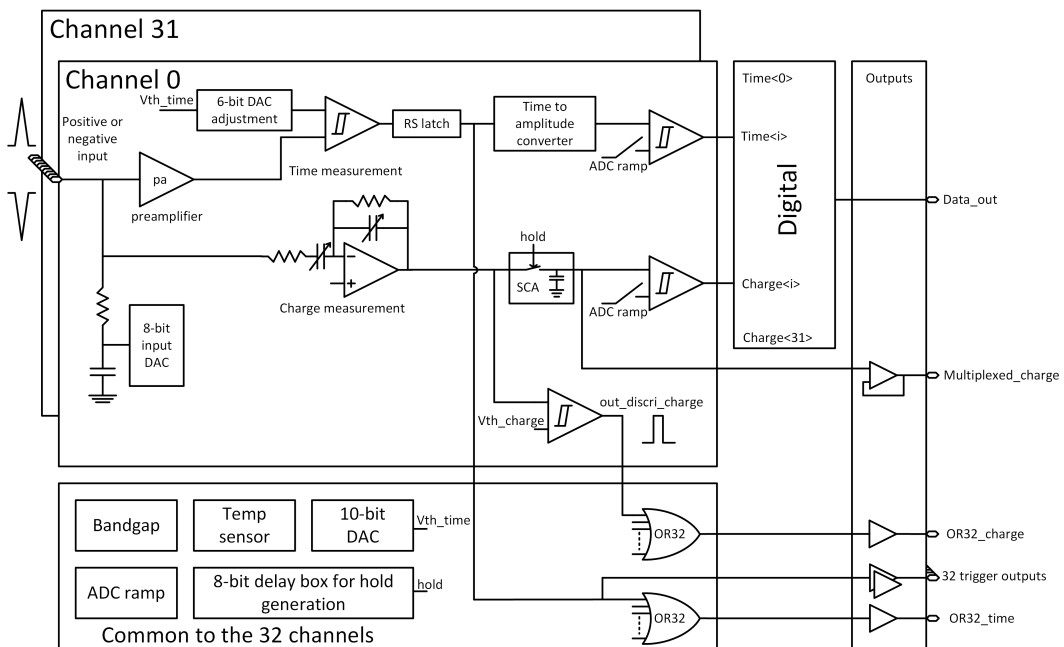


Figure 6.1: PETIROC 2A block diagram.

Nevertheless, in order to adapt this ASIC to CMS, modifications were brought to the PETIROC [177]. In the new CMS RPCROC, the measurement of the charge will be performed by a TimeOverTechnic, taking profit of the capacity the ASIC has in measuring both the leading and trailing edges of the input signals. The dynamic range will be expanded towards lower values to allow for the detection of charges as low as 10 fC. Due to the radiation levels that are foreseen at the level of the iRPCs, the SiGe technology will be replaced by the Taiwan Semiconductor Manufacturing Company (TSMC) 130 nm CMOS, to increase its radiation hardness while keeping fast pre-amplification and discrimination with a very low jitter that can reach less than 20 ps if no internal clock is used, as can be seen from Figure 6.2. The ASIC is associated with an FPGA which purpose is to measure time thanks to a TDC with a time resolution of 50-100 ps developed by Tsinghua University and that will provide a measurement of the signal position along the strip with a precision of a few cm by measuring the

3676 signal timing on both ends of the strips. In order to read-out all 96 strips, 3 ASICs and 3 TDCs, each  
 3677 having an increased number of 64-channels, are hosted on a FEB attached to the chamber.

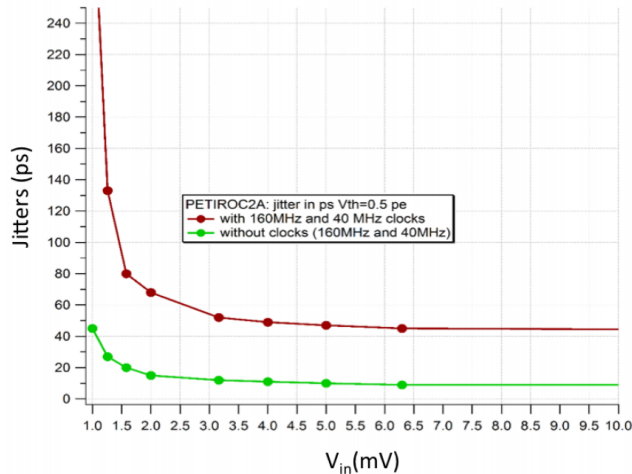


Figure 6.2: The PETIROC time jitter as a function of the input signal amplitude, measured with and without internal clocks.

3678 **6.1.2 INFN Front-End Electronics: a robust back-up solution**

3679 **6.2 Preliminary tests at CERN**



# 7

3680

3681

## Conclusions and outlooks

3682 **7.1 Conclusions**

3683 **7.2 Outlooks**



# A

3684

3685

## A data acquisition software for CAEN VME TDCs

3686

3687 Certifying detectors in the perspective of HL-LHC required to develop tools for the GIF++ experi-  
3688 ment. Among them was the C++ Data Acquisition (DAQ) software that allows to make the commu-  
3689 nications in between a computer and TDC modules in order to retrieve the RPC data [276]. In this  
3690 appendix, details about this software, as of how the software was written, how it functions and how  
3691 it can be exported to another similar setup, will be given.

### 3692 A.1 GIF++ DAQ file tree

3693 GIF++ DAQ source code is fully available on github at [https://github.com/afagot/GIF\\_](https://github.com/afagot/GIF_DAQ)  
3694 DAQ. The software requires 3 non-optional dependencies:

- 3695 • CAEN USB Driver, to mount the VME hardware,  
3696 • CAEN VME Library, to communicate with the VME hardware, and  
3697 • ROOT, to organize the collected data into a TTree.

3698 The CAEN VME library will not be packaged by distributions and will need to be installed man-  
3699 ually. To compile the GIF++ DAQ project via a terminal, from the DAQ folder use the command:

```
3700 mkdir build  
3701 cd build  
3702 cmake ..  
3703 make install
```

3702 The source code tree is provided below along with comments to give an overview of the files' con-  
3703 tent. The different objects created for this project (`v1718`, `v1190a`, `IniFile` & `DataReader`) will be

3704 described in details in the following sections.

3705



## 3706 A.2 Usage of the DAQ

3707 GIF++ DAQ, as used in GIF++, is not a standalone software. Indeed, the system being more com-  
 3708 plexe, the DAQ only is a sub-layer of the software architecture developped to control and monitor  
 3709 the RPCs that are placed into the bunker for performance study in an irradiated environment. The top  
 3710 layer of GIF++ is a Web Detector Control System (webDCS) application. The DAQ is only called  
 3711 by the webDCS when data needs to be acquired. The webDCS operates the DAQ through command  
 3712 line. To start the DAQ, the webDCS calls:

3713

3714    bin/daq /path/to/the/log/file/in/the/output/data/folder

3715 where /path/to/the/log/file/in/the/output/data/folder is the only argument required. This  
 3716 log file is important for the webDCS as this file contains all the content of the communication of the  
 3717 webDCS and the different systems monitored by the webDCS. Its content is constantly displayed  
 3718 during data taking for the users to be able to follow the operations. The communication messages  
 3719 are normally sent to the webDCS log file via the functions declared in file `MsgSvc.h`, typically  
 3720 `MSG_INFO(string message)`.

3721

### 3722 A.3 Description of the readout setup

3723 The CMS RPC setup at GIF++ counts 5 V1190A Time-to-Digital Converter (TDC) manufactured  
 3724 by CAEN [264]. V1190A are VME units accepting 128 independent Multi-Hit/Multi-Event TDC  
 3725 channels whose signals are treated by 4 100 ps high performance TDC chips developed by CERN  
 3726 / ECP-MIC Division. The communication between the computer and the TDCs to transfer data is  
 3727 done via a V1718 VME master module also manufactured by CAEN and operated from a USB  
 3728 port [265]. These VME modules are all hosted into a 6U VME 6021 powered crate manufactured by  
 3729 W-Ie-Ne-R than can accommodate up to 21 VME bus cards [277]. These 3 components of the DAQ  
 3730 setup are shown in Figure A.1.

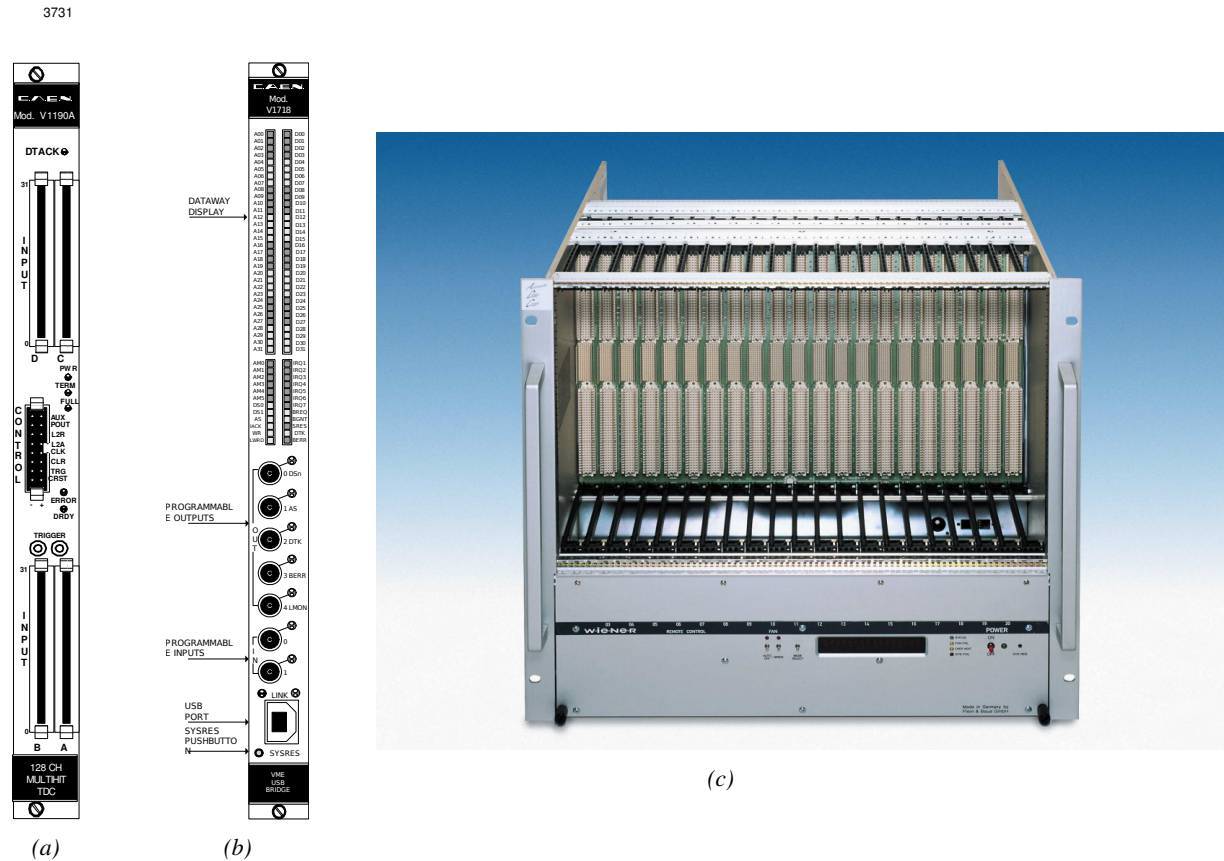


Figure A.1: (A.1a) View of the front panel of a V1190A TDC module [264]. (A.1b) View of the front panel of a V1718 Bridge module [265]. (A.1c) View of the front panel of a 6U 6021 VME crate [277].

### 3732 A.4 Data read-out

3733 To efficiently perform a data readout algorithm, C++ objects to handle the VME modules (TDCs  
 3734 and VME bridge) have been created along with objects to store data and read the configuration file  
 3735 that comes as an input of the DAQ software.

### A.4.1 V1190A TDCs

The DAQ used at GIF takes profit of the *Trigger Matching Mode* offered by V1190A modules. This setting is enabled through the method `v1190a::SetTrigMatching (int ntdcs)` where `ntdcs` is the total number of TDCs in the setup this setting needs to be enabled for (Source Code A.1). A trigger matching is performed in between a trigger time tag, a trigger signal sent into the TRIGGER input of the TDC visible on Figure A.1a, and the channel time measurements, signals recorded from the detectors under test in our case. Control over this data acquisition mode, explained through Figure A.2, is offered via 4 programmable parameters:

- **match window:** the matching between a trigger and a hit is done within a programmable time window. This is set via the method  
`void v1190a::SetTrigWindowWidth(Uint windowHeight, int ntdcs)`
- **window offset:** temporal distance between the trigger tag and the start of the trigger matching window. This is set via the method  
`void v1190a::SetTrigWindowWidth(Uint windowHeight, int ntdcs)`
- **extra search margin:** an extended time window is used to ensure that all matching hits are found. This is set via the method  
`void v1190a::SetTrigSearchMargin(Uint searchMargin, int ntdcs)`
- **reject margin:** older hits are automatically rejected to prevent buffer overflows and to speed up the search time. This is set via the method  
`void v1190a::SetTrigRejectionMargin(Uint rejectMargin, int ntdcs)`

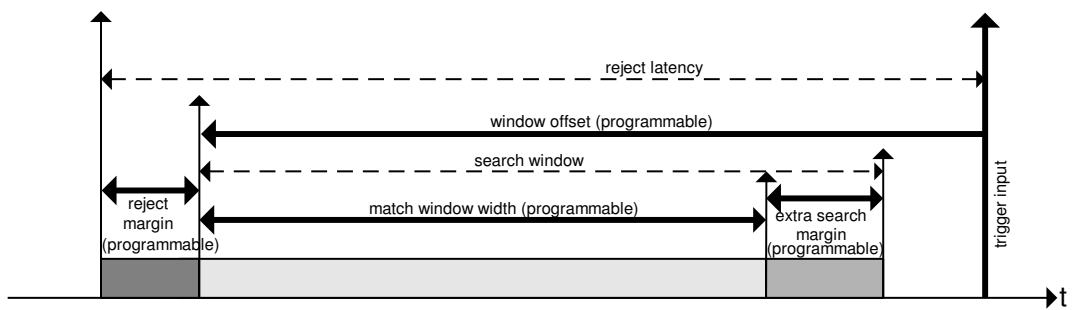


Figure A.2: Module V1190A Trigger Matching Mode timing diagram [264].

Each of these 4 parameters are given in number of clocks, 1 clock being 25 ns long. It is easy to understand at this level that there are 3 possible functioning settings:

- **1:** the match window is entirely contained after the trigger signal,
- **2:** the match window overlaps the trigger signal, or
- **3:** the match window is entirely contained before the trigger signal as displayed on Figure A.2.

In both the first and second cases, the sum of the window width and of the offset can be set to a maximum of 40 clocks, which corresponds to 1  $\mu$ s. Evidently, the offset can be negative, allowing

3764 for a longer match window, with the constraint of having the window ending at most 1  $\mu$ s after the  
3765 trigger signal. In the third case, the maximum negative offset allowed is of 2048 clocks (12 bit) cor-  
3766 responding to 51.2  $\mu$ s, the match window being strictly smaller than the offset. In the case of GIF++,  
3767 the choice has been made to use this last setting by delaying the trigger signal. During the studies  
3768 performed in GIF++, both the efficiency of the RPCs, probed using a muon beam, and the noise or  
3769 gamma background rate are monitored. The extra search and reject margins are left unused.

3770 To probe the efficiency of RPC detectors, the trigger time tag is provided by the coïncidence of  
3771 scintillators when a bunch of muons passes through GIF++ area is used to trigger the data acquisi-  
3772 tion. For this measurement, it is useful to reduce the match window width only to contain the muon  
3773 information. Indeed, the delay in between a trigger signal and the detection of the corresponding  
3774 muon in the RPC being very contant (typically a few tens of ns due to jitter and cable length), the  
3775 muon signals are very localised in time. Thus, due to a delay of approximalety 325 ns in between  
3776 the muons and the trigger, the settings were chosen to have a window width of 24 clocks (600 ns)  
3777 centered on the muon peak thanks to a negative offset of 29 clocks (725 ns).

3778 On the otherhand, monitoring the rates don't require for the DAQ to look at a specific time window.  
3779 It is important to integrate enough time to have a robust measurement of the rate as the number of  
3780 hits per time unit. The triggering signal is provided by the pulse generator integrated into the com-  
3781 munication module V1718 at a frequency of 100 Hz to ensure that the data taking occurs in a random  
3782 way, uncorrelated with beam physics, to probe only the irradiation spectrum on the detectors. The  
3783 match window is set to 400 clocks (10  $\mu$ s) and the negative offset to 401 clocks as it needs to exceed  
3784 the value of the match window.

3785

3786 The v1190a object, defined in the DAQ software as in Source Code A.1, offers the possil-  
3787 ity to store all TDCs in the readout setup into a single object containing a list of hardware ad-  
3788 dresses (addresses to access the TDCs' buffer through the VME crate) and each constructor and  
3789 method acts on the list of TDCs to set the different acquisition parameters as describe above.  
3790 The type of trigger matching is chosen with `v1190a::SetTrigMatching()` and the time substrac-  
3791 tion, used to have a time measurement referring to the beggining of the time window, is set by  
3792 `v1190a::SetTrigTimeSubtraction()`. Then, the wiwdow width and offset are respectively set  
3793 thanks to `v1190a::SetTrigWindowWidth()` and `v1190a::SetTrigWindowOffset()`. The rejection  
3794 and extra search margin, even if left unused and hence set to a default value of 0, can be set through  
3795 `v1190a::SetTrigRejectionMargin()` and `v1190a::SetTrigSearchMargin()`. These methods are  
3796 then called in `v1190a::SetTrigConfiguration()` that uses the information contained in the config-  
3797 uration file `IniFile *iniFile` to set the different TDC parameters. A thorough explaination of the  
3798 content of the configuration file is provided in Section A.5.2.

3799

3800 Among the other methods of class `v1190a` can be found a set of the detection mode (`v1190a::SetTDC`  
3801 `DetectionMode()`), of the TDC time resolution (`v1190a::SetTDCResolution()`), of the dead time  
3802 in between two consecutive signals recorded into a single channel (`v1190a::SetTDCDeadTime()`) or  
3803 of the maximal number of signals that can be recorded per event (`v1190a::SetTDCEventSize()`). To  
3804 help with setting these parameters, `enum` were used (`EdgeMode`, `Resolution`, `DeadTime` and `HitMax`  
3805 are defined in `include/v1190a.h`).

```

3806
class v1190a
{
private :
    long Handle;
    vector<Data32> Address;
    CVDataWidth DataWidth;
    CVAAddressModifier AddressModifier;

public:

    v1190a(long handle, IniFile *inifile, int ntdcs);
    ~v1190a();
    Data16 write_op_reg(Data32 address, int code, string error);
    Data16 read_op_reg(Data32 address, string error);
    void Reset(int ntdcs);
    void Clear(int ntdcs);
    void TestWR(Data16 value,int ntdcs);
    void CheckTDCStatus(int ntdcs);
    void CheckCommunication(int ntdcs);
    void SetTDCTestMode(Data16 mode,int ntdcs);
    void SetTrigMatching(int ntdcs);
    void SetTrigTimeSubtraction(Data16 mode,int ntdcs);
    void SetTrigWindowWidth(Uint windowHeight,int ntdcs);
    void SetTrigWindowOffset(Uint windowOffset,int ntdcs);
    void SetTrigSearchMargin(Uint searchMargin,int ntdcs);
    void SetTrigRejectionMargin(Uint rejectMargin,int ntdcs);
    void GetTrigConfiguration(int ntdcs);
    void SetTrigConfiguration(IniFile *inifile,int ntdcs);
    void SetTDCDetectionMode(Data16 mode,int ntdcs);
    void SetTDCResolution(Data16 lsb,int ntdcs);
    void SetTDCDeadTime(Data16 time,int ntdcs);
    void SetTDCHeadTrailer(Data16 mode,int ntdcs);
    void SetTDCEventSize(Data16 size,int ntdcs);
    void SwitchChannels(IniFile *inifile,int ntdcs);
    void SetIRQ(Data32 level, Data32 count,int ntdcs);
    void SetBlockTransferMode(Data16 mode,int ntdcs);
    void Set(IniFile *inifile,int ntdcs);
    void CheckStatus(CVErrorCodes status) const;
    int ReadBlockD32(Uint tdc, const Data16 address,
                      Data32 *data, const Uint words, bool ignore_berr);
    Uint Read(RAWData *DataList,int ntdcs);
};

3807

```

3808       *Source Code A.1: Description of C++ object v1190a.*

3809       The detection mode corresponds to the the type of edge detection the TDC will be using to  
 3810       record the data. The TDCs can record the time stamp of the leading edge alone, of the trailing edge  
 3811       alone, of both or they can operate in pair mode, meaning that the leading edge is recorded together  
 3812       with the time difference in between leading and trailing edges. This last mode is not very practical  
 3813       for the case of GIF++ measurements as the information is coded into a single words in the TDC's  
 3814       buffer, putting strong constraints on the time wondow and duration of the input signals. Indeed,  
 3815       when recording the edges individually (single edge or both edges), a 32-bit word, of which 18 are  
 3816       used to provide the time information alone, is stored into memory for each signal edge. With the  
 3817       pair mode, instead of having one 32-bit word per edge, only a single 32-bit word is written of which  
 3818       12 are used for the leading edge time information and 6 for the width of the pulse, as described on  
 3819       p73 of reference [264]. This way, eventhough the pair mode is convenient to use as it automatically

3820 correlates a leading edge with the corresponding signal width in a single word, it is advised to be  
 3821 careful when using it and to be aware of the extra time constraints (for both leading time and signal  
 3822 width) that will come for choosing this setting. If it is necessary to work with large input signals,  
 3823 the mode recording both edges will be preferred to the pair mode and the association of a leading  
 3824 and trailing edges pair will then be performed offline by the user. Then, the time resolution is to be  
 3825 chosen in a range from 100 to 800 ps, the dead time in a range from 5 to 100 ns, and the maximal  
 3826 number of hits per event in a range from 0 to 128 with the possibility to choose to have no limits.

#### 3827 A.4.2 DataReader

3828 Enabled thanks to `v1190a::SetBlockTransferMode()`, the data transfer is done via Block Transfer  
 3829 (BLT). Using BLT allows to transfer a fixed number of events called a *block*. This is used together  
 3830 with an Almost Full Level (AFL) of the TDCs' output buffers, defined through `v1190a::SetIRQ()`.  
 3831 This AFL gives the maximum amount of 32735 words (16 bits, corresponding to the depth of a TDC  
 3832 output buffer) that can be written in a buffer before an Interrupt Request (IRQ) is generated and seen by  
 3833 the VME Bridge V1718, which sends a `BUSY` signal intended to stopping the data acquisition during  
 3834 the transfer of the content of each TDC buffers before resuming. For each trigger, 6 words or more  
 3835 are written into the TDC buffer:

- 3836 • **a global header** providing information of the event number since the beginning of the data  
 3837 acquisition,
- 3838 • **a TDC header** which is enabled thanks to `v1190a::SetTDCHeadTrailer()`,
- 3839 • **the TDC data (if any)**, 1 for each hit recorded during the event, providing the channel and the  
 3840 time stamp associated to the hit,
- 3841 • **a TDC error** providing error flags,
- 3842 • **a TDC trailer** which is enabled thanks to `v1190a::SetTDCHeadTrailer()`,
- 3843 • **a global trigger time tag** that provides the absolute trigger time relatively to the last reset,  
 3844 and
- 3845 • **a global trailer** providing the total word count in the event.

3846 CMS RPC FEEs provide with 100 ns long LVDS output signals that are injected into the TDCs'  
 3847 input. Any avalanche signal that gives a signal above the FEEs threshold is thus recorded by the  
 3848 TDCs as a hit within the match window. Each hit is assigned to a specific TDC channel with a time  
 3849 stamp, with a precision of 100 ps. The reference time,  $t_0 = 0$ , is provided by the beginning of the  
 3850 match window. Thus for each trigger, coming from a scintillator coincidence or the pulse generator,  
 3851 a list of hits is stored into the TDCs' buffers and will then be transferred into a ROOT Tree.

3852 When the BLT is used, it is easy to understand that the maximum number of words that have been set  
 3853 as AFL will not be a finite number of events or, at least, the number of events that would be recorded  
 3854 into the TDC buffers will not be a multiple of the block size. In the last BLT cycle to transfer data,  
 3855 the number of events to transfer will most probably be lower than the block size. In that case, the  
 3856 TDC can add fillers at the end of the block but this option requires to send more data to the computer  
 3857 and is thus a little slower. Another solution is to finish the transfer after the last event by sending a  
 3858 bus error that states that the BLT reached the last event in the pile. This method has been chosen in

3859   GIF++.

3860   Due to irradiation, an event in GIF++ can count up to 300 words per TDC. A limit of 4096 words  
 3861   (12 bits) has been set to generate IRQ which represent from 14 to almost 700 events depending on  
 3862   the average of hits collected per event. Then the block size has been set to 100 events with enabled  
 3863   bus errors. When an AFL is reached for one of the TDCs, the VME bridge stops the acquisition by  
 3864   sending a BUSY signal.

3865

3866   The data is then transferred one TDC at a time into a structure called `RAWData` (Source Code A.2).  
 3867   Note that the structure as presented here is used when a single edge detection is used as there is only  
 3868   one time stamp list associated to the hits. When using detection on both edges, a second time stamp  
 3869   list could be added and when using pair detection, a list with the signal width could be added instead.

3870

```
3871   struct RAWData {
 3872     vector<int>                   *EventList;
 3873     vector<int>                   *NHitsList;
 3874     vector<int>                   *QFlagList;
 3875     vector<vector<int> >       *ChannelList;
 3876     vector<vector<float> >    *TimeStampList;
 3877 };
```

3872

*Source Code A.2: Description of data holding C++ structure `RAWData`.*

```
3873   class DataReader
 3874   {
 3875     private:
 3876       bool              StopFlag;
 3877       IniFile *iniFile;
 3878       Data32          MaxTriggers;
 3879       v1718            *VME;
 3880       int             nTDCs;
 3881       v1190a          *TDCs;
 3882       RAWData         TDCData;

 3883     public:
 3884       DataReader();
 3885       virtual ~DataReader();
 3886       void            SetInifile(string inifilename);
 3887       void            SetMaxTriggers();
 3888       Data32          GetMaxTriggers();
 3889       void            SetVME();
 3890       void            SetTDC();
 3891       int             GetQFlag(Uint it);
 3892       void            Init(string inifilename);
 3893       void            FlushBuffer();
 3894       void            Update();
 3895       string          GetFileName();
 3896       void            WriteRunRegistry(string filename);
 3897       void            Run();
 3898 };
```

3874

*Source Code A.3: Description of C++ object `DataReader`.*

3875

3876   In order to organize the data transfer and the data storage, an object called `DataReader` was  
 3877   created (Source Code A.3). On one hand, it has `v1718` and `v1190a` objects as private members for  
 3878   communication purposes, such as VME modules settings via the configuration file `*iniFile` or data

3878 read-out through `v1190a::Read()` and on the other hand, it contains the structure `RAWData` that allows  
 3879 to organise the data in vectors reproducing the tree structure of a ROOT file.  
 3880 Each event is transferred from `TDCData` and saved into branches of a ROOT `TTree` as 3 integers  
 3881 that represent the event ID (`EventCount`), the number of hits read from the TDCs (`nHits`), and the  
 3882 quality flag that provides information for any problem in the data transfer (`qflag`), and 2 lists of  
 3883 *nHits* elements containing the fired TDC channels (`TDCCh`) and their respective time stamps (`TDCTS`),  
 3884 as presented in Source Code A.4. The ROOT file file is named using information contained into  
 3885 the configuration file, presented in section A.5.2. The needed information is extracted using method  
 3886 `DataReader::GetFileName()` and allow to build the output filename format `ScanXXXXXX_HVX_DAQ.root`  
 3887 where `ScanXXXXXX` is a 6 digit number representing the scan number into GIF++ database and `HVX`  
 3888 the HV step within the scan that can be more than a single digit. An example of ROOT data file is  
 3889 provided with Figure A.3.

```
3890
  RAWData TDCData;
  TFile *outputFile = new TFile(outputFileName.c_str(), "recreate");
  TTree *RAWDataTree = new TTree("RAWData", "RAWData");

  int EventCount = -9;
  int nHits = -8;
  int qflag = -7;
  vector<int> TDCCh;
  vector<float> TDCTS;

  RAWDataTree->Branch("EventNumber", &EventCount, "EventNumber/I");
  RAWDataTree->Branch("number_of_hits", &nHits, "number_of_hits/I");
  RAWDataTree->Branch("Quality_flag", &qflag, "Quality_flag/I");
  RAWDataTree->Branch("TDC_channel", &TDCCh);
  RAWDataTree->Branch("TDC_TimeStamp", &TDCTS);

  //...
  //Here read the TDC data using v1190a::Read() and place it into
  //TDCData for as long as you didn't collect the requested amount
  //of data.
  //...

  for(Uint i=0; i<TDCData.EventList->size(); i++) {
    EventCount = TDCData.EventList->at(i);
    nHits = TDCData.NHitsList->at(i);
    qflag = TDCData.QFlagList->at(i);
    TDCCh = TDCData.ChannelList->at(i);
    TDCTS = TDCData.TimeStampList->at(i);
    RAWDataTree->Fill();
  }
}
```

3892 *Source Code A.4: Highlight of the data transfer and organisation within `DataReader::Run()` after the data  
 has been collected into `TDCData`.*

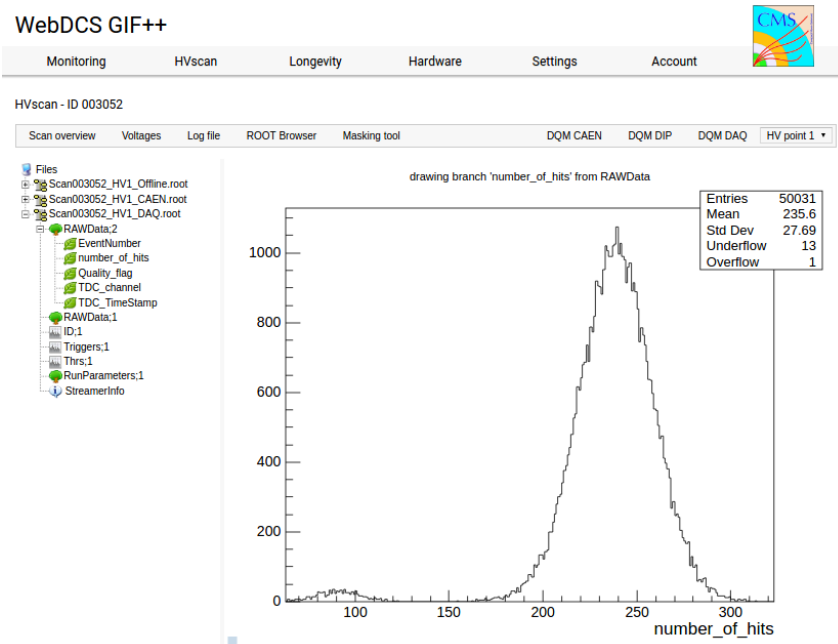


*Figure A.3: Structure of the ROOT output file generated by the DAQ. The 5 branches (EventNumber, number\_of\_hits, Quality\_flag, TDC\_channel and TDC\_TimeStamp) are visible on the left panel of the ROOT browser. On the right panel is visible the histogram corresponding to the variable nHits. In this specific example, there were approximately 50k events recorded to measure the gamma irradiation rate on the detectors. Each event is stored as a single entry in the TTree.*

#### 3893    A.4.3 Data quality flag

3894    Among the parameters that are recorded for each event, the quality flag is determined on the fly  
 3895    by checking the data recorded by every single TDC. An `enum` called `QualityFlag` was written to  
 3896    associate the key `GOOD` to the integer 1 and `CORRUPTED` to 0. From method `v1190a::Read()`, it can  
 3897    be understood that the content of each TDC buffer is readout one TDC at a time. Entries are created  
 3898    in the data list for the first TDC and then, when the second buffer is readout, events corresponding  
 3899    to entries that have already been created to store data for the previous TDC are added to the existing  
 3900    list element. On the contrary, when an event entry has not been yet created in the data list, a new  
 3901    entry is created.

3902    It is possible that each TDC buffer contains a different number of events. In cases where the first  
 3903    element in the buffer list is an event for corresponds to a new entry, the difference in between the  
 3904    entry from the buffer and the last entry in the data list is recorded and checked. If it is greater than 1,  
 3905    what should never be the case, the quality flag is set to `CORRUPTED` for this TDC and an empty entry  
 3906    is created in the place of the missing ones. Missing entries are believe to be the result of a bad hold  
 3907    on the TDC buffers at the moment of the readout. Indeed, the software hold is effective only on 1  
 3908    TDC at a time and no solution as been found yet to completely block the writting in the buffers when  
 3909    an IRQ is received.

3910    At the end of each BLT cycle, the ID of the last entry stored for each TDC buffer is not recorded.  
 3911    When starting the next cycle, if the first entry in the pile corresponds to an event already existing  
 3912    in the list, the readout will start from this list element and will not be able to check the difference

3913 in between this entry's ID and the one of the last entry that was recorded for this TDC buffer in  
 3914 the previous cycle. In the case events were missing, the flag stays at its initial value of 0, which is  
 3915 similar to CORRUPTED and it is assumed that then this TDC will not contribute to number\_of\_hits,  
 3916 TDC\_channel or TDC\_TimeStamp. Finally, since there will be 1 RAWData entry per TDC for each event  
 3917 (meaning nTDCs entries, referring to DataReader private attribute), the individual flags of each TDC  
 3918 will be added together. The final format is an integer composed nTDCs digits where each digit is the  
 3919 flag of a specific TDC. This is constructed using powers of 10 like follows:

3920        TDC 0: QFlag =  $10^0 \times \text{QualityFlag}$

3921        TDC 1: QFlag =  $10^1 \times \text{QualityFlag}$

3922        ...

3923        TDC N: QFlag =  $10^N \times \text{QualityFlag}$

3924        and the final flag to be with N digits:

3925        QFlag = n....3210

3926        each digit being 1 or 0. Below is given an example with a 4 TDCs setup.

3927        If all TDCs were good : QFlag = 1111,

3928        but if TDC 2 was corrupted : QFlag = 1011.

3929        When data taking is over and the data contained in the dynamical RAWData structure is transferred  
 3930 to the ROOT file, all the 0s are changed into 2s by calling the method DataReader::GetQFlag().  
 3931 This will help translating the flag without knowing the number of TDCs beforehand. Indeed, a flag  
 3932 111 could be due to a 3 TDC setup with 3 good individual TDC flags or to a more than 3 TDC setup  
 3933 with TDCs those ID is greater than 2 being CORRUPTED, thus giving a 0.

3934        The quality flag has been introduced quite late, in October 2017 only, to the list of GIFT++ DAQ  
 3935 parameters to be recorded into the output ROOT file. Before this addition, the missing data, corrupting  
 3936 the quality for the offline analysis, was contributing to artificially fill data with lower multiplicity.  
 3937 Looking at TBranch number\_of\_hits provides an information about the data of the full GIFT++  
 3938 setup. When a TDC is not able to transfer data for a specific event, the effect is a reduction of the  
 3939 total number of hits recorded in the full setup, this is what can be seen from Figure A.4. After offline  
 3940 reconstruction detector by detector, the effect of missing events can be seen in the artificially filled  
 3941 bin at multiplicity 0 shown in Figure A.5. Nonetheless, for data with high irradiation levels, as it is  
 3942 the case for Figure A.5a, discarding the fake multiplicity 0 data can be done easily during the offline  
 3943 analysis. At lower radiation, the missing events contribution becomes more problematic as the mul-  
 3944 tiplicity distribution overlaps the multiplicity 0 and that in the same time the proportion of missing  
 3945 events decreases. Attempts to fit the distribution with a Poisson or skew distribution function were  
 3946 not conclusive and this very problem has been at the origin of the quality flag that allows to give a  
 3947 non ambiguous information about each event quality.

3948

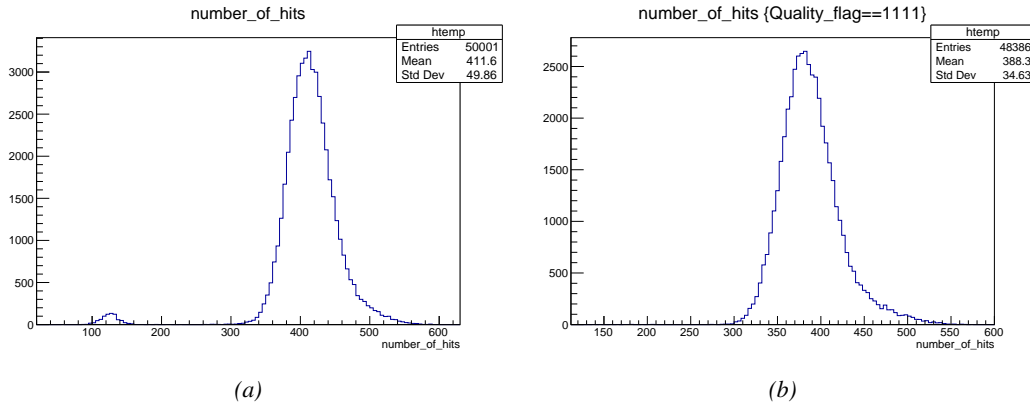


*Figure A.4: The effect of the quality flag is explained by presenting the content of TBranch `number_of_hits` of a data file without `Quality_flag` in Figure A.4a and the content of the same TBranch for data corresponding to a `Quality_flag` where all TDCs were labelled as `GOOD` in Figure A.4b taken with similar conditions. It can be noted that the number of entries in Figure A.4b is slightly lower than in Figure A.4a due to the excluded events.*

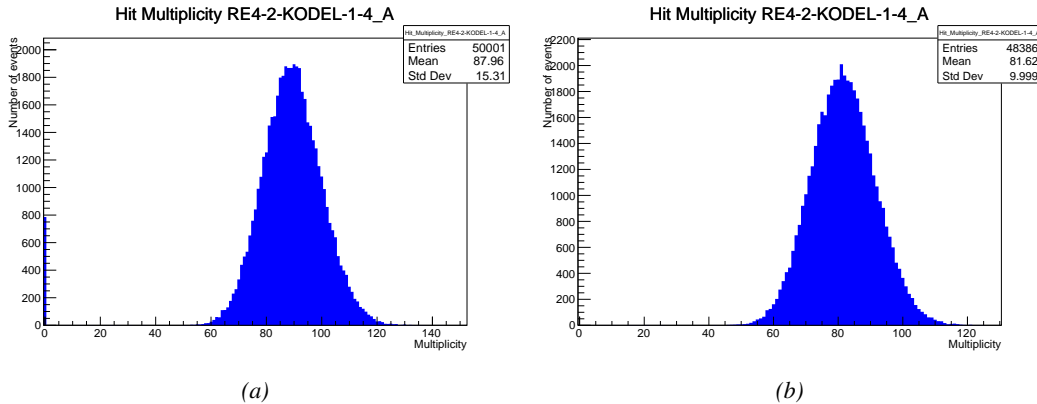


*Figure A.5: Using the same data as previously showed in Figure A.4, the effect of the quality flag is explained by presenting the reconstructed hit multiplicity of a data file without `Quality_flag` in Figure A.5a and the reconstructed content of the same RPC partition for data corresponding to a `Quality_flag` where all TDCs were labelled as `GOOD` in Figure A.5b taken with similar conditions. The artificial high content of bin 0 is completely suppressed.*

## 3949 A.5 Communications

3950 To ensure data readout and dialog in between the machine and the TDCs or in between the webDCS  
 3951 and the DAQ, different communication solutions were used. First of all, it is important to have a  
 3952 module to allow the communication in between the TDCs and the computer from which the DAQ  
 3953 operates. When this communication is effective, shifters using the webDCS to control data taking  
 3954 can thus send instructions to the DAQ.

3955

3956 **A.5.1 V1718 USB Bridge**

3957 In the previous section, the data transfer as been discussed. The importance of the `v1718` object  
 3958 (Source Code A.5), used as private member of `DataReader`, was not explicited. VME master  
 3959 modules are used for communication purposes as they host the USB port that connects the pow-  
 3960 ered crate buffer to the computer were the DAQ is installed. From the source code point of view,  
 3961 this object is used to control the communication status, by reading the returned error codes with  
 3962 `v1718::CheckStatus()`, or to check for IRQs coming from the TDCs through `v1718::CheckIRQ()`.  
 3963 To ensure that triggers are blocked at the hardware level, a NIM pulse is sent out of one of the two  
 3964 first programmable outputs of the module (`v1718::SendBUSY()`) to the VETO of the coïndidence  
 3965 module where the trigger signals originate. As long as this signal is ON, no trigger can reach the  
 3966 TDCs anymore. Finally, used in the case of noise and background measurements in which the trig-  
 3967 ger needs not to be provided by the muon bean but by an uncorrelated source, a pulse generator  
 3968 is enabled with `v1718::RDMTriggerPulse()`. The "random" pulse is sent through the third and  
 3969 fourth outputs of the module. Both the BUSY signal and the random pulse are shaped in the method  
 3970 `v1718::SetPulsers()` where the number of pulses to be generated, their width, as well as the period  
 3971 of the pulse generator is defined.

3972

```
class v1718{
    private:
        int             Handle;
        Data32          Data;           // Data
        CVIRQLevels     Level;         // Interrupt level
        CVAddressModifier AM;          // Addressing Mode
        CVDataWidth     DataSize;      // Data Format
        Data32          BaseAddress;   // Base Address

    public:
        v1718(IniFile *inifile);
        ~v1718();
        long            GetHandle(void) const;
        int             SetData(Data16 data);
        Data16          GetData(void);
        int             SetLevel(CVIRQLevels level);
        CVIRQLevels     GetLevel(void);
        int             SetAM(CVAddressModifier am);
        CVAddressModifier GetAM(void);
        int             SetDataSize(CVDataWidth datasize);
        CVDataWidth     GetDataSize(void);
        int             SetBaseAddress(Data16 baseaddress);
        Data16          GetBaseAddress(void);
        void            CheckStatus(CVErrorCodes status) const;
        bool            CheckIRQ();
        void            SetPulsers(UINT RDM_Frequency);
        void            SendBUSY(PulserLevel level);
        void            RDMTriggerPulse(PulserLevel level);
};
```

3974

*Source Code A.5: Description of C++ object v1718.*

### 3975 A.5.2 Configuration file

3976 The DAQ software takes as input a configuration file written using INI standard [278]. This file is  
 3977 partly filled with the information provided by the shifters when starting data acquisition using the  
 3978 webDCS, as shown by Figure A.6. This information is written in section **[General]** and will later  
 3979 be stored in the ROOT file that contains the DAQ data as can be seen from Figure A.3. Indeed,  
 3980 another `TTree` called `RunParameters` as well as the 2 histograms `ID`, containing the scan number,  
 3981 start and stop time stamps, and `Triggers`, containing the number of triggers requested by the shifter,  
 3982 are available in the data files. Moreover, `ScanID` and `HV` are then used to construct the file name  
 3983 thanks to the method `DataReader::GetFileName()`.

Chamber	RE2-2-NPD-BARC-8	RE2-2-CERN-105	RE2-2-NPD-BARC-9	RE2-2-CERN-105	RE4-2-KODEL-1-4	Max triggers
HV <sub>eff</sub> 1	8600	8500	8600	8500	6500	
HV <sub>eff</sub> 2	8700	8600	8700	8600	6600	
HV <sub>eff</sub> 3	8800	8700	8800	8700	6700	
HV <sub>eff</sub> 4	8900	8800	8900	8800	6800	
HV <sub>eff</sub> 5	9000	8900	9000	8900	6900	
HV <sub>eff</sub> 6	9100	9000	9100	9000	7000	
HV <sub>eff</sub> 7	9200	9100	9200	9100	7100	
HV <sub>eff</sub> 8	9300	9200	9300	9200	7200	
HV <sub>eff</sub> 9	9400	9300	9400	9300	7300	
HV <sub>eff</sub> 10	9500	9400	9500	9400	7400	

Figure A.6: WebDCS DAQ scan page. On this page, shifters need to choose the type of scan (Rate, Efficiency or Noise Reference scan), the gamma source configuration at the moment of data taking, the beam configuration, and the trigger mode. These information will be stored in the DAQ ROOT output. Are also given the minimal measurement time and waiting time after ramping up of the detectors is over before starting the data acquisition. Then, the list of HV points to scan and the number of triggers for each run of the scan are given in the table underneath.

3984 The rest of the information is written beforehand in the configuration file template, as explicated  
 3985 in Source Code A.6, and contains the hardware addresses to the different VME modules in the  
 3986 setup as well as settings for the TDCs. As the TDC settings available in the configuration file are not  
 3987 supposed to be modified, an improvement would be to remove them from the configuration file and  
 3988 to hardcode them inside of the DAQ code itself or to place them into a different INI file that would  
 3989 host only the TDC settings to lower the probability for a bad manipulation of the configuration file  
 3990 that can be modified from one of webDCS' menus.

```
3991 [General]
TdcS=4
ScanID=$scanid
HV=$HV
RunType=$runtype
MaxTriggers=$maxtriggers
Beam=$beam
[VMEInterface]
Type=V1718
BaseAddress=0xFF0000
Name=VmeInterface
int_trig_freq=100
[TDC0]
Type=V1190A
BaseAddress=0x00000000
Name=Tdc0
StatusA00-15=1
StatusA16-31=1
StatusB00-15=1
StatusB16-31=1
StatusC00-15=1
StatusC16-31=1
StatusD00-15=1
StatusD16-31=1
[TDC1]
Type=V1190A
BaseAddress=0x11110000
Name=Tdc1
StatusA00-15=1
StatusA16-31=1
StatusB00-15=1
StatusB16-31=1
StatusC00-15=1
StatusC16-31=1
StatusD00-15=1
StatusD16-31=1
3992 [TDC2]
Type=V1190A
BaseAddress=0x22220000
Name=Tdc2
StatusA00-15=1
StatusA16-31=1
StatusB00-15=1
StatusB16-31=1
StatusC00-15=1
StatusC16-31=1
StatusD00-15=1
StatusD16-31=1
[TDC3]
Type=V1190A
BaseAddress=0x44440000
Name=Tdc3
StatusA00-15=1
StatusA16-31=1
StatusB00-15=1
StatusB16-31=1
StatusC00-15=1
StatusC16-31=1
StatusD00-15=1
StatusD16-31=1
[TDCSettings]
TriggerExtraSearchMargin=0
TriggerRejectMargin=0
TriggerTimeSubtraction=0b1
TdcDetectionMode=0b01
TdcResolution=0b10
TdcDeadTime=0b00
TdcHeadTrailer=0b1
TdcEventSize=0b1001
TdcTestMode=0b0
BLTMode=1
```

*Source Code A.6: INI configuration file template for 4 TDCs. In section [General], the number of TDCs is explicitated and information about the ongoing run is given. Then, there are sections for each and every VME modules. There buffer addresses are given and for the TDCs, the list of channels to enable is given. Finally, in section [TDCSettings], a part of the TDC settings are given.*

```

typedef map< const string, string > IniFileData;

class IniFile{
    private:
        bool          CheckIfComment(string line);
        bool          CheckIfGroup(string line, string& group);
        bool          CheckIfToken(string line, string& key, string& value);
        string         FileName;
        IniFileData   FileData;
        int           Error;

    public:
        IniFile();
        IniFile(string filename);
        virtual ~IniFile();

3994        // Basic file operations
        void          SetFileName(string filename);
        int           Read();
        int           Write();
        IniFileData GetFileData();

        // Data readout methods
        Data32 addressType(string groupname, string keyname, Data32 defaultvalue);
        long intType(string groupname, string keyname, long defaultvalue);
        long long longType(string groupname, string keyname, long long
        4995      defaultvalue);
        string stringType(string groupname, string keyname, string defaultvalue);
        float floatType(string groupname, string keyname, float defaultvalue);

        // Error methods
        string GetErrorMsg();
};

3995      Source Code A.7: Description of C++ object IniFile used as a parser for INI file format.
```

**3996** In order to retrieve the information of the configuration file, the object `IniFile` has been developed
**3997** to provide an INI parser, presented in Source Code A.7. It contains private methods returning a boolean to check the type of line written in the file, whether a comment, a group header or a key line
**3998** (`IniFile::CheckIfComment()`, `IniFile::CheckIfGroup()` and `IniFile::CheckIfToken()`). The
**3999** key may sometimes be referred to as *token* in the source code. Moreover, the private element
**4000** `FileData` is a map of `const` string to string that allows to store the data contained inside the
**4001** configuration file via the public method `IniFile::GetFileData()` following the formatting (see
**4002** method `IniFile::Read()`):

```

4004      string group, token, value;
        // Get the field values for the 3 strings.
        // Then concatenate group and token together as a single string
        // with a dot separation.
        token = group + "." + token;
        FileData[token] = value;
```

4006 More methods have been written to translate the different keys into the right variable format  
 4007 when used by the DAQ. For example, to get a **float** value out of the configuration file data, knowing  
 4008 the group and the key needed, the method `IniFile::floatType()` can be used. It takes 3 arguments  
 4009 being the group name and key name (both `string`), and a default **float** value used as exception in  
 4010 the case the expected combination of group and key cannot be found in the configuration file. This  
 4011 default value is then used and the DAQ continues on working after sending an alert in the log file for  
 4012 further debugging.

4013

### 4014 A.5.3 WebDCS/DAQ intercommunication

4015 When shifters send instructions to the DAQ via the configuration file, it is the webDCS itself that  
 4016 gives the start command to the DAQ and then the 2 softwares use inter-process communication  
 4017 through file to synchronise themselves. This communication file is represented by the variable `const`  
 4018 `string __runstatuspath`.

4019 On one side, the webDCS sends commands or status that are readout by the DAQ:

- 4020 • INIT, status sent when launching a scan and read via function `CtrlRunStatus(...)`,
- 4021 • START, command to start data taking and read via function `CheckSTART()`,
- 4022 • STOP, command to stop data taking at the end of the scan and read via function `CheckSTOP()`,  
4023 and
- 4024 • KILL, command to kill data taking sent by user and read via function `CheckKILL()`. Note that  
4025 the DAQ doesn't stop before the current ROOT file is safely written and saved.

4026 and on the other, the DAQ sends status that are controled by the webDCS:

- 4027 • DAQ\_RDY, sent with `SendDAQReady()` to signify that the DAQ is ready to receive commands  
4028 from the webDCS,
- 4029 • RUNNING, sent with `SendDAQRunning()` to signify that the DAQ is taking data,
- 4030 • DAQ\_ERR, sent with `SendDAQError()` to signify that the DAQ didn't receive the expected com-  
4031 mand from the webDCS or that the launch command didn't have the right number of argu-  
4032 ments,
- 4033 • RD\_ERR, sent when the DAQ wasn't able to read the communication file, and
- 4034 • WR\_ERR, sent when the DAQ wasn't able to write into the communication file.

### 4035 A.5.4 Example of inter-process communication cycle

4036 Under normal conditions, the webDCS and the DAQ processes exchange commands and status via  
 4037 the file hosted at the address `__runstatuspath`, as explained in subsection A.5.3. An example of  
 4038 cycle is given in Table A.1. In this example, the steps 3 to 5 are repeated as long as the webDCS tells  
 4039 the DAQ to take data. A data taking cycle is the equivalent as what is called a *Scan* in GIFT++ jargon,

4040 referring to a set a runs with several HV steps. Each repetition of steps 3 to 5 is then equivalent to a  
 4041 single *Run*.

4042 At any moment during the data taking, for any reason, the shifter can decide that the data taking  
 4043 needs to be stopped before it reached the end of the scheduled cycle. Thus at any moment on the  
 4044 cycle, the content of the inter-process communication file will be changed to `KILL` and the DAQ will  
 4045 shut down right away. The DAQ checks for `KILL` signals every 5s after the TDCs configuration is  
 4046 over. So far, the function `CheckKILL()` has been used only inside of the data taking loop of method  
 4047 `DataReader::Run()` and thus, if the shifter decides to KILL the data taking during the TDC con-  
 4048 figuration phase or the HV ramping in between 2 HV steps, the DAQ will not be stopped smoothly  
 4049 and a *force kill* command will be sent to stop the DAQ process that is still awake on the computer.  
 4050 Improvements can be brought on this part of the software to make sure that the DAQ can safely  
 4051 shutdown at any moment.

4052

step	actions of webDCS	status of DAQ	<code>__runstatuspath</code>
1	launch DAQ ramp voltages ramping over wait for currents stabilization	readout of IniFile configuration of TDCs	INIT
2		configuration done send DAQ ready wait for <code>START</code> signal	DAQ_RDY
3	waiting time over send <code>START</code>		START
4	wait for run to end monitor DAQ run status	data taking ongoing check for <code>KILL</code> signal	RUNNING
5		run over send <code>DAQ_RDY</code> wait for next DCS signal	DAQ_RDY
6	ramp voltages ramping over wait for currents stabilization		DAQ_RDY
3	waiting time over send <code>START</code>		START
4	wait for run to end monitor DAQ run status	update IniFile information data taking ongoing check for <code>KILL</code> signal	RUNNING
5		run over send <code>DAQ_RDY</code> wait for next DCS signal	DAQ_RDY
7	send command <code>STOP</code>	DAQ shuts down	STOP

Table A.1: Inter-process communication cycles in between the webDCS and the DAQ through file string signals.

## A.6 Software export

4053 In section A.2 was discussed the fact that the DAQ as written in its last version is not a standalone  
 4054 software. It is possible to make it a standalone program that could be adapted to any VME setup

4056 using V1190A and V1718 modules by creating a GUI for the software or by printing the log messages  
4057 that are normally printed in the webDCS through the log file, directly into the terminal. This  
4058 method was used by the DAQ up to version 3.0 moment where the webDCS was completed. Also, it  
4059 is possible to check branches of DAQ v2.X to have example of communication through a terminal.

4060 DAQ v2.X is nonetheless limited in its possibilities and requires a lot of offline manual interventions  
4061 from the users. Indeed, there is no communication of the software with the detectors' power  
4062 supply system that would allow for a user a predefine a list of voltages to operate the detectors at  
4063 and loop over to take data without any further manual intervention. In v2.X, the data is taken for a  
4064 single detector setting and at the end of each run, the softwares asks the user if he intends on taking  
4065 more runs. If so, the software invites the user to set the operating voltages accordingly to what is  
4066 necessary and to manual update the configuration file in consequence. This working mode can be a  
4067 very first approach before an evolution and has been successfully used by colleagues from different  
4068 collaborations.

4069 For a more robust operation, it is recommended to develop a GUI or a web application to interface  
4070 the DAQ. Moreover, to limit the amount of manual interventions, and thus the probability to make  
4071 mistakes, it is also recommended to add an extra feature into the DAQ by installing the HV Wrapper  
4072 library provided by CAEN of which an example of use in a similar DAQ software developped by a  
4073 master student of UGent, and called TinyDAQ, is provided on UGent's github. Then, this HV Wrapper  
4074 will help you communicating with and give instructions to a CAEN HV powered crate and can  
4075 be added into the DAQ at the same level where the communication with the user was made in DAQ  
4076 v2.X. In case you are using another kind of power system for your detectors, it is stringly adviced to  
4077 use HV modules or crates that can be remotely controloled via a using C++ libraries.

4078



# B

4079

4080

## Details on the offline analysis package

4081 The data collected in GIF++ thanks to the DAQ described in Appendix A is difficult to interpret by  
4082 a human user that doesn't have a clear idea of the raw data architecture of the ROOT data files. In  
4083 order to render the data human readable, a C++ offline analysis tool was designed to provide users  
4084 with detector by detector histograms that give a clear overview of the parameters monitored during  
4085 the data acquisition [273]. In this appendix, details about this software in the context of GIF++, as  
4086 of how the software was written and how it functions will be given.

### 4087 B.1 GIF++ Offline Analysis file tree

4088 GIF++ Offline Analysis source code is fully available on github at [https://github.com/aafagot/GIF\\_OfflineAnalysis](https://github.com/aafagot/GIF_OfflineAnalysis). The software requires ROOT as non-optionnal dependency  
4089 as it takes ROOT files in input and write an output ROOT file containing histograms. To compile the  
4090 GIF++ Offline Analysis project is compiled with cmake. To compile, first a build/ directory must  
4091 be created to compile from there:

```
4093 mkdir build
4094 cd build
4095 cmake ..
4096 make
4097 make install
```

4095 To clean the directory and create a new build directory, the bash script cleandir.sh can be used:

```
4096
4097 ./cleandir.sh
```

4098 The source code tree is provided below along with comments to give an overview of the files' con-  
4099 tent. The different objects created for this project (`Infrastructure`, `Trolley`, `RPC`, `Mapping`, `RPCHit`,  
4100 `RPCCluster` and `Inifile`) will be described in details in the following sections.

4101

```

GIF_OfflineAnalysis
├── bin
│   └── offlineanalysis ..... EXECUTABLE
├── build..... CMAKE COMPILATION DIRECTORY
└── ...
    ├── include..... LIST OF C++ HEADER FILES
    │   ├── Cluster.h..... DECLARATION OF OBJECT RPCCLUSTER
    │   ├── Current.h..... DECLARATION OF GETCURRENT ANALYSIS MACRO
    │   ├── GIFTrolley.h..... DECLARATION OF OBJECT TROLLEY
    │   ├── Infrastructure.h..... DECLARATION OF OBJECT INFRASTRUCTURE
    │   ├── IniFile.h..... DECLARATION OF OBJECT INI FILE FORINI PARSER
    │   ├── Mapping.h..... DECLARATION OF OBJECT MAPPING
    │   ├── MsgSvc.h..... DECLARATION OF OFFLINE LOG MESSAGES
    │   ├── OfflineAnalysis.h..... DECLARATION OF DATA ANALYSIS MACRO
    │   ├── RPCTracker.h..... DECLARATION OF OBJECT RPC
    │   ├── RPCHit.h..... DECLARATION OF OBJECT RPCHIT
    │   ├── types.h..... DEFINITION OF USEFUL VARIABLE TYPES
    │   └── utils.h..... DECLARATION OF USEFUL FUNCTIONS
    ├── obj..... BINARY FILES CREATED BY COMPILER
    └── ...
        ├── src..... LIST OF C++ SOURCE FILES
        │   ├── Cluster.cc..... DEFINITION OF OBJECT RPCCLUSTER
        │   ├── Current.cc..... DEFINITION OF GETCURRENT ANALYSIS MACRO
        │   ├── GIFTrolley.cc..... DEFINITION OF OBJECT TROLLEY
        │   ├── Infrastructure.cc..... DEFINITION OF OBJECT INFRASTRUCTURE
        │   ├── IniFile.cc..... DEFINITION OF OBJECT INI FILE FORINI PARSER
        │   ├── main.cc..... MAIN FILE
        │   ├── Mapping.cc..... DEFINITION OF OBJECT MAPPING
        │   ├── MsgSvc.cc..... DEFINITION OF OFFLINE LOG MESSAGES
        │   ├── OfflineAnalysis.cc..... DEFINITION OF DATA ANALYSIS MACRO
        │   ├── RPCTracker.cc..... DEFINITION OF OBJECT RPC
        │   ├── RPCHit.cc..... DEFINITION OF OBJECT RPCHIT
        │   └── utils.cc..... DEFINITION OF USEFUL FUNCTIONS
        ├── cleandir.sh..... BASH SCRIPT TO CLEAN BUILD DIRECTORY
        ├── CMakeLists.txt..... SET OF INSTRUCTIONS FOR CMAKE
        ├── config.h.in..... DEFINITION OF VERSION NUMBER
        └── README.md..... README FILE FOR GITHUB

```

4102

## B.2 Usage of the Offline Analysis

4103

In order to use the Offline Analysis tool, it is necessary to know the Scan number and the HV Step of the run that needs to be analysed. This information needs to be written in the following format:

4105

4106

```
Scan00XXXX_HVY
```

4107

where XXXX is the scan ID and Y is the high voltage step (in case of a high voltage scan, data will be taken for several HV steps). This format corresponds to the base name of data files in the database

4108

4109 of the Gif++ webDCS. Usually, the offline analysis tool is automatically called by the webDCS at  
 4110 the end of data taking or by a user from the webDCS panel if an update of the tool was brought.  
 4111 Nonetheless, an expert can locally launch the analysis for tests on the Gif++ computer, or a user can  
 4112 get the code on its local machine from github and download data from the webDCS for its own anal-  
 4113 ysis. To launch the code, the following command can be used from the `GIF_OfflineAnalysis` folder:

4114  
 4115     `bin/offlineanalysis /path/to/Scan00XXXX_HVY`

4116 where, `/path/to/Scan00XXXX_HVY` refers to the local data files. Then, the offline tool will by itself  
 4117 take care of finding all available ROOT data files present in the folder, as listed below:

- 4118     ● `Scan00XXXX_HVY_DAQ.root` containing the TDC data as described in Appendix A.4.2 (events,  
 4119       hit and timestamp lists), and
- 4120     ● `Scan00XXXX_HVY_CAEN.root` containing the CAEN mainframe data recorded by the monitor-  
 4121       ing tool webDCS during data taking (HVs and currents of every HV channels). This file is  
 4122       created independently of the DAQ.

## 4123     **B.2.1 Output of the offline tool**

### 4124     **B.2.1.1 ROOT file**

4125 The analysis gives output ROOT datafiles that are saved into the data folder and called using the  
 4126 naming convention `Scan00XXXX_HVY_Offline.root`. Inside those, a list of `TH1` histograms can be  
 4127 found. Its size will vary as a function of the number of detectors in the setup as each set of histograms  
 4128 is produced detector by detector. For each partition of each chamber, can be found:

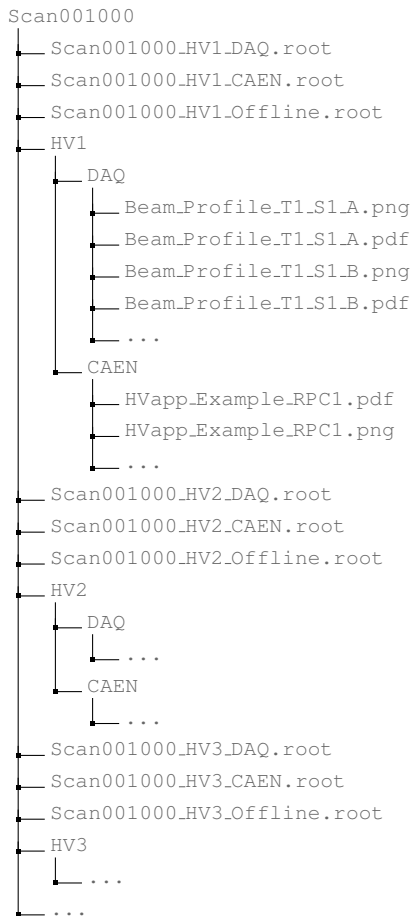
- 4129     ● `Time_Profile_Tt_Sc_p` shows the time profile of all recorded events (number of events per  
 4130       time bin),
- 4131     ● `Hit_Profile_Tt_Sc_p` shows the hit profile of all recorded events (number of events per chan-  
 4132       nel),
- 4133     ● `Hit_Multiplicity_Tt_Sc_p` shows the hit multiplicity (number of hits per event) of all recorded  
 4134       events (number of occurrences per multiplicity bin),
- 4135     ● `Time_vs_Strip_Profile_Tt_Sc_p` shows the 2D time vs strip profile of all recorded events  
 4136       (number of events per time bin per strip),
- 4137     ● `Strip_Mean_Noise_Tt_Sc_p` shows noise/gamma rate per unit area for each strip in a se-  
 4138       lected time range. After filters are applied on `Time_Profile_Tt_Sc_p`, the filtered version  
 4139       of `Hit_Profile_Tt_Sc_p` is normalised to the total integrated time and active detection area  
 4140       of a single channel,
- 4141     ● `Strip_Activity_Tt_Sc_p` shows noise/gamma activity for each strip (normalised version of  
 4142       previous histogram - strip activity = strip rate / average partition rate),
- 4143     ● `Strip_Homogeneity_Tt_Sc_p` shows the *homogeneity* of a given partition ( $\text{homogeneity} = \exp(-\text{strip rates standard deviation}(\text{strip rates in partition}/\text{average partition rate}))$ ),

- 4145     ● `mask_Strip_Mean_Noise_Tt_Sc_p` shows noise/gamma rate per unit area for each masked  
 4146       strip in a selected time range. Offline, the user can control the noise/gamma rate and decide to  
 4147       mask the strips that are judged to be noisy or dead. This is done via the *Masking Tool* provided  
 4148       by the webDCS,
- 4149     ● `mask_Strip_Activity_Tt_Sc_p` shows noise/gamma activity per unit area for each masked  
 4150       strip with respect to the average rate of active strips,
- 4151     ● `NoiseCSize_H_Tt_Sc_p` shows noise/gamma cluster size, a cluster being constructed out of  
 4152       adjacent strips giving a signal at the *same time* (hits within a time window of 25 ns),
- 4153     ● `NoiseCMult_H_Tt_Sc_p` shows noise/gamma cluster multiplicity (number of reconstructed  
 4154       clusters per event),
- 4155     ● `Chip_Mean_Noise_Tt_Sc_p` shows the same information than `Strip_Mean_Noise_Tt_Scp` us-  
 4156       ing a different binning (1 chip corresponds to 8 strips),
- 4157     ● `Chip_Activity_Tt_Sc_p` shows the same information than `strip_Activity_Tt_Scp` using  
 4158       chip binning,
- 4159     ● `Chip_Homogeneity_Tt_Sc_p` shows the homogeneity of a given partition using chip binning,
- 4160     ● `Beam_Profile_Tt_Sc_p` shows the estimated beam profile when taking efficiency scan. This  
 4161       is obtained by filtering `Time_Profile_Tt_Sc_p` to only consider the muon peak where the  
 4162       noise/gamma background has been subtracted. The resulting hit profile corresponds to the  
 4163       beam profile on the detector channels,
- 4164     ● `Efficiency_Fake_Tt_Ss_p` shows the efficiency given by fake hits by probing outside the  
 4165       peak in an uncorrelated window as wide as the peak window,
- 4166     ● `Efficiency_Peak_Tt_Ss_p` shows the efficiency given by hits contained in the peak window,
- 4167     ● `PeakCSize_H_Tt_Sc_p` shows the cluster size that was estimated using all the hits in the peak  
 4168       window,
- 4169     ● `PeakCMult_H_Tt_Sc_p` shows the cluster multiplicity that was estimated using all the hits in  
 4170       the peak window,
- 4171     ● `L0_Efficiency_Tt_Sc_p` shows the level 0 muon efficiency that was estimated **without** muon  
 4172       tracking after correction,
- 4173     ● `MuonCSize_H_Tt_Sc_p` shows the level 0 muon cluster size that was estimated **without** muon  
 4174       tracking after correction, and
- 4175     ● `MuonCMult_H_Tt_Sc_p` shows the level 0 muon cluster multiplicity that was estimated **without**  
 4176       muon tracking after correction.

4177     In the histogram labels, *t* stands for the trolley number (1 or 3), *c* for the chamber slot label in  
 4178       trolley *t* and *p* for the partition label (A, B, C or D depending on the chamber layout) as explained  
 4179       in Chapter 5.3.

4181     In the context of GIF++, an extra script called by the webDCS is called to extract the histograms  
 4182     from the ROOT files. The histograms are then stored in PNG and PDF formats into the correspond-  
 4183     ing folder (a single folder per HV step, so per ROOT file). An example of histogram organisation is  
 4184     given bellow for an hypothetical scan 001000 with at least 3 HV steps and whose chamber located in  
 4185     slot 1 of trolley 1 is called *Example\_RPC1* and has at least 2 read-out partitions A and B. The goal is  
 4186     to then display the histograms graphs on the Data Quality Monitoring (DQM) page of the webDCS,  
 4187     as presented in Figure 5.27, in order for the users to control the quality of the data taking at the end  
 4188     of data taking.

4189



4190

### B.2.1.2 CSV files

4191

Moreover, up to 4 CSV files can be created depending on which ones of the 3 input files were in the data folder:

4193

- Offline-Corrupted.csv , is used to keep track of the amount of data that was corrupted and removed from old data format files that don't contain any data quality flag.

4194

- 4195     ● `Offline-Current.csv`, contains the summary of the currents and voltages applied on each  
 4196       RPC HV channel.
- 4197     ● `Offline-L0-EffCl.csv`, is used to write the efficiencies, cluster size and cluster multiplicity  
 4198       of efficiency runs. Note that `L0` refers here to *Level 0* and means that the results of efficiency and  
 4199       clusterization are a first approximation calculated without performing any muon tracking in  
 4200       between the different detectors. This offline tool provides the user with a preliminar calcula-  
 4201       tion of the efficiency and of the muon event parameters. Another analysis software especially  
 4202       dedicated to muon tracking is called on selected data to retrieve the results of efficiency and  
 4203       muon clusterization using a tracking algorithm to discriminate noise or gamma from muons  
 4204       as muons are the only particles that pass through the full setup, leaving hits than can be used  
 4205       to reconstruct their tracks.
- 4206     ● `Offline-Rate.csv`, is used to write the noise or gamma rates measured in the detector readout  
 4207       partitions.

4208     Note that these 4 CSV files are created along with their *headers* (`Offline-[...]-Header.csv`  
 4209       containing the names of each data columns) and are automatically merged together when the offline  
 4210       analysis tool is called from the webDCS, contrary to the case where the tool is runned locally from  
 4211       the terminal as the merging bash script is then not called. Thus, the resulting files, used to make  
 4212       official plots, are:

- 4213     ● `Corrupted.csv`,
- 4214     ● `Current.csv`,
- 4215     ● `L0-EffCl.csv`.
- 4216     ● `Rate.csv`.

### 4217   **B.3 Analysis inputs and information handling**

4218     The usage of the Offline Analysis tool as well as its output have been presented in the previous sec-  
 4219       tion. It is now important to dig further and start looking at the source code and the inputs necessary  
 4220       for the tool to work. Indeed, other than the raw ROOT data files that are analysed, more information  
 4221       needs to be imported inside of the program to perform the analysis such as the description of the  
 4222       setup inside of GIFT++ at the time of data taking (number of trolleys, of RPCs, dimensions of the  
 4223       detectors, etc...) or the mapping that links the TDC channels to the coresponding RPC channels in  
 4224       order to translate the TDC information into human readable data. Two files are used to transmit all  
 4225       this information:

4226

- 4227     ● `Dimensions.ini`, that provides the necessary setup and RPC information, and
- 4228     ● `ChannelsMapping.csv`, that gives the link between the TDC and RPC channels as well as the  
 4229       *mask* for each channel (masked or not?).

### 4230    B.3.1 Dimensions file and IniFile parser

4231    GIF++ CMS RPC setup consists in detectors held into trolleys inside of the GIF++ bunker. Each of  
 4232    these detector may have a read-out segmented to cover different pseudo-rapidity range once intalled  
 4233    in CMS. The segmentation of the read-out is referred to as "partitions". This input file, present in  
 4234    every data folder, allows the analysis tool to know of the number of active trolleys, the number of  
 4235    active RPCs in those trolleys, and the details about each RPCs such as the number of RPC gaps, the  
 4236    number of pseudo-rapidity partitions, the number of strips per partion or the dimensions. To do so,  
 4237    there are 3 types of groups in the INI file architecture. Groups are sections of the INI file content  
 4238    starting with a title encapsulated in between square brackets. A first general group, appearing only  
 4239    once at the head of the document, gives information about the number of active trolleys as well  
 4240    as their IDs, as presented in Source Code B.1. For each active trolley, a group similar to Source  
 4241    Code B.2 can be found containing information about the number of active detectors in the trolley  
 4242    and their IDs. Each trolley group as a `Tt` name format, where `t` is the trolley ID. Finally, for each  
 4243    detector stored in slots of an active trolley, there is a group providing information about their names  
 4244    and dimensions, as shown in Source Code B.3. Each slot group as a `TtSs` name format, where `s` is  
 4245    the slot ID of trolley `t` where the active RPC is hosted.

```
4246    [General]
4247    nTrolleys=2
4248    TrolleysID=13
```

Source Code B.1: Example of `[General]` group as might be found in `Dimensions.ini`. In GIF++, only 2 trolleys are available to hold RPCs and place them inside of the bunker for irradiation. The IDs of the trolleys are written in a single string as "13" and then read character by character by the program.

```
4249    [T1]
4250    nSlots=4
4251    SlotsID=1234
```

Source Code B.2: Example of trolley group as might be found in `Dimensions.ini`. In this example, the file tells that there are 4 detectors placed in the holding slots of the trolley `T1` and that their IDs, written as a single string variable, are 1, 2, 3 and 4.

```
4251    [T1S1]
4252    Name=RE2-2-NPD-BARC-8
4253    Partitions=3
4254    Gaps=3
4255    Gap1=BOT
4256    Gap2=TN
4257    Gap3=TW
4258    AreaGap1=11694.25
4259    AreaGap2=6432
4260    AreaGap3=4582.82
4261    Strips=32
4262    ActiveArea-A=157.8
4263    ActiveArea-B=121.69
4264    ActiveArea-C=93.03
```

Source Code B.3: Example of slot group as might be found in `Dimensions.ini`. In this example, the file provides information about a detector named `RE2-2-NPD-BARC-8`, having 3 pseudo-rapidity readout partitions and stored in slot `S1` of trolley `T1`. This is a CMS RE2-2 type of detector. This information will then be used for example to compute the rate per unit area calculation.

4253     This information is read-out and stored in a C++ object called `IniFile`, that parses the information  
 4254     of the INI input file and stores it into a local buffer for later use. This INI parser is the exact  
 4255     same one that was previously developed for the GIF++ DAQ and described in Appendix A.5.2.

### 4256     **B.3.2 TDC to RPC link file and Mapping**

4257     The same way the INI dimension file information is stored using `map`, the channel mapping and  
 4258     mask information making the link in between TDC channels and RPC strips is stored and accessed  
 4259     through `map`. First of all, the mapping CSV file is organised into 3 columns separated by tabulations:

4261     RPC_channel	TDC_channel	mask
----------------------	-------------	------

4262         using as formatting for each field:

4263     TSCCC	TCCC	M
----------------	------	---

4265     `TSCCC` is a 5-digit integer where `T` is the trolley ID, `s` the slot ID in which the RPC is held inside  
 4266     the trolley `T` and `ccc` is the RPC channel number, or *strip* number, that can take values up to  
 4267     3-digits depending on the detector,

4268     `TCCC` is a 4 digit integer where `T` is the TDC ID to which the RPC is connected, `ccc` is the TDC  
 4269     channel number linked to the RPC strip that can take values in between 0 and 127, and

4270     `M` is a 1-digit integer indicating if the channel should be considered (`M = 1`) or discarded (`M = 0`)  
 4271         during analysis. Note that the absence of a third column is interpreted by the mapping file  
 4272         parser as `M = 1` by default.

4273     This mapping and masking information is readout and stored thanks to the object `Mapping`, presented in Source Code B.4. Similarly to `IniFile` objects, this class has private methods to provide with parser rules. The first one, `Mapping::CheckIfNewLine()` is used to find the newline character  
 4274     '`\n`' or return character '`\r`' (depending on which kind of operating system interacted with the file).  
 4275     Finding and identifying a newline or return character is used for the simple reason that the masking  
 4276     information has been introduced only during the year 2017 but the channel mapping files exist since  
 4277     2015 and the very beginning of data taking at GIF++. This means that in the older data folders,  
 4278     before the upgrade, the channel mapping file only had 2 columns, the RPC channel and the TDC  
 4279     channel. For compatibility reasons, this method helps controlling the character following the readout  
 4280     of the 2 first fields of a line. In case any end of line character is found, no mask information is present  
 4281     in the file and the default `M = 1` is used. On the contrary, if the next character was a tabulation or a  
 4282     space, the mask information is present.

4283     Once the 3 fields have been readout, the second private method `Mapping::CheckIfTDCCh()` is  
 4284     used to control that the TDC channel is an existing TDC channel by checking its format. Finally,  
 4285     the information is stored into 3 different maps (`Link`, `ReverseLink` and `Mask`) thanks to the public  
 4286     method `Mapping::Read()`. `Link` allows to get the RPC channel by knowing the TDC channel while  
 4287     `ReverseLink` does the opposite by returning the TDC channel by knowing the RPC channel. Finally,  
 4288     `Mask` returns the mask associated to a given RPC channel.

```

4291 typedef map<Uint,Uint> MappingData;

4292 class Mapping {
4293     private:
4294         bool          CheckIfNewLine(char next);
4295         bool          CheckIfTDCCh(Uint channel);
4296         string        FileName;
4297         MappingData  Link;
4298         MappingData  ReverseLink;
4299         MappingData  Mask;
4300         int           Error;
4301
4302     public:
4303         Mapping();
4304         Mapping(string baseName);
4305         ~Mapping();
4306
4307         void SetFileName(const string filename);
4308         int  Read();
4309         Uint GetLink(Uint tdcchannel);
4310         Uint GetReverse(Uint rpcchannel);
4311         Uint GetMask(Uint rpcchannel);
4312     };

```

4293 *Source Code B.4: Description of C++ object Mapping used as a parser for the channel mapping and mask file.*

## 4294 B.4 Description of GIF++ setup within the Offline Analysis tool

4295 In the previous section, the tool input files have been discussed. The dimension file information is  
 4296 stored in a map hosted by the `IniFile` object. But this information is then used to create a series of  
 4297 new objects that helps defining the GIF++ infrastructure directly into the Offline Analysis. Indeed,  
 4298 from the `RPC`, to the more general `Infrastructure`, every element of the GIF++ infrastrucutre is  
 4299 recreated for each data analysis based on the information provided in input. All this information  
 4300 about the infrastructure will be used to assign each hit signal to a specific strip channel of a specific  
 4301 detector, and having a specific active area. This way, rate per unit area calculation is possible.  
 4302

### 4303 B.4.1 RPC objects

4304 `RPC` objects have been developped to represent physical active detectors in GIF++ at the moment  
 4305 of data taking. Thus, there are as many `RPC` objects created during the analysis than there were  
 4306 active `RPCs` tested during a run. Each `RPC` hosts the information present in the corresponding INI  
 4307 slot group, as showed in B.3, and organises it using a similar architecture. This can be seen from  
 4308 Source B.5.

4309 To make the object more compact, the lists of gap labels, of gap active areas and strip active  
 4310 areas are stored into `vector` dynamical containers. `RPC` objects are always contructed thanks to the  
 4311 dimension file information stored into the `IniFILE` and their ID, using the format `TtSs`. Using the  
 4312 `RPC` ID, the constructor calls the methods of `IniFILE` to initialise the `RPC`. The other constructors  
 4313 are not used but exist in case of need. Finally, some getters have been written to access the different  
 4314 private parameters storing the detector information.

4315

### 4316 B.4.2 Trolley objects

4317 Trolley objects have been developed to represent physical active trolleys in GIF++ at the moment  
 4318 of data taking. Thus, there are as many trolley objects created during the analysis than there were  
 4319 active trolleys hosting RPCs under test during a run. Each Trolley hosts the information present in  
 4320 the corresponding INI trolley group, as shown in B.2, and organises it using a similar architecture.  
 4321 In addition to the information hosted in the INI file, these objects have a dynamical container of RPC  
 4322 objects, representing the active detectors the active trolley was hosting at the time of data taking.  
 4323 This can be seen from Source Code B.6.

4324 Trolley objects are always constructed thanks to the dimension file information stored into the  
 4325 IniFILE and their ID, using the format `Tt`. Using the Trolley ID, the constructor calls the methods  
 4326 of `IniFile` to initialise the Trolley. Retrieving the information of the RPC IDs via `SlotsID`, a new  
 4327 RPC is constructed and added to the container `RPCs` for each character in the ID string. The other  
 4328 constructors are not used but exist in case of need. Finally, some getters have been written to access  
 4329 the different private parameters storing the trolley and detectors information.

4330

### 4331 B.4.3 Infrastructure object

4332 The Infrastructure object has been developed to represent the GIF++ bunker area dedicated to  
 4333 CMS RPC experiments. With this very specific object, all the information about the CMS RPC  
 4334 setup within GIF++ at the moment of data taking is stored. It hosts the information present in the  
 4335 corresponding INI general group, as shown in B.1, and organises it using a similar architecture. In  
 4336 addition to the information hosted in the INI file, this object has a dynamical container of Trolley  
 4337 objects representing the active trolleys in GIF++ area, themselves containing RPC objects. This can  
 4338 be seen from Source Code B.7.

4339 The Infrastructure object is always constructed thanks to the dimension file information stored  
 4340 into the `IniFILE`. Retrieving the information of the trolley IDs via `TrolleysID`, a new Trolley is  
 4341 constructed and added to the container `Trolleys` for each character in the ID string. By extension,  
 4342 it is easy to understand that the process described in Section B.4.2 for the construction of RPCs  
 4343 takes place when a trolley is constructed. The other constructors are not used but exist in case of  
 4344 need. Finally, some getters have been written to access the different private parameters storing the  
 4345 infrastructure, trolleys and detectors information.

```

4346 class RPC{
    private:
        string      name;          //RPC name as in webDCS database
        UInt       nGaps;         //Number of gaps in the RPC
        UInt       nPartitions;   //Number of partitions in the RPC
        UInt       nStrips;       //Number of strips per partition
        vector<string> gaps;     //List of gap labels (BOT, TOP, etc...)
        vector<float>  gapGeo;    //List of gap active areas
        vector<float>  stripGeo;  //List of strip active areas

    public:
        RPC();
        RPC(string ID, IniFile* geofile);
        RPC(const RPC& other);
        ~RPC();
        RPC& operator=(const RPC& other);

        string GetName();
        UInt  GetNGaps();
        UInt  GetNPartitions();
        UInt  GetNStrips();
        string GetGap(UInt g);
        float GetGapGeo(UInt g);
        float GetStripGeo(UInt p);
    };

```

4348 *Source Code B.5: Description of C++ objects RPC that describe each active detectors used during data taking.*

```

class Trolley{
    private:
        UInt       nSlots;        //Number of active RPCs in the considered trolley
        string    SlotsID;       //Active RPC IDs written into a string
        vector<RPC*> RPCs;      //List of active RPCs

    public:
        Trolley();
        Trolley(string ID, IniFile* geofile);
        Trolley(const Trolley& other);
        ~Trolley();
        Trolley& operator=(const Trolley& other);

        UInt  GetNSlots();
        string GetSlotsID();
        UInt  GetSlotID(UInt s);
        RPC*  GetRPC(UInt r);
        void  DeleteRPC(UInt r);

        //Methods to get members of RPC objects stored in RPCs
        string GetName(UInt r);
        UInt  GetNGaps(UInt r);
        UInt  GetNPartitions(UInt r);
        UInt  GetNStrips(UInt r);
        string GetGap(UInt r, UInt g);
        float GetGapGeo(UInt r, UInt g);
        float GetStripGeo(UInt r, UInt p);
    };

```

4350 *Source Code B.6: Description of C++ objects Trolley that describe each active trolley used during data taking.*

```

class Infrastructure {
    private:
        Uint             nTrolleys;   //Number of active Trolleys in the run
        string          TrolleysID;  //Active trolley IDs written into a string
        vector<Trolley*> Trolleys;  //List of active Trolleys (struct)

    public:
        Infrastructure();
        Infrastructure(IniFile* geofile);
        Infrastructure(const Infrastructure& other);
        ~Infrastructure();
        Infrastructure& operator=(const Infrastructure& other);

        Uint    GetNTrolleys();
        string GetTrolleysID();
        Uint    GetTrolleyID(Uint t);

4351      Trolley* GetTrolley(Uint t);
        void    DeleteTrolley(Uint t);

        //Methods to get members of GIFTrolley objects stored in Trolleys
        Uint    GetNSlots(Uint t);
        string GetSlotsID(Uint t);
        Uint    GetSlotID(Uint t, Uint s);
        RPC*   GetRPC(Uint t, Uint r);

        //Methods to get members of RPC objects stored in RPCs
        string GetName(Uint t, Uint r);
        Uint    GetNGaps(Uint t, Uint r);
        Uint    GetNPartitions(Uint t, Uint r);
        Uint    GetNStrips(Uint t, Uint r);
        string GetGap(Uint t, Uint r, Uint g);
        float  GetGapGeo(Uint t, Uint r, Uint g);
        float  GetStripGeo(Uint t, Uint r, Uint p);
    };

```

*Source Code B.7: Description of C++ object Infrastructure that contains the full information about CMS RPC experiment in GIF++.*

## **4353 B.5 Handeling of data**

**4354** As discussed in Appendix A.4.2, the raw data uses a `TTree` architecture where every entry is related  
**4355** to a trigger signal provided by a muon or a random pulse, whether the goal of the data taking was to  
**4356** measure the performance of the detector or the noise/gamma background respectively. Each of these  
**4357** entries, referred also as events, contain a more or less full list of hits in the TDC channels to which  
**4358** the detectors are connected. To this list of hits corresponds a list of time stamps, marking the arrival  
**4359** of the hits within the TDC channel.

**4360** The infrastructure of the CMS RPC experiment within `GIF++` being defined, combining the raw  
**4361** data information with the information provided by both the mapping/mask file and the dimension  
**4362** file allows to build new physical objects that will help in computing efficiency or rates.

### 4363 B.5.1 RPC hits

4364 The raw data stored in the ROOT file as output of the GIFT++ DAQ, is readout by the analysis tool  
 4365 using the structure `RAWData` presented in Source Code B.9 that differs from the structure presented  
 4366 in Appendix A.4.2 as it is not meant to hold all of the data contained in the ROOT file. In this sense,  
 4367 this structure is in the case of the offline analysis tool not a dynamical object and will only be storing  
 4368 a single event contained in a single entry of the `TTree`.

4369

```
4369 class RPCHit {
    private:
        Uint Channel;      //RPC channel according to mapping (5 digits)
        Uint Trolley;     //0, 1 or 3 (1st digit of the RPC channel)
        Uint Station;     //Slot where is held the RPC in Trolley (2nd digit)
        Uint Strip;       //RPC strip where the hit occurred (last 3 digits)
        Uint Partition;   //Readout partition along eta segmentation
        float TimeStamp; //Time stamp of the arrival in TDC

    public:
        RPCHit();
        RPCHit(Uint channel, float time, Infrastructure* Infra);
        RPCHit(const RPCHit& other);
        ~RPCHit();
        RPCHit& operator=(const RPCHit& other);

        Uint GetChannel();
        Uint GetTrolley();
        Uint GetStation();
        Uint GetStrip();
        Uint GetPartition();
        float GetTime();
};

4370

4371 typedef vector<RPCHit> HitList;
typedef struct GIFHitList {HitList rpc[NTROLLEYS][NSLOTS][NPARTITIONS];}
    ↪ GIFHitList;

bool SortHitbyStrip(RPCHit h1, RPCHit h2);
bool SortHitbyTime(RPCHit h1, RPCHit h2);
```

4371

*Source Code B.8: Description of C++ object RPCHit.*

4372

```
4372 struct RAWData{
    int iEvent;           //Event i
    int TDCHits;         //Number of hits in event i
    int QFlag;           //Quality flag list (1 flag digit per TDC)
    vector<Uint> *TDCCh; //List of channels giving hits per event
    vector<float> *TDCTS; //List of the corresponding time stamps
};
```

4373

*Source Code B.9: Description of C++ structure RAWData.*

4374 Each member of the structure is then linked to the corresponding branch of the ROOT data tree,  
 4375 as shown in the example of Source Code B.10, and using the method `GetEntry(int i)` of the ROOT  
 4376 class `TTree` will update the state of the members of `RAWData`.

4377 The data is then analysed entry by entry and to each element of the TDC channel list, a `RPCHit` is  
 4378 constructed by linking each TDC channel to the corresponding RPC channel thanks to the Mapping

4379 object. The information carried by the RPC channel format allows to easily retrieve the trolley and  
 4380 slot from which the hit was recorded (see section B.3.2). Using these 2 values, the readout partition  
 4381 can be found by knowing the strip channel and comparing it with the number of partitions and strips  
 4382 per partition stored into the `Infrastructure` object.

```
4383
4384   TTree* dataTree = (TTree*)dataFile.Get("RAWData");
        RAWData data;
        dataTree->SetBranchAddress("EventNumber", &data.iEvent);
        dataTree->SetBranchAddress("number_of_hits", &data.TDCNHits);
        dataTree->SetBranchAddress("Quality_flag", &data.QFlag);
        dataTree->SetBranchAddress("TDC_channel", &data.TDCCh);
        dataTree->SetBranchAddress("TDC_TimeStamp", &data.TDCTS);
```

4385 *Source Code B.10: Example of link in between RAWData and TTree.*

4386 Thus `RPCHit` objects are then stored into 3D dynamical list called `GIFHitList` (Source Code B.8)  
 4387 where the 3 dimensions refer to the 3 layers of the readout in `GIF++`: in the bunker there are *trolleys*  
 4388 ( $\tau$ ) holding detectors in *slots* ( $s$ ) and each detector readout is divided into 1 or more pseudo-rapidity  
 4389 *partitions* ( $p$ ). Using these 3 information allows to assign an address to each readout partition and  
 4390 this address will point to a specific hit list.

4391

### 4392 B.5.2 Clusters of hits

4393 All the hits contained in the ROOT file have been sorted into the different hit lists through the  
 4394 `GIFHitList`. At this point, it is possible to start looking for clusters. A cluster is a group of adjacent  
 4395 strips getting hits within a time window of 25 ns. These strips are then assumed to be part of the same  
 4396 physical avalanche signal generated by a muon passing through the chamber or by the interaction of  
 4397 a gamma stopping into the electrodes of the RPCs.

4398 To keep the cluster information, `RPCCluster` objects have been defined as shown in Source  
 4399 Code B.11. Using the information of each individual `RPCHit` taken out of the hit list, it stores  
 4400 the cluster size (number of adjacent strips composing the cluster), the first and last hit, the center for  
 4401 spatial reconstruction and finally the start and stop time stamps as well as te time spread in between  
 4402 the first and last hit.

4403

4404 To investigate the hit list of a given detector partition, the function `Clusterization()` defined  
 4405 in `include/Cluster.h` needs the hits in the list to be time sorted. This is achieved by calling func-  
 4406 tion `sort()` of library `<algorithm>` using the comparator `SortHitbyTime(RPCHit h1, RPCHit h2)`  
 4407 defined in `include/RPCHit.h` that returns `true` if the time stamp of hit  $h_1$  is lower than that of  $h_2$ .  
 4408 A first isolation of strips is made only based on time information. All the hits within the 25 ns win-  
 4409 dow are taken separately from the rest. Then, this sub-list of hits is sorted this time by ascending  
 4410 strip number, using this time the comparator `SortHitbyStrip(RPCHit h1, RPCHit h2)`. Finally, the  
 4411 groups of adjacent strips are used to construct `RPCCluster` objects that are then stored in a temporary  
 4412 list of clusters that is at the end of the process used to know how many clusters were reconstructed  
 4413 and to fill their sizes into an histogram that will allows to know the mean size of muon or gamma  
 4414 clusters. This method to group hits together into clusters is limited as no systematic study of the  
 4415 average avalanche time development into TDC hits was performed and that there is no correlation

4416 of both spatial and time information to make the first selection of hits. Due to this, two clusters  
 4417 developping consecutively next to each other during a total time longer to 25 ns could be wrongly  
 4418 grouped as a cluster composed of the first developed cluster plus a part of the second cluster while  
 4419 the rest of the second cluster would be placed in a second truncated cluster. This kind of event  
 4420 is not likely but needs to be taken into account nonetheless. A possible improvement would be to  
 4421 identify clusters in a 2D space whose dimensions are time and strip. In this 2D space, the cluster  
 4422 could be geometrically identified as isolated groups of adjacent strips receiving a hit at a similar time.  
 4423

```
4423
4424 class RPCCluster{
4425     private:
4426         Uint ClusterSize; //Size of cluster #ID
4427         Uint FirstStrip; //First strip of cluster #ID
4428         Uint LastStrip; //Last strip of cluster #ID
4429         float Center; //Center of cluster #ID ((first+last)/2)
4430         float StartStamp; //Time stamp of the earliest hit of cluster #ID
4431         float StopStamp; //Time stamp of the latest hit of cluster #ID
4432         float TimeSpread; //Time difference between earliest and latest hits
4433             //of cluster #ID
4434
4435     public:
4436         RPCCluster();
4437         RPCCluster(HitList List, Uint cID, Uint cSize, Uint first, Uint firstID);
4438         RPCCluster(const RPCCluster& other);
4439         ~RPCCluster();
4440         RPCCluster& operator=(const RPCCluster& other);
4441
4442         Uint GetID();
4443         Uint GetSize();
4444         Uint GetFirstStrip();
4445         Uint GetLastStrip();
4446         float GetCenter();
4447         float GetStart();
4448         float GetStop();
4449         float GetSpread();
4450     };
4451
4452     typedef vector<RPCCluster> ClusterList;
4453
4454     //Other functions to build cluster lists out of hit lists
4455     void BuildClusters(HitList &cluster, ClusterList &clusterList);
4456     void Clusterization(HitList &hits, TH1 *hcSize, TH1 *hcMult);
4457 
```

4425

*Source Code B.11: Description of C++ object Cluster.*

## 4426 B.6 DAQ data Analysis

4427 All the ingredients to analyse GIFT++ data have been introduced. This section will focus on the  
 4428 different part of the analysis performed on the data, from determining the type of data the tool is  
 4429 dealing with to calculate the hit and cluster rate per unit area in each detector or reconstructing  
 4430 muon or gamma clusters.

### 4431 B.6.1 Determination of the run type

4432 In GIF++, both the performance of the detectors in detecting muons in an irradiated environment  
 4433 and the gamma or noise background can be independantly measured. These correspond to different  
 4434 run types and hence, to different TDC settings giving different data to look at.

4435 In the case of performance measurements, the trigger for data taking is provided by the coin-  
 4436 cidence of several scintillators when muons from the beam passing through the area are detected.  
 4437 Data is collected in a 600 ns wide window centered around the arrival of muons in the RPCs. The  
 4438 expected time distribution of hits is shown in Figure B.1a. The muon peak is clearly visible in the  
 4439 center of the distribution and is to be extracted from the gamma background that composes the flat  
 4440 part of the distribution.

4441 On the other hand, gamma background or noise measurements are focussed on the non muon  
 4442 related physics and the trigger needs to be independant from the muons to give a good measurement  
 4443 of the gamma/noise distribution as seen by the detectors. The trigger is then provided by a pulse  
 4444 generated by the DAQ at a frequency of 100 Hz whose pulse is not likely to be on time with a muon.  
 4445 In order to increase the integrated time without increasing proportionnaly the acquisition time, the  
 4446 width of the acquisition windows are increased to 10  $\mu$ s. The time distribution of the hits is expected  
 4447 to be flat, as shown by Figure B.1b.

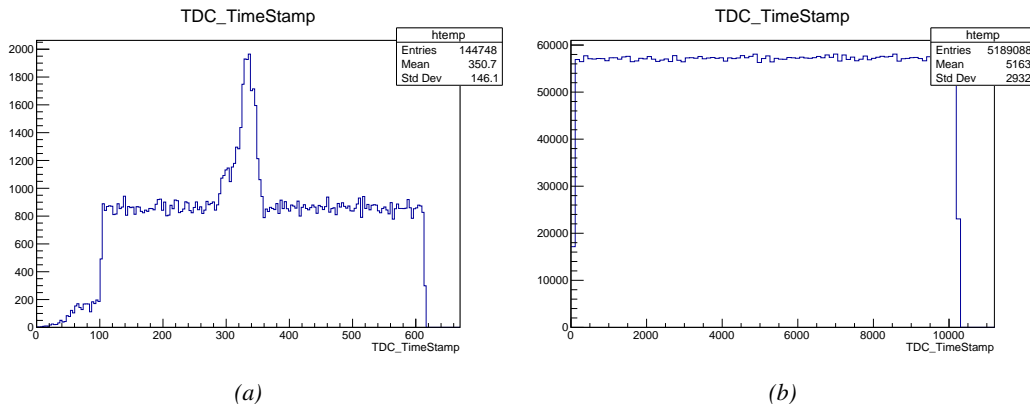


Figure B.1: Example of expected hit time distributions in the cases of efficiency (Figure B.1a) and noise/gamma rate per unit area (Figure B.1b) measurements as extracted from the raw ROOT files. The unit along the x-axis corresponds to ns. The fact that "the" muon peak is not well defined in Figure B.1a is due to the contribution of all the RPCs being tested at the same time that don't necessarily have the same signal arrival time. Each individual peak can have an offset with the ones of other detectors. The inconsistancy in the first 100 ns of both time distributions is an artefact of the TDCs and are systematically rejected during the analysis.

4448 The ROOT files include a `TTree` called `RunParameters` containing, among other things, the infor-  
 4449 mation related to the run type. The run type can then be accessed as described by Source Code B.12  
 4450 and the function `IsEfficiencyRun()` is then used to determine if the run file is an efficiency run or,  
 4451 on the contrary, another type of run (noise or gamma measurement).

4452 Finally, the data files will have a slightly different content whether it was collected before or after  
 4453 October 2017 and the upgrade of the DAQ software that brought a new information into the ROOT  
 4454 output. This is discussed in Appendix A.4.3 and implies that the analysis will differ a little depending  
 4455 on the data format. Indeed, as no information on the data quality is stored, in older data files, the cor-  
 4456 rections for missing events has to be done at the end of the analysis. The information about the type

4457 of data format is stored in the variable **bool** `isNewFormat` by checking the list of branches contained  
 4458 in the data tree via the methods `TTree::GetListOfBranches()` and `TCollection::Contains()`.

```
4459
4460     TTree* RunParameters = (TTree*)dataFile.Get("RunParameters");
4461     TString* RunType = new TString();
4462     RunParameters->SetBranchAddress("RunType", &RunType);
4463     RunParameters->GetEntry(0);
```

4461       *Source Code B.12: Access to the run type contained in `TTree* RunParameters`.*

## 4462     B.6.2 Beam time window calculation for efficiency runs

4463 Knowing the run type is important first of all to know the width of the acquisition window to be used  
 4464 for the rate calculation and finally to be able to seek for muons. Indeed, the peak that appears in the  
 4465 time distribution for each detectors is then fitted to extract the most probable time window in which  
 4466 the tool should look for muon hits. The data outside of this time window is then used to evaluate the  
 4467 noise or gamma background the detector was subjected to during the data taking. Computing the  
 4468 position of the peak is done calling the function `SetBeamWindow()` defined in file `src/RPCHit.cc` that  
 4469 loops a first time on the data. The data is first sorted in a 3D array of 1D histograms (`GIFH1Array`, see  
 4470 `include/types.h`). Then the location of the highest bin is determined using `TH1::GetMaximumBin()`  
 4471 and is used to define a window in which a gaussian fit will be applied to compute the peak width.  
 4472 This window is a 80 ns defined by Formula B.1 around the central bin.

$$(B.1a) \quad t_{center}(ns) = bin \times width_{bin}(ns)$$

$$(B.1b) \quad [t_{low}; t_{high}] = [t_{center} - 40; t_{center} + 40]$$

4473 Before the fit is performed, the average number of noise/gamma hits per bin is evaluated using  
 4474 the data outside of the fit window. Excluding the first 100 ns, the average number of hits per bin  
 4475 due to the noise or gamma is defined by Formula B.2 after extracting the amount of hits in the time  
 4476 windows  $[100; t_{low}]$  and  $[t_{high}; 600]$  thanks to the method `TH1::Integral()`. This average number  
 4477 of hits is then subtracted to every bin of the 1D histogram, in order to *clean* it from the noise or  
 4478 gamma contribution as much as possible to improve the fit quality. Bins where  $\langle n_{hits} \rangle$  is greater  
 4479 than the actual bin content are set to 0.

$$(B.2a) \quad \Delta t_{noise}(ns) = 600 \overbrace{-t_{high} + t_{low}}^{-80ns} - 100 = 420ns$$

$$(B.2b) \quad \langle n_{hits} \rangle = width_{bin}(ns) \times \frac{\sum_{t=100}^{t_{low}} + \sum_{t=t_{high}}^{600}}{\Delta t_{noise}(ns)}$$

4480 Finally, the fit parameters are extracted and saved for each detector in 3D arrays of **float**  
 4481 (`muonPeak`, see `include/types.h`), a first one for the mean arrival time of the muons, `PeakTime`,  
 4482 a second for the height or strength of the peak, `PeakHeight`, and a third one for the width of the  
 4483 peak, `PeakWidth`. The width is on purpose chosen to be wider than the peak and defined as  $6\sigma$  of the  
 4484 gaussian fit, for a peak range being as given by Formula B.3.

$$(B.3) \quad [t_{low}^{peak}; t_{high}^{peak}] = [t_{center}^{peak} - 3\sigma; t_{center}^{peak} + 3\sigma]$$

4485 For a finer analysis, it is advised to determine more precisely the width of the peak to exclude  
 4486 as much noise or background hits as possible. The same settings are applied to every partitions of  
 4487 the same detector. To determine which one of the detector's partitions is directly illuminated by the  
 4488 beam, the peak height of each partition is compared and the highest one is then used to define the  
 4489 peak settings.

4490 It is not possible to identify the particles causing the hits, hence muons, background gamma  
 4491 particles or even noise could be responsible of hits within the time window. To be able to account  
 4492 for this effect, the peak width extracted from the fit on the peak will also be used to define a fake  
 4493 time window, uncorrelated to the muon peak and in which a fake efficiency, contribution from both  
 4494 background and noise, will be measured. This window corresponds to the time range described in  
 4495 Formula B.4.

$$(B.4) \quad [t_{low}^{fake}; t_{high}^{fake}] = [600 - 6\sigma; 600]$$

### 4496 B.6.3 Data loop and histogram filling

4497 3D arrays of histogram are created to store the data and display it on the DQM of GIF++ webDCS  
 4498 for the use of shifters. The dimensions correspond to the different layers held into the GIF++ infras-  
 4499 tructure (trolleys `T` containing RPCs or *slots* `s` each being divided into read-out partitions `p`). These  
 4500 histograms, presented in section B.2.1.1, are filled while looping on the data. Before starting the  
 4501 analysis loop, it is necessary to control the entry quality for the new file formats featuring `QFlag`. If  
 4502 the `QFlag` value for this entry shows that 1 TDC or more have a `CORRUPTED` flag, then this event is  
 4503 discarded. The loss of statistics is low enough to be neglected. `QFlag` is controlled using the func-  
 4504 tion `IsCorruptedEvent()` defined in `src/utils.cc`. As explained in Appendix A.4.3, each digit of  
 4505 this integer represent a TDC flag that can be either 1 or 2. Each 2 is the sign of a `CORRUPTED` state.  
 4506 Then, the data is accessed entry by entry in the ROOT `TTree` using `RAWData` and each hit in the hit  
 4507 list is assigned to a detector channel and saved in the corresponding histograms. As described in  
 4508 Source Code B.13, in the first part of the analysis, in which the loop over the ROOT file's content is  
 4509 performed, the different steps are:

4510 **1- RPC channel assignment and control:** a check is done on the RPC channel extracted thanks  
 4511 to the mapping via the method `Mapping::GetLink()`. If the channel is not initialised and is 0, or if  
 4512 the TDC channel is not contained in a range in between X000 and X127, X being the TDC ID, the  
 4513 hit is discarded. This means there was a problem in the mapping. Often a mapping problem leads to  
 4514 the failure of the offline tool.

4515 **2- Creation of a `RPCHit` object:** to easily get the trolley, slot and partition in which the hit has  
 4516 been assigned, this object is particularly helpful.

4517 **3- General histograms are filled:** the hit is filled into the time distribution, global hit distribution  
 4518 and time versus strip histograms, and if the arrival time is within the first 100 ns, it is discarded and  
 4519 nothing else happens and the loop proceeds with the next hit in the list, going back to step 1.

4520

```

for(int h = 0; h < data.TDCCh->size(); h++) {
    Uint tdcchannel = data.TDCCh->at(h);
    Uint rpcchannel = RPCChMap->GetLink(tdcchannel);
    float timestamp = data.TDCTS->at(h);
    //Get rid of the hits in channels not considered in the mapping
    if(rpcchannel != NOCHANNELLINK) {
        RPCHit hit(rpcchannel, timestamp, GIFInfra);
        Uint T = hit.GetTrolley();
        Uint S = hit.GetStation()-1;
        Uint P = hit.GetPartition()-1;
        //Fill the time and hit profiles
        TimeProfile_H.rpc[T][S][P]->Fill(hit.GetTime());
        HitProfile_H.rpc[T][S][P]->Fill(hit.GetStrip());
        TimeVSChanProfile_H.rpc[T][S][P]->Fill(hit.GetStrip(), hit.GetTime());
        //Reject the 100 first ns due to inhomogeneity of data
        if(hit.GetTime() >= TIMEREJECT) {
            Multiplicity.rpc[T][S][P]++;
            if(IsEfficiencyRun(RunType)) {
                //Define peak time range for efficiency calculation
                float lowlimit_eff = PeakTime.rpc[T][S][P]
                    - PeakWidth.rpc[T][S][P];
                float highlimit_eff = PeakTime.rpc[T][S][P]
                    + PeakWidth.rpc[T][S][P];
                bool peakrange = (hit.GetTime() >= lowlimit_eff
                    && hit.GetTime() < highlimit_eff);
                //Fill hits inside of the defined peak and noise range
                if(peakrange) {
                    BeamProfile_H.rpc[T][S][P]->Fill(hit.GetStrip());
                    PeakHitList.rpc[T][S][P].push_back(hit);
                } else {
                    StripNoiseProfile_H.rpc[T][S][P]->Fill(hit.GetStrip());
                    NoiseHitList.rpc[T][S][P].push_back(hit);
                }
                //Then define time range for fake efficiency
                float highlimit_fake = BMTDCWINDOW;
                float lowlimit_fake = highlimit_fake
                    - (highlimit_eff-lowlimit_eff);
                bool fakerange = (hit.GetTime() >= lowlimit_fake
                    && hit.GetTime() < highlimit_fake);
                //Fill the hits inside of the fake window
                if(fakerange) {
                    FakeHitList.rpc[T][S][P].push_back(hit);
                }
            } else {
                //Fill the hits inside of the defined noise range
                StripNoiseProfile_H.rpc[T][S][P]->Fill(hit.GetStrip());
                NoiseHitList.rpc[T][S][P].push_back(hit);
            }
        }
    }
}

```

4521

*Source Code B.13: For each entry of the raw ROOT data file, the code loops over the list of channels and corresponding time stamps contained in branches `TDC_channel` and `TDC_TimeStamp` and constructs `RPCHit` objects that are filled in the peak, noise and fake hit lists and also fills the time, hit, beam and noise profiles.*

4522

**4- Multiplicity counter:** the hit multiplicity counter of the corresponding detectors is incremented.

4523

4524 **5-a-1 Efficiency runs - Is the hit within the peak window? :** if the hit is contained in the peak  
 4525 window previously defined by Formula B.3, it is filled into the beam hit profile histogram of the  
 4526 corresponding chamber, added into the list of peak hits and increments the counter of *in time* hits.  
 4527 The term *in time* here refers to the hits that are likely to be muons by arriving in the expected time  
 4528 window. If the hit is outside of the peak window, it is filled into the noise profile histogram of  
 4529 the corresponding detector, added into the list of noise/gamma hits and increments the counter of  
 4530 noise/gamma hits.

4531 **5-a-2 Efficiency runs - Is the hit within the fake window? :** if the hit is contained in the fake  
 4532 window previously defined by Formula B.4, it is added into the list of fake hits. Counting the fake  
 4533 hits outside the peak window allows to estimate the probability to detect in time background or noise.

4534 **5-b- Noise/gamma rate runs - Noise histograms are filled:** the hit is filled into the noise profile  
 4535 histogram of the corresponding detector, added into the list of noise/gamma hits and increments the  
 4536 counter of noise/gamma hits.

```
4537
  for(UInt tr = 0; tr < GIFInfra->GetNTrolleys(); tr++) {
    UInt T = GIFInfra->GetTrolleyID(tr);
    for(UInt sl = 0; sl < GIFInfra->GetNSlots(tr); sl++) {
      UInt S = GIFInfra->GetSlotID(tr,sl) - 1;
      UInt nStripsPart = GIFInfra->GetNStrips(tr,sl);
      string rpcID = GIFInfra->GetName(tr,sl);
      for (UInt p = 0; p < GIFInfra->GetNPartitions(tr,sl); p++) {
        //Clusterize noise/gamma data
        sort(NoiseHitList.rpc[T][S][p].begin(),
              NoiseHitList.rpc[T][S][p].end(),SortHitbyTime);
        Clusterization(NoiseHitList.rpc[T][S][p],
                       NoiseCSize_H.rpc[T][S][p],NoiseCMult_H.rpc[T][S][p]);
        //Clusterize muon data and fill efficiency histograms based on
        //the content of peak and fake hit vectors if efficiency run
        if(IsEfficiencyRun(RunType)){
          //Peak data
          sort(PeakHitList.rpc[T][S][p].begin(),
                PeakHitList.rpc[T][S][p].end(),SortHitbyTime);
          Clusterization(PeakHitList.rpc[T][S][p],
                         PeakCSize_H.rpc[T][S][p],PeakCMult_H.rpc[T][S][p]);
          if(PeakHitList.rpc[T][S][p].size() > 0)
            EfficiencyPeak_H.rpc[T][S][p]->Fill(DETECTED);
          else EfficiencyPeak_H.rpc[T][S][p]->Fill(MISSED);

          //Fake data
          if(FakeHitList.rpc[T][S][p].size() > 0)
            EfficiencyFake_H.rpc[T][S][p]->Fill(DETECTED);
          else EfficiencyFake_H.rpc[T][S][p]->Fill(MISSED);
        }
        //Save and reinitialise the hit multiplicity
        HitMultiplicity_H.rpc[T][S][p]->Fill(Multiplicity.rpc[T][S][p]);
        Multiplicity.rpc[T][S][p] = 0;
      }
    }
  }
```

4539 *Source Code B.14: Loops to clusterize the hit lists and fill efficiency and multiplicity histograms.*

4540 After the loop on the hit list of the entry is over, the next step is to clusterize the 3D lists filled

4541 in the previous steps, as displayed in Source Code B.14. A 3D loop is then started over the active  
 4542 trolley, slot and RPC partitions to access these objects. Each `NoiseHitList` and `PeakHitList`, in  
 4543 case of efficiency run, are clusterized as described in section B.5.2. There corresponding cluster size  
 4544 and multiplicity histograms are filled at the end of the clustering process.

4545 Then, the peak and fake efficiency histograms are filled in case of efficiency run. The selection is  
 4546 simply made by checking whether the RPC detected signals in the peak window or/and fake window  
 4547 during this event. In the case a hit is recorded in either of both time windows, the histogram is  
 4548 filled with 1. On the contrary, the histogram is filled with 0. Finally, it is useful to remind that  
 4549 at this level, it is not possible yet to discriminate in between a muon hit and noise or gamma hit.  
 4550 the histograms `PeakCSize_H`, `PeakCMult_H` and `EfficiencyPeak_H` are then subjected to noise and  
 4551 background contamination. This contamination is estimated thanks to the fake efficiency histogram  
 4552 `EfficiencyFake_H` and corrected at the moment the results will be written into output CSV files and  
 4553 the histograms `MuonCSize_H`, `MuonCMult_H` and `Efficiency0_H` will be filled. The correction will be  
 4554 explained in Section B.6.4.3.

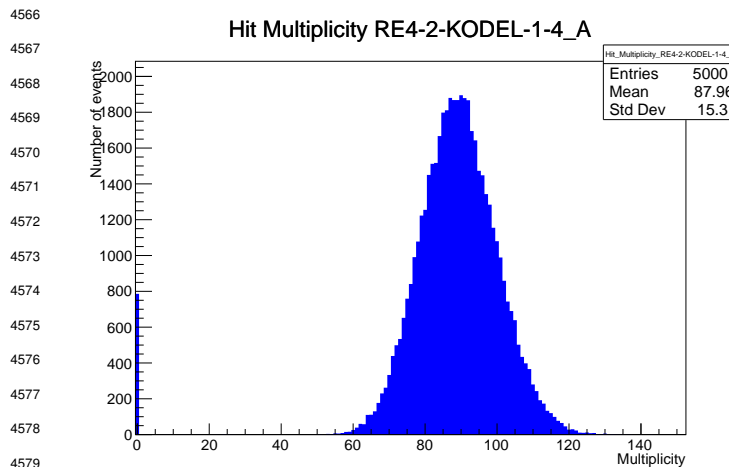
4555 Finally, the loop ends on the filling of the general hit multiplicity histogram of each detector  
 4556 partitions.

#### 4557 **B.6.4 Results calculation**

4558 As mentioned in section B.2.1, the analysis of DAQ data provides the user with 3 CSV files and  
 4559 a ROOT file associated to each and every ROOT data file. The fourth CSV file is provided by the  
 4560 extraction of the CEAN main frame data monitored during data taking and will be discussed later.  
 4561 After looping on the data in the previous part of the analysis macro, the output files are created and a  
 4562 3D loop on each RPC readout partitions is started to extract the histograms parameters and compute  
 4563 the final results.

4564

##### 4565 **B.6.4.1 Rate normalisation**



4580  
 4581 *Figure B.2: The effect of the quality flag is explained by presenting the  
 4582 reconstructed hit multiplicity of a data file without `Quality_flag`. The  
 4583 artificial high content of bin 0 is the effect of corrupted data.*

The hit rate normalization corresponds to translating a number of hits recorded during the full duration of data taking into a rate per unit area value. In order to achieve such result, it is first needed to know the total integrated time and the active area of the read-out partition on which the hits are counted. The total integrated is simply the noise window used for each event multiplied by the total number of events stored in the data file.

Nevertheless, to analyse old data format files, not containing any quality flag, it is

needed to estimate the amount of corrupted data via a fit as the corrupted data will always fill events with a fake "0 multiplicity". Indeed, as no hits were stored in the DAQ ROOT files, these events artificially contribute to fill the bin corresponding to a null multiplicity, as shown in Figure B.2. In the case the mean of the hit multiplicity distribution is high, the contribution of the corrupted data can easily be evaluated for later correction by comparing the level of the bin at multiplicity 0 and of a skew fit curve that should indicate a value consistent with 0. A skew fit has been chosen over a Poisson fit as it was giving better results for lower mean multiplicity values. Nevertheless, for low irradiation cases, as explained in Appendix A.4.3, the hit multiplicity distribution mean is, on the contrary, rather small and the probability to record events without hits can't be considered small anymore, leading to a difficult and non-reliable estimation of the corruption.

```

4584
4585     needed to estimate the amount of corrupted data via a fit as the corrupted data will always fill events
4586     with a fake "0 multiplicity". Indeed, as no hits were stored in the DAQ ROOT files, these events
4587     artificially contribute to fill the bin corresponding to a null multiplicity, as shown in Figure B.2. In
4588     the case the mean of the hit multiplicity distribution is high, the contribution of the corrupted data
4589     can easily be evaluated for later correction by comparing the level of the bin at multiplicity 0 and
4590     of a skew fit curve that should indicate a value consistent with 0. A skew fit has been chosen over
4591     a Poisson fit as it was giving better results for lower mean multiplicity values. Nevertheless, for
4592     low irradiation cases, as explained in Appendix A.4.3, the hit multiplicity distribution mean is, on
4593     the contrary, rather small and the probability to record events without hits can't be considered small
4594     anymore, leading to a difficult and non-reliable estimation of the corruption.

4594
4595     if(!isNewFormat) {
4596         TF1* GaussFit = new TF1("gaussfit","[0]*exp(-0.5*((x-[1])/[2])**2)",0,Xmax);
4597         GaussFit->SetParameter(0,100);
4598         GaussFit->SetParameter(1,10);
4599         GaussFit->SetParameter(2,1);
4600         HitMultiplicity_H.rpc[T][S][p]->Fit(GaussFit,"LIQR","","0.5,Xmax");
4601
4602         TF1* SkewFit = new TF1("skewfit","[0]*exp(-0.5*((x-[1])/[2])**2) / (1 +
4603         <- exp(-[3]*(x-[4])))",0,Xmax);
4604         SkewFit->SetParameter(0,GaussFit->GetParameter(0));
4605         SkewFit->SetParameter(1,GaussFit->GetParameter(1));
4606         SkewFit->SetParameter(2,GaussFit->GetParameter(2));
4607         SkewFit->SetParameter(3,1);
4608         SkewFit->SetParameter(4,1);
4609         HitMultiplicity_H.rpc[T][S][p]->Fit(SkewFit,"LIQR","","0.5,Xmax");
4610
4611         double fitValue = SkewFit->Eval(1,0,0,0);
4612         double dataValue = (double)HitMultiplicity_H.rpc[T][S][p]->GetBinContent(2);
4613         double difference = TMath::Abs(dataValue - fitValue);
4614         double fitTOdataVSentries_ratio = difference / (double)nEntries;
4615         bool isFitGOOD = fitTOdataVSentries_ratio < 0.01;
4616         double nSinglehit = (double)HitMultiplicity_H.rpc[T][S][p]->GetBinContent(1);
4617         double lowMultRatio = nSinglehit / (double)nEntries;
4618         bool isMultLOW = lowMultRatio > 0.4;
4619         if(isFitGOOD && !isMultLOW){
4620             nEmptyEvent = HitMultiplicity_H.rpc[T][S][p]->GetBinContent(1);
4621             nPhysics = (int)SkewFit->Eval(0,0,0,0);
4622             if(nPhysics < nEmptyEvent)
4623                 nEmptyEvent = nEmptyEvent-nPhysics;
4624         }
4625     }
4626     double corrupt_ratio = 100.*(double)nEmptyEvent / (double)nEntries;
4627     outputCorrCSV << corrupt_ratio << '\t';
4628     float rate_norm = 0.;
4629     float stripArea = GIFInfra->GetStripGeo(tr,sl,p);

4630     if(IsEfficiencyRun(RunType)){
4631         float noiseWindow = BMTDCWINDOW - TIMEREJECT - 2*PeakWidth.rpc[T][S][p];
4632         rate_norm = (nEntries-nEmptyEvent)*noiseWindow*1e-9*stripArea;
4633     } else
4634         rate_norm = (nEntries-nEmptyEvent)*RDMNOISEWDW*1e-9*stripArea;

```

*Source Code B.15: Definition of the rate normalisation variable. It takes into account the number of non corrupted entries and the time window used for noise and background calculation, to estimate the total integrated time, and the strip active area to express the result as rate per unit area.*

4597     As can be seen in Source Code B.15, conditions have been applied to prevent bad fits and wrong  
 4598     corruption estimation in cases where :

- 4599     • The difference in between the data for multiplicity 1 and the corresponding fit value should be  
 4600       lower than 1% of the total amount of data :  $\frac{|n_{m=1} - sk(1)|}{N_{tot}} < 0.01$  where  $n_{m=1}$  is the number  
 4601       of entries with multiplicity 1,  $sk(1)$  the value of the skew fit, as defined by Formula 5.2, for  
 4602       multiplicity 1 and  $N_{tot}$  the total number of entries.
- 4603     • The amount of data contained in the multiplicity 0 bin should not exceed 40% of the total  
 4604       data content:  $\frac{n_{m=0}}{N_{tot}} \leq 0.4$  where  $n_{m=0}$  is the number of entries with multiplicity 0. This  
 4605       number has been determined to be the maximum to be able to separate the excess of data due  
 4606       to corruption from the hit multiplicity distribution.

4607     Those 2 conditions need to be fulfilled to estimate the corruption of old data format files. If the  
 4608     fit was successful, the level of corruption is written in `Offline-Corrupted.csv` and the number of  
 4609     corrupted entries, refered as the integer `nEmptyEvent`, is subtracted from the total number of entries  
 4610     when the rate normalisation factor is computed as explicitated in Source Code B.15. Note that for new  
 4611     data format files, the number of corrupted entries being set to 0, the definition of `rate_norm` stays  
 4612     valid.

#### 4613     B.6.4.2 Rate and activity

```
int nNoise = StripNoiseProfile_H.rpc[T][S][p]->GetEntries();
float averageNhit = (nNoise>0) ? (float)(nNoise/nStripsPart) : 1.;

for(Uint st = 1; st <= nStripsPart; st++){
    float stripRate =
        StripNoiseProfile_H.rpc[T][S][p]->GetBinContent(st)/rate_norm;
    float stripAct =
        StripNoiseProfile_H.rpc[T][S][p]->GetBinContent(st)/averageNhit;

    StripNoiseProfile_H.rpc[T][S][p]->SetBinContent(st,stripRate);
    StripActivity_H.rpc[T][S][p]->SetBinContent(st,stripAct);
}
```

4615     *Source Code B.16: Description of the loop that allows to set the content of each strip rate and strip activity  
 channel for each detector partition.*

4616     At this point, the strip rate histograms, `StripNoiseProfile_H.rpc[T][S][p]`, only contain an  
 4617     information about the total number of noise or background rate hits each channel received during the  
 4618     data taking. As described in Source Code B.16, a loop on the strip channels will be used to normalise  
 4619     the content of the rate distribution histogram for each detector partitions. The initial number of hits  
 4620     recorded for a given bin will be extracted and 2 values are computed.

- 4621     • The strip hit rate, defined as the number of hits recorded in the bin normalised like described  
 4622       in the previous section, using the variable `rate_norm` and the corresponding bin in histogram  
 4623       `StripNoiseProfile_H.rpc[T][S][p]` is updated, and
- 4624     • the strip activity, defined as the number of hits recorded in the bin normalised to the average  
 4625       number of hits per bin contained in the partition histogram, using the variable `averageNhit`.  
 4626       This value provides an information on the homogeneity of the detector response to the gamma

4627 background or of the detector noise. An activity of 1 corresponds to an average response.  
 4628 Above 1, the channel is more active than the average and bellow 1, the channel is less active.  
 4629 This value is filled in the histograms `StripActivity_H.rpc[T][S][p]`.

4630 On each detector partitions, which are read-out by a single FEE, all the channels are not pro-  
 4631 cessed by the same chip. Each chip can give a different noise response and hence, histograms using  
 4632 a chip binning are used to investigate chip related noise behaviours. The average values of the strip  
 4633 rate or activity grouped into a given chip are extracted using the using the function `GetChipBin()`  
 4634 and stored in dedicated histograms as described in Source Codes B.17 and B.18 respectively.

```
4635 float GetChipBin(TH1* H, Uint chip){  

  4636   Uint start = 1 + chip*NSTRIPSCHIP;  

   int nActive = NSTRIPSCHIP;  

   float mean = 0.;  

   for(Uint b = start; b <= (chip+1)*NSTRIPSCHIP; b++) {  

     float value = H->GetBinContent(b);  

     mean += value;  

     if(value == 0.) nActive--;  

   }  

   if(nActive != 0) mean /= (float)nActive;  

   else mean = 0.;  

   return mean;  

}
```

4637 *Source Code B.17: Function used to compute the content of a bin for an histogram using chip binning.*

```
4638   for(Uint ch = 0; ch < (nStripsPart/NSTRIPSCHIP); ch++) {  

    ChipMeanNoiseProf_H.rpc[T][S][p]->  

      SetBinContent(ch+1,GetChipBin(StripNoiseProfile_H.rpc[T][S][p],ch));  

    ChipActivity_H.rpc[T][S][p]->  

      SetBinContent(ch+1,GetChipBin(StripActivity_H.rpc[T][S][p],ch));  

  }
```

4639 *Source Code B.18: Description of the loop that allows to set the content of each chip rate and chip activi-  
 tity bins for each detector partition knowing the information contained in the corresponding strip distribution  
 histograms.*

4640 The activity variable is then used to evaluate the homogeneity of the detector response to back-  
 4641 ground or of the detector noise. The homogeneity  $h_p$  of each detector partition can be evaluated  
 4642 using the formula  $h_p = \exp(-\sigma_p^R/\langle R \rangle_p)$ , where  $\langle R \rangle_p$  is the partition mean rate and  $\sigma_p^R$  is the  
 4643 rate standard deviation calculated over the partition channels. The more homogeneously the rates  
 4644 are distributed and the smaller will  $\sigma_p^R$  be, and the closer to 1 will  $h_p$  get. On the contrary, if the  
 4645 standard deviation of the channel's rates is large,  $h_p$  will rapidly get to 0. This value is saved into  
 4646 histograms as shown in Source Code B.19 and could in the future be used to monitor through time,  
 4647 once extracted, the evolution of every partition homogeneity. This could be of great help to under-  
 4648 stand the apparition of eventual hot spots due to ageing of the chambers subjected to high radiation  
 4649 levels. The monitored homogeneity information could then be combined with a monitoring of the  
 4650 activity of each individual channel in order to have a finer information. Monitoring tools have been  
 4651 suggested and need to be developed for this purpose.

```

4652   float MeanPartSDev = GetTH1StdDev(StripNoiseProfile_H.rpc[T][S][p]);
4653   float strip_homog = (MeanPartRate==0)
4654     ? 0.
4655     : exp(-MeanPartSDev/MeanPartRate);
4656   StripHomogeneity_H.rpc[T][S][p]->Fill("exp -#left(#frac{\#sigma_{Strip}
4657     \rightarrow Rate}}{\#mu_{(Strip Rate)}}\#right)",strip_homog);
4658   StripHomogeneity_H.rpc[T][S][p]->GetYaxis()->SetRangeUser(0.,1.);

4653   float ChipStDevMean = GetTH1StdDev(ChipMeanNoiseProf_H.rpc[T][S][p]);
4654   float chip_homog = (MeanPartRate==0)
4655     ? 0.
4656     : exp(-ChipStDevMean/MeanPartRate);
4657   ChipHomogeneity_H.rpc[T][S][p]->Fill("exp -#left(#frac{\#sigma_{(Chip
4658     \rightarrow Rate)}}{\#mu_{(Chip Rate)}}\#right)",chip_homog);
4659   ChipHomogeneity_H.rpc[T][S][p]->GetYaxis()->SetRangeUser(0.,1.);
```

4654      *Source Code B.19: Storage of the homogeneity into dedicated histograms.*

#### 4655      B.6.4.3 Correction of muon performance parameters

4656      By previously filling the peak and fake efficiency histograms as well as the peak and noise cluster  
4657      size and cluster multiplicity it is possible to compute the efficiency of muon detection, the muon  
4658      cluster size, as well as the muon cluster multiplicity. This calculation is based on independant  
4659      event probabilities. The independant events that can be measured in the data are, " $\mu$ : A muon was  
4660      detected" and " $\gamma$ : noise or background was detected". It is trivial to realize that the data in the peak  
4661      window corresponds to the intersection of both events, " $\mu \cup \gamma$ : a muon or noise or background was  
4662      detected". This way, the efficiency measured in the peak window is actually the probability of the  
4663      event  $\mu \cup \gamma$  while the efficiency in the fake window is then the probability of the event  $\gamma$  alone.  
4664      Assuming that  $\mu$  and  $\gamma$  are independant, the probability of their intersection can be written as in  
4665      Formula B.5.

$$(B.5) \quad P(\mu \cup \gamma) = P(\mu) + P(\gamma) - P(\mu)P(\gamma)$$

4666      Isolating the probability of the event  $\mu$  alone, actually corresponding to the muon detection  
4667      efficiency, can be then calculated with the quantities that are contained in the peak and fake histogram  
4668      as in Formula B.6.

$$(B.6) \quad P(\mu) = \frac{P(\mu \cup \gamma) - P(\gamma)}{1 - P(\gamma)} \quad \Leftrightarrow \quad \epsilon_\mu = \frac{\epsilon_{peak} - \epsilon_{fake}}{1 - \epsilon_{fake}}$$

4669      When it comes to the computation of the muon cluster size, a similar reasoning than for the muon  
4670      detection efficiency computation can be used. Indeed, using Formula B.5, out of the total number of  
4671      events where a muon or noise or background can be expressed as a sum of fractions of events  $\mu$ ,  $\gamma$   
4672      and  $\mu \cap \gamma$ , the later being the event corresponding to the detection of both events simultaneously, as  
4673      showed in Formula B.7. The fractions can be expressed as a ratio of the probabilities already known,  
4674      using this time the notation  $P(\mu \cap \gamma)$  instead of  $P(\mu)P(\gamma)$ . This choice was made to make the code  
4675      a little clearer.

$$(B.7) \quad 1 = F_\mu + F_\gamma + F_{\mu \cap \gamma} = \frac{P(\mu) - P(\mu \cap \gamma)}{P(\mu \cup \gamma)} + \frac{P(\gamma) - P(\mu \cap \gamma)}{P(\mu \cup \gamma)} + \frac{P(\mu \cap \gamma)}{P(\mu \cup \gamma)}$$

```

if(IsEfficiencyRun(RunType)){  

    //Evaluate the probabilities for each detection case with errors  

    float P_peak = EfficiencyPeak_H.rpc[T][S][p]->GetMean();  

    float P_fake = EfficiencyFake_H.rpc[T][S][p]->GetMean();  

    float P_muon = (P_peak-P_fake)/(1-P_fake);  

    float P_both = P_muon*P_fake;  

    float P_peak_err = sqrt(P_peak*(1.-P_peak)/nEntries);  

    float P_fake_err = sqrt(P_fake*(1.-P_fake)/nEntries);  

    float P_muon_err = sqrt(P_muon*(1.-P_muon)/nEntries);  

    float P_both_err = sqrt(P_both*(1.-P_both)/nEntries);  

    Efficiency0_H.rpc[T][S][p]->Fill("muon efficiency",P_muon);  

    Efficiency0_H.rpc[T][S][p]->Fill("muon efficiency error",P_muon_err);  

    //For each case get the fraction of events it represents  

    float F_both = P_both/P_peak;  

    float F_muon = (P_muon-P_both)/P_peak;  

    float F_fake = (P_fake-P_both)/P_peak;  

    float F_both_err = F_both*(P_both_err/P_both+P_peak_err/P_peak);  

    float F_muon_err = (P_muon_err+F_both_err+F_muon*P_peak_err)/P_peak;  

    float F_fake_err = (P_fake_err+F_both_err+F_fake*P_peak_err)/P_peak;  

    //Get the measured cluster sizes correcting using the fractions  

    float CS_peak = PeakCSIZE_H.rpc[T][S][p]->GetMean();  

    float CS_fake = NoiseCSIZE_H.rpc[T][S][p]->GetMean();  

    float CS_peak_err = 2*PeakCSIZE_H.rpc[T][S][p]->GetStdDev()  

        /sqrt(PeakCSIZE_H.rpc[T][S][p]->GetEntries());  

    float CS_fake_err = 2*NoiseCSIZE_H.rpc[T][S][p]->GetStdDev()  

        /sqrt(NoiseCSIZE_H.rpc[T][S][p]->GetEntries());  

    float CS_muon = (CS_peak-CS_fake*(F_fake+F_both/2.))/(F_muon+F_both/2.);  

    float CS_muon_err = (CS_peak_err  

        +(F_fake+F_both/2.)*CS_fake_err  

        +CS_muon*F_muon_err  

        +CS_fake*(F_fake_err+F_both_err/2.))  

        /(F_muon+F_both/2.);  

    MuonCSIZE_H.rpc[T][S][p]->Fill("muon cluster size",CS_muon);  

    MuonCSIZE_H.rpc[T][S][p]->Fill("muon cluster size error",CS_muon_err);  

    //Finally get the muon cluster multiplicity as peak-fake  

    float noiseWindow = BMTDCWINDOW - TIMEREJECT - 2*PeakWidth.rpc[T][S][p];  

    float peakWindow = 2*PeakWidth.rpc[T][S][p];  

    float CM_peak = PeakCMult_H.rpc[T][S][p]->GetMean();  

    float CM_fake = NoiseCMult_H.rpc[T][S][p]->GetMean()*peakWindow/noiseWindow;  

    float CM_muon = CM_peak-CM_fake;  

    float CM_peak_err = 2*PeakCMult_H.rpc[T][S][p]->GetStdDev()  

        /sqrt(PeakCMult_H.rpc[T][S][p]->GetEntries());  

    float CM_fake_err = 2*NoiseCMult_H.rpc[T][S][p]->GetStdDev()  

        /sqrt(NoiseCMult_H.rpc[T][S][p]->GetEntries())  

        * peakWindow/noiseWindow;  

    float CM_muon_err = CM_peak_err + CM_fake_err;  

    MuonCMult_H.rpc[T][S][p]->Fill("muon cluster multiplicity",CM_muon);  

    MuonCMult_H.rpc[T][S][p]->Fill("muon cluster multiplicity  

    ↳ error",CM_muon_err);  

    //Write in the output CSV file  

    outputEffCSV << P_muon << '\t' << P_muon_err << '\t'  

        << CS_muon << '\t' << CS_muon_err << '\t'  

        << CM_peak << '\t' << CM_peak_err << '\t';
}

```

4677     Source Code B.20: Analysis algorithm to compute muon efficiency, cluster size and multiplicity knowing the peak and fake efficiency, cluster size and multiplicity.

4678     Each ones of these events have an associated cluster size. The cluster size of the noise or back-  
 4679     ground already is measured thanks to the clusterization of the noise hit list. In the same way, the  
 4680     peak cluster size corresponds to the cluster measured for the event  $\mu \cup \gamma$ . Nevertheless, the cluster  
 4681     of the event  $\mu \cap \gamma$  is not known but it can be assumed that the probability of having more than 1  
 4682     noise or background cluster contained in the peak window is very low if the peak wondow duration  
 4683     is compared to the background rate that rarely seen to go beyond 2000 Hz/cm<sup>2</sup> [to be confirmed].  
 4684     Hence, the cluster size that is likely to be measured in such kind of event where both a muon and a  
 4685     background or noise cluster was recorded is the average of the muon cluster size and the background  
 4686     cluster size. The cluster size  $C_{\mu \cup \gamma}$  probed in the peak can then be written as in Formula B.8 and  
 4687     leads to the expression for the muon cluster size  $C_\mu$  written in Formula B.9.

$$(B.8) \quad C_{\mu \cup \gamma} = C_\mu F_\mu + C_\gamma F_\gamma + \frac{C_\mu + C_\gamma}{2} \times F_{\mu \cap \gamma}$$

$$(B.9) \quad C_\mu = \frac{C_{\mu \cup \gamma} - C_\gamma \times (F_\gamma + F_{\mu \cap \gamma}/2)}{F_\mu + F_{\mu \cap \gamma}/2}$$

4688     Finally, the computation of the muon cluster multiplicity comes quite naturally as the cluster  
 4689     multiplicity measured in the peak to which is subtracted the background cluster multiplpicity taken  
 4690     in a window of similar width. These calculations, as well as the error propagation that was not  
 4691     explicated here, can be seen going through Source Code B.20.

#### 4692     B.6.4.4 Strip masking tool

4693     The offline tool is automatically called at the end of each data taking to analyse the data and offer  
 4694     the shifter DQM histograms to control the data quality. After the histograms have been published  
 4695     online in the DQM page, the shifter can decide to mask noisy or dead channels that will contribute  
 4696     to bias the final rate calculation by editing the mask column of `ChannelsMapping.csv` as can be seen  
 4697     in Figure B.3.

4698     From the code point of view, the function `GetTH1Mean()` is used to retrieve the mean rate par-  
 4699     tition by partition after the rates have been calculated strip by strip and filled into the histograms  
 4700     `StripNoiseProfile_H.rpc[T][S][p]`, as described through Source Code B.21.

4701     Once the mask for each rejected channel has been updated, the shifter can manually run the  
 4702     offline tool again to update the DQM plots, now including the masked strips, as well the rate results  
 4703     written in the output CSV file `Offline-Rate.csv`. If not done during the shifts, the strip masking  
 4704     procedure needs to be carefully done by the person in charge of data analysis on the scans that were  
 4705     selected to produce the final results.

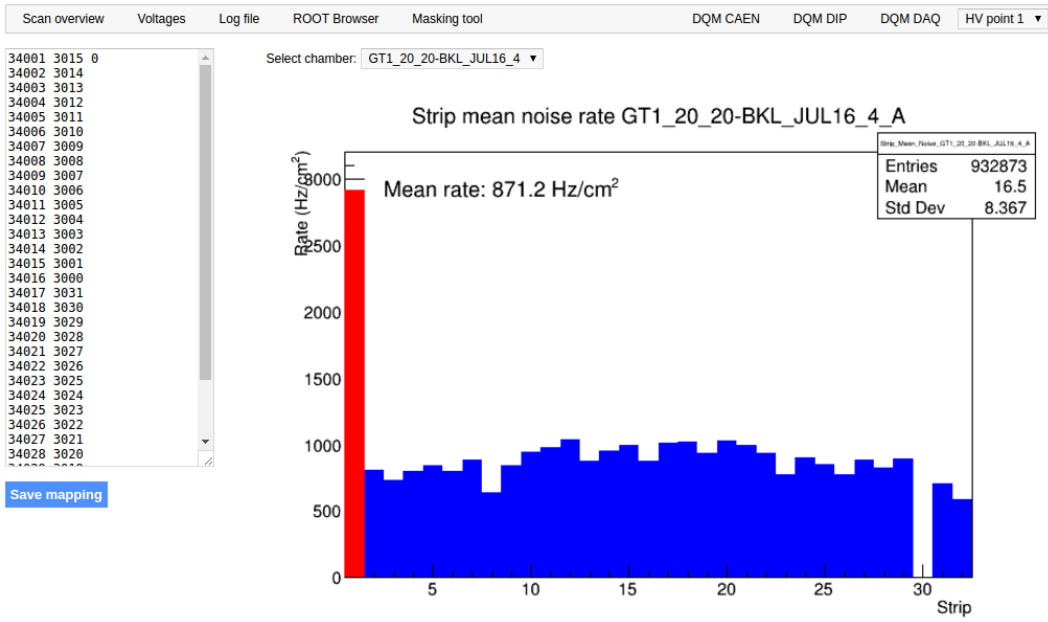


*Figure B.3: Display of the masking tool page on the webDCS. The window on the left allows the shifter to edit ChannelsMapping.csv. To mask a channel, it only is needed to set the 3rd field corresponding to the strip to mask to 0. It is not necessary for older mapping file formats to add a 1 for each strip that is not masked as the code is versatile and the default behaviour is to consider missing mask fields as active strips. The effect of the mask is directly visible for noisy channels as the corresponding bin turns red. The global effect of masking strips will be an update of the rate value showed on the histogram that will take into consideration the rejected channels.*

```

float GetTH1Mean (TH1* H){
    int nBins = H->GetNbinsX();
    int nActive = nBins;
    float mean = 0.;

    for(int b = 1; b <= nBins; b++){
        float value = H->GetBinContent (b);
        mean += value;
        if(value == 0.) nActive--;
    }

    if(nActive != 0) mean /= (float)nActive;
    else mean = 0.;

    return mean;
}

```

*Source Code B.21: The function GetTH1Mean() is used to return the mean along the y-axis of TH1 histograms containing rate information. In order to take into account masked strips whose rate is set to 0, the function looks for masked channels and decrement the number of active channels for each null value found.*

4708 **B.6.4.5 Output CSV files filling**

```

for (UInt tr = 0; tr < GIFInfra->GetNTrolleys(); tr++) {
    UInt T = GIFInfra->GetTrolleyID(tr);
    for (UInt sl = 0; sl < GIFInfra->GetNSlots(tr); sl++) {
        UInt S = GIFInfra->GetSlotID(tr,sl) - 1;
        float MeanNoiseRate = 0.;
        float ClusterRate = 0.;
        float ClusterSDev = 0.;

        for (UInt p = 0; p < GIFInfra->GetNPartitions(tr,sl); p++) {
            float MeanPartRate = GetTH1Mean(StripNoiseProfile_H.rpc[T][S][p]);
            float cSizePart = NoiseCSize_H.rpc[T][S][p]->GetMean();
            float cSizePartErr = (NoiseCSize_H.rpc[T][S][p]->GetEntries()==0)
                ? 0.
                : 2*NoiseCSize_H.rpc[T][S][p]->GetStdDev() /
                    sqrt(NoiseCSize_H.rpc[T][S][p]->GetEntries());
            float cMultPart = NoiseCMult_H.rpc[T][S][p]->GetMean();
            float cMultPartErr = (NoiseCMult_H.rpc[T][S][p]->GetEntries()==0)
                ? 0.
                : 2*NoiseCMult_H.rpc[T][S][p]->GetStdDev() /
                    sqrt(NoiseCMult_H.rpc[T][S][p]->GetEntries());
            float ClustPartRate = (cSizePart==0) ? 0.
                : MeanPartRate/cSizePart;
            float ClustPartRateErr = (cSizePart==0) ? 0.
                : ClustPartRate * cSizePartErr/cSizePart;

            outputRateCSV << MeanPartRate << '\t'
                << cSizePart << '\t' << cSizePartErr << '\t'
                << cMultPart << '\t' << cMultPartErr << '\t'
                << ClustPartRate << '\t' << ClustPartRateErr << '\t';

            RPCArea += stripArea * nStripsPart;
            MeanNoiseRate += MeanPartRate * stripArea * nStripsPart;
            ClusterRate += ClustPartRate * stripArea * nStripsPart;
            ClusterSDev += (cSizePart==0)
                ? 0.
                : ClusterRate*cSizePartErr/cSizePart;
        }
        MeanNoiseRate /= RPCArea;
        ClusterRate /= RPCArea;
        ClusterSDev /= RPCArea;
        outputRateCSV << MeanNoiseRate << '\t' << ClusterRate << '\t'
            << ClusterSDev << '\t';
    }
}

```

4710 *Source Code B.22: Description of rate result calculation and writing into the CSV output Offline-Rate.csv. Are saved into the file for each detector, the mean partition rate, cluster size and cluster mutiplicity, along with their errors, for each partition and as well as a detector average.*

4711 All the histograms have been filled. Parameters will then be extracted from them to compute the  
4712 final results that will later be used to produce plots. Once the results have been computed, the very  
4713 last step of the offline macro is to write these values into the corresponding CSV outputs. Aside of  
4714 the file Offline-Corrupted.csv, 2 CSV files are being written by the macro OfflineAnalysis(),  
4715 Offline-Rates.csv and Offline-L0-EffCl.csv that respectively contain information about noise  
4716 or gamma rates, cluster size and multiplicity, and about level 0 reconstruction of the detector effi-  
4717 ciency, muon cluster size and multiplicity. Details on the computation and file writing are respec-

<sup>4718</sup> tively given in Sources Codes B.22 and B.20.

<sup>4719</sup> **Noise/gamma background variables** are computed and written in the output file for each detector  
<sup>4720</sup> partitions. A detector average of the hit and cluster rate is also provided, as shown through Sources  
<sup>4721</sup> Code B.22. The variables that are written for each partition are:

- <sup>4722</sup> • The mean partition hit rate per unit area, `MeanPartRate`, that is extracted from the histogram  
<sup>4723</sup> `StripNoiseProfile_H` as the mean value along the y-axis, as described in section B.6.4.4. No  
<sup>4724</sup> error is recorded for the hit rate as this is considered a single measurement. No statistical error  
<sup>4725</sup> can be associated to it and the systematics are unknown.
- <sup>4726</sup> • The mean cluster size, `cSizePart`, is extracted from the histogram `NoiseCSize_H` and it's  
<sup>4727</sup> statistical error, `cSizePartErr`, is taken to be  $2\sigma$  of the total distribution.
- <sup>4728</sup> • The mean cluster multiplicity per trigger, `cMultPart`, is extracted from the histogram `NoiseCMult_H`  
<sup>4729</sup> and it's statistical error, `cMultPartErr`, is taken to be  $2\sigma$  of the total distribution. It is impor-  
<sup>4730</sup> tant to point to the fact that this variable gives an information that is dependent on the buffer  
<sup>4731</sup> window width used for each trigger for the calculation.
- <sup>4732</sup> • The mean cluster rate per unit area, `ClustPartRate`, is defined as the mean hit rate normalised  
<sup>4733</sup> to the mean cluster size and it's statistical error, `ClustPartRateErr`, is then obtained using the  
<sup>4734</sup> relative statistical error on the mean cluster size.

<sup>4735</sup> **Muon performance variables** are computed as discussed in the Section B.6.4.3 and written in  
<sup>4736</sup> the output file for each detector partitions as shown through Sources Code B.20. It is reminded that  
<sup>4737</sup> this offline tool doesn't include any tracking algorithm to identify muons from the beam and only  
<sup>4738</sup> relies on the hits arriving in the time window corresponding to the beam time and is corrected thanks  
<sup>4739</sup> to the estimation of the contribution of the background and noise to the efficiency of the detector.  
<sup>4740</sup> Assuming that the detection of background and muons were independent events, a probabilistic  
<sup>4741</sup> approach was then used to correct efficiency, muon cluster size and muon cluster multiplicity. The  
<sup>4742</sup> variables that are written for each partition are:

- <sup>4743</sup> • The muon efficiency, referred to as the probability to detect a muon in the peak window  
<sup>4744</sup> `P_muon`, also filled in histogram `Efficiency0_H`. The statistical error related to the efficiency,  
<sup>4745</sup> `P_muon_err`, is computed using a binomial distribution, as the efficiency measures the proba-  
<sup>4746</sup> bility of "success" and "failure" to detect muons.
- <sup>4747</sup> • The mean muon cluster size, `CS_muon`, and its related statistical error, `CS_muon_err`, also filled  
<sup>4748</sup> in the histogram `MuonCSize_H`.
- <sup>4749</sup> • The mean muon cluster multiplicity, `CM_muon`, and its related statistical error, `CM_muon_err`,  
<sup>4750</sup> also filled in the histogram `MuonCMult_H`.

<sup>4751</sup> In addition to these 2 CSV files, the histograms are saved in ROOT file `Scan00XXXX_HVY_Offline.root`  
<sup>4752</sup> as explained in section B.2.1.1.

## 4753    B.7 Current information extraction

4754 Detectors under test at GIF++ are connected both to a CAEN HV power supply and to a CAEN  
4755 ADC that reads the currents inside of the RPC gaps bypassing the supply cable. During data tak-  
4756 ing, the webDCS records into a ROOT file called `Scan00XXXX_HVY_CAEN.root` histograms with the  
4757 monitored parameters of both CAEN devices. Are recorded for each RPC channels (in most cases,  
4758 a channel corresponds to an RPC gap):

- 4759     • the effective voltage,  $HV_{eff}$ , set by the webDCS using the PT correction on the CAEN power  
4760       supply,
- 4761     • the applied voltage,  $HV_{app}$ , monitored by the CAEN power supply, and the statistical error  
4762       related to the variations of this value through time to follow the variation of the environmental  
4763       parameters defined as the RMS of the histogram divided by the square root of the number of  
4764       recorded points,
- 4765     • the monitored current,  $I_{mon}$ , monitored by the CAEN power supply, and the statistical error  
4766       related to the variations of this value through time to follow the variation of the environmental  
4767       parameters defined as the RMS of the histogram divided by the square root of the number of  
4768       recorded points,
- 4769     • the corresponding current density,  $J_{mon}$ , defined as the monitored current per unit area,  
4770        $J_{mon} = I_{mon}/A$ , where  $A$  is the active area of the corresponding gap,
- 4771     • the ADC current,  $I_{ADC}$ , recorded through the CAEN ADC module that monitors the dark  
4772       current in the gap itself. First of all, the resolution of such a module is better than that of  
4773       CAEN power supplies and moreover, the current is not read-out through the HV supply line  
4774       but directly at the chamber level giving the real current inside of the detector. The statistical  
4775       error is defined as the RMS of the histogram distribution divided by the square root of the  
4776       number of recorded points.

4777 Once extracted through a loop over the element of GIF++ infrastructure via the C++ macro  
4778 `GetCurrent()`, these parameters, organised in 9 columns per detector HV supply line, are written in  
4779 the output CSV file `Offline-Current.csv`. The macro can be found in the file `Current.cc`.

## References

- [1] K. Ruedenberg & W.H.E. Schwarz. “Three Millennia of Atoms and Molecules”. In: *Pioneers of Quantum Chemistry*. Ed. by Angela K. Wilson E. Thomas Strom. Vol. 1122. ACS Symposium Series, 2013, pp. 1–45.
- [2] A. Lavoisier. *Traité élémentaire de chimie*. Éditions la Bibliothèque Digitale, 2014 (first published 1789).
- [3] J. Dalton. *A New System of Chemical Philosophy*. William Dawson & Sons, 1808.
- [4] J. von Fraunhofer. “Bestimmung des Brechungs- und des Farben-Zerstreuungs - Vermögens verschiedener Glasarten, in Bezug auf die Vervollkommnung achromatischer Fernröhre”. In: *Denkschriften der Königlichen Akademie der Wissenschaften zu München*. Die Akademie, 1817, pp. 193–226.
- [5] J.J. Thomson. “XL. Cathode Rays”. In: *The London, Edinburgh, and Dublin Philosophical Magazine and Journal of Science* 44:269 (1897), pp. 293–316.
- [6] J.B. Perrin. “Nouvelles propriétés des rayons cathodiques”. In: *Comptes Rendus Hebdomadaires des Séances de L'Académie des Sciences*. Vol. 121. Académie des Sciences, 1895, pp. 1130–1134.
- [7] H. Becquerel. “Déviation du rayonnement du radium dans un champ électrique”. In: *Comptes Rendus Hebdomadaires des Séances de L'Académie des Sciences*. Vol. 130. Académie des Sciences, 1900, p. 809.
- [8] J.J. Thomson. “XXIV. On the structure of the atom: an investigation of the stability and periods of oscillation of a number of corpuscles arranged at equal intervals around the circumference of a circle; with application of the results to the theory of atomic structure”. In: *The London, Edinburgh, and Dublin Philosophical Magazine and Journal of Science* 7:39 (1904), pp. 237–265.
- [9] E. Rutherford & T. Royds. “XXIV. Spectrum of the radium emanation”. In: *The London, Edinburgh, and Dublin Philosophical Magazine and Journal of Science* 16:92 (1904), pp. 313–317.
- [10] H. Geiger. “On the scattering of the  $\alpha$ -particles by matter”. In: *Proceedings of the Royal Society A* 81 (1908), pp. 174–177.
- [11] H. Geiger & E. Marsden. “On a diffuse reflection of the  $\alpha$ -particles”. In: *Proceedings of the Royal Society A* 82 (1909), pp. 495–500.
- [12] H. Geiger. “The scattering of  $\alpha$ -particles by matter”. In: *Proceedings of the Royal Society A* 83 (1910), pp. 492–504.
- [13] H. Geiger & E. Marsden. “LXI. The laws of deflexion of a particles through large angles”. In: *The London, Edinburgh, and Dublin Philosophical Magazine and Journal of Science* 25:148 (1913), pp. 604–623.

- 4816 [14] E. Rutherford. "LXXIX. The Scattering of  $\alpha$  and  $\beta$  Particles by Matter and the Structure of  
4817 the Atom". In: *The London, Edinburgh, and Dublin Philosophical Magazine and Journal of*  
4818 *Science* 21:125 (1911), pp. 669–688.
- 4819 [15] E. Rutherford. "LIV. Collision of  $\alpha$  particles with light atoms. IV. An anomalous effect in  
4820 nitrogen". In: *The London, Edinburgh, and Dublin Philosophical Magazine and Journal of*  
4821 *Science* 37:222 (1919), pp. 581–587.
- 4822 [16] O. Masson. "XXIV. The constitution of atoms". In: *The London, Edinburgh, and Dublin*  
4823 *Philosophical Magazine and Journal of Science* 41:242 (1921), pp. 281–285.
- 4824 [17] W. Prout. "On the Relation between the Specific Gravities of Bodies in their Gaseous State  
4825 and the Weights of their Atoms." In: *Annals of Philosophy* 6 (1815), pp. 321–330.
- 4826 [18] W. Prout. "Correction of a Mistake in the Essay on the Relation between the Specific Gravities  
4827 of Bodies in their Gaseous State and the Weights of their Atoms". In: *Annals of Philosophy*  
4828 7 (1816), pp. 111–113.
- 4829 [19] E. Rutherford. "Bakerian Lecture: Nuclear constitution of atoms". In: *Proceedings of the*  
4830 *Royal Society A* 97 (1920), pp. 374–400.
- 4831 [20] W. Bothe & H. Becker. "Künstliche Erregung von Kern- $\gamma$ -Strahlen". In: *Zeitschrift für Physik*  
4832 66 (1930), pp. 289–306.
- 4833 [21] H. Becker & W. Bothe. "Die in Bor und Beryllium erregten  $\gamma$ -Strahlen". In: *Zeitschrift für*  
4834 *Physik* 76 (1932), pp. 421–438.
- 4835 [22] I. Curie & F. Joliot. "Émission de protons de grande vitesse par les substances hydrogénées  
4836 sous l'influence de rayons  $\gamma$  très pénétrants". In: *Comptes Rendus Hebdomadaires des Séances*  
4837 *de L'Académie des Sciences*. Vol. 194. Académie des Sciences, 1932, pp. 273–275.
- 4838 [23] J. Chadwick. "Possible Existence of a Neutron". In: *Nature* 129 (1932), p. 312.
- 4839 [24] J. Chadwick. "Bakerian lecture. The neutron". In: *Proceedings of the Royal Society A* 142  
4840 (1933), pp. 1–25.
- 4841 [25] Max Plank. "Ueber das Gesetz der Energieverteilung im Normalspectrum". In: *Annalen Der*  
4842 *Physik* 309 (1901), pp. 553–563.
- 4843 [26] A. Einstein. "Über einen die Erzeugung und Verwandlung des Lichtes betreffenden heuris-  
4844 tischen Gesichtspunkt". In: *Annalen Der Physik* 322 (1905), pp. 132–148.
- 4845 [27] N. Bohr. "I. On the constitution of atoms and molecules". In: *The London, Edinburgh, and*  
4846 *Dublin Philosophical Magazine and Journal of Science* 26:151 (1913), pp. 1–25.
- 4847 [28] H.G.J. Moseley. "XCIII. The high-frequency spectra of the elements". In: *The London, Edin-  
4848 burgh, and Dublin Philosophical Magazine and Journal of Science* 26:156 (1913), pp. 1024–  
4849 1034.
- 4850 [29] A. Sommerfeld. "Zur Quantentheorie der Spektrallinien". In: *Annalen Der Physik* 356 (1916),  
4851 pp. 1–94.
- 4852 [30] P. Zeeman. "XXXII. On the influence of magnetism on the nature of the light emitted by a  
4853 substance". In: *The London, Edinburgh, and Dublin Philosophical Magazine and Journal of*  
4854 *Science* 43:262 (1897), pp. 226–239.
- 4855 [31] P. Zeeman. "VII. Doublets and triplets in the spectrum produced by external magnetic forces".  
4856 In: *The London, Edinburgh, and Dublin Philosophical Magazine and Journal of Science*  
4857 44:266 (1897), pp. 55–60.
- 4858 [32] P. Zeeman. "VII. Doublets and triplets in the spectrum produced by external magnetic forces.—(II.)"  
4859 In: *The London, Edinburgh, and Dublin Philosophical Magazine and Journal of Science*  
4860 44:268 (1897), pp. 255–259.

## BIBLIOGRAPHY

---

- 4861 [33] P. Zeeman. "XXI. Measurements concerning radiation-phenomena in the magnetic field.—(I.)"  
4862 In: *The London, Edinburgh, and Dublin Philosophical Magazine and Journal of Science*  
4863 45:273 (1898), pp. 197–201.
- 4864 [34] W. Gerlach & O. Stern. "Der experimentelle Nachweis der Richtungsquantelung im Mag-  
4865 netfeld". In: *Zeitschrift für Physik* 9 (1922), pp. 349–352.
- 4866 [35] W. Pauli. "Über den Einfluß der Geschwindigkeitsabhängigkeit der Elektronenmasse auf den  
4867 Zeeman-Effekt". In: *Zeitschrift für Physik* 31 (1925), 373–385.
- 4868 [36] W. Pauli. "Über den Zusammenhang des Abschlusses der Elektronengruppen im Atom mit  
4869 der Komplexstruktur der Spektren". In: *Zeitschrift für Physik* 31 (1925), 765–783.
- 4870 [37] G.E. Uhlenbeck & S. Goudsmit. "Spinning Electrons and the Structure of Spectra". In: *Nature*  
4871 117 (1926), pp. 264–265.
- 4872 [38] W. Pauli. "Zur Quantenmechanik des magnetischen Elektrons". In: *Zeitschrift für Physik* 43  
4873 (1927), 601–623.
- 4874 [39] L. De Broglie. "Recherches sur la théorie des Quanta". PhD thesis. University of Paris, 1924.
- 4875 [40] E. Schrödinger. "An Undulatory Theory of the Mechanics of Atoms and Molecules". In:  
4876 *Phys. Rev.* 28 (1927), pp. 1049–1070.
- 4877 [41] P. Dirac. "The quantum theory of the emission and absorption of radiation". In: *Proceedings  
4878 of the Royal Society A* 114 (1928), pp. 243–265.
- 4879 [42] P. Dirac. "The quantum theory of the electron". In: *Proceedings of the Royal Society A* 117  
4880 (1928), pp. 610–624.
- 4881 [43] J. R. Oppenheimer. "On the Theory of Electrons and Protons". In: *Phys. Rev.* 35 (1930),  
4882 pp. 562–563.
- 4883 [44] P. Dirac. "Quantised singularities in the electromagnetic field". In: *Proceedings of the Royal  
4884 Society A* 133 (1931), pp. 60–72.
- 4885 [45] J. R. Oppenheimer. "Note on the Theory of the Interaction of Field and Matter". In: *Phys.  
4886 Rev.* 35 (1930), pp. 461–477.
- 4887 [46] H.A. Bethe. "The Electromagnetic Shift of Energy Levels". In: *Phys. Rev.* 72 (1947), pp. 339–  
4888 341.
- 4889 [47] H.F.J. Dyson. "The Radiation Theories of Tomonaga, Schwinger, and Feynman". In: *Phys.  
4890 Rev.* 75 (1949), pp. 486–502.
- 4891 [48] H. Yukawa. "On the Interaction of Elementary Particles. I". In: *Proc. Phys. Math. Soc. Jap.*  
4892 17 (1935), pp. 48–57.
- 4893 [49] C.D. Anderson & S.H. Neddermeyer. "Cloud Chamber Observations of Cosmic Rays at 4300  
4894 Meters Elevation and Near Sea-Level". In: *Phys. Rev.* 50 (1936), pp. 263–271.
- 4895 [50] S.H. Neddermeyer & C.D. Anderson. "Note on the Nature of Cosmic-Ray Particles". In:  
4896 *Phys. Rev.* 51 (1937), pp. 884–886.
- 4897 [51] J.C. Street & E.C. Stevenson. "New Evidence for the Existence of a Particle of Mass Inter-  
4898 mediate Between the Proton and Electron". In: *Phys. Rev.* 52 (1937), pp. 1003–1004.
- 4899 [52] C.M.G. Lattes et al. "Processes involving charged mesons". In: *Nature* 159 (1947), pp. 694–  
4900 697.
- 4901 [53] C.M.G. Lattes et al. "Observations on the Tracks of Slow Mesons in Photographic Emulsions  
4902 (Part 1)". In: *Nature* 160 (1947), pp. 453–456.

- 4903 [54] C.M.G. Lattes et al. “Observations on the Tracks of Slow Mesons in Photographic Emulsions  
4904 (Part 2)”. In: *Nature* 160 (1947), 486–492.
- 4905 [55] R. Blokland et al. “High Energy Photons from Proton-Nucleon Collisions”. In: *Phys. Rev.*  
4906 77 (1950), pp. 213–218.
- 4907 [56] G.D. Rochester & C.C. Butler. “Evidence for the Existence of New Unstable Elementary  
4908 Particles”. In: *Nature* 160 (1947), 855–857.
- 4909 [57] A. Pais. “Some Remarks on the V-Particles”. In: *Phys. Rev.* 86 (1952), pp. 663–672.
- 4910 [58] M. Gell-Mann. “Symmetries of Baryons and Mesons”. In: *Phys. Rev.* 125 (1962), pp. 1067–  
4911 1084.
- 4912 [59] K. Nishijima & T. Nakano. “Charge Independence for V-particles”. In: *Progress of Theoretical  
4913 Physics* 10 (1953), 581–582.
- 4914 [60] K. Nishijima. “Charge Independence Theory of V-Particles”. In: *Progress of Theoretical  
4915 Physics* 13 (1955), pp. 285–304.
- 4916 [61] M. Gell-Mann. “The interpretation of the new particles as displaced charge multiplets”. In:  
4917 *Il Nuovo Cimento* 4 (1956), 848–866.
- 4918 [62] W. Heisenberg. “Über den Bau der Atomkerne. I”. In: *Zeitschrift für Physik* 77 (1932), 1–11.
- 4919 [63] V.E. Barnes et al. “Observation of a Hyperon with Strangeness Minus Three”. In: *Phys. Rev.  
4920 Lett.* 12 (1964), pp. 204–206.
- 4921 [64] M. Gell-Mann. “A schematic model of baryons and mesons”. In: *Physics Letters* 8 (1964),  
4922 pp. 214–215.
- 4923 [65] G. Zweig. *An SU(3) Model for Strong Interaction Symmetry and its Breaking*. Tech. rep.  
4924 CERN-TH-401. CERN, 1964.
- 4925 [66] G. Zweig. *An SU(3) Model for Strong Interaction Symmetry and its Breaking (II)*. Tech. rep.  
4926 CERN-TH-412. CERN, 1964.
- 4927 [67] E.D. Bloom et al. “High-Energy Inelastic  $e - p$  Scattering at  $6^\circ$  and  $10^\circ$ ”. In: *Phys. Rev. Lett.*  
4928 23 (1969), pp. 930–934.
- 4929 [68] M. Breidenbach et al. “Observed Behavior of Highly Inelastic Electron-Proton Scattering”.  
4930 In: *Phys. Rev. Lett.* 23 (1969), pp. 935–939.
- 4931 [69] B.J. Bjørken & S.L. Glashow. “Elementary particles and SU(4)”. In: *Physics Letters* 11  
4932 (1964), pp. 255–257.
- 4933 [70] J. Iliopoulos & L. Maiani S. Glashow. “Weak Interactions with Lepton-Hadron Symmetry”.  
4934 In: *Phys. Rev. D* 2 (1970), pp. 1285–1292.
- 4935 [71] J.H. Christenson et al. “Evidence for the  $2\pi$  Decay of the  $K_2^0$  Meson”. In: *Phys. Rev. Lett.* 13  
4936 (1964), pp. 138–140.
- 4937 [72] M. Kobayashi & T. Maskawa. “CP-Violation in the Renormalizable Theory of Weak Inter-  
4938 action”. In: *Progress of Theoretical Physics* 49 (1973), pp. 652–657.
- 4939 [73] H. Harari. “A new quark model for hadrons”. In: *Physics Letters B* 57 (1975), pp. 265–269.
- 4940 [74] B. Richter et al. “Discovery of a Narrow Resonance in  $e^+e^-$  Annihilation”. In: *Phys. Rev.  
4941 Lett.* 33 (1974), pp. 1406–1408.
- 4942 [75] S. Ting et al. “Experimental Observation of a Heavy Particle  $J$ ”. In: *Phys. Rev. Lett.* 33  
4943 (1974), pp. 1404–1405.
- 4944 [76] S.W. Herb et al. “Observation of a Dimuon Resonance at 9.5 GeV in 400 GeV Proton-  
4945 Nucleus Collisions”. In: *Phys. Rev. Lett.* 39 (1977), pp. 252–255.

## BIBLIOGRAPHY

---

- 4946 [77] S. Abashi et al. “Search for High Mass Top Quark Production in  $\bar{p}p$  Collisions at  $\sqrt{s} =$   
4947 1.8 TeV”. In: *Phys. Rev. Lett.* 74 (1995), pp. 2422–2426.
- 4948 [78] F. Abe et al. “Observation of Top Quark Production in  $\bar{p}p$  Collisions with the Collider De-  
4949 tector at Fermilab”. In: *Phys. Rev. Lett.* 74 (1995), pp. 2626–2631.
- 4950 [79] F. Tkachov. “A contribution to the history of quarks: Boris Struminsky’s 1965 JINR publi-  
4951 cation”. In: (2009).
- 4952 [80] O.W. Greenberg. “Spin and Unitary-Spin Independence in a Paraquark Model of Baryons  
4953 and Mesons”. In: *Phys. Rev. Lett.* 13 (1964), pp. 598–602.
- 4954 [81] M.Y. Han & Y. Nambu. “Three-Triplet Model with Double  $SU(3)$  Symmetry”. In: *Phys.*  
4955 *Rev.* 139 (1965), B1006–B1010.
- 4956 [82] R.P. Feynman. “The behavior of hadron collisions at extreme energies”. In: *Conf. Proc.*  
4957 C690905 (1969), pp. 237–258.
- 4958 [83] J.D. Bjorken & E.A. Paschos. “Inelastic Electron-Proton and  $\gamma$ -Proton Scattering and the  
4959 Structure of the Nucleon”. In: *Phys. Rev.* 185 (1969), pp. 1975–1982.
- 4960 [84] M. Gell-Mann & H. Leutwyler H. Fritzsch. “Advantages of the color octet gluon picture”.  
4961 In: *Physics Letters B* 47 (1973), pp. 365–368.
- 4962 [85] D.J. Gross & F. Wilczek. “Ultraviolet Behavior of Non-Abelian Gauge Theories”. In: *Phys.*  
4963 *Rev. Lett.* 30 (1973), pp. 1343–1346.
- 4964 [86] H.D. Politzer. “Reliable Perturbative Results for Strong Interactions?” In: *Phys. Rev. Lett.* 30  
4965 (1973), pp. 1346–1349.
- 4966 [87] S. Bethke. “ $\alpha_s$  2002”. In: *Nuclear Physics B* 121 (2003), pp. 74–81.
- 4967 [88] E. Fermi. “Versuch einer Theorie der  $\beta$ -Strahlen. I”. In: *Zeitschrift für Physik* 88 (1934),  
4968 pp. 161–177.
- 4969 [89] W. Pauli. “Dear radioactive ladies and gentlemen”. In: *Phys. Today* 31N9 (1978), p. 27.
- 4970 [90] C.L. Cowan Jr. et al. “Detection of the Free Neutrino: a Confirmation”. In: *Science* 20 (1956),  
4971 pp. 103–104.
- 4972 [91] E.J. Konopinski & H.M. Mahmoud. “The Universal Fermi Interaction”. In: *Phys. Rev.* 92  
4973 (1953), pp. 1045–1049.
- 4974 [92] J. Steinberger et al. L.M. Lederman M. Schwartz. “Observation of High-Energy Neutrino Re-  
4975 actions and the Existence of Two Kinds of Neutrinos”. In: *Phys. Rev. Lett.* 9 (1962), pp. 36–  
4976 44.
- 4977 [93] T.D. Lee & C.N. Yang. “Question of Parity Conservation in Weak Interactions”. In: *Phys.*  
4978 *Rev.* 104 (1956), pp. 254–258.
- 4979 [94] G. Gamow & E. Teller. “Selection Rules for the  $\beta$ -Disintegration”. In: *Phys. Rev.* 49 (1936),  
4980 pp. 895–899.
- 4981 [95] C.S. Wu et al. “Experimental Test of Parity Conservation in Beta Decay”. In: *Phys. Rev.* 105  
4982 (1957), pp. 1413–1415.
- 4983 [96] S. Weinberg. “A Model of Leptons”. In: *Phys. Rev. Lett.* 19 (1967), pp. 1264–1266.
- 4984 [97] Y. Nambu & G. Jona-Lasinio. “Dynamical Model of Elementary Particles Based on an Anal-  
4985 ogy with Superconductivity. I”. In: *Phys. Rev.* 122 (1961), pp. 345–358.
- 4986 [98] Y. Nambu & G. Jona-Lasinio. “Dynamical Model of Elementary Particles Based on an Anal-  
4987 ogy with Superconductivity. II”. In: *Phys. Rev.* 124 (1961), pp. 246–254.

- 4988 [99] & J. R. Schrieffer J. Bardeen L.N. Cooper. “Microscopic Theory of Superconductivity”. In: *Phys. Rev.* 106 (1957), pp. 162–164.
- 4989
- 4990 [100] Y. Nambu. “Quasi-Particles and Gauge Invariance in the Theory of Superconductivity”. In: *Phys. Rev.* 117 (1960), pp. 648–663.
- 4991
- 4992 [101] J. Goldstone. “Quasi-Particles and Gauge Invariance in the Theory of Superconductivity”. In: *Il Nuovo Cimento* 19 (1961), pp. 154–164.
- 4993
- 4994 [102] P.W. Anderson. “Plasmons, Gauge Invariance, and Mass”. In: *Phys. Rev.* 130 (1963), pp. 439–442.
- 4995
- 4996 [103] J. Schwinger. “Gauge Invariance and Mass”. In: *Phys. Rev.* 125 (1962), pp. 397–398.
- 4997 [104] F. Englert & R. Brout. “Broken Symmetry and the Mass of Gauge Vector Mesons”. In: *Phys. Rev. Lett.* 13 (1964), pp. 321–323.
- 4998
- 4999 [105] P.W. Higgs. “Broken Symmetries and the Masses of Gauge Bosons”. In: *Phys. Rev. Lett.* 13 (1964), pp. 508–509.
- 5000
- 5001 [106] & T.W.B. Kibble G.S. Guralnik C.R. Hagen. “Global Conservation Laws and Massless Particles”. In: *Phys. Rev. Lett.* 13 (1964), pp. 585–587.
- 5002
- 5003 [107] Wikipedia. *Standard Model*. 2018. URL: [https://en.wikipedia.org/wiki/Standard\\_Model](https://en.wikipedia.org/wiki/Standard_Model).
- 5004
- 5005 [108] UA1 Collaboration. “Experimental observation of isolated large transverse energy electrons with associated missing energy at  $s = 540 \text{ GeV}$ ”. In: *Physics Letters B* 122 (1983), pp. 103–116.
- 5006
- 5007
- 5008 [109] UA2 Collaboration. “Observation of single isolated electrons of high transverse momentum in events with missing transverse energy at the CERN pp collider”. In: *Physics Letters B* 122 (1983), pp. 476–485.
- 5009
- 5010
- 5011 [110] UA1 Collaboration. “Experimental observation of lepton pairs of invariant mass around  $95 \text{ GeV}/c^2$  at the CERN SPS collider”. In: *Physics Letters B* 126 (1983), pp. 398–410.
- 5012
- 5013 [111] UA2 Collaboration. “Evidence for  $Z_0 \rightarrow e^+e^-$  at the CERN pp collider”. In: *Physics Letters B* 129 (1983), pp. 130–140.
- 5014
- 5015 [112] ATLAS Collaboration. “Observation of a new particle in the search for the Standard Model Higgs boson with the ATLAS detector at the LHC”. In: *Physics Letters B* 716 (2012), pp. 1–29.
- 5016
- 5017
- 5018 [113] CMS Collaboration. “Observation of a new boson at a mass of 125 GeV with the CMS experiment at the LHC”. In: *Physics Letters B* 716 (2012), pp. 30–61.
- 5019
- 5020 [114] CMS Collaboration ATLAS Collaboration. “Combined Measurement of the Higgs Boson Mass in  $pp$  Collisions at  $\sqrt{s} = 7$  and 8 TeV with the ATLAS and CMS Experiments”. In: *Physical Review Letters* 114 (2015). 191803.
- 5021
- 5022
- 5023 [115] M. Tanabashi et al. (Particle Data Group). “Review of Particle Physics”. In: *Phys. Rev. D* 98 (2018), p. 030001.
- 5024
- 5025 [116] A.A. Arkhipov. “Proton proton total cross-sections from the window of cosmic ray experiments”. In: *Elastic and diffractive scattering. Proceedings, 9th Blois Workshop, Pruhonice, Czech Republic*. 2001, pp. 293–304.
- 5026
- 5027
- 5028 [117] H. Pointcaré. “The Milky Way and the Theory of Gases”. In: *Popular Astronomy* 14 (1906), pp. 475–488.
- 5029
- 5030 [118] J.C. Kapteyn. “First Attempt at a Theory of the Arrangement and Motion of the Sidereal System”. In: *Astrophysical Journal* 55 (1922), p. 302.
- 5031

## BIBLIOGRAPHY

---

- 5032 [119] F. Zwicky. “Republication of: The redshift of extragalactic nebulae (First published in  
5033 1933)”. In: *General Relativity and Gravitation* 41 (2009), pp. 207–224.
- 5034 [120] F. Zwicky. “On the Masses of Nebulae and of Clusters of Nebulae”. In: *Astrophysical Journal* 86 (1937), p. 217.
- 5035 [121] H.W. Babcock. “The rotation of the Andromeda Nebula”. In: *Lick Observatory bulletin* 498  
5037 (1939), pp. 41–51.
- 5038 [122] V.C. Rubin & W.K. Ford Jr. “Rotation of the Andromeda Nebula from a Spectroscopic  
5039 Survey of Emission Regions”. In: *Astrophysical Journal* 159 (1970), p. 379.
- 5040 [123] D.H. Rogstad & G.S. Shostak. “Gross Properties of Five Scd Galaxies as Determined from  
5041 21-CENTIMETER Observations”. In: *Astrophysical Journal* 176 (1972), p. 315.
- 5042 [124] Planck Collaboration. “Planck 2015 results. XIII. Cosmological parameters”. In: *A&A* 594.A13  
5043 (2016).
- 5044 [125] N. Jarosik et al. “Seven-year Wilkinson Microwave Anisotropy Probe (WMAP\*) observa-  
5045 tions: Sky maps, Systematic errors, and Basic Results”. In: *ApJS* 192.14 (2011).
- 5046 [126] E. Verlinde. “Emergent Gravity and the Dark Universe”. In: *SciPost Phys.* 2 (2017), p. 016.
- 5047 [127] A. Maeder. “An alternative to the  $\Lambda$ CDM model: the case of scale invariance”. In: *ApJ*  
5048 834.194 (2017).
- 5049 [128] E. Corbelli & P. Salucci. “The extended rotation curve and the dark matter halo of M33”.  
5050 In: *Monthly Notices of the Royal Astronomical Society* 311 (2000), pp. 441–447.
- 5051 [129] S. Dimopoulos & H. Georgi. “Softly broken supersymmetry and SU(5)”. In: *Nuclear Physics*  
5052 B 193 (1981), pp. 150–162.
- 5053 [130] F. Tanedo. *The Hierarchy Problem: why the Higgs has a snowball’s chance in hell*. 2012.  
5054 URL: [https://www.quantumdiaries.org/2012/07/01/the-hierarchy-  
5055 problem-why-the-higgs-has-a-snowballs-chance-in-hell/](https://www.quantumdiaries.org/2012/07/01/the-hierarchy-problem-why-the-higgs-has-a-snowballs-chance-in-hell/).
- 5056 [131] M. Kamionkowski & K. Griest G. Jungman. “Supersymmetric dark matter”. In: *Physics*  
5057 *Reports* 267 (1996), pp. 10–14.
- 5058 [132] & P. Nath A.H. Chamseddine R. Arnowitt. “Locally Supersymmetric Grand Unification”.  
5059 In: *Phys. Rev. Lett.* 49 (1982), pp. 970–974.
- 5060 [133] A. Askew et al. “Searching for dark matter at hadron colliders”. In: *International Journal*  
5061 *of Modern Physics A* 29 (2014), p. 1430041.
- 5062 [134] S. Dimopoulos & G. Dvali N. Arkani-Hamed. “The hierarchy problem and new dimensions  
5063 at a millimeter”. In: *Physics Letters B* 429 (1998), pp. 263–272.
- 5064 [135] S. Dimopoulos & G. Dvali N. Arkani-Hamed. “Phenomenology, astrophysics, and cosmol-  
5065 ogy of theories with submillimeter dimensions and TeV scale quantum gravity”. In: *Phys.*  
5066 *Rev. D* 59 (1999), p. 086004.
- 5067 [136] T. Kaluza. “Zum Unitsproblem der Physik”. In: *Sitzungsber. Preuss. Akad. Wiss. Berlin*  
5068 (*Math. Phys.*) 1921 (1921), pp. 966–972.
- 5069 [137] O. Klein. “The Atomicity of Electricity as a Quantum Theory Law”. In: *Nature* 118 (1926),  
5070 p. 516.
- 5071 [138] L. Randall & R. Sundrum. “Large Mass Hierarchy from a Small Extra Dimension”. In:  
5072 *Phys. Rev. Lett.* 83 (1999), pp. 3370–3373.
- 5073 [139] L. Randall & R. Sundrum. “An Alternative to Compactification”. In: *Phys. Rev. Lett.* 83  
5074 (1999), pp. 4690–4693.

- 5075 [140] M. Strassler & K. Zurek. “Echoes of a hidden valley at hadron colliders”. In: *Phys. Let. B*  
5076 651 (2007), pp. 374–379.
- 5077 [141] A. Sakharov. “Violation of CP i variance, C asymmetry, and baryon asymmetry of the uni-  
5078 verse”. In: *JETP Letters* 5 (1967), pp. 24–27.
- 5079 [142] M.E. Shaposhnikov & G. Farrar. “Baryon asymmetry of the Universe in the minimal stan-  
5080 dard model”. In: *Phys. Rev. Lett.* 70 (1993), pp. 2833–2836.
- 5081 [143] V.A.Rubakov & M.E. Shaposhnikov V.A. Kuzmin. “On anomalous electroweak baryon-  
5082 number non-conservation in the early universe”. In: *Physics Letters B* 155 (1985), pp. 36–  
5083 42.
- 5084 [144] M. Drewes & M. Shaposhnikov L. Canetti. “Matter and antimatter in the universe”. In: *New  
5085 J. Phys.* 14.095012 (2012).
- 5086 [145] CMS Collaboration. “Search for black holes and sphalerons in high-multiplicity final states  
5087 in proton-proton collisions at  $\sqrt{s} = 13$  TeV”. In: *Journal of High Energy Physics* 11 (2018).
- 5088 [146] B. Shuve & Y. Cui. “Probing baryogenesis with displaced vertices at the LHC”. In: *Journal  
5089 of High Energy Physics* 2 (2015).
- 5090 [147] The ACME Collaboration. “Order of Magnitude Smaller Limit on the Electric Dipole Mo-  
5091 ment of the Electron”. In: *Science* 343 (2014), pp. 269–272.
- 5092 [148] N. Neri et al. “On the search for the electric dipole moment of strange and charm baryons  
5093 at LHC”. In: *The European Physical Journal C* 77 (2017), p. 181.
- 5094 [149] J. Stevens & M. Sher. “Detecting a heavy neutrino electric dipole moment at the LHC”. In:  
5095 *Physics Letters B* 777 (2018), pp. 246–249.
- 5096 [150] D.S. Harmer & K.C. Hoffman R. Davis Jr. “Search for Neutrinos from the Sun”. In: *Physical  
5097 Review Letters* 20 (1968), pp. 1205–1209.
- 5098 [151] B. Pontecorvo. “Neutrino Experiments and the Problem of Conservation of Leptonic Charge”.  
5099 In: *Sov. Phys. JETP* 26 (1968), pp. 984–988.
- 5100 [152] SNO Collaboration. “Direct Evidence for Neutrino Flavor Transformation from Neutral-  
5101 Current Interactions in the Sudbury Neutrino Observatory”. In: *Physical Review Letters*  
5102 89.011301 (2002).
- 5103 [153] M. Nakagawa & S. Sakata Z. Maki. “Remarks on the Unified Model of Elementary Parti-  
5104 cles”. In: *Progress of Theoretical Physics* 28 (1962), pp. 870–880.
- 5105 [154] P. Minkowski. “ $\mu \rightarrow e\gamma$  at a rate of one out of  $10^9$  muon decays?” In: *Physics Letters B*  
5106 67 (1977), pp. 421–428.
- 5107 [155] R.N. Mohapatra & G. Senjanović. “Neutrino Mass and Spontaneous Parity Nonconserva-  
5108 tion”. In: *Phys. Rev. Lett.* 44 (1980), pp. 912–915.
- 5109 [156] CERN. Geneva. LHC Experiments Committee. *CMS Physics Technical Design Report Vol-  
5110 ume II: Physics Performance*. Tech. rep. CERN-LHCC-2006-021 ; CMS-TDR-8-2. CMS  
5111 Collaboration, 2006.
- 5112 [157] P.W.F. Valle. “Neutrino physics overview”. In: *J. Phys.: Conf. Ser.* 53 (2006), pp. 473–505.
- 5113 [158] T. Massam et al. “Experimental observation of antideuteron production”. In: *Il Nuovo Ci-  
5114 mento A* 63 (1965), pp. 10–14.
- 5115 [159] ALEPH Collaboration. “Determination of the number of light neutrino species”. In: *Physics  
5116 Letters B* 231 (1989), pp. 519–529.
- 5117 [160] CERN, ed. (1985).

---

## BIBLIOGRAPHY

---

- 5118 [161] CERN, ed. (1986).
- 5119 [162] CERN, ed. (1994).
- 5120 [163] CERN, ed. (1998).
- 5121 [164] CERN, ed. (1999).
- 5122 [165] CERN. Geneva. LHC Experiments Committee. *Letter of Intent for A Large Ion Collider*  
5123 *Experiment [ALICE]*. Tech. rep. CERN-LHCC-93-016. ALICE Collaboration, 1993.
- 5124 [166] CERN. Geneva. LHC Experiments Committee. *ATLAS : technical proposal for a general-*  
5125 *purpose pp experiment at the Large Hadron Collider at CERN*. Tech. rep. CERN-LHCC-94-  
5126 43. ATLAS Collaboration, 1994.
- 5127 [167] CERN. Geneva. LHC Experiments Committee. *CMS : letter of intent by the CMS Col-*  
5128 *laboration for a general purpose detector at LHC*. Tech. rep. CERN-LHCC-92-003. CMS  
5129 Collaboration, 1992.
- 5130 [168] CERN. Geneva. LHC Experiments Committee. *LHCb : letter of intent*. Tech. rep. CERN-  
5131 LHCC-95-5. LHCb Collaboration, 1995.
- 5132 [169] L. Evans and P. Bryant. “LHC Machine”. In: *JINST* 3 (2008). S08001.
- 5133 [170] LHCb Collaboration. “Observation of  $J/\psi p$  Resonances Consistent with Pentaquark States  
5134 in  $\Lambda_b^0 \rightarrow J/\psi K^- p$  Decays”. In: *Physical Review Letters* 115 (2015). 072001.
- 5135 [171] LHCb Collaboration. “Observation of  $J/\psi \phi$  Structures Consistent with Exotic States from  
5136 Amplitude Analysis of  $B^+ \rightarrow J/\psi \phi K^+$  Decays”. In: *Physical Review Letters* 118 (2017).  
5137 022003.
- 5138 [172] ALICE Collaboration. *First results from proton-lead collisions*. URL: <http://aliceinfo.cern.ch/Public/en/Chapter1/results-pPb.html>.
- 5140 [173] ATLAS Collaboration. “Observation of a New  $\chi_b$  State in Radiative Transitions to  $\Upsilon(1S)$   
5141 and  $\Upsilon(2S)$  at ATLAS”. In: *Physical Review Letters* 108 (2012). 152001.
- 5142 [174] LHCb Collaboration. “First Evidence for the Decay  $B_s^0 \rightarrow \mu^+ \mu^-$ ”. In: *Physical Review*  
5143 *Letters* 110 (2013). 021801.
- 5144 [175] CERN. Geneva. *High-Luminosity Large Hadron Collider (HL-LHC) Technical Design Re-*  
5145 *port V. 0.1*. Tech. rep. CERN-2017-007-M. 2017.
- 5146 [176] CERN. Geneva. LHC Experiments Committee. *CMS, the Compact Muon Solenoid : tech-*  
5147 *nical proposal*. Tech. rep. CERN-2015-005. 2015.
- 5148 [177] CERN. Geneva. LHC Experiments Committee. *The Phase-2 Upgrade of the CMS Muon*  
5149 *Detectors*. Tech. rep. CERN-LHCC-2017-012, CMS-TDR-016. CMS Collaboration, 2017.
- 5150 [178] X. Tata M. Drees. “Signals for heavy exotics at hadron colliders and supercolliders”. In:  
5151 *Physics Letters B* 252 (1990), pp. 695–702.
- 5152 [179] D.A. Milstead et al. “Stable massive particles at colliders”. In: *Physics Reports* 438 (2007),  
5153 pp. 1–63.
- 5154 [180] Z. Ligeti et al. “Supermodels for early LHC”. In: *Physics Letters B* 690 (2010), pp. 280–  
5155 288.
- 5156 [181] CMS Collaboration. “Search for long-lived charged particles in proton-proton collisions at  
5157  $\sqrt{s} = 13$  TeV”. In: *Phys. Rev. D* 94 (2016), p. 112004.
- 5158 [182] V. Khachatryan et al. “Search for long-lived charged particles in proton-proton collisions at  
5159  $\sqrt{s} = 13$  TeV”. In: *Phys. Rev. D* 94 (2017). 112004.

- 5160 [183] M. Shaposhnikov A. Kusenko. “Supersymmetric Q-balls as dark matter”. In: *Physics Letters B* 418 (1998), pp. 46–54.
- 5161
- 5162 [184] B. Koch et al. “Black holes at LHC?” In: *J. Phys. G: Nucl. Part. Phys.* 34 (2007). S535.
- 5163 [185] J. Schwinger. “Magnetic Charge and Quantum Field Theory”. In: *Phys. Rev.* 144 (1966). 1087.
- 5164
- 5165 [186] M Yu Khlopov et al. “Dark matter with invisible light from heavy double charged leptons of almost-commutative geometry?” In: *Class. Quantum Grav.* 23 (2006). 7305.
- 5166
- 5167 [187] PoS, ed. *Search for Heavy Stable Charged Particles in CMS*. Vol. 084-EPS-HEP2009. 2009, p. 438.
- 5168
- 5169 [188] L.E. Medina Medrano et al. “Studies on Luminous Region, Pile-up and Performance for HL-LHC Scenarios”. In: *Proc. of International Particle Accelerator Conference (IPAC’17), Copenhagen, Denmark, 14-19 May, 2017*. JACoW, 2017, pp. 1908–1911.
- 5170
- 5171
- 5172 [189] CMS Collaboration. *CMS Luminosity - Public Results*. Version 158. 2019. URL: <https://twiki.cern.ch/twiki/bin/view/CMSPublic/LumiPublicResults>.
- 5173
- 5174 [190] CERN. Geneva. LHC Experiments Committee. *Technical Proposal for the Phase-II Upgrade of the CMS Detector*. Tech. rep. CERN-LHCC-2015-010, CMS-TDR-15-02. CMS Collaboration, 2015.
- 5175
- 5176
- 5177 [191] CERN. Geneva. LHC Experiments Committee. *The Phase-2 Upgrade of the CMS Level-1 Trigger - Interim Report to the LHCC*. Tech. rep. CERN-LHCC-2017-013, CMS-TDR-017. CMS Collaboration, 2017.
- 5178
- 5179
- 5180 [192] CERN. Geneva. LHC Experiments Committee. *The CMS muon project : Technical Design Report*. Tech. rep. CERN-LHCC-97-032. CMS Collaboration, 1997.
- 5181
- 5182 [193] CERN. Geneva. LHC Experiments Committee. *High-Luminosity Large Hadron Collider (HL-LHC) Preliminary Design Report*. Tech. rep. CERN-LHCC-94-38. CMS Collaboration, 1994.
- 5183
- 5184
- 5185 [194] F. Sauli. “GEM: A new concept for electron amplification in gas detectors”. In: *Nucl. Instr. Meth. Phys. Res.* 386 (1997), pp. 531–534.
- 5186
- 5187 [195] CERN. Geneva. LHC Experiments Committee. *CMS Technical Design Report for the Muon Endcap GEM Upgrade*. Tech. rep. CERN-LHCC-2015-012, CMS-TDR-013. CMS Collaboration, 2015.
- 5188
- 5189
- 5190 [196] A. Gelmi. *CMS iRPC at HL-LHC: background study*. 2018. URL: [https://indico.cern.ch/event/732794/contributions/3021836/attachments/1657792/2654574/iRPC\\_bkg\\_study\\_Upgrade29\\_05\\_18.pdf](https://indico.cern.ch/event/732794/contributions/3021836/attachments/1657792/2654574/iRPC_bkg_study_Upgrade29_05_18.pdf).
- 5191
- 5192
- 5193 [197] A. Gelmi & E. Voevodina. “Background rate study for the CMS improved-RPC at HL-LHC using GEANT4”. In: *Nucl. Instr. Meth. Phys. Res. A* (2018).
- 5194
- 5195 [198] IEEE, ed. *Petiroc, a new front-end ASIC for time of flight application*. Vol. 2013 IEEE Nuclear Science Symposium and Medical Imaging Conference (2013 NSS/MIC). 2014.
- 5196
- 5197 [199] JINST, ed. *Petiroc and Citiroc: front-end ASICs for SiPM read-out and ToF applications*. Vol. Topical Workshop on Electronics for Particle Physics 2013 (TWEPP-13). 2014.
- 5198
- 5199 [200] P.Bortignon. “Design and performance of the upgrade of the CMS L1 muon trigger”. In: *Nucl. Instr. Meth. Phys. Res.* 824 (2016), pp. 256–257.
- 5200
- 5201 [201] The European Parliament and the Council of the European Union. “Regulation (EU) No 517/2014 of 16 April 2014 on fluorinated greenhouse gases and repealing Regulation (EC) No 842/2006”. In: *Official Journal of the European Union* 150 (2014), pp. 195–230.
- 5202
- 5203

---

## BIBLIOGRAPHY

---

- 5204 [202] D. Piccolo. *Preliminary results of Resistive Plate Chambers operated with eco-friendly gas*  
5205 *mixtures for application in the CMS experiment*. 2016. URL: <https://indico.ugent.be/event/0/session/18/contribution/28/material/slides/0.pdf>.
- 5207 [203] R. Santonico and R. Cardarelli. “Development of resistive plate counters”. In: *Nucl. Instr.*  
5208 *Meth. Phys. Res.* 187 (1981), pp. 377–380.
- 5209 [204] Yu.N. Pestov and G.V. Fedotovich. *A picosecond time-of-flight spectrometer for the VEPP-*  
5210 *2M based on local-discharge spark counter*. Tech. rep. SLAC-TRANS-0184. SLAC, 1978.
- 5211 [205] W.W. Ash, ed. *Spark Counter With A Localized Discharge*. Vol. SLAC-R-250. 1982, pp. 127–  
5212 131.
- 5213 [206] I. Crotty et al. “The non-spark mode and high rate operation of resistive parallel plate cham-  
5214 bers”. In: *NIMA* 337 (1993), pp. 370–381.
- 5215 [207] I. Crotty et al. “Further studies of avalanche mode operation of resistive parallel plate cham-  
5216 bers”. In: *NIMA* 346 (1994), pp. 107–113.
- 5217 [208] R. Cardarelli et al. “Avalanche and streamer mode operation of resistive plate chambers”. In:  
5218 *NIMA* 382 (1996), pp. 470–474.
- 5219 [209] R. Cardarelli et al. “Performance of a resistive plate chamber operating with pure  $CF_3Br$ ”. In:  
5220 *NIMA* 333 (1993), pp. 399–403.
- 5221 [210] M. Abbrescia et al. “Performance of a Resistive Plate Chamber operated in avalanche mode  
5222 under  $^{137}Cs$  irradiation”. In: *NIMA* 392 (1997), pp. 155–160.
- 5223 [211] M. Abbrescia et al. “Properties of C2H2F4-based gas mixture for avalanche mode operation  
5224 of resistive plate chambers”. In: *NIMA* 398 (1997), pp. 173–179.
- 5225 [212] P. Camarri et al. “Streamer suppression with SF6 in RPCs operated in avalanche mode”. In:  
5226 *NIMA* 414 (1998), pp. 317–324.
- 5227 [213] E. Cerron Zeballos et al. “Effect of adding SF6 to the gas mixture in a multigap resistive  
5228 plate chamber”. In: *NIMA* 419 (1998), pp. 475–478.
- 5229 [214] E. Cerron Zeballos et al. “A new type of resistive plate chamber: The multigap RPC”. In:  
5230 *NIMA* 374 (1996), pp. 132–135.
- 5231 [215] M.C.S. Williams. “The development of the multigap resistive plate chamber”. In: *Nucl.*  
5232 *Phys. B* 61 (1998), pp. 250–257.
- 5233 [216] H. Czyrkowski et al. “New developments on resistive plate chambers for high rate opera-  
5234 tion”. In: *NIMA* 419 (1998), pp. 490–496.
- 5235 [217] CERN. Geneva. LHC Experiments Committee. *ATLAS muon spectrometer: Technical de-  
5236 sign report*. Tech. rep. CERN-LHCC-97-22. ATLAS Collaboration, 1997.
- 5237 [218] CERN. Geneva. LHC Experiments Committee. *ALICE Time-Of-Flight system (TOF) : Tech-  
5238 nical Design Report*. Tech. rep. CERN-LHCC-2000-012. ALICE Collaboration, 2000.
- 5239 [219] The CALICE collaboration. “First results of the CALICE SDHCAL technological proto-  
5240 type”. In: *JINST* 11 (2016).
- 5241 [220] PoS, ed. *Density Imaging of Volcanoes with Atmospheric Muons using GRPCs*. International  
5242 Europhysics Conference on High Energy Physics - HEP 2011. 2011.
- 5243 [221] C. Lippmann. “Detector Physics of Resistive Plate Chambers”. PhD thesis. Johann Wolf-  
5244 gang Goethe-Universität, 2003.
- 5245 [222] W. Riegler. “Induced signals in resistive plate chambers”. In: *NIMA* 491 (2002), pp. 258–  
5246 271.

- 5247 [223] M. Abbrescia et al. “Effect of the linseed oil surface treatment on the performance of resistive plate chambers”. In: *NIMA* 394 (1997), pp. 13–20.
- 5248
- 5249 [224] G.Battistoni et al. “Sensitivity of streamer mode to single ionization electrons”. In: *NIMA* 235 (1985), pp. 91–97.
- 5250
- 5251 [225] M. Abbrescia et al. “Cosmic ray tests of double-gap resistive plate chambers for the CMS experiment”. In: *NIMA* 550 (2005), pp. 116–126.
- 5252
- 5253 [226] JINST, ed. *Performance of the Resistive Plate Chambers in the CMS experiment*. The 9<sup>th</sup> International Conference on Positioin Sensitive Detectors. 2012.
- 5254
- 5255 [227] PoS, ed. *The CMS RPC detector performance during Run-II data taking*. The European Physical Society Conference on High Energy Physics (EPS-HEP2017). 2018.
- 5256
- 5257 [228] Honeywell International Inc. *Solstice(R) ze Refrigerant (HFO-1234ze): The Environmental Alternative to Traditional Refrigerants*. Tech. rep. FPR-003/2015-01. 2015.
- 5258
- 5259 [229] E. Cerron Zeballos et al. “A comparison of the wide gap and narrow gap resistive plate chamber”. In: *NIMA* 373 (1996), pp. 35–42.
- 5260
- 5261 [230] ALICE Collaboration. “A study of the multigap RPC at the gamma irradiation facility at CERN”. In: *NIMA* 490 (2002), pp. 58–70.
- 5262
- 5263 [231] B. Bonner et al. “A multigap resistive plate chamber prototype for time-of-flight for the STAR experiment at RHIC”. In: *NIMA* 478 (2002), pp. 176–179.
- 5264
- 5265 [232] S. Yang et al. “Test of high time resolution MRPC with different readout modes for the BESIII upgrade”. In: *NIMA* 763 (2014), pp. 190–196.
- 5266
- 5267 [233] A. Akindinov et al. “RPC with low-resistive phosphate glass electrodes as a candidate for the CBM TOF”. In: *NIMA* 572 (2007), pp. 676–681.
- 5268
- 5269 [234] JINST, ed. *Development of the MRPC for the TOF system of the MultiPurpose Detector*. RPC2016: XII Workshop on Resistive Plate Chambers and Related Detectors. 2016.
- 5270
- 5271 [235] M.C.S. Williams. “Particle identification using time of flight”. In: *Journal of Physics G* 39 (2012).
- 5272
- 5273 [236] A. Aliche et al. “Aging and rate effects of the Multigap RPC studied at the Gamma Irradiation Facility at CERN”. In: *NIMA* 579 (2007), pp. 979–988.
- 5274
- 5275 [237] M. Abbrescia et al. “The simulation of resistive plate chambers in avalanche mode: charge spectra and efficiency”. In: *NIMA* 431 (1999), pp. 413–427.
- 5276
- 5277 [238] JINST, ed. *Description and simulation of physics of Resistive Plate Chambers*. RPC2016: XII Workshop on Resistive Plate Chambers and Related Detectors. 2016.
- 5278
- 5279 [239] V. Fran ais. “Description and simulation of the physics of Resistive Plate Chambers”. PhD thesis. LPC - Laboratoire de Physique Corpusculaire - Clermont-Ferrand, 2017.
- 5280
- 5281 [240] H. Bethe. “Zur Theorie des Durchgangs schneller Korpuskularstrahlen durch Materie”. In: *Annalen der Physik* 397 (1930), pp. 325–400.
- 5282
- 5283 [241] International Commission on Radiation Units and Measurements. *Stopping Powers for Electrons and Positions*. Tech. rep. Report 37. 1984.
- 5284
- 5285 [242] International Commission on Radiation Units and Measurements. *Stopping Power and Ranges for Protons and Alpha Particles*. Tech. rep. Report 49. 1994.
- 5286
- 5287 [243] H. Bichsel. “A method to improve tracking and particle identification in TPCs and silicon detectors”. In: *NIMA* 562 (2006), pp. 154–197.
- 5288

## BIBLIOGRAPHY

---

- 5289 [244] W. W. M. Allison and J. H. Cobb. “Relativistic charged particle identification by energy  
5290 loss”. In: *Annual Review of Nuclear and Particle Science* 30 (1980), 253–298.
- 5291 [245] International Commission on Radiation Units and Measurements. *Average energy to pro-  
5292 duce an ion pair*. Tech. rep. Report 31. 1994.
- 5293 [246] I.B. Smirnov. “Modeling of ionization produced by fast charged particles in gases”. In:  
5294 *NIMA* 554 (2005), pp. 474–493.
- 5295 [247] J. Phys.: Conf. Ser., ed. <https://doi.org/10.1088/1742-6596/587/1/012035> *Results of the CAL-  
5296 ICE SDHCAL technological prototype*. 16th International Conference on Calorimetry in  
5297 High Energy Physics (CALOR 2014). 2015.
- 5298 [248] W. Riegler et al. “Detector physics and simulation of resistive plate chambers”. In: *NIMA*  
5299 500 (2003), pp. 144–162.
- 5300 [249] I.B. Smirnov. *HEED++ simulation program*. 2010. URL: <http://ismirnov.web.cern.ch/ismirnov/heed>.
- 5302 [250] S.F. Biagi. “Monte Carlo simulation of electron drift and diffusion in counting gases under  
5303 the influence of electric and magnetic fields”. In: *NIMA* 421 (1999), pp. 234–240.
- 5304 [251] W. H. Furry. “On Fluctuation Phenomena in the Passage of High Energy Electrons through  
5305 Lead”. In: *Phys. Rev.* 52 (1937), pp. 569–581.
- 5306 [252] H. Genz. “Single electron detection in proportional gas counters”. In: *Nucl. Instr. and Meth.*  
5307 112 (1973), pp. 83–90.
- 5308 [253] M. Abbrescia et al. “Resistive plate chambers performances at cosmic rays fluxes”. In:  
5309 *NIMA* 359 (1995), pp. 603–609.
- 5310 [254] M. Abbrescia et al. “Resistive plate chambers performances at low pressure”. In: *NIMA* 394  
5311 (1997), pp. 341–348.
- 5312 [255] M. Abbrescia. “Operation, performance and upgrade of the CMS Resistive Plate Chamber  
5313 system at LHC”. In: *NIMA* 732 (2013), pp. 195–198.
- 5314 [256] F. Thyssen. “Commissioning, Operation and Performance of the CMS Resistive Plate Cham-  
5315 ber System”. PhD thesis. Universiteit Gent, 2014.
- 5316 [257] M. Bianco. “ATLAS RPC certification and commissioning with cosmic rays”. PhD thesis.  
5317 Università del Salento, 2007.
- 5318 [258] M. Bianco. “ATLAS RPC certification with cosmic rays”. In: *NIMA* 602 (2009), pp. 700–  
5319 704.
- 5320 [259] M. Abbrescia et al. “Study of long-term performance of CMS RPC under irradiation at the  
5321 CERN GIF”. In: *NIMA* 533 (2004), pp. 102–106.
- 5322 [260] H.C. Kim et al. “Quantitative aging study with intense irradiation tests for the CMS forward  
5323 RPCs”. In: *NIMA* 602 (2009), pp. 771–774.
- 5324 [261] S. Agosteo et al. “A facility for the test of large-area muon chambers at high rates”. In:  
5325 *NIMA* 452 (2000), pp. 94–104.
- 5326 [262] PoS, ed. *CERN GIF ++ : A new irradiation facility to test large-area particle detectors for  
5327 the high-luminosity LHC program*. Vol. TIPP2014. 2014, pp. 102–109.
- 5328 [263] D. Pfeiffer et al. “The radiation field in the Gamma Irradiation Facility GIF++ at CERN”.  
5329 In: *NIMA* 866 (2017), pp. 91–103.
- 5330 [264] CAEN. *Mod. V1190-VX1190 A/B, 128/64 Ch Multihit TDC*. 14th ed. 2016.
- 5331 [265] CAEN. *Mod. VI718 VME USB Bridge*. 9th ed. 2009.

- 5332 [266] A. Fagot. *GIF Cosmic Muon Monte Carlo Simulation*. 2017. URL: <https://github.com/afagot/Cosmics-Simulation>.
- 5333
- 5334 [267] G. Pugliese et al. “Long-term performance of double gap resistive plate chambers under
- 5335 gamma irradiation”. In: *NIMA* 477 (2002), pp. 293–298.
- 5336 [268] G. Pugliese et al. “Aging study for resistive plate chambers of the CMS muon trigger detec-
- 5337 tor”. In: *NIMA* 515 (2003), pp. 342–347.
- 5338 [269] M. Capeans et al. on behalf of the GIF and GIF++ User Communities. “A GIF++ Gamma
- 5339 Irradiation Facility at the SPS H4 Beam Line”. CERN-SPSC-2009-029 / SPSC-P-339. 2009.
- 5340 [270] R. Guida et al. “Results about HF production and bakelite analysis for the CMS Resistive
- 5341 Plate Chambers”. In: *NIMA* 594 (2008), pp. 140–147.
- 5342 [271] F. Bellini et al. “Study of HF production in BaBar Resistive Plate Chambers”. In: *NIMA* 594
- 5343 (2008), pp. 33–38.
- 5344 [272] J. Eysermans. *WebDCS GIF++*. CERN. 2016. URL: <https://www.webdcs.cern.ch>.
- 5345
- 5346 [273] S. Carrillo A. Fagot. *GIF++ Offline Analysis v6*. 2017. URL: [https://github.com/afagot/GIF\\_OfflineAnalysis](https://github.com/afagot/GIF_OfflineAnalysis).
- 5347
- 5348 [274] H. Reithler. *Filters for GIF++*. RWTH Aachen University, CMS-CERN. 2013. URL: <https://edms.cern.ch/document/1324028/1>.
- 5349
- 5350 [275] R. Cardarelli et al. “RPC performance vs. front-end electronics”. In: *NIMA* 661 (2012),
- 5351 S198–S200.
- 5352 [276] A. Fagot. *GIF++ Data Acquisition Software for CMS RPC*. 2016. URL: [https://github.com/afagot/GIF\\_DAQ](https://github.com/afagot/GIF_DAQ).
- 5353
- 5354 [277] W-Ie-Ne-R. *VME 6021-23 VXI*. 5th ed. 2016.
- 5355 [278] Wikipedia. *INI file*. 2017. URL: [https://en.wikipedia.org/wiki/INI\\_file](https://en.wikipedia.org/wiki/INI_file).